Models of the Oxygen-Evolving Complex of Photosystem II

Thesis by
Jacob Steven Kanady

In Partial Fulfillment of the Requirements for the Degree of

Doctor of Philosophy

Division of Chemistry and Chemical Engineering

CALIFORNIA INSTITUTE OF TECHNOLOGY
Pasadena, California
2015

(Defended on 4 August 2014)

Dedicated to Andi.
Without her I would have never made it.

ACKNOWLEDGEMENTS

Over my five years at Caltech I have had the privilege to meet and work with a lot of great people while still still being able to spend time with my closest friends and family in Southern California. I would like to acknowledge up front that without my family, especially my wife Andi, there is no chance that I would have made it through. Now then:

I would first like to thank my advisor, Theodor Agapie. He has shown unflagging support of my scientific career, pushing me to apply for, and get with his helpl, the NSF, a trip to the Inorganic Chemistry G.R.C., and a trip to the Lindau Nobelauretes Meeting in Germany. And even when I was thinking about leaving and applying for jobs, although he disagreed with me, he supported me. He was also patient with me when science took longer than expected, took the time to talk to me about issues big and small, and always showed me respect. He also got me to experience the Eastern Sierras; without the group trips, I would never have gone on out there on my own. For all this, thank you.

Thanks to my committee members Jonas Peters, Mark Davis, Harry Gray, and Bob Grubbs. They gave excellent advice throughout my five years, and it was always evident that they cared about my progress and my future career. I would like to especially thank committee chair Jonas, for spending extra time with me after my props exam to discuss the beginnings of my independent career.

My graduate work was not done in a vacuum, and I would therefore like to acknowledge my fellow Agapie group members. Obviously, first and foremost, Dr. Emily Tsui. Much of the work in this thesis was done in collaboration with her. Her intensity and rigor made our science, and my scientific skill, much better. Thanks for the fun trips to Northern California and Mt. Whitney too!

I would like to thank the rest of Team Cubane. Dr. Po-Heng Lin's super-cool attitude and general goofiness was always appreciated, and without his work I would not have the dangler results that I do. Sandy Suseno's no-nonsense, straight-shootin' style will be missed, and the time I spent with Davide Lionetti on that high-vac line will be remembered much more fondly than when we were in the depths of it. I would also like to send my best wishes to those in the group carrying on the metal oxo torch: H.B. Lin,

Dr Zhiji Han, Dr. Siti Riduan, and Dr. Graham de Ruiter. Your lack of fear will suit this project well.

To rest of the group: Guy, you helped me through more stuff than you know. Thanks for being a good dude. Kyle, thanks for playing music that reminded me of home, and taking all the warmth into your legs so the rest of us could chill. Those days were always good. Justin, Thanks for humoring me with the glovebox trap situation; that…conversation taught me a lot, so thanks. Buss, thanks for getting me to go to the second pass and giving me something to chase up Mt. Whitney. To the Youngin's Marcus and Jes: thanks for being fun and nice people to be around; keep it up! Finally, to the original four: thank you all for setting up the lab and giving us examples of how to do synthetic inorganic chemistry and how to (and how not to) get enough sleep. Maddy, thanks for trying to herd cats and keep the lab safe. Paul and Sibo: thanks for all the great music. I really appreciate all the music you both introduced me to.

I would like to mention my two mentees, Wei Jian Ong and Alessandro Maggi; I learned a lot from both of you about leadership and communication. Thank you for forcing me to step-up and mature some.

The Caltech staff were *extremely* helpful. Thanks to Agnes Tong for talking me through some bad times; Mona Shahgholi for keeping the ESI working, which was absolutely critical for all of my projects; Dave VanderVelde for keeping the NMRs running; Mike Day and Mike Takase for help with some really tough crystallography; and finally Larry Henling, who helped me at all hours to mount crystals and solve their structures. He was also a great outfielder during softball season.

I would like to thank my collaborators. At LBNL, Dr. Rosalie Tran, Dr. Benedikt Lassalle, Dr. Ruchira Chatterjee, Dr. Cheraz Gul, and Dr. Junko Yano for X-ray spectroscopy and letting me tag along to a beamtime at SSRL. At UC Davis, Dr. Jamie Stull, Dr. Troy Stich, Luo Lu, and Prof. Dave Britt for EPR and their hospitality during my visit. At Caltech, Dr. José Mendoza-Cortés, Dr. Robert Nielson, and Prof. Bill Goddard III for computation and surviving the book chapter preparation process. At the Max Planck Institute Für Chemische EnergieKonversion, Dr. Vlad Martin-Diaconescu, Dr. Matti van Schooneveld, Vera Krewald, Prof. Dimitrios Manganas, and Prof. Serena DeBeer for computation and a range of spectroscopies. Without all of your

work, our understanding of our compounds and their relevance in the community would be greatly diminished.

Before my time at Caltech, a few people really helped start my scientific career. My high school chemistry teacher Mr. Ray Cruickshank first planted the seed. My undergraduate advisor Prof. Chris Vanderwal supported me and really introduced me to the idea of graduate school as an option, and my mentor Dr. Grant Shibuya's excellent lab technique set an great example when I began with research. I would also like to acknowledge Prof. Andy Borovik for getting me excited about bioinorganic chemistry, and Prof. Keith Woerpel for all of the life advice and honest friendship.

Finally, I would like to thank my friends and family. I have made some great friends here at Caltech. Davide and Mike, thanks for chilling with me the first few years. Drinking and golfing was always fun. Thanks to Grant, Naeem, Joey, Ryan, and Peter for pulling me through here at the end. I would also like to mention the Cp-Allstars; thanks for the good times and excuse to be outside. From home, I would like to thank James, my best man and best friend, for always giving me perspective on what is important in life and to always remember to chill out.

To my sister Jesica, you have always set the example for me and I had loved talking science and life with you. To my brother-in-law Nathan: thank you for being such a great friend and getting me to the top of Mt. Whitney. To Yen and Phiet, thank you for supporting me with love and food and advice. To my parents, thank you for rasing me to be curious and planting the desire to understand the world around me. Also for feeding me and clothing me and sending me to college.

Last, to my wife Andi: thank you for being the one thing in my life I am sure of, for loving me and listening to me, for taking me all over the world. I can't imagine my life without you.

With that, To Science!

RESPECTIVE CONTRIBUTIONS

Much of the work described in this thesis is the result of collaborative efforts. Specific notes are included for compounds not synthesized by the author; some general comments are given here.

Many of the studies of multimetallic clusters were carried out in close collaboration with Dr. Emily Y. Tsui. She originally synthesized and characterized the triarylbenzene ligand framework used throughout this thesis. She synthesized the first metal complexes of the ligand (M = Cu^{II}, Fe^{II}, Zn^{II}), of which magnetic susceptibility data are presented in Chapter 2, which Dr. Tsui and I collected in collaboration. All magnetic data was fit using a Matlab program written by Dr. Tsui. Additionally, the PMe_3 studies of the oxidized heterometallic cubane clusters (Chapter 5) were run in collaboration with Dr. Tsui.

In Chapter 3, the X-ray absorption spectroscopy studies were carried out by Drs. Rosalie Tran and Junko Yano, and the electron paramagnetic resonance studies were carried out by Dr. Jamie Stull, Dr. Troy Stich, Mr. Luo Lu, and Prof. R. David Britt. In Chapter 3, the magnetic susceptibility studies of the tetramanganese clusters were carried out in collaboration with Dr. Emily Tsui and Dr. Po-Heng Lin. In Chapter 5, the computational work was performed by Dr. José L. Mendoza-Cortés, Dr. Robert J. Nielson, and Prof. William A. Goddard III. The late Dr. Michael Day solved a number of the single crystal X-ray diffraction structures presented.

ABSTRACT

In the five chapters that follow, I delineate my efforts over the last five years to synthesize structurally and chemically relevant models of the Oxygen Evolving Complex (OEC) of Photosystem II. The OEC is nature's only water oxidation catalyst, in that it forms the dioxygen in our atmosphere necessary for oxygenic life. Therefore understanding its structure and function is of deep fundamental interest and could provide design elements for artificial photosynthesis and manmade water oxidation catalysts. Synthetic endeavors towards OEC mimics have been an active area of research since the mid 1970s and have mutually evolved alongside biochemical and spectroscopic studies, affording ever-refined proposals for the structure of the OEC and the mechanism of water oxidation. This research has culminated in the most recent proposal: a low symmetry Mn_4CaO_5 cluster with a distorted Mn_3CaO_4 cubane bridged to a fourth, dangling Mn. To give context for how my graduate work fits into this rich history of OEC research, Chapter 1 provides a historical timeline of proposals for OEC structure, emphasizing the role that synthetic Mn and MnCa clusters have played, and ending with our Mn_3CaO_4 heterometallic cubane complexes.

In Chapter 2, the triarylbenzene ligand framework used throughout my work is introduced, and trinuclear clusters of Mn, Co, and Ni are discussed. The ligand scaffold consistently coordinates three metals in close proximity while leaving coordination sites open for further modification through ancillary ligand binding. The ligands coordinated could be varied, with a range of carboxylates and some less coordinating anions studied. These complexes' structures, magnetic behavior, and redox properties are discussed.

Chapter 3 explores the redox chemistry of the trimanganese system more thoroughly in the presence of a fourth Mn equivalent, finding a range of oxidation states and oxide incorporation dependent on oxidant, solvent, and Mn salt. Oxidation states from Mn^{II}_4 to $Mn^{III}Mn^{IV}_3$ were observed, with 1-4 O^{2-} ligands incorporated, modeling the photoactivation of the OEC. These complexes were studied by X-ray diffraction, EPR, XAS, magnetometry, and CV.

As Ca^{2+} is a necessary component of the OEC, Chapter 4 discusses synthetic strategies for making highly structurally accurate models of the OEC containing both Mn and Ca in the Mn_3CaO_4 cubane + dangling Mn geometry. Structural and

electrochemical characterization of the first Mn_3CaO_4 heterometallic cubane complex—and comparison to an all-Mn Mn_4O_4 analog—suggests a role for Ca^{2+} in the OEC. Modification of the Mn_3CaO_4 system by ligand substitution affords low symmetry Mn_3CaO_4 complexes that are the most accurate models of the OEC to date.

Finally, in Chapter 5 the reactivity of the Mn_3MO_4 cubane complexes toward O-atom transfer is discussed. The metal M strongly affects the reactivity. The mechanisms of O-atom transfer and water incorporation from and into Mn_4O_4 and Mn_4O_3 clusters, respectively, are studied through computation and ^{18}O-labeling studies. The μ_3-oxos of the Mn_4O_4 system prove fluxional, lending support for proposals of O^{2-} fluxionality within the OEC.

TABLE OF CONTENTS

CHAPTER 1

HISTORICAL PERSPECTIVE & GENERAL INTRODUCTION

Published in part as:

Kanady, J. S.; Mendoza-Cortes, J. L.; Goddard, W. A.; Agapie, T. The Oxygen-Evolving Complex of Photosystem II: Structural, Computational, and Synthetic Advances Through the Years. In *Metalloproteins: Structure, Functions, and Interactions*, Goddard, W. A., Cho, A. E., Eds. Taylor & Francis Group, LLC; New York. *In Press.*

1.1 Photosynthesis and Photosystem II

One of the most fascinating and important transformations in nature is the biological generation of O_2 by the Oxygen Evolving Complex (OEC) of Photosystem II (PSII) in cyanobacteria and plants.[1] This transformation was responsible for the formation of the oxygenic atmosphere that has shaped the evolution of life on Earth as we know it. In this process, solar energy is converted to the reducing equivalents and proton gradient necessary to power carbon dioxide fixation and other processes of life, while forming dioxygen as byproduct. The biological catalyst, PSII, has been studied in detail for more than 50 years. Progress in understanding the site of catalysis, the OEC, has depended on advances in several fields, including biochemistry, biophysics, spectroscopy, inorganic chemistry, and computational chemistry. While many properties of the OEC are well documented and generally agreed upon, many aspects of the catalytic site remain controversial, with computational and experimental chemists still pushing the boundaries of our understanding of the OEC. In this chapter, the structural and mechanistic proposals of the OEC as they were reported chronologically and the technologies and methodologies that supported them, with a focus on the insight gained from recent synthetic inorganic work in the field, are reviewed to put this thesis into historical context.

Photosystem II is a 350 kDa homo-dimer in the thylakoid membrane with ca. 20 protein subunits.[1f, h] PSII absorbs photons that drive the separation of charge, which is transferred through several redox cofactors. The ultimate electron donor is water, being oxidized to O_2 and releasing four electrons and four protons. The chemiosmotic gradient generated by proton release powers ATP synthesis. The electrons are transferred from the site of catalysis, the OEC, through tyrosine D1-Tyr161 (Y_Z) to chlorophyll *a* P680,

pheophytin *a*, quinone A, and quinone B (Figure 1.1). Structurally, the D1 and D2 subunits make up the main membrane-bound core of PSII, with D1 containing much of the electron transfer pathway.[2] The other membrane bound subunits mainly function as a light absorption antenna via a multitude of cofactors to transfer the exciton to P680. There are also a number of extrinsic, water-soluble subunits that bind to the lumenal side of PSII that are proposed to stabilize the binding of the Ca^{2+} and Cl^{-} cofactors necessary for efficient oxygen evolution.[3]

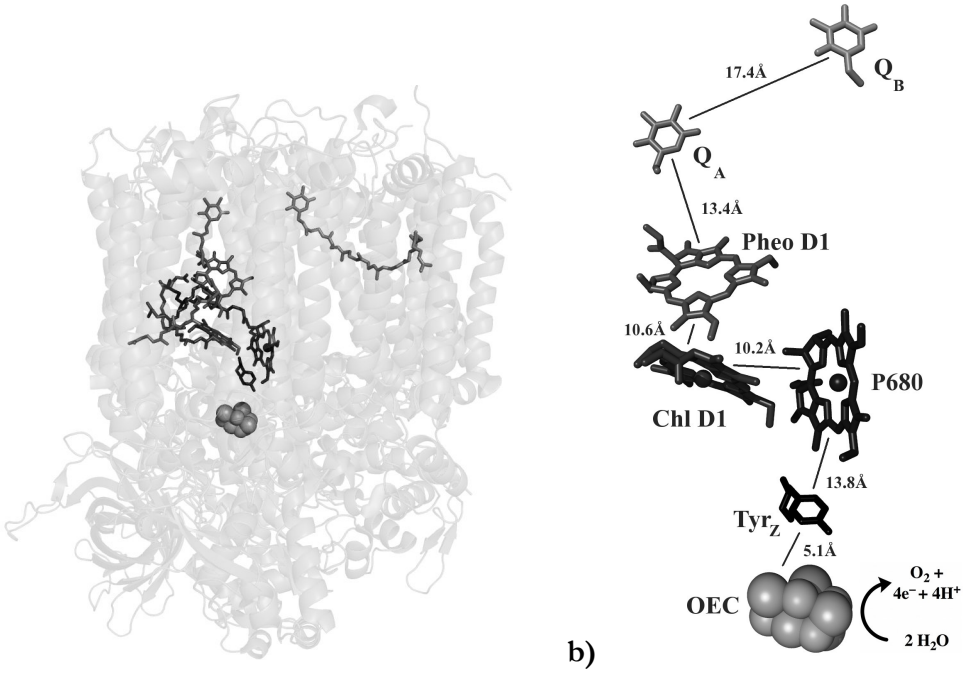

Figure 1.1 Electron transfer pathway shown in the overall PSII structure given by the 1.9Å diffraction data.[2b] (a) distances (b) aliphatic tails of the quinones, PheoD1, and chlorophylls are not shown for clarity.

1.2 The Oxygen-Evolving Complex: Composition and Kok Cycle

The OEC is located on the lumenal face of PSII with the majority of ligating side chains from the D1 subunit, positioning it approximately 5 Å away from Y_z.[2b] Manganese, calcium, and chloride are all necessary for OEC function. The OEC has been known to

contain Mn since the 1950s,[4] although oxygenic photosynthesis has been known to be Mn dependent for much longer.[5] As PSII isolation and purification methodology improved, the stoichiometry of four for Mn was verified by a number of methods, including quantitative electron paramagnetic resonance (EPR) spectroscopy of released Mn^{2+}, [6] and atomic absorption spectroscopy.[7] The specific importance of Ca^{2+} over other dications was proposed in the 1970s based on O_2 evolution activities at variable Ca^{2+} concentrations and the catalytic ineffectiveness or inhibitory effects of other dications.[8] [,3, 9] Given the redox nature of the catalytic reaction, the role of the redox inactive Ca^{2+} has been debated. Notably, the only metal to substitute for Ca^{2+} and generate a catalytic system, albeit with lower activity, is Sr^{2+}.[10] A single Ca^{2+} center is required for the restoration of the catalytic activity.[11] The close association of the redox inactive metal with the OEC was supported by early EPR data on Sr^{2+} substituted samples.[12] Removal of Ca^{2+} was shown by spectroscopy to arrest the catalytic cycle at intermediate states and affect electron transfer, further supporting the role of Ca^{2+} in catalysis.[13] More recently, EPR and XAS studies indicate that Ca^{2+} is part of the OEC.[14]

Until recently, Cl^- was also thought to be part of the OEC, as it is a native cofactor for O_2 production[15] and found to have a 1:1 stoichiometry with the OEC, based on $^{36}Cl^-$ labeling analysis.[16] However, more recent structural work suggests a role as H-bond acceptor in the secondary coordination sphere of the OEC.[2b, 17]

The OEC must be reassembled frequently under full solar flux due to photoxidative damage.[18] The assembly of the OEC, called photoactivation,[4b, 19] requires Mn^{2+}, Ca^{2+}, Cl^-, bicarbonate, water, and photogenerated oxidizing equivalents from P680.[20] A mechanism has been proposed based on kinetic and spectroscopic data: Mn^{2+} first binds to a "high-affinity"

site proposed to contain D1-Asp170,[21] and is photooxidized in low quantum yield to Mn^{3+}, giving intermediate one (IM_1). The quantum efficiency of this initial oxidation is dependent on the presence of Ca^{2+}, which can bind either before or after the initial Mn^{2+}.[22] Ca^{2+} is proposed to bridge to the Mn^{3+} center through oxide or hydroxide bridges. After binding a second Mn^{2+} and photooxidation, a rate limiting protein conformation change affords IM_2 that is quickly transformed into the OEC with additional Mn^{2+} equivalents in kinetically unresolved steps that must include deprotonation and incorporation of water as oxide donors.[20d, e, 22-23]

With respect to the mechanism of catalysis, a dependence of O_2 production on the number of short flashes of light on chloroplasts was discovered as early as the 1960s.[24] Dark-adapted chloroplasts gave a spike in O_2 production on the third millisecond flash, followed by shorter spikes every four subsequent flashes until steady state O_2 production was observed. Kok proposed that each flash corresponded to a photooxidative event, with three oxidizing equivalents stored until the fourth flash, upon which four-electron oxidation of water to O_2 occurs. In this so-called S-state cycle (Scheme 1.1), S_1 is the dark stable state and S_4 is the transiently formed state that releases O_2 and relaxes back to S_0. The four oxidations of the OEC have to be negative of $E^{o\prime}$= ca. 0.9V as necessitated by the potential of the $P680^+$; concurrent deprotonation helps keep the overall OEC charge low and thus levels the potentials of the S-state transition.[25] For the S-state cycle two possibilities have been put forward for the Mn oxidation states: the 'high' (Scheme 1.1) and the 'low' pathways. The high oxidation state pathway has been supported by electron paramagnetic resonance (EPR),[26] ^{55}Mn electron nuclear double resonance (ENDOR),[27] x-ray absorption spectroscopy (XAS),[28] and Kβ x-ray emission spectroscopy (XES).[29] However, biochemical and

spectroscopic data has also been interpreted to support the lower oxidation state cycle with a $Mn^{II}Mn^{III}{}_2Mn^{IV}$ or $Mn^{III}{}_4$ S_1 state.[30]

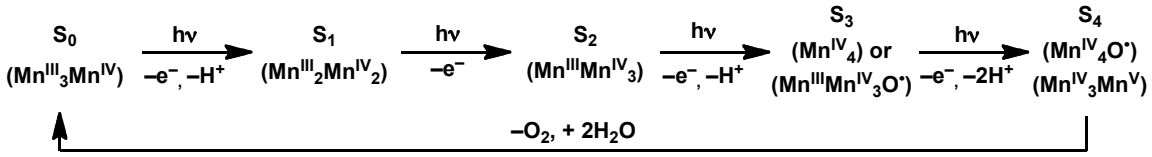

Scheme 1.1. The high oxidation state pathway for the S-state cycle.

Utilizing time-resolved mass spectrometry, Ollinger and Radmer[31] and then Messinger, Wydrzynski and coworkers[32] studied the kinetics of substrate water binding to the OEC throughout the S-state cycle. These studies found that: water is exchangeable through S_3, suggesting no intermediate oxidations of water occur;[31] in all of the S-states there are kinetically distinct, fast (40 s^{-1} for S_3 to $\geq$ 120 s^{-1} for S_0 & S_1) and slow (0.02 s^{-1} for S_1 to 10 s^{-1} for S_0) exchanging substrate waters, consistent with two separate sites of water coordination to the OEC;[32a, c, 33] both substrate waters are bound by the S_2 state;[32e] and Sr^{2+} substitution of Ca^{2+} gives an increase in rate for the slow exchanging water, suggesting it is bound to Ca^{2+}.[32f] There are a number of possible ways to explain the slow and fast exchanging waters, including protonation state, $Mn^{III,IV}$ or Ca^{2+} coordination, and terminal or bridging ligation mode. Thus, these studies are an important consideration for many mechanistic proposals for O-O bond formation (see Section 1.4).

1.3 Structural Proposals for the OEC: A Historical Perspective

Structural understanding of the OEC has gradually developed over the last 30 years, with many methods across multiple disciplines being paramount. Although multiple XRD structures are now known and provide the location and amino acid ligands of the OEC,[2, 17, 34]

changes in the structure of the OEC due to reductive X-ray damage have been a concern.[35] EPR[36] and XAS[37]—techniques used to study the OEC since the early 1980s[38]—complement the XRD data to afford more complete structural information. Crucial for these two methods was the parallel growth in the synthetic inorganic coordination chemistry of manganese, particularly of multinuclear cluster chemistry (Section 1.5).[39] The synthetic systems not only showed what was chemically reasonable to propose for the OEC based on precedent, but just as importantly they acted as spectroscopic benchmarks, providing starting points for hypotheses on how the OEC's spectra relate to structure. Simple synthetic complexes were also key in benchmarking quantum mechanical (QM) computation,[40] which has emerged as a crucial method in the study of the OEC. QM methods have improved drastically in the last decade to allow for structural hypotheses for every S state and mechanisms for substrate water incorporation and O_2 formation.[40g, 41]

With all of these different methods, and the improvements to each over time, numerous OEC structures have been proposed with a significant amount of disagreement and controversy over the years. The main models discussed over the last 25 years are shown schematically in Figure 1.2. One of the earliest models for the OEC with a specified geometry for the four manganese centers was the Mn_4O_4 cubane / Mn_4O_6 adamantane model proposed by Brudvig and Crabtree in 1986 (Figure 1.2a).[42] They proposed that a *pseudo*-Jahn-Teller distorted Mn_4O_4 cubane could explain their recent EPR data on the S_2 state that suggested two antiferromagnetically coupled dimers ferromagnetically coupled to the other.[43] They also posited that a large structural change in the S_2 to S_3 transition was consistent with x-ray absorption near-edge spectroscopy (XANES) K-edge data of the time that showed a decrease in edge energy between S_2 and S_3.[44] However, the high symmetry of

the proposed cubane and adamantane geometries did not prove consistent with extended x-ray absorption fine structure (EXAFS) reported subsequently.[45]

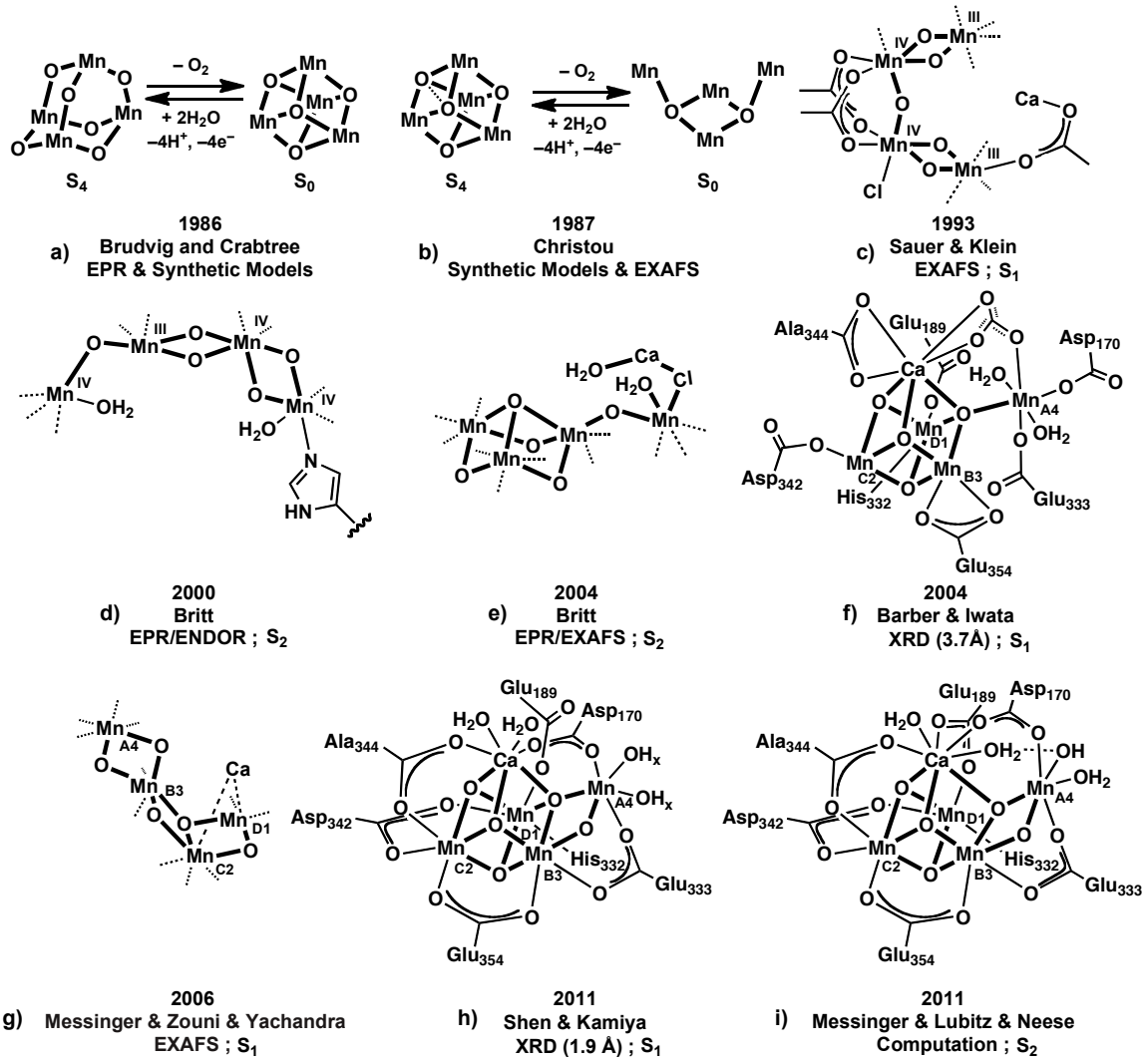

Figure 1.2. Key structural models of the OEC. The research group, year, main spectroscopic support, and S-state are included below each structure. Crystal structure resolutions are in parentheses. Dashed lines represent generic coordination sites and could represent amino acids or water. In f through i, Mn numbering combines EXAFS nomenclature (Mn_{A-D})[14c] with that of the 2005 and 2011 crystal structures (Mn_{1-4})[2b, 34c] in the style of ref. 46.

Another OEC model based on a Mn_4O_4 cubane was put forward soon after and was dubbed the "double-pivot" mechanism by Vincent and Christou (Figure 1.2b).[47] Here, a Mn_4O_2 butterfly structure in the S_0 to S_2 states was proposed to bind and deprotonate two water molecules to afford a $Mn_4O_2(OH)_2$ cubane structure that upon double deprotonation affords dioxygen and the S_0 butterfly structure. Key to the proposal was a synthetically characterized Mn_4O_2 structure (Figure 1.4c) that contained Mn-Mn vectors at ca. 2.7 and 3.3 Å, similar to those found in past EXAFS studies.[38d, 48] Although further EXAFS studies[49] were not consistent with this proposal, synthetic work by the groups of Christou and Dismukes detailed a variety of structural motifs and properties of clusters of these types. (Section 1.5).

A structural model based on oriented-membrane-EXAFS was proposed in 1993 and is generally referred to as the "dimer-of-dimers" model.[50] The basic structure is two $Mn_2(\mu_2\text{-}O)_2$ dimers connected through a mono-μ-O and/or k^2-carboxylates (Figure 1.2c). The Cl^- and Ca^{2+} cofactors were originally proposed to bind Mn and to bridge to the end of one Mn_2O_2 dimer unit through a carboxylate, respectively. The dimer-of-dimers served as the basis for a number of mechanistic proposals, including a metalloradical mechanism[51] and a nucleophilic attack by calcium-ligated hydroxide/water on an electrophilic $Mn^V{=}O$.[52]

A different structure, the "trimer/monomer," "3+1", or "dangling Mn" model (Figure 1.2d,e), was proposed based on EPR experiments. Britt and coworkers posited that the magnetic interaction of the Mn in the dimer-of-dimers model could not explain the high-spin g=4.1 signal and the changes to the g=2 multiline signal upon addition of methanol and ammonia.[53] The 3+1 motif, which had been included as a possible structure based on EXAFS data on S_2 (i.e., Figure 9 of ref. 54), could explain the EPR data as a strongly

antiferromagnetically coupled III,IV,IV trimer only weakly coupled to the fourth, "dangling" Mn^{IV}. A handful of trimer/monomer arrangements were proposed that fit the EPR and EXAFS data of the time.[26] Soon after this, the first crystal structures of PSII were reported,[2a, 34a] and although the resolution was only 3.8 Å (2001) or 3.7 Å (2003), the manganese electron density was consistent with a 3+1 arrangement. In 2004, based on a higher resolution of 3.5 Å, Barber and Iwata proposed a more specific structure: a Mn_3CaO_4 cubane with a fourth manganese connected by a cubane oxygen (Figure 1.2f).[34b] This was consistent with the EPR proposal and also the Ca K-edge XAS data that suggested a Ca-Mn distance of 3.4 Å.[14b] In 2005, a higher resolution structure of 3.0 Å was published that reported the OEC in a 3+1 arrangement as being more distorted and elongated than a cubane motif, without proposing the position for the bridging oxides (the same group published a 2.9 Å PSII structure in 2009 with no change to the OEC geometry).[17, 34c]

XAS studies in 2005 showed that the x-ray dose used in the XRD analysis of PSII caused reductive damage to the OEC, shedding doubt on the accuracy of the proposed OEC arrangement as based on crystal structures.[35] Polarized EXAFS studies at much lower X-ray dosage on PSII single crystals were used to provide an updated structure of the OEC (Figure 1.2g) with an asymmetric dimer of Mn_2O_2 diamond cores.[14c] A different interpretation of the EXAFS data invoked a cubane with a dangler motif.[25d] In 2011 a significantly higher resolution (1.9 Å) crystal structure was published[2b] with purported X-ray dosage below the damage level reported in 2005. Here a "chair" geometry of the Mn_4CaO_5 was observed at atomic resolution, similar to that proposed in the 2004 crystal structure, but with an extra μ_2-O between the dangling Mn and the cubane (Figure 1.2h, Figure 1.3).

There has been controversy over the OEC assignment in this recent XRD study because some of the Mn–O bond lengths are not consistent with a supposed S_1 oxidation state of $Mn^{III}_2Mn^{IV}_2$. Three explanations have come out in the literature, all based on computational modeling: the OEC structure is accurate and supports the low-oxidation state Kok cycle, with a Mn^{III}_4 S_1 state;[30c, 55] X-ray damage has produced a mixture of reduced oxidation states including S_{-n} states;[56] and the observed electron density is a superposition of two S_1 substates in equilibrium by a μ-O migration and proton transfer.[57] Another computational study suggested a similar substate equilibrium for S_2, claiming to explain the

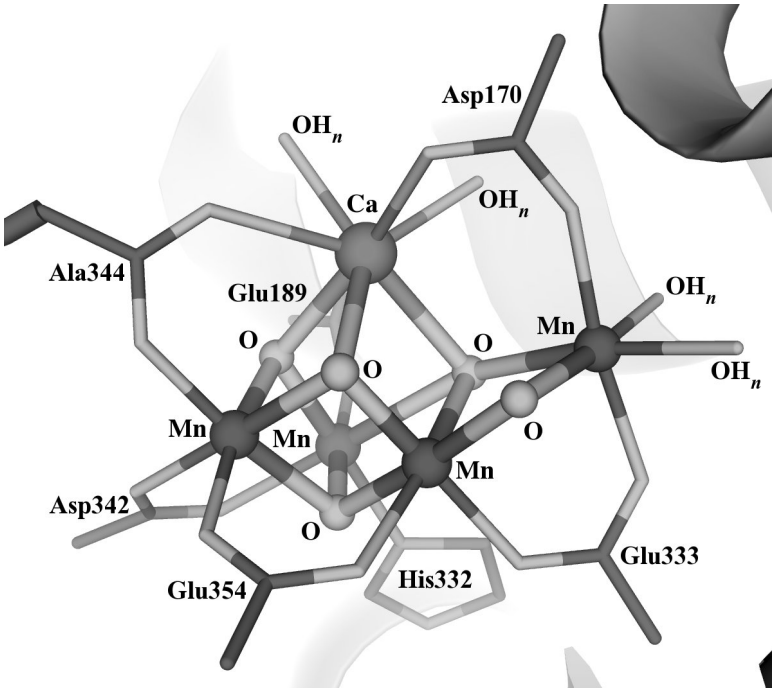

Figure 1.3. The oxygen-evolving complex as described by the 1.9 Å resolution crystal structure.[2b]

two S_2 EPR signals through changes in the magnetic coupling caused by μ-O migration from the cubane unit to form a diamond core with the dangling Mn (Figure 1.2i).[56a, 58] Although some controversy still remains about the structural assignment of the OEC from the 1.9 Å

PSII structure, the present data converge toward a cluster with a $CaMn_3$ site (part of a cubane or distorted cubane) and a dangler Mn center, with bridging oxido moieties.

1.4 Mechanism of O–O bond formation

Paralleling the wide assortment of OEC structures put forward, several mechanisms for O-O bond formation have been proposed.[1g, 25d, 36c, 41a, 59] Consistency with XAS, EPR, XRD, and substrate water exchange studies are required for advancing any mechanism, and developments in these fields have disproved many past proposals, such as the adamantane and double-pivot mechanisms discussed above.[42, 45, 47a, 49, 60] As with the structural hypotheses, some mechanisms have their basis in the chemistry of synthetic transition metal complexes. Copper has been shown to break and form the O-O bond of O_2 in an equilibrium between a $Cu^{III}_2(\mu_2\text{-}O)_2$ diamond core and a $Cu^{II}_2(\mu\text{-}h^2\text{:}h^2\text{-}O_2)$ bridging peroxide.[61] Similar proposals for diamond core O-O bond formation in the OEC exist (Scheme 1.2a); [1d, 47a, 62] however, the fast and slow water exchange kinetics are difficult to explain by such mechanisms.[60] Dinuclear ruthenium water oxidation catalysts have been shown to function through a H-bonding, nucleophilic water attacking a Ru^V-oxo intermediate,[59c, 63] and a Mn_2O_2 O_2-evolving catalyst has been proposed to act similarly through a Mn^V-oxo[64] or Mn^{IV}-oxyl radical.[40d] Water attack on an electrophilic $Mn^{IV/V}$-oxo has likewise been proposed for the OEC, with the attacking water in a number of different states, both terminal and bridging: as a H-bonding water/hydroxide,[32a] as Mn^{n+}-bound water/hydroxide,[51] or as Ca^{2+}-bound water/hydroxide (Scheme 1.2b).[52, 64a, 65] Brudvig and Batista proposed a Ca^{2+}-OH_2 nucleophilic attack mechanism supported by QM/MM calculations;[40f, g, 65c] however, another

QM approach used for the OEC and the first coordination shell implicated a different ground state structure.[66]

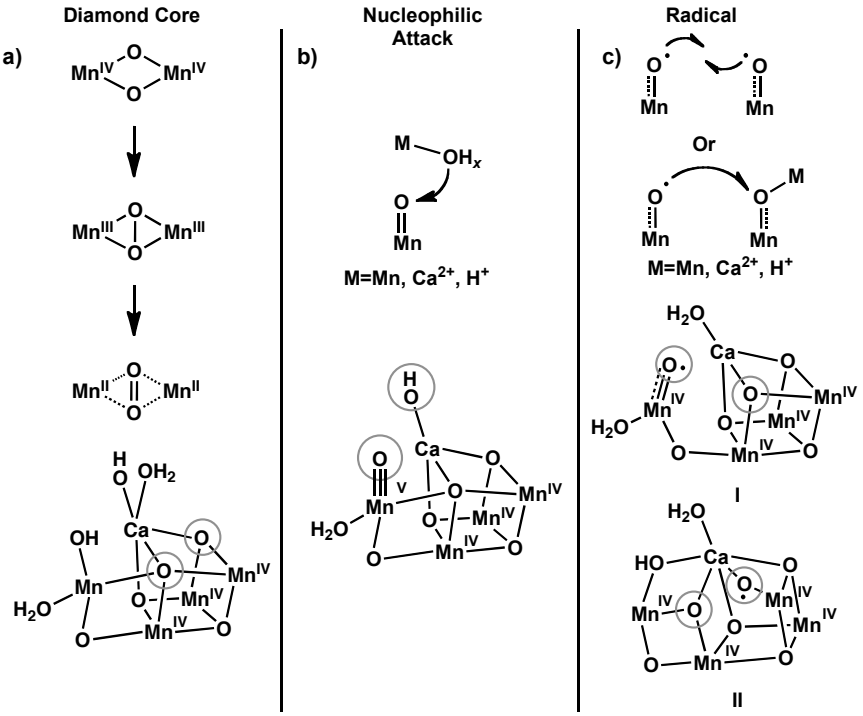

Scheme 1.2. Proposed mechanisms for O-O bond formation depicted minimally with metal-oxo species (top) and as part of the most recent structural models of the OEC (bottom).

The computational work of Siegbahn has supported an oxyl radical (Mn^{IV}-$O^{\bullet}$) in O-O bond formation at the OEC (Scheme 1.2c).[40b-d, 41a, 66-67] Others have proposed mechanisms including radical intermediates as well.[68] Both terminal[67b] (Scheme 1.2c-I) and bridging[41a] (Scheme 1.2c-II) oxyl radical intermediates have been discussed, with recent computational work supporting the coupling of a Mn/Mn/Ca-μ_3-oxo and a Mn/Ca-μ_2-oxyl in the S_4 state (Scheme 1.2c-II).[69] Recent ^{17}O-ENDOR studies mapped the substrate water exchange kinetics onto both the nucleophilic attack or bridging oxyl-coupling mechanisms.[46] Overall, a truly interdisciplinary approach of combining spectroscopy, structural characterization,

computation, and comparisons to synthetic models has funneled the mechanistic proposals for water oxidation to only a few candidates. Further detailing the mechanism of O-O bond formation is very desirable for both fundamental reasons and application toward the development of practical artificial catalysts. Additional studies from multiple perspectives are necessary to achieve that goal.

1.5 Synthetic OEC Model Coordination Complexes and a General Introduction

Synthetic manganese coordination clusters have played an important role in our understanding of the OEC, both inspiring the structural and mechanistic hypotheses of their time, and also being targeted due to the OEC structural motifs proposed based on other various analytical techniques. Model complexes, detailed in a number of reviews,[39] have been an instrumental benchmarking tool for XAS, EPR, water exchange rates, and computation. This historically collaborative effort is highlighted by numerous examples over the past 40 years, from the original manganese-bipyridine dimer and tetramanganese dimer-of-dimer models, to the more recent manganese/calcium heterometallic models.

In 1972, Stoufer and coworkers published the X-ray crystal structure of di-μ-oxo-tetrakis(2,2´-bipyridine)dimanganese(III,IV), showing a Mn-Mn distance of 2.716Å and finding strong antiferromagnetic coupling (Figure 1.4a).[70] These two observations on a model complex were utilized to conclude that the Mn_2O_2 diamond core was a key structural motif within the OEC: comparison of the S_2-state multiline EPR signal to that of the complex[38a, b, 71] supported the idea of an antiferromagnetic $Mn^{III}Mn^{IV}$ pair within the OEC, and the original OEC EXAFS studies of 1981[38d] found Mn-Mn distances of 2.7 Å, consistent with the Mn_2O_2 core characterized by crystallography. More recently, a similar

Mn_2O_2 dimer using terpyridine rather than bipyridine was reported to oxidize water using hypochlorite (NaOCl) or oxone (H_2SO_5) as the stoichiometric oxidant (Figure 1.4h).[64] Relevant to mechanistic interpretations for the OEC, the water exchange rates of the Mn^{III}-O-Mn^{IV} units of the bi- and terpyridine manganese dimers were measured by a time-resolved mass spectrometry technique.[60, 72] The exchange rates were much slower (10^{-3}-10^{-4} s^{-1}) than those of the OEC (ca. 1 s^{-1}), which is not consistent with mechanisms that invoked bridging oxo units as substrate water in the OEC.

Wieghardt and coworkers synthesized the first Mn^{IV}_4 complex, a $Mn_4O_6^{4+}$ adamantane stabilized by three chelating 1,4,7-triazacyclononane ligands (Figure 1.4b).[73] With this precedent, the adamantane/cubane mechanistic proposal for the OEC invoked access to such a high oxidation state cluster.[42] Each Mn^{IV} displays a *pseudo*-octahedral coordination environment with three μ_2-oxido and three terminal N donors. Armstrong and coworkers further studied the Mn_4O_6 adamantane core structure, evaluating the effect of altering the chelating N_3 ligand on the basicity of the μ_2-oxido moiety and on the pH dependent reduction potential.[74] More recently, the Mn^{IV}-O-Mn^{IV} water exchange rate of the adamantane geometry was measured to be $\leq 10^{-8}$ s^{-1}.[60]

The Mn_4O_4 cubane geometry was common to both the adamantane/cubane (1986) and the double-pivot (1987) mechanisms.[42, 47b] Tetramanganese complexes had been isolated in such a geometry;[75] however, these were low oxidation state Mn^{II}_4 structures with μ_3-alkoxides rather than oxides. Christou and coworkers synthesized the first cubane complex with μ_3-O bridges: $[Mn^{III}_3Mn^{IV}O_3Cl_6(ImH)(OAc)_3]^{2-}$ (ImH = neutral imidazole; Figure 1.4d).[76] Over the following decade, the $Mn^{III}_3Mn^{IV}O_3X$ cubanes/partial cubanes were studied

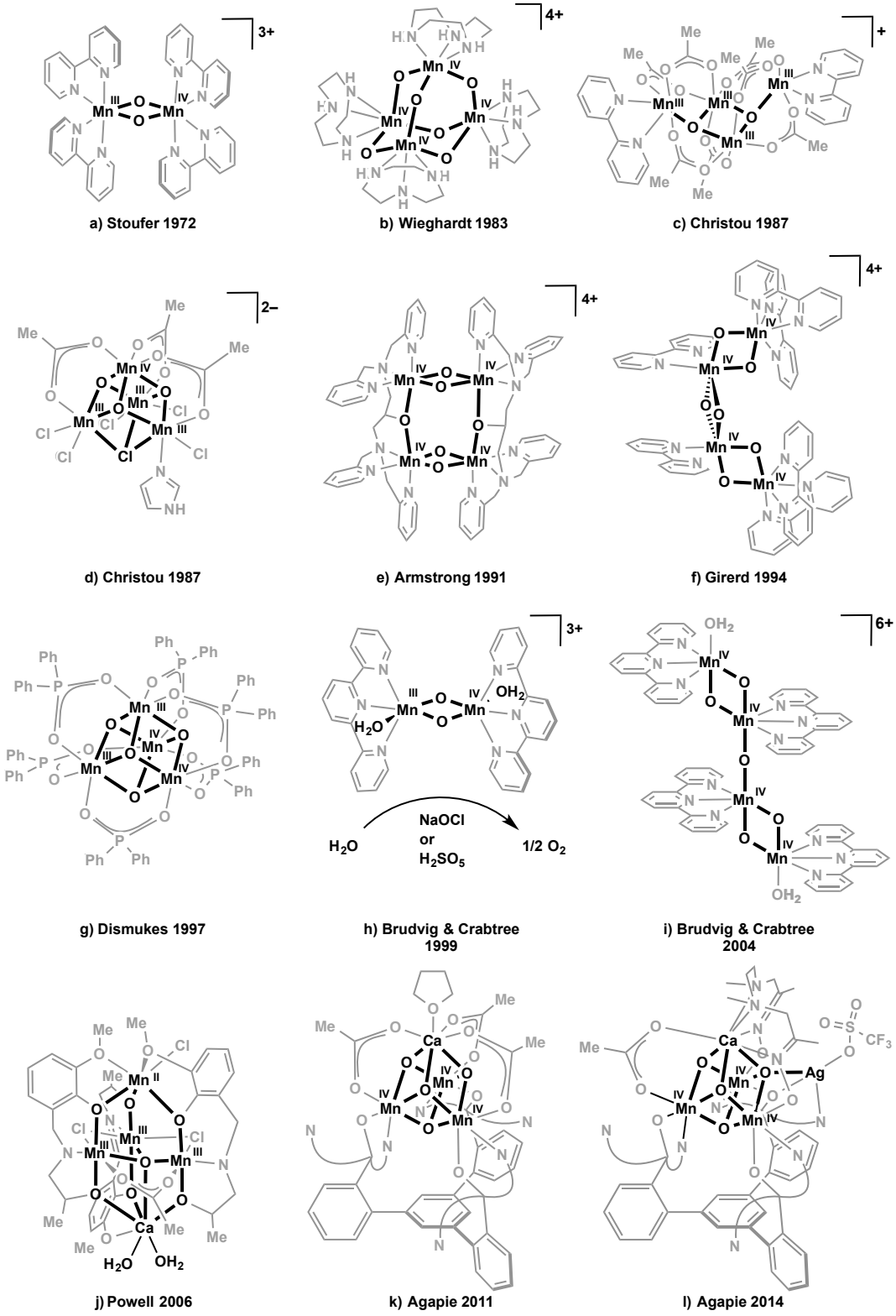

Figure 1.4. Selection of synthetic models relevant to the OEC.

in great detail, with variation of terminal ligands (Cl^-, pyridines, acetylacetonates, etc) and the anionic μ_3-X position (X = Cl^-,Br^-, I^-, F^-, N_3^-, O_2CR^-, OMe^-, and OH^-).[76-77] For example, they were able to synthetically model the S_1 to S_2 step of the proposed double pivot mechanism,[77a] utilizing a $Mn^{III}{}_4O_2$ butterfly complex (Figure 1.4c) to form a $Mn^{III}{}_3Mn^{IV}O_3Cl$ cubane by addition of chloride and disproportionation. In another reactivity study, water was selectively deprotonated and incorporated into the μ_3-X position, modeling a key functional step in OEC photoassembly and turnover.[77i]

Extensive magnetism[77b, d, g, h, k, m] and XAS[77j] studies were performed on the Mn_4O_3X cubanes to test the hypothesis that the OEC was not a high symmetry cubane structure.[45b, 48] Although the K-edge XANES and EXAFS spectra looked superficially similar to those of the OEC in the S_1 state, detailed analysis indicated that the structural motif contained in these synthetic clusters did not match the data from the biological system. Also of note, the K-edge energy varied by more than 3 eV for a series of cubanes in the same oxidation state and similar geometry, supporting the notion that in addition to the formal metal oxidation state, the nature of the ligands strongly affects the edge energy. This convolution of effects complicates the interpretation of the edge energies of various clusters and continues to cause disagreement over the oxidation state of the OEC.[30b]

Other systems that gave some support for the double pivot mechanism were the diarylphosphinate-stabilized $Mn^{III}{}_2Mn^{IV}{}_2O_4{}^{6+}$/$Mn^{III}Mn^{IV}{}_3O_4{}^{7+}$ cubanes synthesized by Dismukes and coworkers (Figure 1.4g).[78] They found that these cubane complexes lose one phosphinate ligand and a molecule of O_2 upon UV photolysis in the gas phase,[79] indicating the ability of a Mn_4O_4 cubane to form dioxygen as previously proposed for PSII.[47a] This system was later found to electrochemically oxidize water if imbedded in Nafion;[80] however,

further study showed that decomposition to an amorphous manganese oxide provided the active catalyst.[81] The Mn_3-μ_3-O water exchange rates measured in organic solvent (10^{-5} s^{-1}) were one to two orders of magnitude slower than the synthetic complex Mn^{III}-μ_2-O-Mn^{IV} rate (10^{-3}-10^{-4} s^{-1}) and thus much slower than those found for the OEC.[82]

As spectroscopic[6, 43, 83] and biochemical[7] support for a tetramanganese OEC grew, Mn_4 complexes were targeted that contained the 2.7 and 3.3 Å Mn-Mn vectors reported for the OEC.[39a, d] For example, alongside the butterfly systems discussed above,[84] Armstrong's group reported a series of dimer-of-dimer geometries.[85] They contained two 2.7 Å Mn-Mn vectors each, and the EPR of the highest oxidation state dimer—with two Mn^{III}-$(\mu\text{-O})_2$-Mn^{IV} diamond cores (Figure 1.4e)—modeled that of the S_1 state. Towards modeling the EXAFS dimer-of-dimers proposal in 1993,[50] complexes such as the Mn^{IV}_4 diamond core chain structure by Girerd and coworkers (Figure 1.4f)[86] and the $[Mn^{IV}$-$(\mu_2\text{-O})_2$-$Mn^{IV}]_2O$ dimer-of-dimers by Brudvig and coworkers (Figure 1.4i)[87] were reported.

Based on Ca K-edge XAS data, the calcium ion was proposed to be closely associated with the tetramanganese motif of the OEC, with a Mn-Ca vector of 3.4 Å.[14b] In agreement, the 2004 crystal structure proposed an OEC structure displaying a Mn_3CaO_4 cubane moiety. Calcium is necessary for photoactivation (cluster assembly from Mn^{2+} in solution under light) and turnover of the OEC. Synthetic Mn/Ca complexes were targeted to understand the effect of the redox inactive metal on the chemistry of manganese clusters. The first high oxidation state Mn/Ca cluster was isolated in 2005 and contained a Mn_4CaO_4 motif quite similar to the 2004 crystal structure as part of a high nuclearity $Mn_{13}Ca_2O_{10}$ cluster coordinated by benzoates.[88] A Ca K-edge XAS study on this cluster showed a Mn-Ca vector of ca. 3.5 Å similar to the one in the OEC.[89] Two Mn/Ca complexes have been

synthesized with the correct Mn_4Ca metal stoichiometry, although in low oxidation state and with low oxide content. The first contains a trigonal bipyramidal arrangement of metals with a Mn^{II} and Ca^{2+} at the two vertices and one μ_4-oxide, with a low $Mn^{III}_3Mn^{II}$ oxidation state (Figure 1.4j).[90] Similar complexes isolated later by the same group showed O_2 evolution in the presence of O-atom transfer agents and water.[91] A more recent cluster displays a Mn^{III}_4 metallocrown moiety with a Ca^{2+} center coordinated to one side of the crown and chelated by carboxylates; this cluster contains no bridging oxido ligands.[92] Other Mn/Ca structures—a low oxidation state $Mn^{II}_4Ca_2$ cluster[93] and a high nuclearity $Mn^{III}_6Ca_2O_2$ complex[94]—have also been reported.

Most of the multinuclear complexes discussed above were synthesized by self-assembly methodology that offers only low control over the geometry and nuclearity of the final complex. Although this manganese cluster chemistry has been invaluable to understanding the OEC, new methods for the controlled synthesis of Mn/Ca complexes are important, especially with the structure of the OEC emerging as a low symmetry Mn_4CaO_5 cubane/open cubane. In related bioinorganic studies, Holm and coworkers pioneered a synthetic protocol, termed "subsite-specific functionalization," to study the properties of ubiquitous Fe_4S_4 biological clusters. A wide array of ligand-differentiated $Fe_4S_4X_3X'$ and metal-differentiated Fe_3MS_4 complexes was accessible using this methodology.[95] The basis of this synthetic strategy is a semi-rigid tridentate ligand design that can accommodate binding three metals of the Fe_4S_4 core, leaving the fourth metal center open to ligand substitution or replacement by a heterometal.

Toward well-defined, rational syntheses of heterometallic metal-oxide clusters as models of the OEC, the application of the site-differentiated functionalization methodology

based on ligand design was employed by our group to access a series of Mn_3MO_n OEC model complexes.[96] My contributions to this body of work are the focus of this thesis.

The ligand framework I used was designed to bind three metal centers in close proximity, to accommodate multiple coordination modes, to be oxidatively robust, and to promote site-differentiated functionalization to allow access to 1) models of the OEC and 2) site-differentiated metal-oxido clusters in general. As discussed in Chapter 2, these design criteria led to 1,3,5-tris(2-di(2'-pyridyl)hydroxymethylphenyl)benzene (**H_3L**, or **L^{3-}**), a 1,3,5-triarylbenzene framework appended with dipyridyl-alcohols in one of the *ortho* positions of each of the three arenes on the periphery. The variability in the binding mode of dipyridyl ketone and the corresponding hemiacetal or *gem*-diol is well documented,[97] and indeed plays an important role in the chemistry of this multinucleating ligand **L^{3-}**, as will be shown throughout the following chapters. Trimetallic Mn^{II}_3, Co^{II}_3, and Ni^{II}_3 species were isolated upon treatment with $M(OAc)_2$ and base. The three alkoxide moieties bridge between metal centers, forming a chair-shaped M_3O_3 ring, and the two pyridines of each aryl arm bind to two separate metals, resulting in a structure with *pseudo-C_3* symmetry.[96b] The magnetism, redox properties, and ancillary ligand substitution are discussed.

Incorporation of a site-differentiated metal was first studied by addition of a fourth Mn equivalent to the trimanganese(II) complex of ligand **L^{3-}** in the presence of various oxidants. A range of complexes could be isolated by varying the Mn salt, oxidant, and solvent used, as delineated in Chapter 3. The various Mn_4O_n (n = 1-4) complexes observed varied in oxidation state from Mn^{II}_4 through $Mn^{III}Mn^{IV}_3$, and were characterized by XAS and EPR spectroscopy as benchmarks for the OEC photoactivation process.

Isolation of a Mn_4O_4 cubane led us to hypothesize that a heterometallic Mn_3CaO_4 cubane OEC model could be made using our ligand framework. Indeed, a $Mn^{IV}_3CaO_4$ cubane was successfully synthesized (Figure 1.4k), as examined in Chapter 4. These complexes have been instrumental in studying the reactivity and properties of complicated clusters structurally related to the OEC. These studies indicate that a potential role of the redox-inactive metal, Ca^{2+}, is to tune the reduction potential of the cluster. Synthetic strategies to further functionalize the Mn_3CaO_4 cluster to better model the low symmetry Mn_4CaO_5 OEC are also explored, showing the most accurate OEC model complexes to date (Figure 1.4l).

Finally, initial reactivity studies of the Mn_3MO_4 heterometallic cubanes are communicated in Chapter 5. The site-differentiated metal has a strong affect on not only the reduction potential of the cluster, but also the ability to transfer an O-atom to phosphine, which was studied by computation. In the Mn_4O_4 case, clean transfer affords a partial cubane Mn_4O_3 complex. Interconversion of these species could be accomplished by oxidative water incorporation into the partial cubane, mimicking a key step in OEC formation and turnover. Additionally, μ-oxido migration was shown to occur through an ^{18}O labeling study within $Mn_4O_{3,4}$ clusters, supporting recent proposals for equilibria between different structures of the OEC dependent on oxide migration.

1.6 Conclusion

New synthetic systems, spectroscopic methodologies, computations, and the concurrent collaborations have produced ever-refined structures of the OEC and more accurate mechanisms for OEC action. Biochemical and spectroscopic experimental results

on PSII provided the motivation for synthetic experiments key to benchmarking and supporting various proposals. These synthetic models in turn inspired new structural and mechanistic proposals and were crucial for testing computational methods as these became powerful enough to study metalloenzymes. More recently, crystal structures have provided atomic coordinates for more powerful computational work. The recent high-resolution crystal structure of PSII has prompted spectroscopic, synthetic, and computational developments. Overall, the interplay of synthetic, structural, spectroscopic, mechanistic, and computational work has led to tremendous insight into the chemistry and properties of manganese clusters relevant to the OEC. Despite these advances, the mechanism of water oxidation remains debated. The development of more accurate models, including of the full OEC, is a direction that will likely provide exciting new insight toward understanding not only the function of the biological system, but also toward delineating the design elements for improved catalysts for artificial photosynthesis.

REFERENCES

1. (a) Joliot, P.; Kok, B., Oxygen Evolution in Photosynthesis. In *Bioenergetics of photosynthesis*, Govindjee, Ed. Academic Press: New york, 1975; pp 387-411.(b) Pecoraro (ed.), V. L., *Manganese Redox Enzymes*. VCH Publishers, Inc.: New York, 1992.(c) Debus, R. J. *Biochim. Biophys. Acta* **1992,** *1102*, 269-352.(d) Yachandra, V. K.; Sauer, K.; Klein, M. P. *Chem. Rev.* **1996,** *96*, 2927-2950.(e) Ort, D. R.; Yocum (eds.), C. F., *Oxygenic Photosynthesis: The Light Reactions*. Kluwer Academic Publishers: Dordrecht, 1996.(f) Wydrzynski, T.; Satoh (eds.), K., *The Light-Driven Water: Plastoquinone Oxidoreductase*. Springer: Dordrecht, 2005; Vol. 22.(g) McEvoy, J. P.; Brudvig, G. W. *Chem. Rev.* **2006,** *106*, 4455-4483.(h) Babcock, G. T.; Yocum, C., Dioxygen Production: Photosystem II. In *Biological Inorganic Chemistry, Structure*

and Reactivity, Bertini, I.; Stiefel, E.; Valentine, J. S.; Gray, H., Eds. University Science Books: Sausalito, California, 2007; pp 302-318.

2. (a) Zouni, A.; Witt, H.-T.; Kern, J.; Fromme, P.; Krauß, N.; Saenger, W.; Orth, P. *Nature* **2001,** *409*, 739-743.(b) Umena, Y.; Kawakami, K.; Shen, J.-R.; Kamiya, N. *Nature* **2011,** *473*, 55-U65.
3. Yocum, C. F. *Biochim. Biophys. Acta* **1991,** *1059*, 1-15.
4. (a) Kessler, E. *Arch. Biochem. Biophys.* **1955,** *59*, 527-529.(b) Cheniae, G. M.; Martin, I. F. *Biochem. Bioph. Res. Co.* **1967,** *28*, 89-95.
5. Emerson, R.; Lewis, C. M. *Am. J. Bot.* **1939,** *26*, 808-822.
6. Yocum, C. F.; Yerkes, C. T.; Blankenship, R. E.; Sharp, R. R.; Babcock, G. T. *Proc. Natl. Acad. Sci. USA* **1981,** *78*, 7507-7511.
7. (a) Murata, N.; Miyao, M.; Omata, T.; Matsunami, H.; Kuwabara, T. *Biochim. Biophys. Acta* **1984,** *765*, 363-369.(b) Ohno, T.; Satoh, K.; Katoh, S. *Biochim. Biophys. Acta* **1986,** *852*, 1-8.
8. (a) Piccioni, R. G.; Mauzerall, D. C. *Biochim. Biophys. Acta* **1976,** *423*, 605-609.(b) Piccioni, R. G.; Mauzerall, D. C. *Biochim. Biophys. Acta* **1978,** *504*, 384-397.
9. (a) Ghanotakis, D. F.; Topper, J. N.; Babcock, G. T.; Yocum, C. F. *Febs Lett.* **1984,** *170*, 169-173.(b) Yocum, C. F. *Coordin. Chem. Rev.* **2008,** *252*, 296-305.
10. Ghanotakis, D. F.; Babcock, G. T.; Yocum, C. F. *Febs Lett.* **1984,** *167*, 127-130.
11. Ädelroth, P.; Lindberg, K.; Andreasson, L.-E. *Biochemistry* **1995,** *34*, 9021-9027.
12. Boussac, A.; Rutherford, A. W. *Biochemistry* **1988,** *27*, 3476-3483.
13. (a) Boussac, A.; Zimmermann, J.-L.; Rutherford, A. W. *Biochemistry* **1989,** *28*, 8984-8989.(b) Sivaraja, M.; Tso, J.; Dismukes, G. C. *Biochemistry* **1989,** *28*, 9459-9464.(c) Ono, T.-a.; Inoue, Y. *Biochim. Biophys. Acta* **1990,** *1020*, 269-277.(d) Boussac, A.; Sétif, P.; Rutherford, A. W. *Biochemistry* **1992,** *31*, 1224-1234.
14. (a) Kim, S. H.; Gregor, W.; Peloquin, J. M.; Brynda, M.; Britt, R. D. *J. Am. Chem. Soc.* **2004,** *126*, 7228-7237.(b) Cinco, R. M.; Holman, K. L. M.; Robblee, J.; Yano, J.; Pizarro, S. A.; Bellacchio, E.; Sauer, K.; Yachandra, V. K. *Biochemistry* **2002,** *41*, 12928-12933.(c) Yano, J.; Kern, J.; Sauer, K.; Latimer, M. J.; Pushkar, Y.; Biesiadka, J.; Loll, B.; Saenger, W.; Messinger, J.; Zouni, A.; Yachandra, V. K. *Science* **2006,** *314*, 821-825.

15. (a) Arnon, D. I.; Whatley, F. R. *Science* **1949,** *110*, 554-556.(b) Izawa, S.; Heath, R. L.; Hind, G. *Biochim. Biophys. Acta* **1969,** *180*, 388-398.

16. Lindberg, K.; Vanngard, T.; Andreasson, L.-E. *Photosynth. Res.* **1993,** *38*, 401-408.

17. Guskov, A.; Kern, J.; Gabdulkhakov, A.; Broser, M.; Zouni, A.; Saenger, W. *Nat. Struct. Mol. Biol.* **2009,** *16*, 334-342.

18. Chow, W. S.; Aro, E.-M., Photoinactivation and Mechanisms of Recovery. In *The Light-Driven Water: Plastoquinone Oxidoreductase*, Wydrzynski, T. J.; Satoh, K., Eds. Springer: Dordrecht, 2005; Vol. 22, pp 627-648.

19. Cheniae, G. M.; Martin, I. F. *Biochim. Biophys. Acta* **1971,** *253*, 167-181.

20. (a) Miller, A.-F.; Brudvig, G. W. *Biochemistry* **1989,** *28*, 8181-8190.(b) Miller, A.-F.; Brudvig, G. W. *Biochemistry* **1990,** *29*, 1385-1392.(c) Burnap, R. L. *Phys. Chem. Chem. Phys.* **2004,** *6*, 4803-4809.(d) Bartlett, J. E.; Baranov, S. V.; Ananyev, G. M.; Dismukes, G. C. *Philos. Trans. R. Soc. B-Biol. Sci.* **2008,** *363*, 1253-1261.(e) Dasgupta, J.; Ananyev, G. M.; Dismukes, G. C. *Coordin. Chem. Rev.* **2008,** *252*, 347-360.

21. Campbell, K. A.; Force, D. A.; Nixon, P. J.; Dole, F.; Diner, B. A.; Britt, R. D. *J. Am. Chem. Soc.* **2000,** *122*, 3754-3761.

22. Tyryshkin, A. M.; Watt, R. K.; Baranov, S. V.; Dasgupta, J.; Hendrich, M. P.; Dismukes, G. C. *Biochemistry* **2006,** *45*, 12876-12889.

23. (a) Ananyev, G. M.; Dismukes, G. C. *Biochemistry* **1997,** *36*, 11342-11350.(b) Zaltsman, L.; Ananyev, G. M.; Bruntrager, E.; Dismukes, G. C. *Biochemistry* **1997,** *36*, 8914-8922.(c) Dasgupta, J.; Tyryshkin, A. M.; Baranov, S. V.; Dismukes, G. C. *Appl. Magn. Reson.* **2010,** *37*, 137-150.

24. (a) Joliot, P. *Biochim. Biophys. Acta* **1965,** *102*, 116-134.(b) Joliot, P.; Joliot, A. *Biochim. Biophys. Acta* **1968,** *153*, 625-634.(c) Kok, B.; Forbush, B.; McGloin, M. *Photochem. Photobiol.* **1970,** *11*, 457-475.

25. (a) Förster, V.; Junge, W. *Photochem. Photobiol.* **1985,** *41*, 183-190.(b) Caudle, M. T.; Pecoraro, V. L. *J. Am. Chem. Soc.* **1997,** *119*, 3415-3416.(c) Schlodder, E.; Witt, H.-T. *J. Biol. Chem.* **1999,** *274*, 30387-30392.(d) Dau, H.; Haumann, M. *Coordin. Chem. Rev.* **2008,** *252*, 273-295.

26. Carrell, T. G.; Tyryshkin, A. M.; Dismukes, G. C. *J. Biol. Inorg. Chem.* **2002,** *7*, 2-22.

27. Kulik, L.; Epel, B.; Lubitz, W.; Messinger, J. *J. Am. Chem. Soc.* **2007,** *129*, 13421-13435.

28. Roelofs, T. A.; Liang, W. C.; Latimer, M. J.; Cinco, R. M.; Rompel, A.; Andrews, J. C.; Sauer, K.; Yachandra, V. K.; Klein, M. P. *Proc. Natl. Acad. Sci. USA* **1996,** *93*, 3335-3340.

29. (a) Bergmann, U.; Grush, M. M.; Horne, C. R.; DeMarois, P.; Penner-Hahn, J. E.; Yocum, C. F.; Wright, D. W.; Dubé, C. E.; Armstrong, W. H.; Christou, G.; Eppley, H. J.; Cramer, S. P. *J. Phys. Chem. B* **1998,** *102*, 8350-8352.(b) Visser, H.; Anxolabéhère-Mallart, E.; Bergmann, U.; Glatzel, P.; Robblee, J.; Cramer, S. P.; Girerd, J.-J.; Sauer, K.; Klein, M. P.; Yachandra, V. K. *J. Am. Chem. Soc.* **2001,** *123*, 7031-7039.(c) Pizarro, S. A.; Glatzel, P.; Visser, H.; Robblee, J. H.; Christou, G.; Bergmann, U.; Yachandra, V. K. *Phys. Chem. Chem. Phys.* **2004,** *6*, 4864-4870.

30. (a) Kolling, D. R. J.; Cox, N.; Ananyev, G. M.; Pace, R. J.; Dismukes, G. C. *Biophys. J.* **2012,** *103*, 313-322.(b) Pace, R. J.; Jin, L.; Stranger, R. *Dalton Trans.* **2012,** *41*, 11145-11160.(c) Gatt, P.; Petrie, S.; Stranger, R.; Pace, R. J. *Angew. Chem. Int. Ed.* **2012,** *51*, 12025-12028.

31. Radmer, R.; Ollinger, O. *Febs Lett.* **1986,** *195*, 285-289.

32. (a) Messinger, J.; Badger, M.; Wydrzynski, T. *Proc. Natl. Acad. Sci. USA* **1995,** *92*, 3209-3213.(b) Messinger, J.; Hillier, W.; Badger, M.; Wydrzynski, T. *Photosynthesis: From Light to Biosphere, Vol Ii* **1995**, 283-286.(c) Hillier, W.; Messinger, J.; Wydrzynski, T. *Biochemistry* **1998,** *37*, 16908-16914.(d) Hillier, W.; Messinger, J.; Wydrzynski, T. *Photosynthesis: Mechanisms and Effects, Vols I-V* **1998**, 1307-1310.(e) Hendry, G.; Wydrzynski, T. *Biochemistry* **2002,** *41*, 13328-13334.(f) Hendry, G.; Wydrzynski, T. *Biochemistry* **2003,** *42*, 6209-6217.(g) Hillier, W.; Wydrzynski, T. *Coordin. Chem. Rev.* **2008,** *252*, 306-317.(h) Singh, S.; Debus, R. J.; Wydrzynski, T.; Hillier, W. *Philos. Trans. R. Soc. B-Biol. Sci.* **2008,** *363*, 1229-1234.

33. Hillier, W.; Wydrzynski, T. *Biochemistry* **2000,** *39*, 4399-4405.

34. (a) Kamiya, N.; Shen, J.-R. *Proc. Natl. Acad. Sci. USA* **2003,** *100*, 98-103.(b) Ferreira, K. N.; Iverson, T. M.; Maghlaoui, K.; Barber, J.; Iwata, S. *Science* **2004,** *303*, 1831-1838.(c) Loll, B.; Kern, J.; Saenger, W.; Zouni, A.; Biesiadka, J. *Nature* **2005,** *438*, 1040-1044.(d) Barber, J.; Murray, J. W. *Coordin. Chem. Rev.* **2008,** *252*, 233-243.(e) Barber, J.; Murray, J.

W. *Philos. Trans. R. Soc. B-Biol. Sci.* **2008,** *363*, 1129-1137.(f) Koua, F. H. M.; Umena, Y.; Kawakami, K.; Shen, J.-R. *Proc. Natl. Acad. Sci. USA* **2013,** *110*, 3889-3894.

35. Yano, J.; Kern, J.; Irrgang, K.-D.; Latimer, M. J.; Bergmann, U.; Glatzel, P.; Pushkar, Y.; Biesiadka, J.; Loll, B.; Sauer, K.; Messinger, J.; Zouni, A.; Yachandra, V. K. *Proc. Natl. Acad. Sci. USA* **2005,** *102*, 12047-12052.

36. (a) Zheng, M.; Dismukes, G. C. *Inorg. Chem.* **1996,** *35*, 3307-3319.(b) Peloquin, J. M.; Britt, R. D. *Biochim. Biophys. Acta, Bioenerg.* **2001,** *1503*, 96-111.(c) Britt, R. D.; Campbell, K. A.; Peloquin, J. M.; Gilchrist, M. L.; Aznar, C. P.; Dicus, M. M.; Robblee, J.; Messinger, J. *Biochim. Biophys. Acta, Bioenerg.* **2004,** *1655*, 158-171.(d) Haddy, A. *Photosynth. Res.* **2007,** *92*, 357-368.

37. (a) Ono, T.-a.; Noguchi, T.; Inoue, Y.; Kusunoki, M.; Matsushita, T.; Oyanagi, H. *Science* **1992,** *258*, 1335-1337.(b) Robblee, J.; Cinco, R. M.; Yachandra, V. K. *Biochim. Biophys. Acta, Bioenerg.* **2001,** *1503*, 7-23.(c) Sauer, K.; Yano, J.; Yachandra, V. K. *Coordin. Chem. Rev.* **2008,** *252*, 318-335.(d) Dau, H.; Grundmeier, A.; Loja, P.; Haumann, M. *Philos. Trans. R. Soc. B-Biol. Sci.* **2008,** *363*, 1237-1243.(e) Yano, J.; Kern, J.; Pushkar, Y.; Sauer, K.; Glatzel, P.; Bergmann, U.; Messinger, J.; Zouni, A.; Yachandra, V. K. *Philos. Trans. R. Soc. B-Biol. Sci.* **2008,** *363*, 1139-1147.

38. (a) Dismukes, G. C.; Siderer, Y. *Febs Lett.* **1980,** *121*, 78-80.(b) Dismukes, G. C.; Siderer, Y. *Proc. Natl. Acad. Sci. USA* **1981,** *78*, 274-278.(c) Kirby, J. A.; Goodin, D. B.; Wydrzynski, T.; Robertson, A. S.; Klein, M. P. *J. Am. Chem. Soc.* **1981,** *103*, 5537-5542.(d) Kirby, J. A.; Robertson, A. S.; Smith, J. P.; Thompson, A. C.; Cooper, S. R.; Klein, M. P. *J. Am. Chem. Soc.* **1981,** *103*, 5529-5537.

39. (a) Christou, G. *Acc. Chem. Res.* **1989,** *22*, 328-335.(b) Wieghardt, K. *Angew. Chem. Int. Ed.* **1989,** *28*, 1153-1172.(c) Limburg, J.; Szalai, V. A.; Brudvig, G. W. *J. Chem. Soc.-Dalton Trans.* **1999**, 1353-1361.(d) Mukhopadhyay, S.; Mandal, S. K.; Bhaduri, S.; Armstrong, W. H. *Chem. Rev.* **2004,** *104*, 3981-4026.(e) Cady, C. W.; Crabtree, R. H.; Brudvig, G. W. *Coordin. Chem. Rev.* **2008,** *252*, 444-455.(f) Meelich, K.; Zaleski, C. M.; Pecoraro, V. L. *Philos. Trans. R. Soc. B-Biol. Sci.* **2008,** *363*, 1271-1279.(g) Mullins, C. S.; Pecoraro, V. L. *Coordin. Chem. Rev.* **2008,** *252*, 416-443.

40. (a) Blomberg, M. R. A.; Siegbahn, P. E. M.; Styring, S.; Babcock, G. T.; Akermark, B.; Korall, P. *J. Am. Chem. Soc.* **1997,** *119*, 8285-8292.(b) Siegbahn, P. E. M.; Crabtree, R. H. *J. Am. Chem. Soc.* **1999,** *121*, 117-127.(c) Siegbahn, P. E. M. *Inorg. Chem.* **2000,** *39*, 2923-2935.(d) Lundberg, M.; Blomberg, M. R. A.; Siegbahn, P. E. M. *Inorg. Chem.* **2004,** *43*, 264-274.(e) Lundberg, M.; Siegbahn, P. E. M. *J. Comput. Chem.* **2005,** *26*, 661-667.(f) Sproviero, E. M.; Gascón, J. A.; McEvoy, J. P.; Brudvig, G. W.; Batista, V. S. *J. Inorg. Biochem.* **2006,** *100*, 786-800.(g) Sproviero, E. M.; Gascón, J. A.; McEvoy, J. P.; Brudvig, G. W.; Batista, V. S. *Coordin. Chem. Rev.* **2008,** *252*, 395-415.(h) Orio, M.; Pantazis, D. A.; Petrenko, T.; Neese, F. *Inorg. Chem.* **2009,** *48*, 7251-7260.(i) Batista, V. S.; Wang, T.; Brudvig, G. *J. Chem. Theory Comput.* **2010,** *6*, 755-760.(j) Batista, V. S.; Wang, T.; Brudvig, G. W. *J. Chem. Theory Comput.* **2010,** *6*, 2395-2401.

41. (a) Siegbahn, P. E. M. *Acc. Chem. Res.* **2009,** *42*, 1871-1880.(b) Gatt, P.; Stranger, R.; Pace, R. J. *J. Photoch. Photobio. B* **2011,** *104*, 80-93.

42. Brudvig, G. W.; Crabtree, R. H. *Proc. Natl. Acad. Sci. USA* **1986,** *83*, 4586-4588.

43. Beck, W. F.; Depaula, J. C.; Brudvig, G. W. *J. Am. Chem. Soc.* **1986,** *108*, 4018-4022.

44. Goodin, D. B.; Yachandra, V. K.; Britt, R. D.; Sauer, K.; Klein, M. P. *Biochim. Biophys. Acta* **1984,** *767*, 209-216.

45. (a) McDermott, A. E.; Yachandra, V. K.; Guiles, R. D.; Cole, J. L.; Dexheimer, S. L.; Britt, R. D.; Sauer, K.; Klein, M. P. *Biochemistry* **1988,** *27*, 4021-4031.(b) Penner-Hahn, J.; Fronko, R. M.; Pecoraro, V. L.; Yocum, C. F.; Betts, S. D.; Bowlby, N. R. *J. Am. Chem. Soc.* **1990,** *112*, 2549-2557.

46. Rapatskiy, L.; Cox, N.; Savitsky, A.; Ames, W. M.; Sander, J.; Nowaczyk, M. M.; Rögner, M.; Boussac, A.; Neese, F.; Messinger, J.; Lubitz, W. *J. Am. Chem. Soc.* **2012,** *134*, 16619-16634.

47. (a) Christou, G.; Vincent, J. B. *Biochim. Biophys. Acta* **1987,** *895*, 259-274.(b) Vincent, J. B.; Christou, G. *Inorg. Chim. Acta, Bioinorg.* **1987,** *136*, L41-L43.

48. Yachandra, V. K.; Guiles, R. D.; McDermott, A. E.; Britt, R. D.; Dexheimer, S. L.; Sauer, K.; Klein, M. P. *Biochim. Biophys. Acta* **1986,** *850*, 324-332.

49. George, G. N.; Prince, R. C.; Cramer, S. P. *Science* **1989,** *243*, 789-791.

50. Yachandra, V. K.; DeRose, V. J.; Latimer, M. J.; Mukerji, I.; Sauer, K.; Klein, M. P. *Science* **1993,** *260*, 675-679.

51. Hoganson, C. W.; Babcock, G. T. *Science* **1997,** *277*, 1953-1956.

52. Pecoraro, V. L.; Baldwin, M. J.; Caudle, M. T.; Hsieh, W.-Y.; Law, N. A. *Pure Appl. Chem.* **1998,** *70*, 925-929.

53. Peloquin, J. M.; Campbell, K. A.; Randall, D. W.; Evanchik, M. A.; Pecoraro, V. L.; Armstrong, W. H.; Britt, R. D. *J. Am. Chem. Soc.* **2000,** *122*, 10926-10942.

54. DeRose, V. J.; Mukerji, I.; Latimer, M. J.; Yachandra, V. K.; Sauer, K.; Klein, M. P. *J. Am. Chem. Soc.* **1994,** *116*, 5239-5249.

55. Petrie, S.; Gatt, P.; Stranger, R.; Pace, R. J. *Phys. Chem. Chem. Phys.* **2012,** *14*, 11333-11343.

56. (a) Ames, W.; Pantazis, D. A.; Krewald, V.; Cox, N.; Messinger, J.; Lubitz, W.; Neese, F. *J. Am. Chem. Soc.* **2011,** *133*, 19743-19757.(b) Luber, S.; Rivalta, I.; Umena, Y.; Kawakami, K.; Shen, J.-R.; Kamiya, N.; Brudvig, G. W.; Batista, V. S. *Biochemistry* **2011,** *50*, 6308-6311.(c) Siegbahn, P. E. M. *Chemphyschem* **2011,** *12*, 3274-3280.(d) Galstyan, A.; Robertazzi, A.; Knapp, E. W. *J. Am. Chem. Soc.* **2012,** *134*, 7442-7449.

57. Kusunoki, M. *J. Photoch. Photobio. B* **2011,** *104*, 100-110.

58. (a) Pantazis, D. A.; Ames, W.; Cox, N.; Lubitz, W.; Neese, F. *Angew. Chem. Int. Ed.* **2012,** *51*, 9935-9940.(b) Isobe, H.; Shoji, M.; Yamanaka, S.; Umena, Y.; Kawakami, K.; Kamiya, N.; Shen, J.-R.; Yamaguchi, K. *Dalton Trans.* **2012,** *41*, 13727-13740.

59. (a) Volkov, A. G. *Bioelectroch. Bioener.* **1989,** *21*, 3-24.(b) Tommos, C.; Babcock, G. T. *Acc. Chem. Res.* **1998,** *31*, 18-25.(c) Liu, F.; Concepcion, J. J.; Jurss, J. W.; Cardolaccia, T.; Templeton, J. L.; Meyer, T. J. *Inorg. Chem.* **2008,** *47*, 1727-1752.(d) Brudvig, G. W. *Philos. Trans. R. Soc. B-Biol. Sci.* **2008,** *363*, 1211-1218.

60. Tagore, R.; Chen, H.; Crabtree, R. H.; Brudvig, G. W. *J. Am. Chem. Soc.* **2006,** *128*, 9457-9465.

61. Halfen, J. A.; Mahapatra, S.; Wilkinson, E. C.; Kaderli, S.; Young, V. G. J.; Que Jr., L.; Zuberbühler, A. D.; Tolman, W. B. *Science* **1996,** *271*, 1397-1400.

62. Dasgupta, J.; van Willigen, R. T.; Dismukes, G. C. *Phys. Chem. Chem. Phys.* **2004,** *6*, 4793-4802.

63. Yang, X.; Baik, M.-H. H. *J. Am. Chem. Soc.* **2006,** *128*, 7476-7485.

64. (a) Limburg, J.; Vrettos, J. S.; Liable-Sands, L. M.; Rheingold, A. L.; Crabtree, R. H.; Brudvig, G. W. *Science* **1999,** *283*, 1524-1527.(b) Limburg, J.; Vrettos, J. S.; Chen, H.; de Paula, J. C.; Crabtree, R. H.; Brudvig, G. W. *J. Am. Chem. Soc.* **2001,** *123*, 423-430.

65. (a) Vrettos, J. S.; Limburg, J.; Brudvig, G. W. *Biochim. Biophys. Acta, Bioenerg.* **2001,** *1503*, 229-245.(b) McEvoy, J. P.; Brudvig, G. W. *Phys. Chem. Chem. Phys.* **2004,** *6*, 4754-4763.(c) Sproviero, E. M.; Gascón, J. A.; McEvoy, J. P.; Brudvig, G. W.; Batista, V. S. *J. Am. Chem. Soc.* **2008,** *130*, 3428-3442.

66. Siegbahn, P. E. M. *J. Am. Chem. Soc.* **2009,** *131*, 18238-18239.

67. (a) Siegbahn, P. E. M. *Chem.-Eur. J.* **2006,** *12*, 9217-9227.(b) Siegbahn, P. E. M. *Chem.-Eur. J.* **2008,** *14*, 8290-8302.

68. (a) Haumann, M.; Junge, W. *Biochim. Biophys. Acta, Bioenerg.* **1999,** *1411*, 86-91.(b) Liang, W. C.; Roelofs, T. A.; Cinco, R. M.; Rompel, A.; Latimer, M. J.; Yu, W. O.; Sauer, K.; Klein, M. P.; Yachandra, V. K. *J. Am. Chem. Soc.* **2000,** *122*, 3399-3412.(c) Messinger, J. *Phys. Chem. Chem. Phys.* **2004,** *6*, 4764-4771.

69. Siegbahn, P. E. M. *Phys. Chem. Chem. Phys.* **2012,** *14*, 4849-4856.

70. Plaksin, P. M.; Palenik, G. J.; Stoufer, R. C.; Mathew, M. *J. Am. Chem. Soc.* **1972,** *94*, 2121-2122.

71. Cooper, S. R.; Dismukes, G. C.; Klein, M. P.; Calvin, M. *J. Am. Chem. Soc.* **1978,** *100*, 7248-7252.

72. Tagore, R.; Crabtree, R. H.; Brudvig, G. W. *Inorg. Chem.* **2007,** *46*, 2193-2203.

73. (a) Wieghardt, K.; Bossek, U.; Gebert, W. *Angew. Chem. Int. Ed.* **1983,** *22*, 328-329.(b) Wieghardt, K.; Bossek, U.; Nuber, B.; Weiss, J.; Bonvoisin, J.; Corbella, M.; Vitols, S. E.; Girerd, J.-J. *J. Am. Chem. Soc.* **1988,** *110*, 7398-7411.

74. (a) Hagen, K. S.; Westmoreland, T. D.; Scott, M. J.; Armstrong, W. H. *J. Am. Chem. Soc.* **1989,** *111*, 1907-1909.(b) Dubé, C. E.; Wright, D. W.; Armstrong, W. H. *J. Am. Chem. Soc.* **1996,** *118*, 10910-10911.(c) Dubé, C. E.; Wright, D. W.; Pal, S.; Bonitatebus Jr., P. J.; Armstrong, W. H. *J. Am. Chem. Soc.* **1998,** *120*, 3704-3716.

75. (a) McKee, V.; Shepard, W. B. *J. Chem. Soc.-Chem. Commun.* **1985**, 158-159.(b) Brooker, S.; McKee, V.; Shepard, W. B.; Pannell, L. K. *J. Chem. Soc.-Dalton Trans.* **1987**, 2555-2562.

76. Bashkin, J. S.; Chang, H.-R.; Streib, W. E.; Huffman, J. C.; Hendrickson, D. N.; Christou, G. *J. Am. Chem. Soc.* **1987,** *109*, 6502-6504.

77. (a) Wang, S. Y.; Folting, K.; Streib, W. E.; Schmitt, E. A.; McCusker, J. K.; Hendrickson, D. N.; Christou, G. *Angew. Chem. Int. Ed.* **1991,** *30*, 305-306.(b) Hendrickson, D. N.; Christou, G.; Schmitt, E. A.; Libby, E.; Bashkin, J. S.; Wang, S. Y.; Tsai, H.-L.; Vincent, J. B.; Boyd, P. D. W.; Huffman, J. C.; Folting, K.; Li, Q.; Streib, W. E. *J. Am. Chem. Soc.* **1992,** *114*, 2455-2471.(c) Wang, S. Y.; Tsai, H.-L.; Streib, W. E.; Christou, G.; Hendrickson, D. N. *J. Chem. Soc.-Chem. Commun.* **1992**, 1427-1429.(d) Wemple, M. W.; Tsai, H.-L.; Folting, K.; Hendrickson, D. N.; Christou, G. *Inorg. Chem.* **1993,** *32*, 2025-2031.(e) Wang, S. Y.; Tsai, H.-L.; Hagen, K. S.; Hendrickson, D. N.; Christou, G. *J. Am. Chem. Soc.* **1994,** *116*, 8376-8377.(f) Wemple, M. W.; Adams, D. M.; Folting, K.; Hendrickson, D. N.; Christou, G. *J. Am. Chem. Soc.* **1995,** *117*, 7275-7276.(g) Wemple, M. W.; Adams, D. M.; Hagen, K. S.; Folting, K.; Hendrickson, D. N.; Christou, G. *J. Chem. Soc.-Chem. Commun.* **1995**, 1591-1593.(h) Aubin, S. J.; Wemple, M. W.; Adams, D. M.; Tsai, H.-L.; Christou, G.; Hendrickson, D. N. *J. Am. Chem. Soc.* **1996,** *118*, 7746-7754.(i) Aromí, G.; Wemple, M. W.; Aubin, S. J.; Folting, K.; Hendrickson, D. N.; Christou, G. *J. Am. Chem. Soc.* **1998,** *120*, 5850-5851.(j) Cinco, R. M.; Rompel, A.; Visser, H.; Aromí, G.; Christou, G.; Sauer, K.; Klein, M. P.; Yachandra, V. K. *Inorg. Chem.* **1999,** *38*, 5988-5998.(k) Andres, H.; Basler, R.; Güdel, H.-U.; Aromí, G.; Christou, G.; Büttner, H.; Rufflé, B. *J. Am. Chem. Soc.* **2000,** *122*, 12469-12477.(l) Aromí, G.; Bhaduri, S.; Artús, P.; Folting, K.; Christou, G. *Inorg. Chem.* **2002,** *41*, 805-817.(m) Aliaga-Alcalde, N.; Edwards, R. S.; Hill, S. O.; Wernsdorfer, W.; Folting, K.; Christou, G. *J. Am. Chem. Soc.* **2004,** *126*, 12503-12516.

78. (a) Ruettinger, W. F.; Campana, C.; Dismukes, G. C. *J. Am. Chem. Soc.* **1997**, 6670-6671.(b) Ruettinger, W. F.; Ho, D. M.; Dismukes, G. C. *Inorg. Chem.* **1999**, 1036-+.

79. Ruettinger, W.; Yagi, M.; Wolf, K.; Bernasek, S.; Dismukes, G. C. *J. Am. Chem. Soc.* **2000**, 10353-10357.

80. (a) Brimblecombe, R.; Swiegers, G. F.; Dismukes, G. C.; Spiccia, L. *Angew. Chem. Int. Ed.* **2008,** *47*, 7335-7338.(b) Brimblecombe, R.; Kolling, D. R. J.; Bond, A. M.; Dismukes, G. C.; Swiegers, G. F.; Spiccia, L. *Inorg. Chem.* **2009,** *48*, 7269-7279.(c) Brimblecombe, R.;

Koo, A.; Dismukes, G. C.; Swiegers, G. F.; Spiccia, L. *J. Am. Chem. Soc.* **2010,** *132*, 2892-+.

81. Hocking, R. K.; Brimblecombe, R.; Chang, L.-Y.; Singh, A.; Cheah, M. H.; Glover, C.; Casey, W. H.; Spiccia, L. *Nat. Chem.* **2011,** *3*, 461-466.
82. Ohlin, C. A.; Brimblecombe, R.; Spiccia, L.; Casey, W. H. *Dalton Trans.* **2009**, 5278-5280.
83. (a) Guiles, R. D.; Zimmermann, J.-L.; McDermott, A. E.; Yachandra, V. K.; Cole, J. L.; Dexheimer, S. L.; Britt, R. D.; Wieghardt, K.; Bossek, U.; Sauer, K.; Klein, M. P. *Biochemistry* **1990,** *29*, 471-485.(b) Kim, D. H.; Britt, R. D.; Klein, M. P.; Sauer, K. *J. Am. Chem. Soc.* **1990,** *112*, 9389-9391.
84. Vincent, J. B.; Christmas, C.; Huffman, J. C.; Christou, G.; Chang, H.-R.; Hendrickson, D. N. *J. Chem. Soc.-Chem. Commun.* **1987**, 236-238.
85. (a) Chan, M. K.; Armstrong, W. H. *J. Am. Chem. Soc.* **1989,** *111*, 9121-9122.(b) Chan, M. K.; Armstrong, W. H. *J. Am. Chem. Soc.* **1990,** *112*, 4985-4986.(c) Chan, M. K.; Armstrong, W. H. *J. Am. Chem. Soc.* **1991,** *113*, 5055-5057.
86. Philouze, C.; Blondin, G.; Girerd, J.-J.; Guilhem, J.; Pascard, C.; Lexa, D. *J. Am. Chem. Soc.* **1994,** *116*, 8557-8565.
87. Chen, H.; Faller, J. W.; Crabtree, R. H.; Brudvig, G. W. *J. Am. Chem. Soc.* **2004,** *126*, 7345-7349.
88. Mishra, A.; Wernsdorfer, W.; Abboud, K. A.; Christou, G. *Chem. Commun.* **2005**, 54-56.
89. Mishra, A.; Yano, J.; Pushkar, Y.; Yachandra, V. K.; Abboud, K. A.; Christou, G. *Chem. Commun.* **2007**, 1538-1540.
90. Hewitt, I. J.; Tang, J.-K.; Madhu, N. T.; Clérac, R.; Buth, G.; Anson, C. E.; Powell, A. K. *Chem. Commun.* **2006**, 2650-2652.
91. Nayak, S.; Nayek, H. P.; Dehnen, S.; Powell, A. K.; Reedijk, J. *Dalton Trans.* **2011,** *40*, 2699-2702.
92. Koumousi, E. S.; Mukherjee, S.; Beavers, C. M.; Teat, S. J.; Christou, G.; Stamatatos, T. C. *Chem. Commun.* **2011,** *47*, 11128-11130.
93. Jerzykiewicz, L. B.; Utko, J.; Duczmal, M.; Sobota, P. *Dalton Trans.* **2007**, 825-826.
94. Kotzabasaki, V.; Siczek, M.; Lis, T.; Milios, C. J. *Inorg. Chem. Commun.* **2011,** *14*, 213-216.

95. (a) Stack, T. D. P.; Holm, R. H. *J. Am. Chem. Soc.* **1987,** *109*, 2546-2547.(b) Stack, T. D. P.; Holm, R. H. *J. Am. Chem. Soc.* **1988,** *110*, 2484-2494.(c) Ciurli, S.; Carrie, M.; Weigel, J. A.; Carney, M. J.; Stack, T. D. P.; Papaefthymiou, G. C.; Holm, R. H. *J. Am. Chem. Soc.* **1990,** *112*, 2654-2664.(d) Ciurli, S.; Holm, R. H. *Inorg. Chem.* **1991,** *30*, 743-750.(e) Zhou, J.; Holm, R. H. *J. Am. Chem. Soc.* **1995,** *117*, 11353-11354.(f) Zhou, J.; Raebiger, J. W.; Crawford, C. A.; Holm, R. H. *J. Am. Chem. Soc.* **1997,** *119*, 6242-6250.

96. (a) Kanady, J. S.; Tsui, E. Y.; Day, M. W.; Agapie, T. *Science* **2011,** *333*, 733-736.(b) Tsui, E. Y.; Kanady, J. S.; Day, M. W.; Agapie, T. *Chem. Commun.* **2011,** *47*, 4189-4191.(c) Kanady, J. S.; Mendoza-Cortes, J. L.; Tsui, E. Y.; Nielsen, R. J.; Goddard III, W. A.; Agapie, T. *J. Am. Chem. Soc.* **2013,** *135*, 1073-1082.(d) Kanady, J. S.; Tran, R.; Stull, J. A.; Lu, L.; Stich, T. A.; Day, M. W.; Yano, J.; Britt, R. D.; Agapie, T. *Chem Sci* **2013,** *4*, 3986-3996.(e) Tsui, E. Y.; Tran, R.; Yano, J.; Agapie, T. *Nat. Chem.* **2013,** *5*, 293-299.(f) Tsui, E. Y.; Agapie, T. *Proc. Natl. Acad. Sci. USA* **2013**, In Press.(g) Tsui, E. Y.; Kanady, J. S.; Agapie, T. *Inorg. Chem.* **2013,** *52*, 13833-13848.

97. Stamatatos, T. C.; Efthymiou, C. G.; Stoumpos, C. C.; Perlepes, S. P. *Eur. J. Inorg. Chem.* **2009**, 3361-3391.

CHAPTER 2

Trinuclear First Row Transition Metal Complexes of a Hexapyridyl, Trialkoxy 1,3,5-Triarylbenzene Ligand

Published in part as:

Tsui, E. Y.; Kanady, J. S.; Day, M. W.; Agapie, T. *Chem. Comm.* **2011**, *47*, 4189-4191.

ABSTRACT

Trinuclear complexes of Mn^{II}, Co^{II}, and Ni^{II} were synthesized using a ligand architecture based upon a 1,3,5-triarylbenzene core decorated with six pyridines and three alkoxide moieties. The geometry of metal coordination by the framework is conserved, and while the ancillary counteranions' coordination modes are variable, the core bond distances vary only slightly. A number of carboxylates can be used as ancillary ligands, as well as weakly coordinating BF_4^- and ClO_4^-, which affects their oxidation chemistry. The complexes are characterization via X-ray diffraction, NMR, and, for the acetate series, magnetism studies and cyclic voltammetry.

INTRODUCTION

The active sites of several enzymes involved in dioxygen chemistry (laccase, ascorbate oxidase, the oxygen evolving center of photosystem II) display three or more first row transition metal centers.[1] Synthetic catalysts for water oxidation are also proposed to be multinuclear.[2] In continued efforts to rationally design multinucleating scaffolds, a 1,3,5-triarylbenzene framework was utilized to hold three multidentate binding sites near each other. 1,3,5-Tris(2-(di(2-pyridyl)hydroxymethyl)phenyl)benzene (**H_3L**, Scheme 2.1) is accessible in two steps from commercially available starting materials.[3] Dr. Emily Tsui synthesized trinuclear copper complexes supported by framework **L^{3-}** containing a conserved $Cu_3(\mu\text{-}OR)_3$ central moiety; varying the capping anions from halides, phosphate, tetrafluoroborate, and triflate causes subtle structural changes that affect the magnetism of these complexes. [3]

Protonated and deprotonated dipyridylhydroxymethyl moieties are known to exhibit an array of coordination modes, from tridentate N,O,N coordination of a single metal center to more complicated bridging patterns of up to three metals.[4] Although the $M^{II}_3(\mu\text{-}OR)_3$ structural motif is commonly reported in the literature, it is generally found in higher nuclearity, self-assembled clusters in complexes of 2,2´-dipyridylketone[4] and as part of tetranuclear clusters such as cubanes[5] and defective dicubanes[6] The motif is less common in trinuclear complexes.[7] There are no examples of three Mn^{II} centers bridged by alkoxides, although amido-bridged[8] and carboxylate-bridged[9] complexes do exist as self-assembled clusters. To further investigate the metal coordination potential of **H_3L** and its control over cluster nuclearity, trinuclear complexes of **L^{3-}** containing other first row transition metals were targeted.

RESULTS & DISCUSSION

2.1 Synthesis of Mn^{II}_3, Co^{II}_3, and Ni^{II}_3 complexes

Metallation studies were initiated with the acetate salts of the first-row metals Mn^{II}, Fe^{II}, Co^{II}, Ni^{II}, Cu^{II}, and Zn^{II} in the presence of base (Scheme 2.1; Dr. Emily Tsui synthesized the Fe^{II}, Cu^{II}, and Zn^{II} complexes). The addition of three equivalents of solid $M^{II}(OAc)_2 \bullet xH_2O$ to a suspension of **H_3L** in acetonitrile or a mixture of acetonitrile/water followed by three equivalents of a base such as sodium hydroxide or triethylamine resulted in complete dissolution of insoluble materials within 12 hours. Analytically pure crystals were obtained by vapor diffusion of diethyl ether into dichloromethane or chloroform solutions of the reaction products.

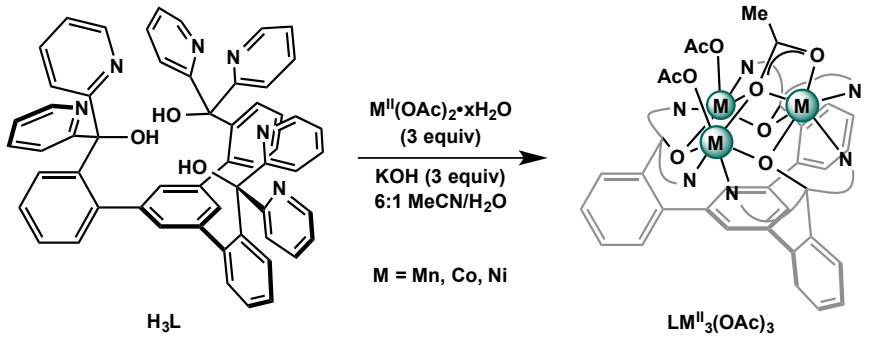

Scheme 2.1 Synthesis of trinuclear complexes of Mn^{II}, Co^{II}, and Ni^{II}. Related complexes of Fe^{II}, Cu^{II}, and Zn^{II} also synthesized by Dr. Emily Tsui.

Single crystal X-ray diffraction (XRD) studies demonstrate the trinucleating nature of the deprotonated **H_3L** framework to give complexes generally formulated as $LM_3(OAc)_3$ (Figure 2.1). The three metal centers are bridged by three alkoxides forming a six membered ring, and the pendant pyridines coordinate with the two pyridines of each dipyridyl moiety bound to adjacent metal centers. The coordination environment is completed by acetate counterions.

The LM_3 core displays pseudo-C_3 symmetry induced by a twist of each dipyridylmethoxide arm. This binding mode renders the two pyridines of each arm different, which is reflected in variations in the M–N bond lengths (Table 2.1). The M–O (alkoxide) bonds are also differentiated, albeit less than the M–N bonds—the largest difference observed is about 0.05 Å. The elongated M–N bonds correspond to the three pyridines *trans* to alkoxide ligands. The pyridines located below the plane of the three metals and displaying shorter M–N distances are roughly *trans* to the bridging acetates. M–O (alkoxide) bonds *trans* to acetates are slightly shorter than those *trans* to pyridines. These variations may be caused by larger *trans* influences of pyridine and alkoxide vs acetate, but distortions caused by steric strain in the ligand framework cannot be ruled out. Consistent with the increase in the ionic radius, the metal-ligand distances increase from Ni to Mn and the M–M distances increase from 3.182(4) Å for Ni to 3.415(1)–3.464(1) Å for Mn. The ligand framework accommodates the different size metals by allowing for twist around the aryl-aryl bonds and of the C–O vector vs the plane of the pendant arene.

Table 2.1 Metal–metal and average metal–nitrogen distances

Compound	M–N *trans* to alkoxide (Å)	M–N *trans* to acetate (Å)	M–M (Å)
$LMn_3(OAc)_3$	2.336(3)	2.232(6)	3.415(1)–3.464(1)
$LMn_3(O_2CPh)_3$	2.377(1)	2.239(1)	3.405(1)–3.481(1)
LMn_3(*p*-Me_2N-benzoate)$_3$	2.394(2)	2.241(2)	3.364(1)–3.485(1)
$LCo_3(OAc)_3$	2.213(2)	2.091(2)	3.228(2)
$LCo_3(O_2CPh)_3$	2.195(3)	2.058(3)	3.337(1)–3.372(1)
LCo_3(*p*-toluate)$_3$	2.210(2)	2.099(2)	3.2391(4)–3.3375(4)
LCo_3(*p*-Me_2N-benzoate)$_3$	2.199(11)	2.051(10)	3.192(2)–3.364(2)
$LNi_3(OAc)_3$	2.127(3)	2.037(3)	3.182(4)

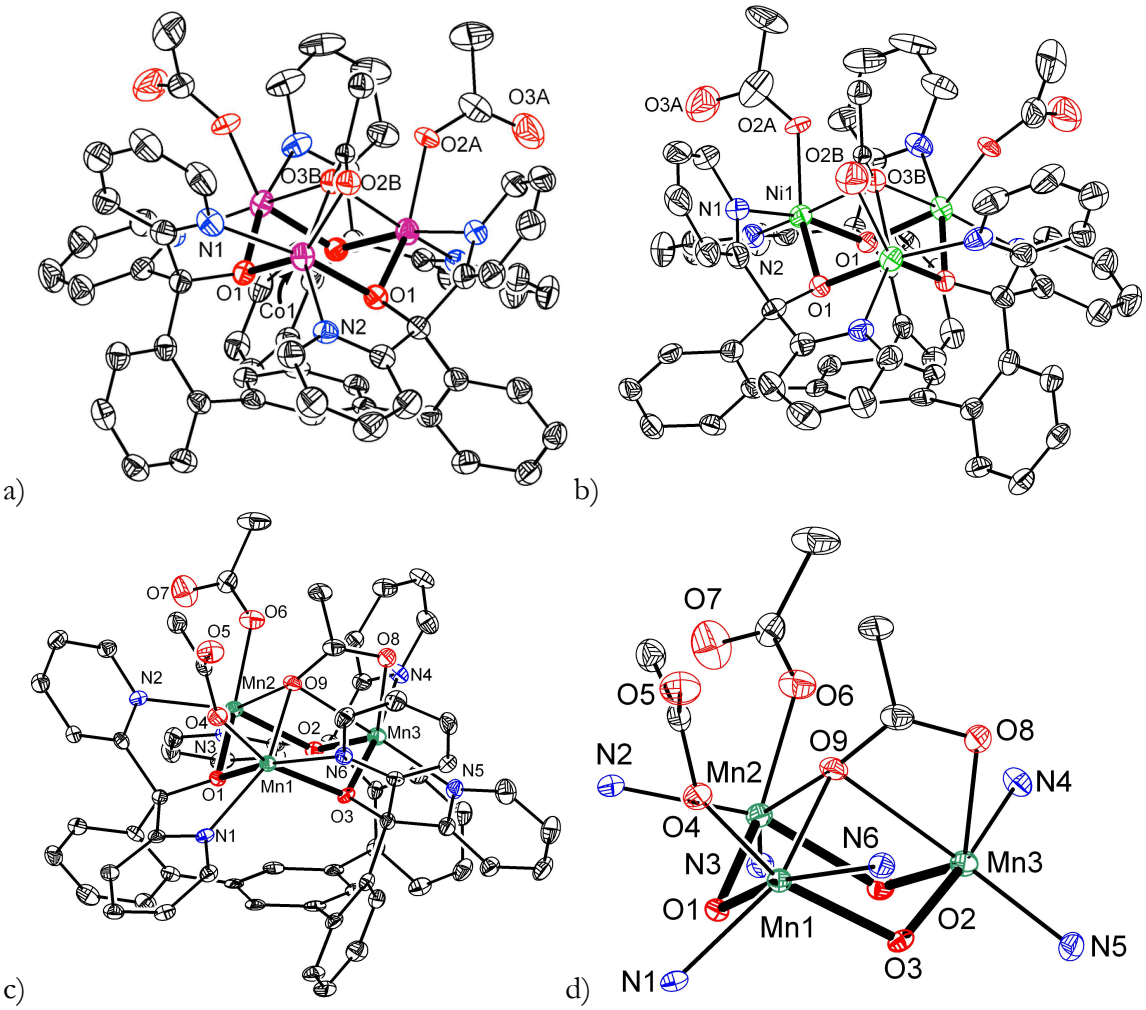

Figure 2.1 a-c) Solid-state structures of $LCo_3(OAc)_3$, $LNi_3(OAc)_3$, and $LMn_3(OAc)_3$, respectively. d) Coordination environments of $LMn_3(OAc)_3$. The $M^{II}_3(\mu\text{-OR})_3$ structural motif is bolded; thermal ellipsoids are drawn at 50% probability; hydrogen atoms and solvent are not shown for clarity.

Systematically changing the nature of the metal centers from Mn^{II} to Zn^{II} does not disrupt the trinuclear core, but changes the binding mode of the acetates. Three capping acetates are present for $LM_3(OAc)_3$ (M = Mn–Ni); two acetates bind in monodentate and one in bidentate fashion. The bidentate acetate bridges two or three metal centers via a μ_2- or μ_3-oxygen atom. For M = Cu and Zn, single crystal XRD studies show two acetates bound to the trimetallic core. However, a third outer-sphere

acetate required for charge balance could not be located due to disorder. This change in coordination mode may be due to the smaller size of Cu^{II} and Zn^{II} hindering the binding of a third acetate.

^{1}H NMR spectroscopy and mass spectrometry studies confirm that the trinuclear cores of the complexes are maintained in solution. These complexes are soluble in dichloromethane, chloroform, methanol, and water, with much lower solubility in acetonitrile and tetrahydrofuran. Electrospray ionization mass spectrometry (ESI-MS) showed a single peak for all complexes equivalent to $[LM_3(OAc)_2]^+$. The ^{1}H NMR spectra of $LCo_3(OAc)_3$ and $LNi_3(OAc)_3$ display fourteen resonances, with chemical shifts between –20 and 160 ppm for these paramagnetic species. Thirteen resonances correspond to protons on framework L, consistent with the *pseudo*-C_3-geometry observed in the solid state. The single peak assigned to the acetate counterions is indicative of fluxional processes that exchange the capping ligands on the NMR timescale. The ^{1}H NMR spectrum of $LMn_3(OAc)_3$ shows four broad peaks between –20 to 50 ppm. The peak broadening observed is consistent with the faster relaxation rates (τ_s^{-1}) for Ni^{II} (10^{10}–10^{12} sec^{-1}) and high spin Co^{II} (10^{11}–10^{12} sec^{-1}) compared to Mn^{II} (10^8–10^9 sec^{-1}).[10]

Analogous to the acetate complexes, a series of *para*-substituted benzoate complexes of Mn and Co were synthesized. The nickel complexes proved more difficult to synthesize and multiple products were observed in their NMR spectra. The carboxylate series contained—in order of increasing donor ability—*p*-trifluoromethylbenzoate, benzoate, *p*-toluate, *p*-^{t}butylbenzoate, and *p*-*N*,*N*-

dimethylaminobenzoate. The $M(O_2CAr)_2 \bullet xH_2O$ salts were synthesized by a literature procedure[11] and mixed with $\mathbf{H_3L}$ under the same conditions as the metal acetate salts.

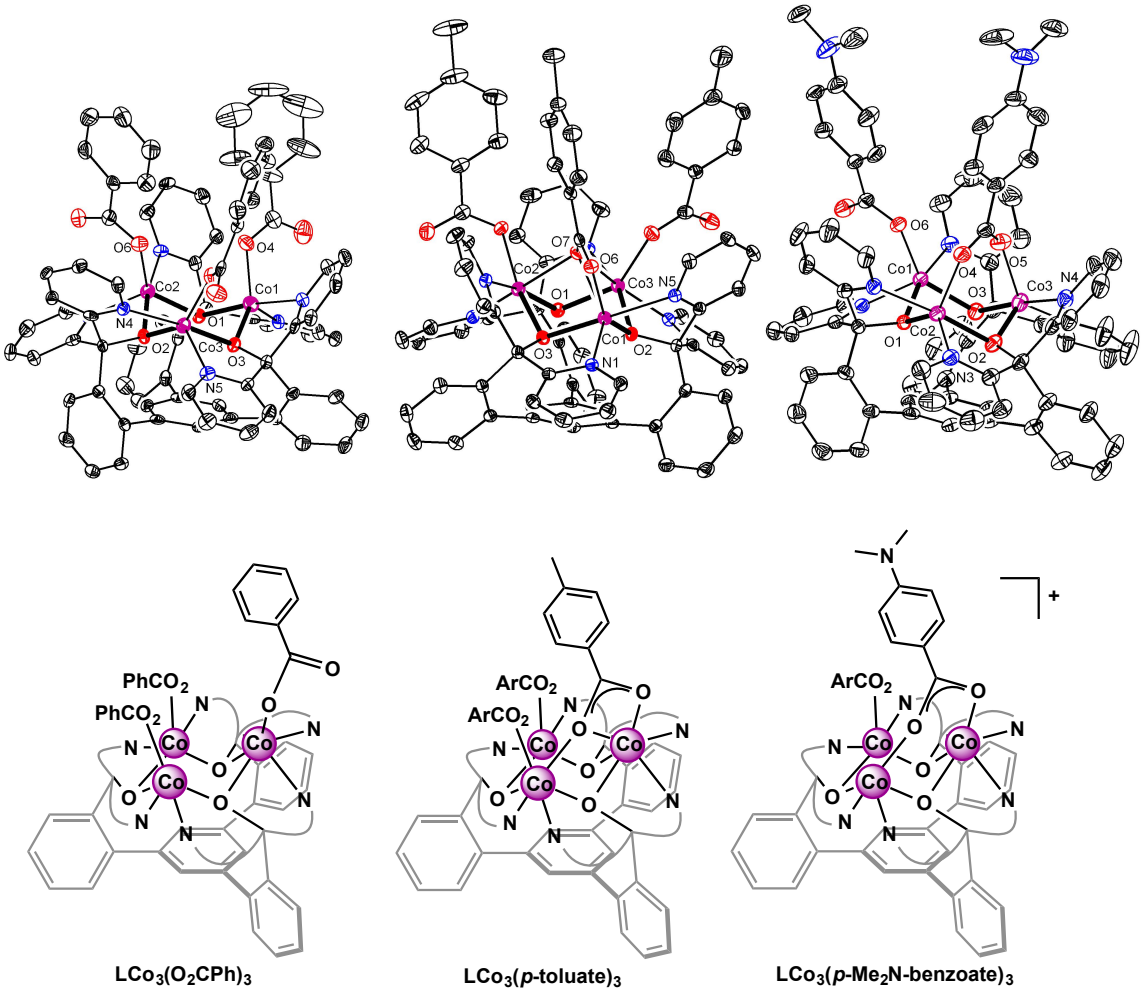

Figure 2.2 From left to right, the solid-state structures (top) and schematic representations (bottom) of the tricobalt complexes with benzoate, *p*-toluate, and *p*-dimethylaminobenzoate as the counterion. The $M^{II}_3(\mu\text{-OR})_3$ structural motif is bolded; thermal ellipsoids are drawn at 50% probability; hydrogen atoms and solvent molecules are not shown for clarity.

All five trinuclear cobalt carboxylate complexes—$LCo_3(O_2CAr)_3$—were successfully crystallized in 20-80% yield. A number of single crystals diffracted well

(Figure 2.2). As expected, the trinuclear metal-alkoxo ring structure was observed. The bond distances were consistent with the $LCo_3(OAc)_3$ structure, with the range of analogous bonds throughout the series being less than 0.05Å (Table 2.1). Of note is the variable carboxylate binding mode: with benzoate all three cobalt centers are only five-coordinate with no central bridging atom, toluate binds analogously to acetate, and a p-dimethylaminobenzoate is outersphere. ^{1}H NMR spectrum is similar to that of $LCo_3(OAc)_3$, with the benzoates fluxional on the NMR time scale. Solubility also parallels $LCo_3(OAc)_3$.

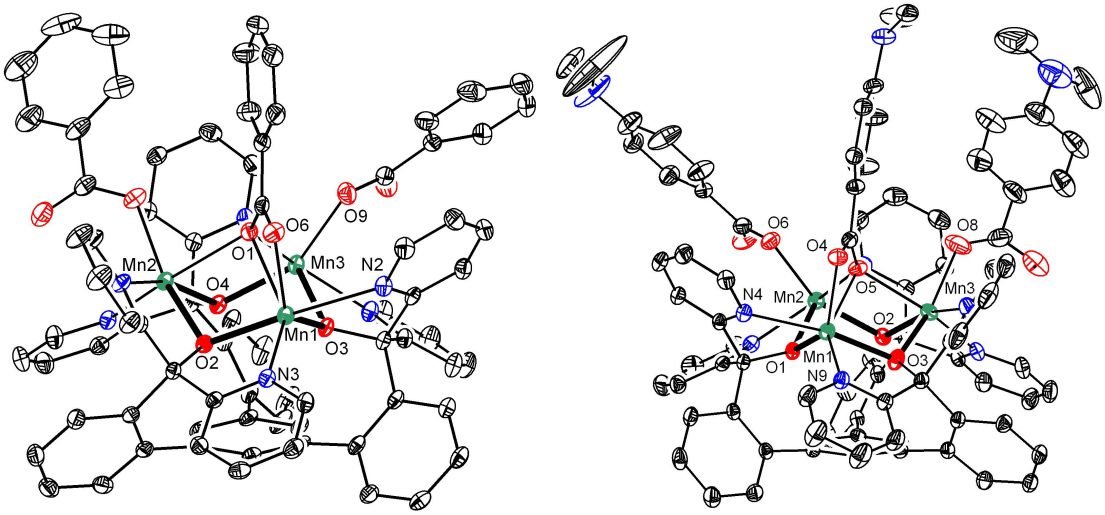

Figure 2.3 The solid-state structures of $LMn_3(O_2CPh)_3$ (left) and $LMn_3(p\text{-}Me_2N\text{-benzoate})_3$ (right). The $M^{II}_3(\mu\text{-}OR)_3$ structural motif is bolded; thermal ellipsoids are drawn at 50% probability; hydrogen atoms and solvent molecules are not shown for clarity.

The manganese carboxylate series has also been synthesized. ESI-MS supported the formation of the five $LMn_3(O_2CAr)_3$ complexes: the only peak in the spectra corresponds to $[LMn_3(O_2CAr)_2]^+$. However, isolation proved difficult due to the solubility, which varied upon moving to more nonpolar carboxylates. While the acetate,

benzoate, and *p*-dimethylaminobenzoate complexes have no solubility in diethyl ether and are crystallized by vapor diffusion of ether into chlorinated solvent solutions, the *p*-trifluomethylbenzoate and *p*-^{t}butylbenzoate complexes were soluble in diethyl ether. All complexes were also soluble in methanol, suggesting the possibility of carboxylate dissociation in more polar solvents and tighter carboxylate binding in less polar solvents to form a nonpolar cage around the metal-alkoxo core. The solid-state structures of $LMn_3(O_2CPh)_3$ and LMn_3(*p*-Me_2N-benzoate)$_3$ are almost perfectly homologous to the acetate complex, with the same carboxylate binding motif and range between all analogous bonds of less than 0.03Å (Table 2.1; Figure 2.3).

Looking to change the coordination environment of the three metals, complexes with more weakly coordinating counterions—tetrafluoroborate, perchlorate, nitrate, *etc.*—were targeted. For cobalt, three equivalents of $Co(BF_4)_2 \bullet xH_2O$ or $Co(NO_3)_2 \bullet 6H_2O$ were reacted with **H_3L** and three equivalents of NaOH in a 2:1 CH_3CN/H_2O mixture. A red powder was isolated upon removal of solvent *in vacuo* and recrystallization from $EtOH/Et_2O$ affords $[LCo_3(NO_3)_2(EtOH)](NO_3)$ and $[LCo_3(OH)(EtOH)_3](BF_4)_2$ (Figure 2.4). In $[LCo_3(NO_3)_2(EtOH)](NO_3)$ each metal has a unique coordination environment. Co1 has a κ^2 nitrate, Co2 is six-coordinate with a terminal nitrate and a μ_2 nitrate oxygen, and Co3 is five coordinate bound by a solvent ethanol. The third nitrate counterion is outersphere. For $[LCo_3(OH)(EtOH)_3](BF_4)_2$, the BF_4 anions are all outer-sphere. The solid-state structure included three terminal ethanol ligands with a central ligand that is probably a μ_3-hydroxide; based on a Cambridge Crystallographic Database search, known $Co_3(\mu_3\text{-}O)$ complexes are all in higher oxidation states than Co^{II}_3.

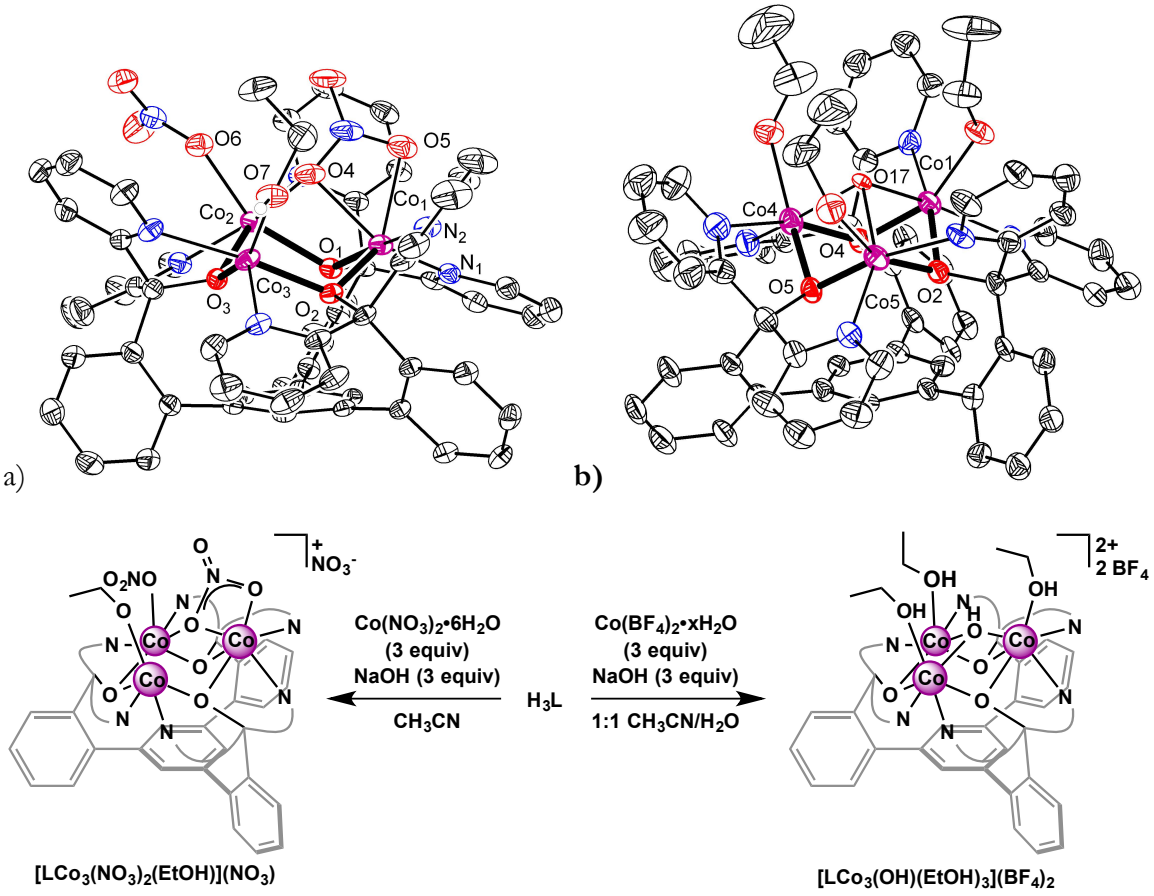

Figure 2.4. a) The solid-state structure and schematic of $[LCo_3(NO_3)_2(EtOH)](NO_3)$ and b) $[LCo_3(OH)(EtOH)_3](BF_4)_2$. Thermal ellipsoids are drawn at 50% probability; hydrogen atoms, disordered counterions, and solvent molecules are not shown for clarity.

Moreover, comparison to bond lengths in other $Co_3(\mu_3\text{-}OH)$ complexes support a hydroxo—2.143(6)Å in $[LCo_3(OH)(EtOH)_3](BF_4)_2$ versus 2.103Å for an acetate bridged trinuclear complex[12] and 2.160Å for a phenoxide stabilized species.[13] The ^{1}H NMR spectra of $[LCo_3(NO_3)_2(EtOH)](NO_3)$ and $[LCo_3(OH)(EtOH)_3](BF_4)_2$ contain broadened and shifted spectra similar to the cobalt carboxylate complexes. The ESI-MS of $[LCo_3(OH)(EtOH)_3](BF_4)_2$ gave a single peak in wet chloroform corresponding to

$LCo_3(H_2O)_2$, supporting a fluxional and therefore open coordination pocket above the three cobalts that could be used for substrate binding for a hypothetical catalytic process or for coordination of other, more complex ligand scaffolds to complement $\mathbf{L}^{3-}$.

For manganese, manganese(II) perchlorate hydrate was mixed with $\mathbf{H_3L}$ and base in CH_3CN/H_2O. In the absence of O_2, a yellow species was observed in solution and ESI-MS support the existence of $LMn_3(ClO_4)_3$, with peaks corresponding to $LMn_3(ClO_4)_2]^+$ and $[LMn_3(ClO_4)_2(H_2O)_2]^+$. Purification attempts of this Mn^{II}_3 species were unsuccessful; however, introduction of dioxygen to the yellow CH_3CN/H_2O solution gives a brown solution over 12 hours. ESI-MS suggested the possibility of LMn_3O species. Crystalline material was formed by vapor diffusion of Et_2O into CH_3CN, and an X-ray diffraction study revealed $[LMn_3O(CH_3CN)_3]^{n+}(ClO_4)_n$ (Figure 2.5).

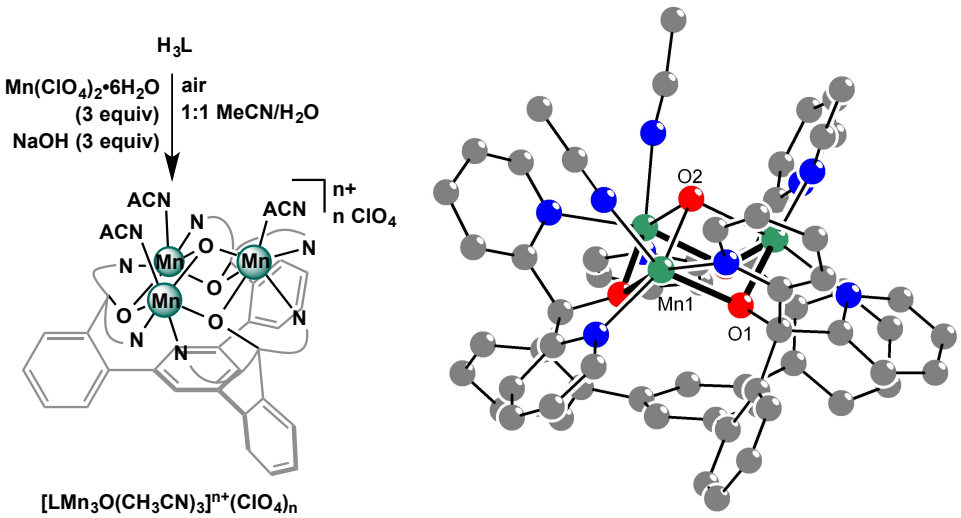

Figure 2.5 Synthesis (left) and ball-and-stick solid-state structure (right) of $[LMn_3O(CH_3CN)_3]^{n+}(ClO_4)_n$. Hydrogen atoms, disordered counterions and solvent molecules are not shown for clarity.

A μ_3-oxo or hydroxo bridges the three Mn centers, paralleling the LM_3O motif found for cobalt in $[LCo_3(OH)(EtOH)_3](BF_4)_2$, and three terminal acetonitrile molecules fill the coordination sphere. The color change from yellow to brown suggests oxidation by O_2, and the bond distances are shorter as compared to the divalent species. The average Mn–Mn distance is 3.4 Å for $LMn_3(OAc)_3$ compared to 3.2 Å for $[LMn_3O(CH_3CN)_3]^{n+}(ClO_4)_n$. However, the data set was fairly poor and only connectivity can be established; manganese oxidation state and perchlorate content is unknown. The incorporation of a single oxygen donor upon oxidation in air contrasts sharply with the reaction of $LMn_3(OAc)_3$ with air and other oxidants (see Chapter 3), likely due to the different coordinating abilities of ClO_4^- and acetate. This difference highlights the importance of the counterions in the formation of clusters supported by the $\mathbf{L}^{3-}$ framework: the framework stabilizes three metal centers in close proximity, but the ancillary ligands dictate the further reactivity—fourth metal incorporation, reduction potential, *etc.*—of the cluster. This concept is borne out in the following chapters.

2.2 Magnetic susceptibility studies

The magnetism of triangular clusters has been studied in the context of spin frustration and molecular magnets.[14] Although several alkoxo-bridged Ni^{II}_3 and Cu^{II}_3 complexes have been studied,[7b, 15] there have been fewer investigations of Mn^{II}_3, Fe^{II}_3, and Co^{II}_3 cores. Triangular clusters of manganese and iron more commonly contain higher oxidation state metal centers.[16] The present $LM_3(OAc)_3$ family provides an opportunity to systematically study the magnetic interactions of several divalent

transition metals in a single trinuclear system, allowing for better understanding of the magnetostructural characteristics of trinuclear complexes.

Magnetic susceptibility measurements were performed on powdered crystalline samples of $LM_3(OAc)_3$ (M = Mn, Fe, Co, Ni, Cu) in the temperature range 4–300 K. At room temperature, the $\chi_M T$ values approach 12.0, 9.0, 6.7, 3.3, and 1.0 cm^3 K mol^{-1}, respectively (Figure 2.6). The difference between these and the spin-only values may be due to spin-orbit coupling and population of excited states.[17] Upon cooling, the $\chi_M T$ values decrease gradually and then drop sharply below 40 K, indicating the presence of antiferromagnetic exchange interactions. With the exception of the $\chi_M T$ values of $LCu_3(OAc)_3$, which approach a plateau near the expected value for the spin-only $S = 1/2$ state (ca. 0.4 cm^3 K mol^{-1}), the $\chi_M T$ plots do not approach obvious limiting values at 4 K.

To determine the magnitude of exchange between neighboring metal centers, the magnetic behavior of the compounds was analyzed using the isotropic spin Hamiltonian (Eqn. 1) considering the two exchange pathways of an isosceles triangular arrangement. Application of the Van Vleck equation according to the Kambe vector method[18] yields the magnetic susceptibility equation (Eqn. 2).

$$H = -2J[(S_1S_2) + (S_2S_3)] - 2J_{13}(S_3S_1) \quad (1)$$

$$\chi_M = \frac{N_A\beta^2 g^2}{3kT}\left(\frac{\sum S'(S'+1)(2S'+1)\Omega(S')\exp(-W(S')/kT)}{\sum(2S'+1)\Omega(S')\exp(-W(S')/kT)}\right) \quad (2)$$

The Curie-Weiss parameter θ was included to account for possible intermolecular interactions.[19]

The fits were not appreciably improved when modelling two J values instead of one; as a result, the magnetism data were simulated for an equilateral triangle arrangement of spins, corresponding to the approximate C_3-symmetry of the $M_3(OR)_3$ cores (without acetates).[20] It should be noted that the modeled parameters approximate the spins of each compound as isotropic and do not account for the lowered symmetry

Table 2.2 Magnetic susceptibility parameters.[22]

Compound	J (cm^{-1})	g	θ (K)	R ($\times 10^{-4}$)
$LMn_3(OAc)_3$	−1.1	1.97	0.53	10
$LFe_3(OAc)_3$	−1.4	1.99	2.35	1.6
$LCo_3(OAc)_3$	−1.2	2.30	0.23	1.9
$LNi_3(OAc)_3$	−1.2	2.11	0.74	0.4
$LCu_3(OAc)_3$	−13.7	2.01	0.75	12

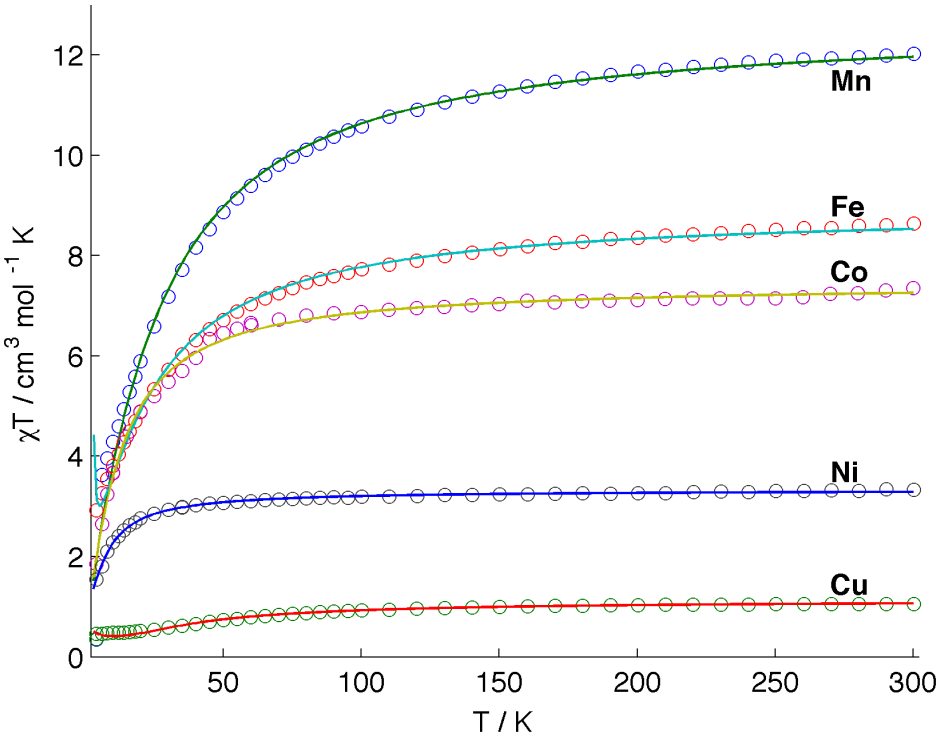

Figure 2.6 Plots of $\chi_M T$ vs. T for trinuclear complexes $LM^{II}_3(OAc)_3$. Solid lines show the best fits obtained. Compounds M=Fe & Cu synthesized by Dr Emily Tsui.

of each complex induced by the coordinated acetates. Nevertheless, the simulated magnetic susceptibility parameters (Table 2.2) show a good fit to the experimental data (R~10^{-4}). In accordance with the $\chi_M T$ plots, the simulated parameters show that compounds $LM_3(OAc)_3$ display weak antiferromagnetic exchange coupling (Table 2.2). Except for $LCu_3(OAc)_3$ (J = –13.7 cm^{-1}), the best fits were obtained with $|J| < 2$ cm^{-1}. Although the ground states are predicted to be $S = 0$ or $S = 1/2$ for an equilateral triangle of antiferromagnetically coupled ions, such small J values indicate that higher spin states are thermally populated even at low temperatures.[21] For these complexes, the presence of spin equilibria between these states is consistent with the observation that no limiting values of $\chi_M T$ are reached at 4 K.

Due to the presence of multiple types of bridging ligands, it is difficult to definitively assign the exchange pathways in these $LM_3(OAc)_3$ complexes.[23] Since there are few alkoxo-bridged trinuclear complexes containing metals other than Cu^{II}—and none with Fe^{II} to our knowledge—there is yet no clear correlation between the J constants and common structural parameters such as M–M distances or M–O–M angles.[24] Previously studied acetate-bridged trinuclear clusters of divalent metals have been shown to have similar intramolecular exchange interactions.[25] Alkoxo- and phenoxo-bridged tricobalt(II), trinickel(II), and triiron(III) clusters all show small antiferromagnetic coupling.[7d, 26] While there are no examples of Mn^{II} bridged by alkoxides, amido-bridged[8] or carboxylate-bridged[9] Mn^{II} clusters also demonstrated antiferromagnetic coupling of magnitudes similar to $LMn_3(OAc)_3$.

2.3 Electrochemical and chemical oxidation studies.

The electrochemistry of the acetate series $LMn_3(OAc)_3$, $LCo_3(OAc)_3$, and $LNi_3(OAc)_3$ was explored with cyclic voltammetry. $LMn_3(OAc)_3$ showed an irreversible oxidation wave at –0.31V versus Fc/Fc^+ in dichloromethane with 1.0M $^nBu_4NClO_4$ electrolyte (Figure 2.7a), which is consistent with its reaction with dioxygen (see Chapter 3). The returning anodic reduction wave only appears if the cell is scanned cathodically first, demonstrating the reduction of this oxidized species back to a new, reduced species. Scanning further anodically shows another oxidation at +0.5V, but this proves irreversible with only a small cathodic return wave appearing at 0 V. No reduction events occur before the solvent limit if scanned cathodically first. The number of electrons passed in this oxidation—to give $Mn_2^{II}Mn^{III}$, $Mn^{II}Mn_2^{III}$, or Mn_3^{III} with one, two, or three electrons passed, respectively—is unknown.

Figure 2.7b shows the CV of $LCo_3(OAc)_3$ in CH_2Cl_2 at 500 mV/s. There are no reversible waves—the first anodic wave at +0.4V Fc/Fc^+ produces a new species reduced on the cathodic return at –0.8V. The cathodic wave only appears if the cell is scanned anodically to produce the first oxidation and therefore likely forms another new species. Two more oxidations are seen at more oxidizing potentials—+0.7V and +1.0V—and a third may arise at +1.3V before the solvent limit. Scanning cathodically first shows no reduction events before the solvent limit. The lack of oxidation below 0.4V is consistent with the stability of this compound to air, as compared to the trimanganese complex. With respect to $LNi_3(OAc)_3$, no redox processes occurred within the solvent limit of CH_3CN.

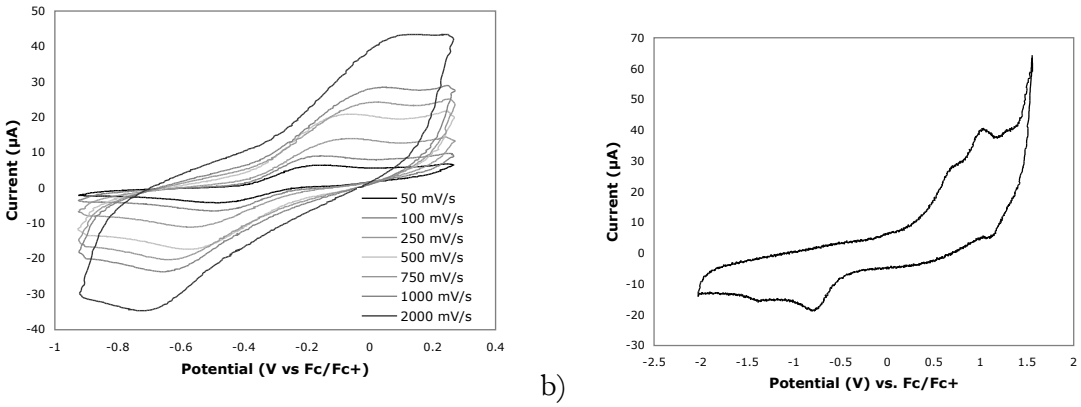

a) b)

Figure 2.7 a) Cyclic voltammetry of $LMn_3(OAc)_3$ in DCM with 1.0M $^nBu_4NClO_4$. b) Cyclic voltammetry studies of $LCo_3(OAc)_3$ in DCM with 1.0M $^nBu_4NPF_6$. All were scanned in the anodic direction first.

The pattern of irreversible oxidation of $LMn_3(OAc)_3$ at low potential, irreversible oxidation of $LCo_3(OAc)_3$ at higher potential, and no oxidation of $LNi_3(OAc)_3$ before the solvent limit is consistent with the increasing difficulty of oxidation across the first-row transition metals. Chemical oxidation corraborates the cyclic voltammetry findings: $LMn_3(OAc)_3$ reacts quickly when introduced to dioxygen, $LCo_3(OAc)_3$ is stable in air but reacts exothermically with hydrogen peroxide, giving unisolated species, and $LNi_3(OAc)_3$ reacts with neither.

CONCLUSIONS

The triarylbenzene ligand framework **H_3L** has proven amenable to metallation by a range of divalent, first-row transition metal salts. The scaffold supports the three metal centers in a conserved, trinuclear core geometry. Such complexes have displayed solubility in a range of solvents, from water to diethyl ether, and have generally proven amenable to crystallization. The $M_3(\mu\text{-}OR)_3$ core is conserved throughout the Mn, Co,

and Ni series, and the core bond distances vary only slightly when the anion is altered. The metal-ligand and metal-metal distances increase from nickel to manganese as expected from the ionic radii; for example, the metal-metal distances are 3.182(4) for $LNi_3(OAc)_3$, 3.228(2) for $LCo_3(OAc)_3$, and 3.415(1)–3.464(1) for $LMn_3(OAc)_3$. The counterions can be varied from acetate, with a series of benzoates synthesized for the Co^{II} and Mn^{II} systems. More weakly coordinating anions can also be utilized to create a more open trinuclear site. Magnetism studies support weak, antiferromagnetic coupling between the Mn^{II}, Co^{II}, and Ni^{II} centers, and cyclic voltammetry shows irreversible oxidations for Mn and Co and no oxidations for Ni.

EXPERIMENTAL SECTION

General Considerations

Reactions performed under inert atmosphere were carried out in a glovebox under a nitrogen atmosphere. Anhydrous THF was purchased from Aldrich in 18 L Pure-Pac™ containers. Anhydrous dichloromethane, acetonitrile, diethyl ether, and THF were purified by sparging with nitrogen for 15 minutes and then passing under nitrogen pressure through a column of activated A2 alumina (Zapp's). All non-dried solvents used were reagent grade or better. All NMR solvents were purchased from Cambridge Isotope Laboratories, Inc. $CDCl_3$, CD_2Cl_2, and CD_3CN were dried over calcium hydride, then degassed by three freeze-pump-thaw cycles and vacuum-transferred prior to use. ^1H NMR and ^{13}C NMR spectra were recorded on a Varian 300 MHz instrument or a Varian 500 MHz instrument, with shifts reported relative to the residual solvent peak. Elemental analyses were performed by Midwest Microlab, LLC,

Indianapolis, IN. High resolution mass spectrometry data (HRMS) were obtained at the California Institute of Technology Mass Spectrometry Facility. UV-Vis spectra were taken on a Varian Cary 50 spectrophotometer using a quartz crystal cell.

Electrochemical measurements were recorded under a nitrogen atmosphere in a MBraun glovebox at 25 °C with a Pine Instrument Company AFCBP1 bipotentiostat. An auxiliary Pt-coil electrode, a Ag/Ag^+ reference electrode (0.01 M $AgNO_3$ in CH_3CN), and a 3.0 mm glassy carbon electrode disc (BASI) were used. Data were recorded using the Pine Instrument Company AfterMath software package. All reported values were referenced to an internal ferrocene/ferrocenium couple. The electrolyte solutions were 0.1 M $^n Bu_4NClO_4$ in CH_2Cl_2 in the study of $LMn_3(OAc)_3$ and 0.1M $^n Bu_4NPF_6$ in CH_2Cl_2 for $LCo_3(OAc)_3$.

Unless indicated otherwise, all commercial chemicals were used as received. Di(2-pyridyl)ketone was purchased from Aldrich or from Frontier Chemicals. 1,3,5-tris(2-bromophenyl)benzene[27] was prepared according to literature procedures.

Synthetic Procedures

Synthesis of 1, 3, 5-Tris(2-di(2'-pyridyl)hydroxymethylphenyl)benzene (H_3L). In the glovebox, a 1L Erlenmeyer flask was equipped with a stir bar and charged with 1,3,5-tris(2-bromophenyl)benzene (8.83 g, 16.26 mmol) and Et_2O (325 mL). The off-white suspension was frozen in the cold well. While thawing, *t*-BuLi (1.7 M in pentane, 59 mL, 100 mmol) was poured in quickly. The mixture was stirred 1.5 hours as it came to room temperature. The solution flashed green immediately upon *t*-BuLi addition,

followed by yellow. As it warmed, the solution became dark red and homogeneous, then light orange/pink and heterogeneous. The mixture was refrozen in the cold well. While thawing, a solution of di(2-pyridyl)ketone (8.98 g, 48.8 mmol) in 2:1 Et_2O/THF (70 mL) was added. The solution turned dark yellow and thick. The reaction mixture was allowed to warm to room temperature and stirred for 8 h under nitrogen. The mixture was taken out of the glovebox and poured into water (~500 mL). The resulting orange solid was collected by filtration and washed with water and Et_2O. The solid was dissolved in CH_2Cl_2 and extracted twice with water and once with brine and dried over magnesium sulfate, then filtered. The solvent was removed under reduced pressure, and the yellow-orange solid was precipitated from acetone to yield the product as a white solid (9.64 g, 69%). ^{1}H NMR (300 MHz, $CDCl_3$, 25 °C): δ 8.41 (d, *J* = 6 Hz, 6 H, *a*), 7.66 (bs, 6 H, *c*), 7.55 (bs, 6 H, *d*), 7.25 (t, *J* = 7.5 Hz, 3 H, *f*), 7.13 (t, *J* = 7.5 Hz, 3 H, *g*), 7.02 (bs, 6 H, *b*), 6.81 (bs, 3 H, *e*), 6.74 (*J* = 6 Hz, 3 H, *h*), 6.37 (bs, 3 H, OH), 6.14 (bs, 3 H, *j*). ^{13}C NMR ($CDCl_3$): δ 164.0, 147.2, 144.0, 143.5, 139.5, 136.2, 133.2, 129.2, 126.6, 126.1, 123.7, 121.9, 81.9. IR (CH_2Cl_2): 3330, 1751 cm^{-1}. HRMS (FAB+): calcd. for $C_{57}H_{43}N_6O_3$: 859.3397; found: 859.3436 [M+H].

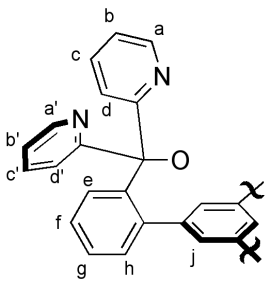

Synthesis of $LMn_3(OAc)_3$. Under an N_2 atmosphere a solid mixture of **H_3L** (8.64g, 10.0 mmol) and $Mn(OAc)_2$ (5.22g, 30.2 mmol) was suspended in degassed H_2O (15mL) and CH_3CN (65 mL). A solution of KOH (1.7g, 30.2 mmol) in degassed H_2O (10 mL) was added to the tan suspension under stirring. Over approximately thirty minutes, the solution became more clear and yellow, but never became fully homogeneous. If stirring

was stopped, two liquid layers became visible: the top, dark yellow CH_3CN layer and clear and colorless bottom H_2O layer. After stirring for 5 h, the reaction mixture was filtered through celite to remove a small amount of brown solid. The clear and colorless bottom layer was separated by pipette from the clear and yellow top layer to remove a majority of the KOAc side product. The CH_3CN solution was concentrated *in vacuo* to give a yellow powder. $CHCl_3$ (*ca.* 20 mL) was added and removed *in vacuo* twice to remove any CH_3CN and H_2O. The yellow powder was dissolved in $CHCl_3$, filtered through Celite, and Et_2O was vapor diffused into the $CHCl_3$ solution to afford yellow crystals of **1** (10.77g, 81% for **1**•$CHCl_3$). $CHCl_3$ could be removed by triturating **1**•$CHCl_3$ in THF for *ca.* 3 h and collecting the yellow solid by filtration (10.00g, 78% for **1**•THF). ^{1}H NMR (300 MHz, $CDCl_3$, 25 ºC): δ 41.76 ($\Delta\nu_{1/2}$ = 2000 Hz), 11.15 ($\Delta\nu_{1/2}$ = 1230 Hz), 4.49 ($\Delta\nu_{1/2}$ = 850 Hz), –10.56 ($\Delta\nu_{1/2}$ = 1530 Hz). UV-Vis (CH_2Cl_2, λ_{max} (ε)): 256 (47,200 M^{-1} cm^{-1}); 350 (585 M^{-1} cm^{-1}) nm. Anal. Calcd. for $C_{63}H_{48}Mn_3N_6O_9$: C, 63.17; H, 4.04; N, 7.02. Found: C, 62.96; H, 4.20; N, 6.77.

Synthesis of $LCo_3(OAc)_3$. **H_3L** (310.5 mg, 0.36 mmol) was suspended in a 1:1 solution of CH_3CN and H_2O (~6 mL). $Co(OAc)_2$•$4H_2O$ (270.1 mg, 1.08 mmol) was added as a crystalline solid to the stirring suspension. To this mixture, a 1 M KOH solution in H_2O (1.1 mL) was added dropwise. The reaction was stirred at room temperature until it became a homogenous solution (12 h), then the solvent was removed *in vacuo*. The red-purple solid was extracted with CH_2Cl_2, and the resulting red solution was dried *in vacuo* for 8 h. The resulting red-purple powder was dissolved in $CHCl_3$ and diethyl ether was allowed to diffuse into the solution slowly as a vapor. White precipitate collected at the bottom of the vial and the red homogeneous solution was decanted off. This

precipitation procedure was repeated until no more white precipitate appeared and the red crystalline clusters of $LCo_3(OAc)_3$ were collected (250 mg, 57%). ^{1}H NMR (300 MHz, $CDCl_3$, 25 °C): δ 128.16 (3 H), 89.12 (3 H), 65.30 (3 H), 57.02 (3 H), 36.52 (3 H), 27.29 (3 H). 16.67 (3 H), 14.72 (9 H), 10.17 (3 H), 8.99(3 H), 6.06 (3 H), 1.01 (3 H), –0.42 (3 H), –14.24 (3H). UV-Vis: (CH_2Cl_2, λ_{max} (ε)): 251 (39,000 M^{-1} cm^{-1}); 331 (2350 M^{-1} cm^{-1}); 457 (76 M^{-1} cm^{-1}); 551 (86 M^{-1} cm^{-1}); 580 (70 M^{-1} cm^{-1}) nm. Anal. Calcd. for $C_{63}H_{48}Co_3N_6O_9$: C, 62.54; H, 4.00; N, 6.95. Found: C, 62.36; H, 4.02; N, 6.90.

Synthesis of $LNi_3(OAc)_3$. **H_3L** (270.4 mg, 0.31 mmol) was suspended in a 1:1 solution of CH_3CN and H_2O (~5 mL). $Ni(OAc)_2$•$4H_2O$ (235.0 mg, 0.94 mmol) was added as a crystalline solid to the stirring suspension. To this, a 1 M KOH solution in H_2O (0.94 mL) was added dropwise. When all of the **H_3L** was dissolved to give a green homogeneous solution (~12 h), the solvent was removed under reduced pressure. The green residue was taken up in CH_2Cl_2 and a white solid was filtered from the green solution. The solution was pumped down and dried *in vacuo* for 8 h. The resulting green powder was dissolved in $CHCl_3$ and diethyl ether was allowed to diffuse into the solution as a vapor. White precipitate collected at the bottom of the vial and the green homogeneous solution was decanted off. This precipitation procedure was repeated until no more white precipitate appeared and green crystalline clusters of $LNi_3(OAc)_3$ grew (100 mg, 27%). ^{1}H NMR (300 MHz, $CDCl_3$, 25 °C): δ 150.81 (3 H), 136.93 (3 H), 58.87 (3 H), 46.53 (3 H), 34.58 (3 H), 32.08 (3 H), 21.36 (9 H), 15.85 (3 H), 12.31 (6 H), 10.76 (3 H), 7.74 (3 H), 4.90 (3 H), 3.8 (3 H). UV-Vis: (CH_2Cl_2, λ_{max} (ε)): 254 (35,900 M^{-}

^{1} cm^{-1}); 385 (192 M^{-1} cm^{-1}); 450 (45 M^{-1} cm^{-1}); 500 (29 M^{-1} cm^{-1}); 676 (37 M^{-1} cm^{-1}) nm. Anal. Calcd. for $C_{63}H_{48}N_6Ni_3O_9$: C, 62.58; H, 4.00; N, 6.95. Found: C, 62.49; H, 4.20; N, 7.05.

Synthesis of LMn_3(benzoate)$_3$. Under an N_2 atmosphere, **H_3L** (67.6 mg, 0.08 mmol) and $Mn(O_2CPh)_2 \bullet xH_2O$ (78.7 mg, 0.24 mmol) were combined in a scintillation vial equipped with a stirbar, to which a 1:1 CH_3CN/H_2O solution was added. To the stirring tan suspension was added a 1 M solution of KOH in H_2O (0.24 mL). After the solution became yellow and mostly homogeneous, the solution was filtered through celite, and volatile material was removed *in vacuo*. The residue was partially dissolved in CH_2Cl_2, then dried under vacuum twice to ensure evaporation of CH_3CN and H_2O. The residue was triturated in CH_2Cl_2 and a white solid was filtered from the yellow solution. Yellow crystals were grown by vapor diffusion of diethyl ether into a CH_2Cl_2 solution of $LMn_3(O_2CPh)_3$. ^{1}H NMR (300MHz, CD_2Cl_2, 25 °C): δ 43.76 ($\Delta\nu_{1/2}$ = 3600 Hz), 10.23 ($\Delta\nu_{1/2}$ = 1050 Hz), 1.95 ($\Delta\nu_{1/2}$ = 800 Hz), –10.69 ($\Delta\nu_{1/2}$ = 1600 Hz).

Synthesis of LMn_3(*p*-dimethylaminobenzoate)$_3$. Under an N_2 atmosphere, **H_3L** (176.5 mg, 0.21 mmol) and Mn(*p*-dimethylaminobenzoate)$_2 \bullet xH_2O$ (258.4 mg, 0.62 mmol) were combined in a scintillation vial equipped with a stirbar, to which a 2:1 CH_3CN/H_2O solution was added. To the stirring tan suspension was added a 1 M solution of KOH in H_2O (0.24 mL). After the solution became yellow and homogeneous the volatile material was removed *in vacuo*. The residue was partially dissolved in CH_2Cl_2 then dried under vacuum twice to ensure evaporation of CH_3CN and H_2O. The residue was triturated in CH_2Cl_2 and a white solid was filtered from the

yellow solution. Orange crystals were grown by vapor diffusion of diethyl ether into a CH_2Cl_2 solution of LMn_3(*p*-dimethylaminobenzoate)$_3$. ^{1}H NMR (300MHz, CD_2Cl_2, 25 °C): δ 40.95 ($\Delta\nu_{1/2}$ = 2200 Hz), 11.03 ($\Delta\nu_{1/2}$ = 1500 Hz), 8.83 ($\Delta\nu_{1/2}$ = 1300 Hz), –9.120 ($\Delta\nu_{1/2}$ = 1500 Hz).

Synthesis of LCo_3(benzoate)$_3$.H_3L (53.5 mg, 0.06 mmol) was suspended in a 2:1 CH_3CN/H_2O solution and $Co(O_2CPh)_2$ (56.2 mg, 0.18 mmol) was added as a powder to the stirring solution. After the solution became red and mostly homogeneous, the solution was filtered through celite, and volatile material was removed *in vacuo*. The resulting solid was triturated in Et_2O to remove any benzoic acid, and the solids were collected by filtration. The solid was dried *in vacuo* and then crystals were grown by vapor diffusion of diethyl ether into a $CHCl_3$ solution of $LCo_3(O_2CPh)_3$ (15.3 mg, 15%). ^{1}H NMR (300 MHz, $CDCl_3$, 25 °C): δ 128.64 (3 H), 70.17 (3 H), 62.48 (3 H), 60.01 (3 H), 31.64 (3 H), 25.07 (6 H), 14.12 (3 H), 7.62 (3 H), 5.81 (3H), 2.13 (6 H), –0.88 (3 H), –1.08 (3 H), –1.57 (3 H), –19.80 (3 H), –24.33 (6 H).

Synthesis of LCo_3(*p*-toluate)$_3$. H_3L (53.5 mg, 0.06 mmol) was suspended in a 1:1 CH_3CN/H_2O solution and Co(*p*-toluate)$_2$•xH_2O (56.2 mg, 0.18 mmol) was added as a powder to the stirring solution. After the solution became red and homogeneous, the volatile material was removed *in vacuo*. The resulting solid was triturated in Et_2O to remove any toluic acid, and the solids were collected by filtration. The purple solid was dried *in vacuo* and then crystals were grown by vapor diffusion of diethyl ether into a

$CHCl_3$ solution of LCo_3(*p*-toluate)$_3$ (31.5 mg, 37%). ^{1}H NMR (300 MHz, $CDCl_3$, 25 °C): δ 137.96 (3 H) 74.01 (3 H), 61.47 (3 H), 57.62 (3 H), 30.48 (3 H), 30.48 (3 H), 26.88 (3 H), 22.57 (3 H), 12.56 (3 H), 9.24 (3 H), 6.31(3 H), 1.21 (6 H), –0.26 (9H), –1.46 (3 H), –1.71 (3 H), –18.65 (3 H), –25.20 (6H).

Synthesis of LCo_3(*p*-dimethylaminobenzoate)$_3$. H_3L (38.9 mg, 0.043 mmol) was suspended in a 1:1 CH_3CN/H_2O solution and Co(*p*-^{t}butylbenzoate)$_2$•xH_2O (61.0 mg, 0.14 mmol) was added as a powder to the stirring solution. After the solution became red and homogeneous, the volatile material was removed *in vacuo*. The resulting purple solid was triturated in Et_2O to remove any ^{t}butylbenzoic acid, and the solids were collected by filtration. The purple solid was dried *in vacuo* and then crystals were grown by vapor diffusion of diethyl ether into a $CHCl_3$ solution of LCo_3(*p*-^{t}butylbenzoate)$_3$ (52 mg, 74%). ^{1}H NMR (300 MHz, $CDCl_3$, 25 °C): δ 136.71 (3 H), 72.91 (3 H), 61.23 (3 H), 57.64 (3 H), 30.47 (3 H), 26.26 (3 H), 23.11 (3 H), 12.79 (3 H), 8.63 (3 H), 6.10 (3 H), 1.04 (6 H), –1.72 (3 H), –1.79 (3 H), –2.37 (27 H), –19.30 (3 H), –26.82 (6 H). Anal. Calcd. for $C_{90}H_{78}Co_3N_6O_9$: C, 69.10; H, 5.03; N, 5.37. Found: C, 63.88; H, 4.68; N, 4.36.

Synthesis of [LCo_3(EtOH)(NO_3)$_2$](NO_3). H_3L (40 mg, 0.05 mmol) was taken up in CH_3CN (0.8 mL). Co(NO_3)$_2$•6H_2O (40.7 mg, 0.14 mmol) was added as a solid and quickly gave a fusia and clear solution. To this, a 0.2M solution of NaOH in H_2O (0.75 mL) was added to give a red solution. This was pumped down to give a pink powder, which in turn was triturated in cold absolute EtOH. Solid, white $NaNO_3$ was filtered off to give a red solution. Crystalline material was obtained by vapor diffusion of Et_2O into

EtOH. ^{1}H NMR (300 MHz, CDCl3, 25 °C): δ 60.0 (3H), 50.0 (3H), 36.1 (3H), 10.8 (3H), 9.2 (3H), 6.9 (3H), 5.1 (15H), -0.3 (3H), -2.5 (3H), -14.8 (3H).

Synthesis of $[LCo_3(EtOH)_3(OH)](BF_4)_2$. **$H_3L$** (53 mg, 0.06 mmol) was suspended in a 1:1 CH_3CN/H_2O solution and $Co(BF_4)_2•xH_2O$ (63 mg, 0.18 mmol). To the resulting red-orange and clear solution was added 1.0 M NaOH in H_2O (0.19 mL). After 6 h, the volatile material was removed *in vacuo*. The resulting red powder was dissolved in EtOH and diethyl ether was allowed to diffuse into the solution slowly as a vapor. White precipitate collected at the bottom of the vial and the red homogeneous solution was decanted off. This precipitation procedure was repeated until no more white precipitate appeared and the red crystalline clusters of $LCo_3(EtOH)_3(OH)](BF_4)_2$ were collected. ^{1}H NMR (300 MHz, CD_3OD, 25 °C): δ 49.16 (3 H), 42.31 (3 H), 39.03 (3 H), 35.08 (3 H), 10.33 (3 H), 9.36 (3 H), 5.26 (15 H), 1.68 (3 H), –3.13 (3 H), –11.23 (3 H).

Synthesis of $[LMn_3O(CH_3CN)_3]^{n+}(ClO_4)_n$. **$H_3L$** (50.5 mg, 0.06 mmol) was suspended in CH_3CN (1 mL) and H_2O (1 mL). To this tan suspension, the light pink $Mn(ClO_4)_2•6H_2O$ was added as a solid. No change was observed until three equivalents of NaOH (1.0M, 0.18 mL) were added, leading to a brown, mostly homogeneous solution. After stirring for *ca.* 12 hours, the volatile material was removed *in vacuo*. The solid was fractionated with dichloromethane, and from the dichloromethane solution crystalline precipitate forms. This solid was recrystallized from vapor diffusion of Et_2O

into an acetonitrile solution. ^{1}H NMR (300 MHz, CD_3CN, 25 °C): δ 40.44, 34.25, 7.89, 7.46, 6.18, 2.41, –14.49, –17.30.

Magnetic Susceptibility Measurements

General Considerations. Magnetic susceptibility measurements were carried out in the Molecular Materials Research Center in the Beckman Institute of the California Institute of Technology on a Quantum Design MPMS instrument running MPMS Multivu software. Crystalline samples (0.030–0.100 g) were powdered and suspended in clear plastic straws in gelatin capsules. Data were recorded at 0.5 and 5 T from 4–300 K. Diamagnetic corrections were made using Pascal's constants as follows: –710, –645, and –645 × 10^{-6} cm^3/mol, respectively, for M = Mn, Co, and Ni. The data for $LMn_3(OAc)_3$ were processed and simulated with the inclusion of one equivalent of chloroform, which was found to be in the sample by both elemental analysis and ^{1}H NMR spectroscopy. Anal. Calcd. for $C_{64}H_{39}Cl_3Mn_3N_6O_9$ ($LMn_3(OAc)_3$•$CHCl_3$): C, 58.35; H, 3.75; N, 6.38. Found: C, 58.74; H, 3.87; N, 6.31.

The $\chi_M T$ data were fit to the magnetic susceptibility equation derived from the isotropic spin Hamiltonian for two coupling constants, J and J_{13} (Eq. 1).

$$\hat{H} = -2J[(\hat{S}_1\hat{S}_2)+(\hat{S}_2\hat{S}_3)]-2J_{13}(\hat{S}_3\hat{S}_1)] \qquad (1)$$

The Kambe vector method[18a] yields the magnetic susceptibility equation [Eq. (2)]. In this equation, spin levels are defined by the quantum number $S' = 3S, 3S–1, 3S–2, \ldots, 0$ or ½, where S = 5/2, 3/2, and 1, respectively for M = Mn, Co, and Ni. Application

of the Van Vleck equation gives the energy of each spin state [Eq. (3)].[21a] The multiplicity of each spin level is defined by $\Omega(S')$.

$$\chi_M = \frac{N_A \beta^2 g^2}{3kT} \frac{\sum S'(S'+1)(2S'+1)\Omega(S')\exp(-W(S')/kT)}{\sum (2S'+1)\Omega(S')\exp(-W(S')/kT)} \qquad (2)$$

$$W(S') = -J[S'(S'+1) - 3S(S+1)] \qquad (3)$$

The data were fit using Matlab by minimizing $R = \sum |(\chi_M T)_{obs} - (\chi_M T)_{calcd}|^2 / \sum (\chi_M T)_{obs}{}^2$.

Crystallographic Information

Crystallographic data have been deposited at the CCDC, 12 Union Road, Cambridge CB2 1EZ, UK and copies can be obtained on request, free of charge, by quoting the publication citation and the deposition numbers 787163 (Mn), 777599 (Co), 803595 (Ni).

As only these three acetate complexes were published, the refinements for all the other, unpublished complexes were never finalized. As such, their refinement data is not included in Table 2.3. All of the most up-to-date refinements and notes on their quality as of this writing can be found on RecipricalNet (http://reciprocalnet.caltech.edu) with the appropriate jskXX code, which can be found in the file "JSKanady XRD structure list.pdf" on the Agapie Group server in the directory LANGLEYSERVER/group/Structures/JacobKanady.

Table 2.3. Crystal and refinement data for $LM_3(OAc)_3$ (M = Mn, Co, Ni).

	$LMn_3(OAc)_3$	$LCo_3(OAc)_3$	$LNi_3(OAc)_3$
CCDC number	787163	777599	803593
empirical formula	$C_{63}H_{48}Mn_3N_6O_9$	$C_{63}H_{48}Co_3N_6O_9$	$C_{63}H_{48}Mn_3N_6O_9$
formula wt	1197.90	1209.89	1209.17
T (K)	100(2)	100(2)	100(2)
a, Å	10.5708(8)	20.8675(10)	20.7019(9)
b, Å	19.6592(14)	20.8675(10)	20.7019(9)
c, Å	20.2109(15)	10.5670(6)	10.6229(6)
α, deg	71.889(4)	90	90
β, deg	88.967(4)	90	90
γ, deg	75.160(4)	120	120
V, $Å^3$	3850.2(5)	3985.0(4)	3942.7(3)
Z	2	3	3
cryst syst	triclinic	trigonal	trigonal
space group	P-1	R 3	R 3
d_{calcd}, g/cm^3	1410	1512	1528
θ range, deg	2.00–30.2	2.23–30.10	1.97–30.16
μ, mm^{-1}	0.531	0.993	1.132
abs cor	none	Semi-empirical from equivalents	none
GOF	2.775	2.172	2.887
R1,[a] wR2[b] (I> 2σ(I))	0.0504, 0.0863	0.0380, 0.0788	0.0443, 0.0690

[a] $R1 = \sum ||F_o| - |F_c|| / \sum |F_o|$. [b] $wR2 = \{\sum [w(F_o^2 - F_c^2)^2] / \sum [w(F_o^2)^2]\}^{1/2}$.

Special refinement details for $LMn_3(OAc)_3$. Crystals were mounted in a loop with oil and then placed on the diffractometer under a nitrogen stream at 100K. The solvent are contains four molecules of chloroform and one of diethyl ether. Although they were discernable we were unable to obtain a satisfactory solvent model due to disorder. Due to the considerable percentage of the unit cell occupied by the solvent (37.4%) and the presence of strong scatterers (12 Cl atoms) SQUEEZE[28] was employed to produce a bulk solvent correction to the observed intensities. The program accounted for 430 electrons of approximately 550 expected. The resulting model is vastly superior to the model including solvent specifically. Refinement of F^2 against ALL reflections. The weighted R-factor (*w*R) and goodness of fit (S) are based on F^2, conventional R-factors (R) are based on F, with F set to zero for negative F^2. The threshold expression of $F^2 > 2s(F^2)$ is used only for calculating R-factors(gt) *etc.* and is not relevant to the choice of reflections for refinement. R-factors based on F^2 are statistically about twice as large as those based on F, and R-factors based on ALL data will be even larger. All esds (except the esd in the dihedral angle between two l.s. planes) are estimated using the full covariance matrix. The cell esds are taken into account individually in the estimation of esds in distances, angles, and torsion angles; correlations between esds in cell parameters are only used when they are defined by crystal symmetry. An approximate (isotropic) treatment of cell esds is used for estimating esds involving l.s. planes.

Special refinement details for $LCo_3(OAc)_3$. Crystals were mounted on a glass fiber using Paratone oil and then placed on the diffractometer under a nitrogen stream at 100K. The molecule sits around a 3-fold axis. The bound acetate displays two bonding

modes, both mono- and bi-dentate. The populations of both modes were refined to a ratio of 73:27, respectively. The bi-dentate mode places one oxygen and the methyl group nearly on the 3-fold axis and so cannot be present more than 1/3rd of the time. A refined population of 27% suggests a mixture in the crystal with a species where all three acetate ligands are mono-dentate. Refinement of F^2 against ALL reflections. The weighted R-factor (*w*R) and goodness of fit (S) are based on F^2, conventional R-factors (R) are based on F, with F set to zero for negative F^2. The threshold expression of $F^2 > 2s(F^2)$ is used only for calculating R-factors(gt) etc. and is not relevant to the choice of reflections for refinement. R-factors based on F^2 are statistically about twice as large as those based on F, and R-factors based on ALL data will be even larger. All esds (except the esd in the dihedral angle between two l.s. planes) are estimated using the full covariance matrix. The cell esds are taken into account individually in the estimation of esds in distances, angles and torsion angles; correlations between esds in cell parameters are only used when they are defined by crystal symmetry. An approximate (isotropic) treatment of cell esds is used for estimating esds involving l.s. planes.

Special refinement details for $LNi_3(OAc)_3$. Crystals were mounted on a glass fiber using Paratone oil and then placed on the diffractometer under a nitrogen stream at 100K. The molecule sits around a 3-fold axis. The bound acetate displays two bonding modes, both mono- and bi-dentate. The populations of both modes were refined to a ratio of 74:26, respectively. The bi-dentate mode places one oxygen and the methyl group nearly on the 3-fold axis and so cannot be present more than 1/3rd of the time. A refined population of 26% suggests a mixture in the crystal with a species where all

three acetate ligands are mono-dentate. Refinement of F^2 against ALL reflections. The weighted R-factor (*w*R) and goodness of fit (S) are based on F^2, conventional R-factors (R) are based on F, with F set to zero for negative F^2. The threshold expression of $F^2 > 2s(F^2)$ is used only for calculating R-factors(gt) *etc.* and is not relevant to the choice of reflections for refinement. R-factors based on F^2 are statistically about twice as large as those based on F, and R-factors based on ALL data will be even larger. All esds (except the esd in the dihedral angle between two l.s. planes) are estimated using the full covariance matrix. The cell esds are taken into account individually in the estimation of esds in distances, angles and torsion angles; correlations between esds in cell parameters are only used when they are defined by crystal symmetry. An approximate (isotropic) treatment of cell esds is used for estimating esds involving l.s. planes.

REFERENCES

1. (a) Holm, R. H.; Kennepohl, P.; Solomon, E. I. *Chem. Rev.* **1996,** *96*, 2239-2314.(b) McEvoy, J. P.; Brudvig, G. W. *Chem. Rev.* **2006,** *106*, 4455-4483.
2. (a) Kanan, M. W.; Yano, J.; Surendranath, Y.; Dinca, M.; Yachandra, V. K.; Nocera, D. G. *J. Am. Chem. Soc.* **2010,** *132*, 13692-13701.(b) Risch, M.; Khare, V.; Zaharieva, I.; Gerencser, L.; Chernev, P.; Dau, H. *J. Am. Chem. Soc.* **2009,** *131*, 6936-6937.
3. Tsui, E. Y.; Day, M. W.; Agapie, T. *Angew. Chem. Int. Ed.* **2011,** *50*, 1668-1672.
4. Stamatatos, T. C.; Efthymiou, C. G.; Stoumpos, C. C.; Perlepes, S. P. *Eur. J. Inorg. Chem.* **2009**, 3361-3391.
5. Papaefstathiou, G. S.; Escuer, A.; Mautner, F. A.; Raptopoulou, C.; Terzis, A.; Perlepes, S. P.; Vicente, R. *Eur. J. Inorg. Chem.* **2005**, 879-893.
6. (a) Efthymiou, C. G.; Raptopoulou, C. P.; Terzis, A.; Boca, R.; Korabic, M.; Mrozinski, J.; Perlepes, S. P.; Bakalbassis, E. G. *Eur. J. Inorg. Chem.* **2006**, 2236-

2252.(b) Serna, Z. E.; Lezama, L.; Urtiaga, M. K.; Arriortua, M. I.; Barandika, M. G.; Cortes, R.; Rojo, T. *Angew. Chem. Int. Ed.* **2000,** *39*, 344-347.

7. (a) Abrahams, B. F.; Hudson, T. A.; Robson, R. *Chem. Eur. J.* **2006,** *12*, 7095-7102.(b) Kodera, M.; Tachi, Y.; Kita, T.; Kobushi, H.; Sumi, Y.; Kano, K.; Shiro, M.; Koikawa, M.; Tokii, T.; Ohba, M.; Okawa, H. *Inorg. Chem.* **2000,** *39*, 226-234.(c) Kohn, R. D.; Haufe, M.; Kociok-Kohn, G.; Filippou, A. C. *Inorg. Chem.* **1997,** *36*, 6064-6069.(d) Labisbal, E.; Rodriguez, L.; Souto, O.; Sousa-Pedrares, A.; Garcia-Vazquez, J. A.; Romero, J.; Sousa, A.; Yanez, M.; Orallo, F.; Real, J. A. *Dalton Trans.* **2009**, 8644-8656.(e) Telfer, S. G.; Kuroda, R.; Lefebvre, J.; Leznoff, D. B. *Inorg. Chem.* **2006,** *45*, 4592-4601.
8. Hatnean, J. A.; Raturi, R.; Lefebvre, J.; Leznoff, D. B.; Lawes, G.; Johnson, S. A. *J. Am. Chem. Soc.* **2006,** *128*, 14992-14999.
9. Christian, P.; Rajaraman, G.; Harrison, A.; Helliwell, M.; McDouall, J. J. W.; Raftery, J.; Winpenny, R. E. P. *Dalton Trans.* **2004**, 2550-2555.
10. Bertini, I.; Luchinat, C., *NMR of paramagnetic Species in Biological Systems*. Benjamin Cummings: Menlo Park, California, 1986.
11. Wemple, M. W.; Tsai, H. L.; Wang, S. Y.; Claude, J. P.; Streib, W. E.; Huffman, J. C.; Hendrickson, D. N.; Christou, G. *Inorg. Chem.* **1996,** *35*, 6437-6449.
12. Reynolds, R. A.; Yu, W. O.; Dunham, W. R.; Coucouvanis, D. *Inorg. Chem.* **1996,** *35*, 2721-2722.
13. Higgs, T. C.; Carrano, C. J. *Inorg. Chem.* **1997,** *36*, 291-297.
14. (a) Wang, L.-L.; Sun, Y.-M.; Yu, Z.-Y.; Qi, Z.-N.; Liu, C.-B. *The Journal of Physical Chemistry A* **2009,** *113*, 10534-10539.(b) Ferrer, S.; Lloret, F.; Bertomeu, I.; Alzuet, G.; Borras, J.; Garcia-Granda, S.; Liu-Gonzalez, M.; Haasnoot, J. G. *Inorg. Chem.* **2002,** *41*, 5821-5830.
15. Inoue, M.; Ikeda, C.; Kawata, Y.; Venkatraman, S.; Furukawa, K.; Osuka, A. *Angew. Chem. Int. Ed.* **2007,** *46*, 2306-2309.
16. A CSD search for oxygen atom-bridged trinuclear clusters with two N-donors per metal centers resulted in only one example of a complex with three Mn^{II} centers and

no results for three Fe^{II} centers. The remaining search results contained Mn^{IV}_3 and Fe^{III}_3 clusters.

17. Drago, R. S., *Physical methods for chemists*. Surfside Scientific Publishers: Gainesville, 1992.
18. (a) Kambe, K. *J. Phys. Soc. Jpn.* **1950,** *5*, 48-51.(b) Sinn, E. *Coord. Chem. Rev.* **1970,** *5*, 313-&.
19. Crawford, V. H.; Richardson, H. W.; Wasson, J. R.; Hodgson, D. J.; Hatfield, W. E. *Inorg. Chem.* **1976,** *15*, 2107-2110.
20. The magnetic susceptibility parameters were determined by minimizing $R = \sum \left| (\chi_M T)_{obs} - (\chi_M T)_{calcd} \right|^2 / \sum (\chi_M T)_{obs}{}^2$.
21. (a) Mabbs, F. E.; Machin, D. J., *Magnetism and Transition Metal Complexes*. Dover Publications, Inc.: Mineola, 2008.(b) Haddadpour, S.; Niedermeyer, H.; Clerac, R.; Dehnen, S. *Dalton Trans.* **2009**, 8162-8164.
22. For $LMn_3(OAc)_3$, the discrepancy between the expected g-value of 2.00 and the fitted value of 1.97 may be accounted for by small amounts of solvent in the sample detected by ^{1}H NMR spectroscopy.
23. Kahn, O., *Molecular Magnetism*. VCH Publishers, Inc.: New York, 1993.
24. Jiang, Y.-B.; Kou, H.-Z.; Wang, R.-J.; Cui, A.-L.; Ribas, J. *Inorg. Chem.* **2005,** *44*, 709-715.
25. Reynolds, R. A.; Yu, W. O.; Dunham, W. R.; Coucouvanis, D. *Inorg. Chem.* **1996,** *35*, 2721-2722.
26. (a) Adams, H.; Fenton, D. E.; Cummings, L. R.; McHugh, P. E.; Ohba, M.; Okawa, H.; Sakiyama, H.; Shiga, T. *Inorg. Chim. Acta* **2004,** *357*, 3648-3656.(b) Boskovic, C.; Rusanov, E.; Stoeckli-Evans, H.; G¸del, H. U. *Inorg. Chem. Commun.* **2002,** *5*, 881-886.
27. Feng, X. L.; Wu, J. S.; Enkelmann, V.; Mullen, K. *Org. Lett.* **2006,** *8*, 1145-1148.
28. Vandersluis, P.; Spek, A. L. *Acta Crystallogr. A* **1990,** *46*, 194-201.

CHAPTER 3

ROLE OF OXIDO INCORPORATION AND LIGAND LABILITY IN EXPANDING REDOX ACCESSIBILITY OF STRUCTURALLY RELATED Mn_4 CLUSTERS

Published in part as:

Kanady, J. S.; Tran, R.; Stull, J. A.; Lu, L.; Stich, T. A.; Day, M. W.; Yano, J.; Britt, R. D.; Agapie, T. *Chem. Sci.* **2013,** *4*, 3986-3996.

ABSTRACT

Photosystem II supports four manganese centers through nine oxidation states from manganese(II) during assembly through to the most oxidized state before O_2 formation and release. The protein-based carboxylate and imidazole ligands allow for significant changes of the coordination environment during the incorporation of hydroxido and oxido ligands upon oxidation of the metal centers. We report the synthesis and characterization of a series of tetramanganese complexes in four of the six oxidation states from $Mn^{II}_3Mn^{III}$ to $Mn^{III}_2Mn^{IV}_2$ with the same ligand framework (**L**) by incorporating four oxido ligands. A 1,3,5-triarylbenzene framework appended with six pyridyl and three alkoxy groups was utilized along with three acetate anions to access tetramanganese complexes, Mn_4O_x, with x = 1, 2, 3, and 4. Six clusters in various states were isolated and characterized by crystallography. Four others were observed electrochemically, accessing in total eight oxidation states from Mn^{II}_4 to $Mn^{III}Mn^{IV}_3$. Chemical redox reactions of the $Mn^{III}_2Mn^{IV}_2O_4$ cubane provided reduced ($Mn^{III}_3Mn^{IV}O_4$) and oxidized ($Mn^{III}Mn^{IV}_3O_4$) cubanes that, while unstable, could be frozen for spectroscopic analysis before decomposition. This structurally related series of compounds was characterized by EXAFS, XANES, EPR, magnetism, and cyclic voltammetry. Similar to the ligands in the active site of the protein, the ancillary ligand (**L**) is preserved throughout the series and changes its binding mode between the low and high oxido-content clusters. Implications for the rational assembly and properties of high oxidation state metal-oxido clusters are presented.

INTRODUCTION

In biological systems, the oxidation of water to dioxygen is performed by the oxygen-evolving complex (OEC) of photosystem II (PSII).[1] In the catalytic cycle, or Kok cycle,[2] four photo-generated oxidizing equivalents sequentially oxidize the OEC, which releases O_2 upon the fourth oxidation. Although the oxidation states are still debated,[3] a common assignment of the intermediates, denoted S_n states (n = 0-4), range in oxidation state from S_0, $Mn^{III}_3Mn^{IV}$, to S_4, Mn^{IV}_4-ligand radical or $Mn^{IV}_3Mn^{V}$ (Scheme 3.1).[1, 4] While highly efficient, the OEC must be reassembled frequently under full solar flux due to photooxidative damage to the inorganic cluster and D1 peptide.[5] The process by which the OEC is assembled, called photoactivation,[6] uses Mn^{2+}, Ca^{2+}, Cl^-, bicarbonate, water, and oxidizing equivalents generated by light absorption.[7] Although bicarbonate is not coordinated to the fully assembled OEC,[8] spectroscopic evidence supports a role for bicarbonate in photoactivation of the cluster.[9] Kinetically distinct species in photoactivation has been defined,[9c, 10] and reduction of the intermediates in the Kok cycle have led to species in oxidation states lower than S_0 (S_n with n = –1, –2, –3) with S_{-3} corresponding to a putative $Mn^{II}Mn^{III}_3$ oxidation state.[11]

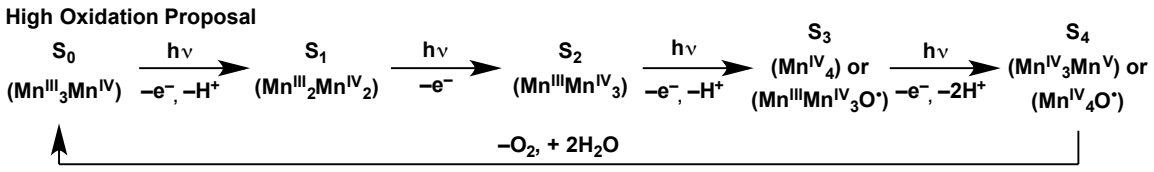

Scheme 3.1. The S-state cycle of the OEC.

A remarkable characteristic of PSII is its ability to support four manganese centers over a considerable span of oxidation states from four Mn^{II} at the beginning of photoactivation to four Mn^{IV} before O–O bond formation utilizing the same, protein-

defined set of carboxylate and imidazole ligands. To do so, water is concurrently incorporated and deprotonated to form hydroxido and oxido donors that stabilize the higher oxidation states of the Mn_4CaO_x cluster. Moreover, during catalytic turnover, lower oxidation state and lower oxygen-atom content moieties must be generated upon loss of O_2. Thus, the protein-derived ligand set available must stabilize the constant reorganization, reoxidation, and reoxygenation of the Mn_4CaO_x cluster.

A large effort to synthetically model the OEC has produced a variety of di-, tri-, and tetramanganese-oxido clusters.[12] These models have provided invaluable spectroscopic benchmarks in the characterization of the OEC and have helped elucidate the chemistry of multinuclear clusters in general. No single system has been shown to stabilize manganese oxidation states as widely as PSII. In this chapter I report a synthetic framework with a well-defined ligand set that supports tetranuclear, manganese-oxido clusters over the eight oxidation states from Mn^{II}_4 to $Mn^{III}Mn^{IV}_3$. Stepwise oxido incorporation stabilizes the increasing oxidation state, which vary from Mn^{II}_4 to $Mn^{III}Mn^{IV}_3$ with 1-4 oxido donors. Structural (XRD) and spectroscopic (XAS, EPR) characterization, interconversion and redox processes of these clusters, the role of the ancillary ligands, and the relation to the OEC are discussed.

RESULTS & DISCUSSION

3.1 Synthesis of Tetramanganese Clusters

We have reported a ligand framework—1,3,5-tris(2-di(2'-pyridyl)hydroxymethylphenyl)benzene (**H_3L**) (Scheme 3.2)—that supports multimetallic complexes of a variety of first-row transition metals.[13] Starting from **H_3L**,

trimanganese(II) complex **1** was synthesized upon *in situ* deprotonation and reaction with three equivalents of $Mn^{II}(OAc)_2$ (Scheme 3.2).[13b] In order to access tetramanganese clusters in a range of oxidation states and oxido content, **1** was treated with oxygenating reagents and Mn^{II} precursors under a variety of reaction conditions.

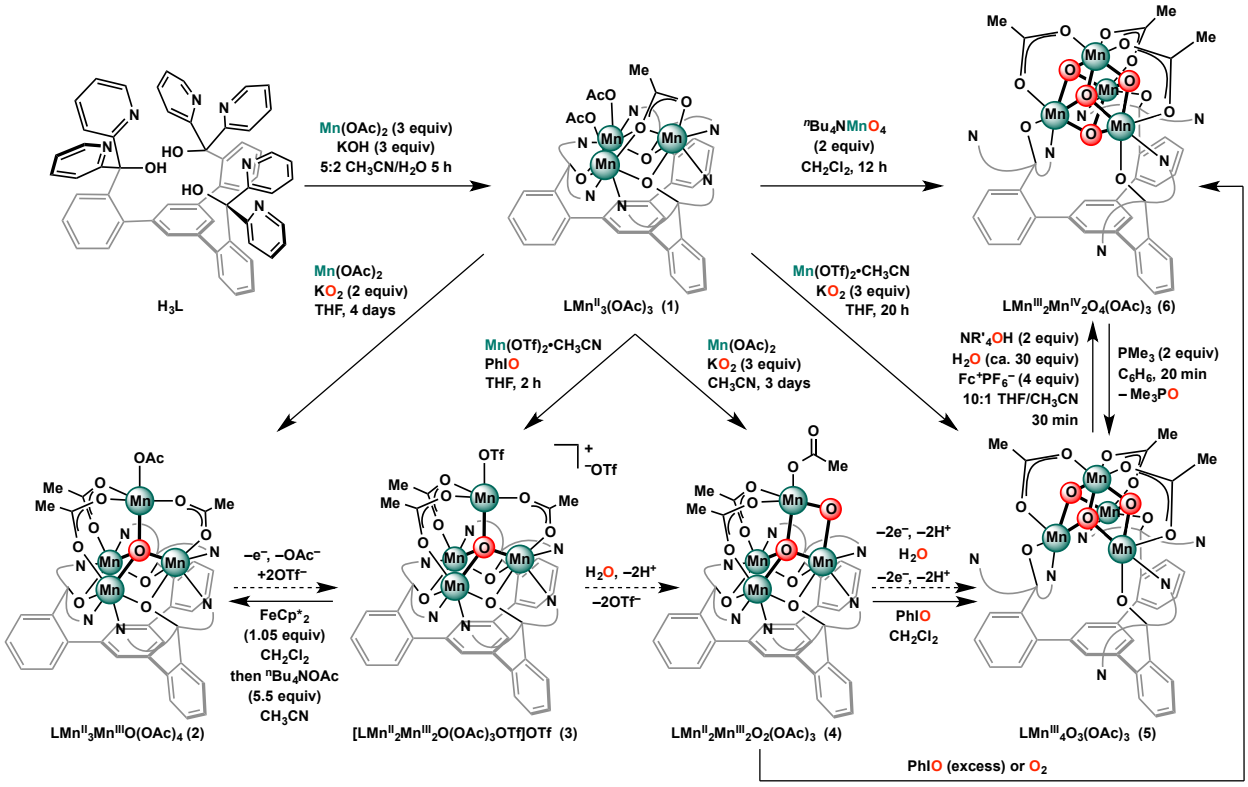

Scheme 3.2 Synthesis and interconversion of tetramanganese complexes **2**-**6**. Dashed arrows represent conceptual conversions involving water, proton and electron transfers. Curved lines represent 2-pyridyl groups. OAc = acetate. OTf = trifluoromethanesulfonate. Fc^+ = ferrocenium.

The addition of a solution of $Mn(OTf)_2•CH_3CN$ (OTf = trifluoromethanesulfonate) in tetrahydrofuran (THF) to a suspension of **1** in THF followed by one equivalent of iodosobenzene (PhIO) led to a color change from yellow to brown/purple over 2 hours (Scheme 3.2). Electrospray ionization mass spectrometry

(ESI-MS) analysis of purified purple product suggests oxygen and manganese incorporation, with peaks at 1417.0 and 1268.3 *m/z* – $[LMn_4O_1(OAc)_3(OTf)]^+$ and $[LMn_4O_1(OAc)_3]^+$. A single crystal X-ray diffraction (XRD) study is consistent with the ESI-MS findings and supports the structure of **3** as a tetramanganese monooxido species (*vide infra*).

The addition of KO_2 to an equimolar mixture of **1** and $Mn(OAc)_2$ or $Mn(OTf)_2$•CH_3CN allowed the isolation of different complexes as a function of reaction solvent. A brown solid **2** precipitated from the heterogeneous mixture of **1**, $Mn(OAc)_2$, and KO_2 in THF upon stirring for 4 days. ESI-MS of **2** shows a single peak at 1268.4 *m/z*, corresponding to $[LMn_4O_1(OAc)_3]^+$, and an XRD study confirms the structure of **2** as a tetramanganese monooxido species similar to complex **3** (Figure 3.1).

The reaction of **1** with KO_2 and $Mn(OAc)_2$ in acetonitrile generated tan precipitate **4** after 3.5 days of stirring. As observed in THF, **2** was the major species in solution at early reaction times (<10h, ^{1}H NMR spectroscopy), yet as the reaction progressed, **4** became dominant. The ESI-MS spectrum displays major peaks at 1225.2, 1268.2, and 1285.0 *m/z*, assigned to $[LMn_4O_2(OAc)_2]^+$, $[LMn_4O_1(OAc)_3]^+$, and $[LMn_4O_2(OAc)_3H]^+$, respectively. Vapor diffusion of Et_2O into a DMF solution of **4** gave crystals amenable to XRD (*vide infra*).

The addition of an equivalent of $Mn(OTf)_2$•CH_3CN and KO_2 (2.5 equiv) to trimanganese complex **1** in THF and stirring for 20 hours afforded a red-brown solution. Concentration *in vacuo* and extraction into benzene generated **5** as an orange-red powder (Scheme 3.2). Compound **5** displays paramagnetically shifted and broadened peaks between 25 and –55 ppm in the ^{1}H NMR spectrum. ESI-MS of the reaction

mixture showed peaks at 1241.0 m/z – $[LMn_4O_3(OAc)_2]^+$ – and 1300.1 m/z – $[LMn_4O_3(OAc)_3]^+$ consistent with a species similar to that of Mn_4O_4 cubane **6** but with one less oxygen. Recrystallization by vapor diffusion of hexane into a THF solution afforded crystals amenable to x-ray diffraction (Figure 3.1).

When **1** was treated with two equivalents of nBu$_4$NMnO$_4$, concentrated *in vacuo* and extracted with benzene, a red/brown powder **6** could be isolated that showed a major peak at ESI-MS peaks at 1256.0 m/z – $[LMn_4O_4(OAc)_2]^+$. Crystallization supported this stoichiometry, showing a Mn_4O_4 cubane structure (Figure 3.1). Compound **6** could also be synthesized using **5** and iodosobenzene or water, base, and oxidizing equivalents; this conversion will be studied in detail in Chapter 5. The cubane moiety of **6** could be further functionalized by the selective removal of an acetate ligand with one equivalent of trimethylsilyl triflate followed by addition of nitrogenous donors such as dimethylpyrazole (Scheme 3.3). This reaction sequence allowed isolation of a cationic $Mn^{III}_2Mn^{IV}_2O_4$ cubane complex (**7**).

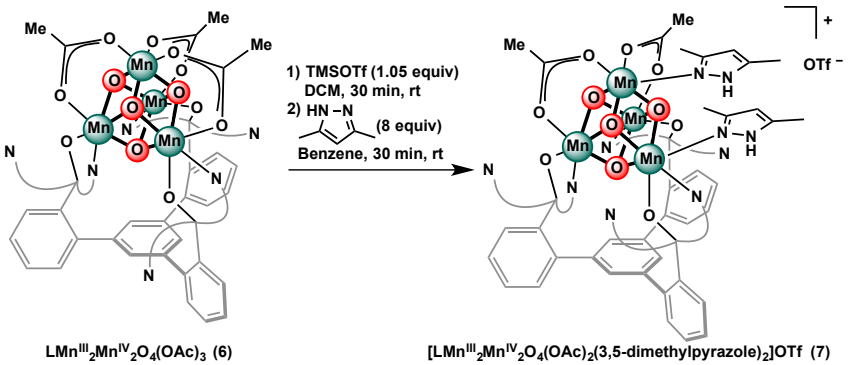

Scheme 3.3 Synthesis of asymmetric, cationic Mn_4O_4 cubane **7**.

Complexes **2**-**7** are ^{1}H NMR active with paramagnetically broadened and shifted peaks (see Appendix A). While the resonances could not be assigned to specific

protons, NMR was still useful in observing the reaction mixtures and purity of the samples.

Although a large variety of manganese cluster models of the OEC have been reported,[12a, b] the family of compounds reported here is unique in displaying significant variation in oxidation state and the number of oxido ligands for four manganese centers supported by the same set of ancillary ligands. Previously reported tetramanganese-oxido complexes vary in shape, containing butterfly,[14] planar,[15] linear,[16] cubic,[17] adamantane,[18] and dimer-of-dimer[19] geometries. The isolation of oxido-content homologs is rare.[20,21]

3.2 Solid-State Structures

The crystal structure of **3** shows three basal metal centers bridged by three alkoxides forming a six-membered ring, and the pyridines of each dipyridyloxymethyl moiety coordinate to adjacent metal centers. This motif is conserved from the trinuclear **1**.[13b] A centrally located μ_4-oxido and three κ^2-acetates bridge these three basal manganese centers to a fourth manganese that is capped by a OTf^- (Figure 3.1). An outer-sphere OTf^- is present in the solid-state, consistent with a $Mn^{II}_2Mn^{III}_2$ oxidation state assignment. Comparison to structurally related Mn_4-μ_4-O motifs that have been previously characterized[22] supports the presence of Mn^{II} and/or Mn^{III} in **3**. Elemental analysis results indicate the presence of two triflate anions in the isolated crystalline powder, supporting the oxidation state assignment as $Mn^{II}_2Mn^{III}_2$. In agreement, the cyclic voltammogram of **3** shows two reduction events accessing $Mn^{II}_3Mn^{III}$ and Mn^{II}_4 oxidation states (Figure 3.8 in the Experimental Section).

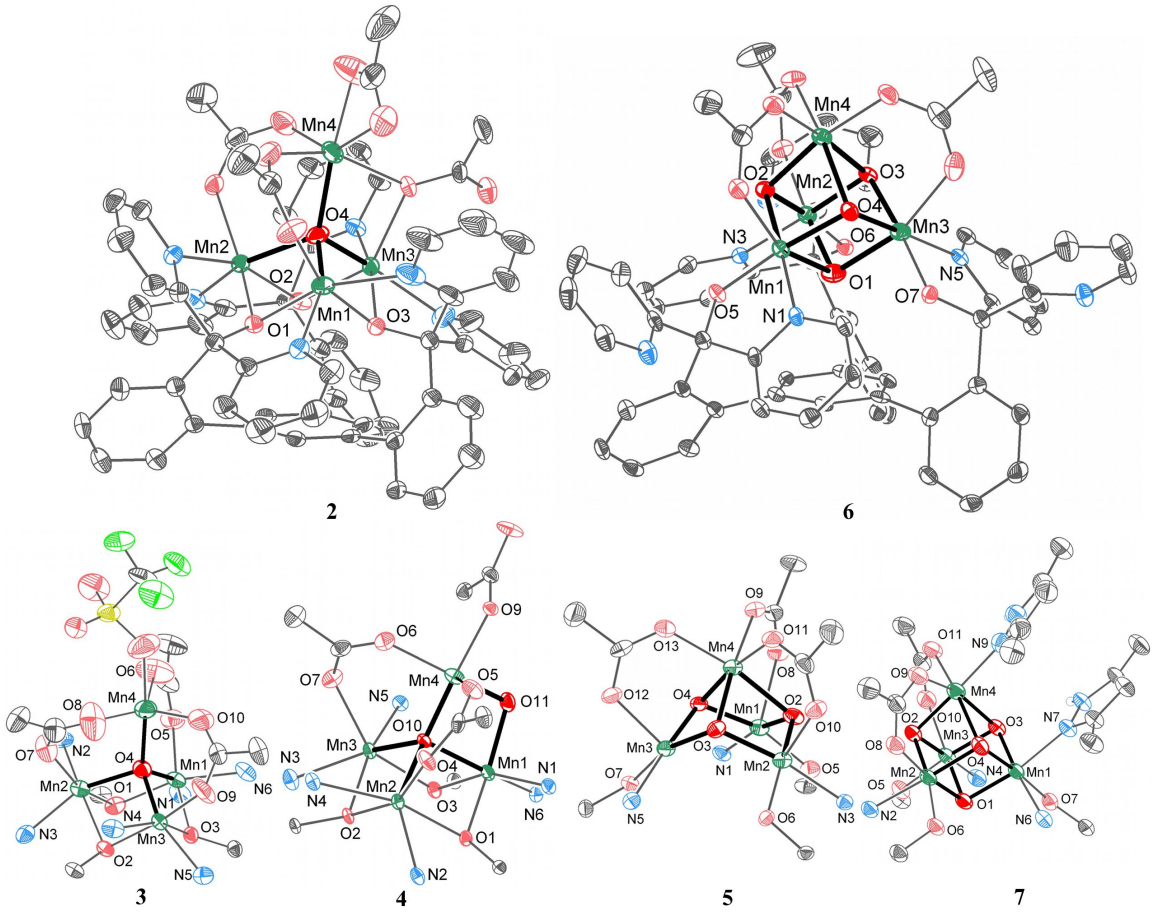

Figure 3.1 Solid-state structures of complexes **2**-**5** and **7**. Top: Depictions of full molecules **2** and **7**; Bottom: Truncated Mn_4O_x cores. Thermal ellipsoids are drawn at 50% probability. Hydrogen atoms, outersphere anions, and solvent molecules are not shown for clarity. Bolded bonds highlight the Mn_4O_x cores. See Experimental Section for detailed crystallographic information.

In contrast to **3**, **2** has the apical metal center capped by an acetate rather than trifluoromethanesulfonate and no outer-sphere anion, indicating a one-electron reduced state, assigned as $Mn^{II}_3Mn^{III}$ (Figure 3.1). The acetate bridging Mn3-Mn4 adopts two bridging modes, one mode is the usual κ^2 mode as in the other acetates and the other has a single oxygen atom forming the bridge, as shown in the figure. Mn1 has a shorter

bond to O4 (the central μ_4-oxido) than the other three Mn centers: 1.919(4) versus 2.041(4), 2.049(4), and 2.157(3). This short distance is most consistent with the literature Mn^{III}-oxido distances in Mn_4-μ_4-O motifs,[22] while the other three distances match Mn^{II}-oxido distances. Furthermore, the successful conversion of **3** to **2** with one equivalent of a one-electron reductant indicates that **3** and **2** differ by a single electron in oxidation state, consistent with oxidation state assignments of **2** and **3** as stated (*vide infra*).

For **4**, the trimanganese-tris-μ_2-alkoxide core as found in **1**-**3** is present, and similar to **2**, a μ_4-oxide and two κ^2-acetates connect the fourth manganese center to the basal trinuclear core. Unlike **2** and **3**, however, a second oxido ligand is present, bridging the apical manganese to a basal manganese (O11 of **4** in Figure 3.1). Analysis of the structural parameters supports an oxidation state assignment as $Mn^{II}_2Mn^{III}_2$. Within the diamond core, the Mn–O bond distances are Mn4-O11, 1.8576(17) Å; Mn4-O10, 1.8295(17) Å; Mn1-O11, 1.8638(19) Å; Mn1-O10, 1.9639(16)Å; and the Mn1-Mn4 distance is 2.7921(6)Å. These parameters are consistent with Mn^{III}. The other manganese centers in the base have similar Mn-alkoxide and Mn-pyridine distances to **1**, and are thus assigned as Mn^{II} ions. The $Mn_4(\mu_4\text{-O})(\mu_2\text{-O})$ structural motif has not been previously described, although Mn_4O_2 complexes of butterfly[14], planar[15], fused-cubane[23], and ladder-like[24] shapes have been reported, for example.

Complex **5** displays the ligand coordination mode found in the cubane complexes **6** and **7**:[13b] Different from **1**-**4**, the three alkoxides bind terminally to three Mn centers, three pyridines are unbound, and the Mn_4 unit moves away from the triarylbenzene framework. The three basal manganese centers are each pseudo-square

Table 3.1 Selected Structural Parameters of **2**-**7**.

Complex	Metal ion	Average Mn–oxo distance (Å)	Average Mn–Mn distance (Å)	Oxidation state
2 $Mn^{II}_3Mn^{III}O$	Mn1	1.919(4)	3.2	Mn(III)
	Mn2	2.157(3)	3.3	Mn(II)
	Mn3	2.041(4)	3.2	Mn(II)
	Mn4	2.049(3)	3.5	Mn(II)
Overall Average		**2.04** ± 0.10	**3.31** ± 0.22	
3 $Mn^{II}_2Mn^{III}_2O$	Mn1	2.068(2)	3.3	Mn(III)
	Mn2	2.095(3)	3.2	Mn(II)
	Mn3	1.980(3)	3.2	Mn(III)
	Mn4	2.048(3)	3.5	Mn(II)
Overall Average		**2.05** ± 0.05	**3.32** ± 0.21	
4 $Mn^{II}_2Mn^{III}_2O_2$	Mn1	1.91 ± 0.07	3.0	Mn(III)
	Mn2	2.099(2)	3.3	Mn(II)
	Mn3	2.174(2)	3.3	Mn(II)
	Mn4	1.84 ± 0.02	3.3	Mn(III)
Overall Average		**1.96** ± 0.14	**3.24** ± 0.29	
5 $Mn^{III}_4O_3$	Mn1	1.88 ± 0.03	3.1	Mn(III)
	Mn2	1.89 ± 0.05	3.1	Mn(III)
	Mn3	1.884 ± 0.004	3.1	Mn(III)
	Mn4	2.02 ± 0.12	2.8	Mn(III)
Overall Average		**1.93** ± 0.09	**3.03** ± 0.21	
6 $Mn^{III}_2Mn^{IV}_2O_4$	Mn1	2.04 ± 0.19	3.0	Mn(III)
	Mn2	1.86 ± 0.02	2.9	Mn(IV)
	Mn3	1.93 ± 0.07	2.9	Mn(IV)
	Mn4	2.01 ± 0.16	2.9	Mn(III)
Overall Average		**1.96** ± 0.13	**2.92** ± 0.10	
7 $Mn^{III}_2Mn^{IV}_2O_4$	Mn1	1.87 ± 0.02	2.9	Mn(IV)
	Mn2	1.88 ± 0.01	2.9	Mn(IV)
	Mn3	2.00 ± 0.10	2.9	Mn(III)
	Mn4	2.06 ± 0.15	2.9	Mn(III)
Overall Average		**1.95** ± 0.09	**2.91** ± 0.09	

[a] The bond distance with the corresponding XRD esd in parentheses are given for Mn centers with one Mn–O bond. The average Mn–O distance with a standard deviation is given for Mn centers with multiple Mn–O bonds.

pyramidal and supported by one terminal alkoxide and one pyridyl group from the ligand framework; three pyridyl groups, one per arm, remain unbound. The fourth, apical manganese center is *pseudo*-octahedral and bound through three κ^2-acetates and

three μ_3-oxides to the three basal manganese centers. This arrangement generates a partial cubane missing the "basal" oxido moiety directly above the center of the triarylbenzene motif. Analysis of the Mn–ligand distances and absence of outer-sphere counterions indicate that all metal centers are Mn^{III}. Notably, the incomplete cubane motif Mn_4O_3 has not been isolated previously, although a $[Mn^{III}{}_3Mn^{IV}O_3L_6]^+$ (L = diphenylphosphinate) species was observed by ESI-MS.[25] Complexes with the $Mn^{III}{}_3Mn^{IV}O_3X$ formulation where X is a bridging monoanion (X = Cl^-, I^-, F^-, N_3^-, O_2CR^-, OMe^-, and OH^-) have been studied extensively.[13c, 20-21, 26]

Compound **6** was characterized by XRD and contains a Mn_4O_4 cubane (Figure 3.1). The structural parameters are consistent with the presence of two d^3 Mn^{IV} centers, displaying short, similar Mn–O bonds and two d^4 Mn^{III} centers with longer, distorted Mn–O coordination (Table 3.1). This is consistent with the lack of counterions in the crystal lattice, and supports a $Mn^{III}{}_2Mn^{IV}{}_2O_4$ oxidation state. The solid-state structure of **7** parallels the structures of complexes **5** and **6**.[13c, 26d] In **7**, one of the bridging acetates is replaced with two 3,5-dimethylpyrazoles that π-stack with a pyridine of the ligand framework (Figure 3.1). The N–H groups of the pyrazoles H-bond to a triflate counterion. As in **6**, two manganese centers show axial distortion as expected for *psuedo*-octahedral Mn^{III}, and two have shorter Mn-O distances consistent with Mn^{IV} (Table 3.1).

The four manganese centers in **2**, **3**, **5**, **6**, and **7** form a tetrahedron with the pseudo-C_3 axis of the ligand architecture coincident with one of the C_3 axes of the tetrahedron. Complex **4** is more asymmetric, with the top manganese leaning off-axis to accommodate the $Mn^{III}{}_2O_2$ diamond core. It is remarkable that the four manganese

centers hold the same relative geometry through six oxidation states (eight including electrochemically observed species; see below and the Experimental Section) and the incorporation of four oxides. This tetrahedron contracts as the oxido content increases: this translates into shorter average metal-oxido and metal-metal distances (Table 3.1). For example, the average Mn–Mn distances decreases from 3.32±0.21 Å in **3** to 2.92±0.10 Å in **6**.

3.3 XAS

Mn XANES. Mn K-edge X-ray absorption near-edge spectroscopy (XANES) was used to further characterize the metal oxidation states for complexes **3**-**6**. In addition to the oxidation state, XANES is also sensitive to the coordination environment surrounding the metal site.[27] Figure 3.2 compares the Mn XANES spectra of these four complexes with the spectrum of the OEC in the S_1-state. Although the spectral features may be influenced by the variation in geometry and the number of oxido ligands, the absorption energy shifts and edge shapes are consistent with the Mn oxidation state assignments summarized in Table 3.1. There is a clear trend of the rising edge position shifting to higher energy with increasing Mn oxidation.

To determine the absorption edge positions for complexes **3**-**6**, inflection-point energies (IPE) from second-derivative zero crossings were obtained. The following values are the calculated IPEs for four complexes: 6547.7 ± 0.1 eV (**3**), 6548.0 ± 0.1 eV (**4**), 6549.7 ± 0.1 eV (**5**), and 6551.2 ± 0.1 eV (**6**). Previous studies on sets of model Mn complexes with similar ligands have shown that the IPE increases by 1-2 eV to higher energy upon Mn oxidation.[28] Changing from complexes **4** to **5** and **5** to **6** gives an

observed IPE shift of ~1.5-1.7 eV to higher energy, providing support for Mn oxidation state increase. In contrast, the IPE shift is only ~0.3 eV between complexes **3** and **4**, suggesting that no Mn-based oxidation occurs in this conversion. The small IPE shift observed here is likely due to the additional oxido ligand.

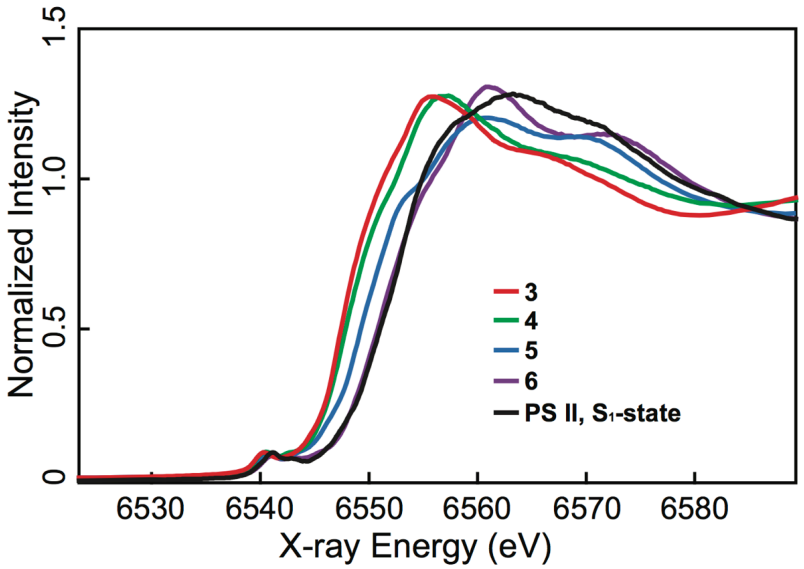

Figure 3.2 Normalized Mn K-edge XANES spectra from complexes **3**-**6** compared with the spectrum from spinach PS II in the S_1-state.

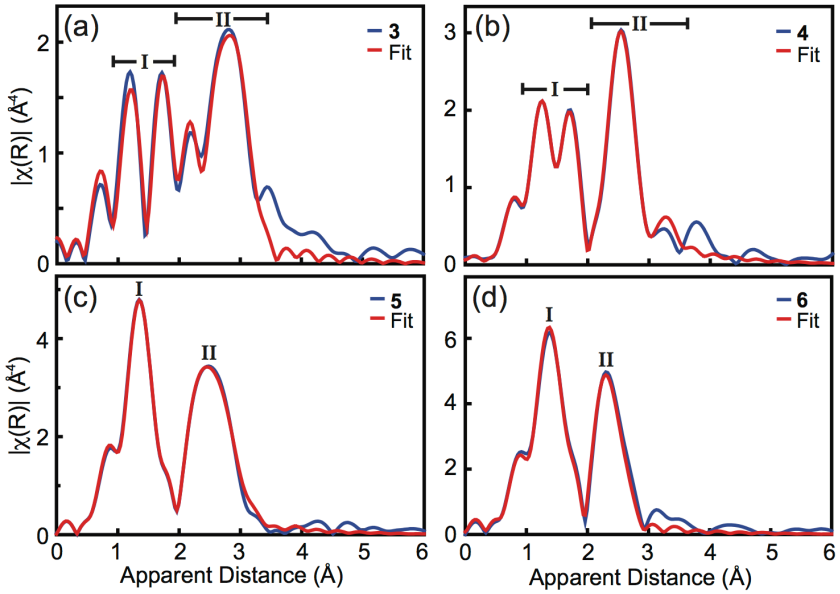

Figure 3.3 Fourier transforms of the Mn EXAFS for complexes **3**-**6** (blue) with fits (red). The EXAFS curve-fitting parameters are summarized in Table 3.3.

The absorption edge energy position of complex **6** is closest to that for the S_1-state of PS II, where the formal Mn oxidation state is assigned as $Mn^{III}_2Mn^{IV}_2$.[29] Taken together with the structural analysis and chemical reactivity of these four complexes, the Mn XANES results support the formal oxidation state assignments of **3**-**6** as $Mn^{II}_2Mn^{III}_2$ (**3**), $Mn^{II}_2Mn^{III}_2$ (**4**), Mn^{III}_4 (**5**), and $Mn^{III}_2Mn^{IV}_2$ (**6**).

Mn EXAFS. Complexes **3**-**6** have also been characterized by Mn K-edge extended X-ray absorption fine structure (EXAFS), and the detailed curve-fitting parameters are summarized in Table 3.3 (See Experimental Section). In general, the EXAFS results for these four complexes agree well with the solid-state structure distances reported in Table 3.1. Figure 3.3 shows the Fourier transform (FT) of the k^3-weighted Mn EXAFS and corresponding fits for these complexes. All FT peaks occur at an apparent distance (R'), which is shorter than the actual interaction distances (R) by ~0.5 Å due to the scattering phase shift. The shoulder peak occurring below R' = 1 Å arises from incomplete background removal.

For complexes **3** and **4** (Figure 3.3, a and b), the FT features can be separated into two regions described as metal-ligand interactions (region I, 1 Å < R' < 2 Å) and mixed metal-metal/metal-ligand interactions (region II, 2 Å < R' < 3.5 Å). Due to the close proximity of the Mn-C and Mn-Mn interactions in these two complexes (~2.9-3.1 Å and ~3.1 Å, respectively), it was necessary to include Mn–C interaction distances in order to obtain reasonable fitting results for complexes **3** and **4**.

In contrast, the requirement for including Mn-C interactions in the FT fits for complexes **5** and **6** (Figure 3.3, c and d) was less obvious due to smeared scattering distributions. In these complexes, the Mn-C distances varied and their contributions to

the EXAFS spectra were smaller relative to that for complexes **3** and **4**. For complex **5**, peaks I and II can be described as metal-ligand and mixed metal-ligand/metal-metal interactions, respectively. Peak I contains Mn-O and Mn-O/N contributions at ~1.9 and ~2.1 Å, and peak II consists of Mn-Mn (~2.8 and ~3.2 Å) and Mn-C (2.9-3.0 Å) interactions. For complex **6** (Figure 3.3d), peak I corresponds to metal-ligand interactions and peak II corresponds to metal-metal interactions. The metal-ligand distances for Mn-O and Mn-O/N were resolved at ~1.9 and ~2.1 Å, respectively; the Mn-Mn interactions were approximated to ~2.8 Å in peak II. These agree well with the average XRD distances summarized for **6** in Table 3.1.

3.4 Magnetism

Magnetic susceptibility measurements were performed on powdered crystalline samples of **3**-**6** in the temperature range 4–300 K. At room temperature, the $\chi_M T$ values approach 10.3, 10.5, 5.0, and 6.0 cm^3 K mol^{-1}, respectively (Figure 3.4). All are below the spin-only values at 300 K and decrease as temperature decreases, indicative of dominant antiferromagnetic coupling. Antiferromagnetically coupled manganese clusters in the literature have also shown significant deviation at 300 K from the expected spin-only value.[30]

For **3**, the $\chi_M T$ value decreases to 6.8 cm^3 mol^{-1} K at 45 K and then increases to a maximum value of 7.2 at 10 K before dropping again, likely due to low temperature effects such as intermolecular exchange interactions. Upon cooling, the $\chi_M T$ value of **4** decreases gradually and then drops sharply below 30 K and does not approach an

obvious limiting value at 4 K. The $\chi_M T$ value of **5** and **6** decrease gradually to 0.4 and 0.8 $cm^3\ mol^{-1}\ K$ at 4 K, respectively.

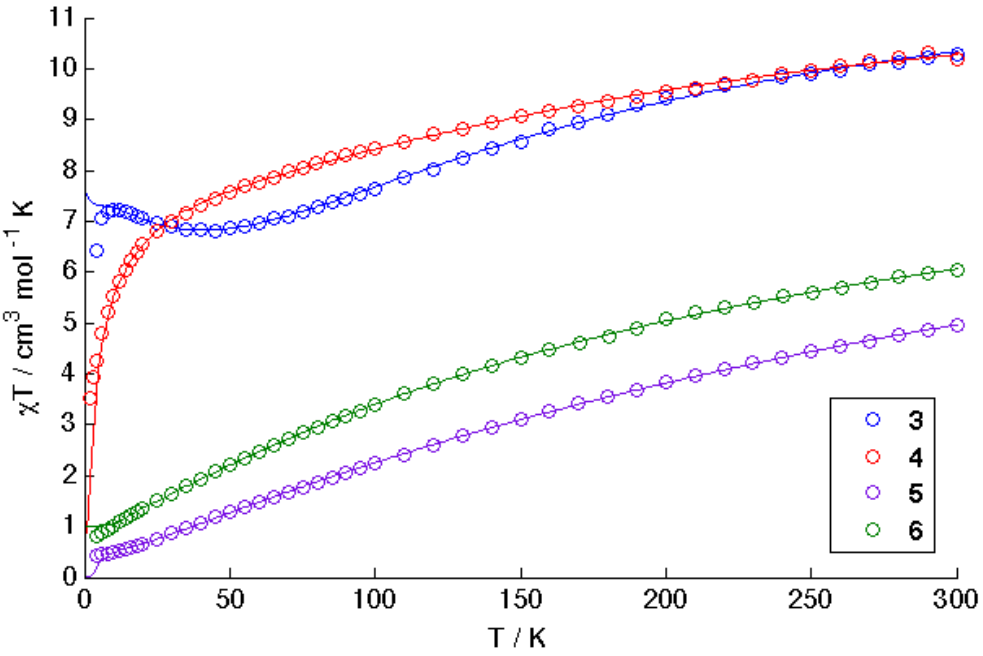

Figure 3.4 $\chi_M T$ vs. T data (circles) and fits (lines) for compounds **3**-**6**. See Table 3.2 for fit parameters.

Table 3.2 Magnetic susceptibility fitting parameters

Compound	**3**	**4**	**6**	**5**
Diamagnetic Correction ($\times 10^{-6}$ cm^3/mol)	–777	–681	–722	–691
J_{nm} [a] (cm^{-1})	–1.97	+0.91	–13.9	J_{TOP} [b] = –30.7
J_{nn} (cm^{-1})	–9.90	–0.28	–6.3	J_{BOT} = –39.3
J_{mm} (cm^{-1})	+3.61	–22.9	–18.2	--
g	1.87	1.81	2.02	2.01
R (x 10^{-5})	1.9	1.4	1.6	4.1

[a] n and m refer to the oxidation states of the Mn centers whose interaction the coupling constant is representing. n=2 and m=3 for complexes **3** and **4**, whereas n=3 and m=4 for **6**.

[b] J_{TOP} describes the three interactions of the six-coordinate Mn^{III} center with the five-coordinate Mn^{III} centers in **5**. J_{BOT} describes the interactions between the three five-coordinate Mn^{III} centers.

To determine the magnitude of exchange between neighboring metal centers in **3**, **4**, and **6**, the magnetic behavior of the compounds was analyzed using the isotropic spin Hamiltonian considering the three exchange pathways of an asymmetric tetrahedron (See Exp. Section for coupling scheme). Ideally, a four J coupling scheme would be used to model all of the different Mn-Mn interactions; however, to determine the eigenvalues using the Kambe[31] method, we modeled the four $Mn^{II}Mn^{III}$ interactions in each of **3** and **4** with one J (J_{nm} in Table 3.2). Similarly, the four $Mn^{III}Mn^{IV}$ interactions in **6** were modeled with one coupling constant. The J values for all coupling pathways are relatively small (<25 cm^{-1}, ca. 0.07 kcal/mol), with antiferromagnetic values greater than ferromagnetic values, as is consistent with the decreasing $\chi_M T$ values.

The exchange parameters of **5** were analyzed using a two exchange pathway model based on the *psuedo-C_3* symmetry of **5** (See Exp. Section).[32] Both types of $Mn^{III}Mn^{III}$ interactions were antiferromagnetic, with couplings of –39.3 cm^{-1} between the three, basal five-coordinate Mn and –30.7 cm^{-1} between the top, six-coordinate Mn and the basal, five-coordinate Mn. These values are similar to $Mn^{III}{}_2(\mu_3\text{-}O)_2$ systems with similar Mn-O-Mn angles.[14]

3.5 EPR

X-band continuous-wave (CW) EPR studies were performed on frozen solution samples of complexes **3**-**7** (Figure 3.5)**.** All species explored exhibit significant temperature-dependent lineshape changes. These spectral changes are diagnostic of exchange-coupled spin systems with (at least some) rather small exchange coupling constants (i.e., on the order of $k_B T$), consistent with magnetic susceptibility results

(Table 3.2). That the overall integrated intensity of the EPR spectrum increases with increasing temperature also indicates that anti-ferromagnetic couplings, in particular, are dominant. At higher temperatures, states with larger *S*-values are populated and the transition between spin levels of these states have larger transitions probabilities that gave rise to increased signal intensity.

Each of the complexes **3**-**7** is expected to have an even number of unpaired electrons and, in the case of maximal antiferromagnetic coupling, we would expect an $S_T = 0$ ground state. Nonetheless, all of the complexes give rise to EPR signals owing to thermal population of paramagnetic excited states that are quite low in energy. In addition, exchange-coupled systems with three or more spin centers can exhibit "spin-frustration" in which all pair-wise couplings that are antiferromagnetic (i.e., negative *J*-value) are not achievable. This leads to ground state total spin quantum numbers that are greater than zero.

In the example of complex **3**, neglecting any contribution to the eigenvalue from zero-field splitting, using the *J*-values in Table 3.2 predicts that the ground state is $S = 3$ with an $S = 4$ excited state approximately 0.2 cm^{-1} higher in energy at zero field. These manifolds are roughly equally populated at 5 K. The next excited state—predicted to be an $S = 4$ manifold—is 13.3 cm^{-1} higher in energy and should be appreciably populated at 15-20 K. This state could give rise to the temperature-dependent signals discussed next. The 5 K CW EPR spectrum of **3** contains weak signals at low field. As the temperature is increased up to 25 K, a negative feature becomes more prominent at $g = 15.2$ that then starts to diminish at 40 K. A corresponding feature appears in the parallel-mode spectrum (data not shown). These two properties confirm the

formulation of **3** as being an integer spin system with a large value for the ground state *S*.

The 5 K EPR spectrum of **4** is weak and broad with two clear resonances at g = 7.4 and 2.9 that become slightly broader as the temperature is raised until 50 K when they begin to disappear. The g = 7.4 feature also has a corresponding negative peak in the parallel-mode spectrum (data not shown). The relatively large value for J_3 pairs the spins of the two Mn^{III} ions, thus the lowest energy states of **4** consist of the 36 microstates of the exchange-coupled Mn^{II} ions.

A multiline feature containing 11 peaks centered at g = 1.98 and split by 9.5–12.9 mT is faintly visible at all temperatures explored. This signal is reminiscent of spectra for weakly coupled $Mn^{III,IV}$ dimers in which the exchange coupling is small compared to the zero-field splitting of the Mn^{III} ion. The amount to which this signal contributed to the spectrum varied with different preparations of **4**, leading to the conclusion that the corresponding species is likely a degradation product.

The spectrum of **5** collected at 5 K reveals two peaks at g = 7.57 and 4.95. The feature at g = 4.95 disappears quickly when the temperature is raised from 5 K whereas the feature at g = 7.57 exhibits Curie-type behavior (i.e. is proportional to 1/T). An additional feature appears at g = 2.5 at temperatures above 25 K. Overall, the spectrum of **5** is very reminiscent of that for a mononuclear Mn^{IV} center (cf. for example, the spectrum of Mn^{IV} 3,5-di-tert-butylquinone[33]). However, we interpret the marked increase in integrated spectral intensity with increasing temperature as being diagnostic of these resonances arising from an exchange-coupled system, not a mononuclear one.

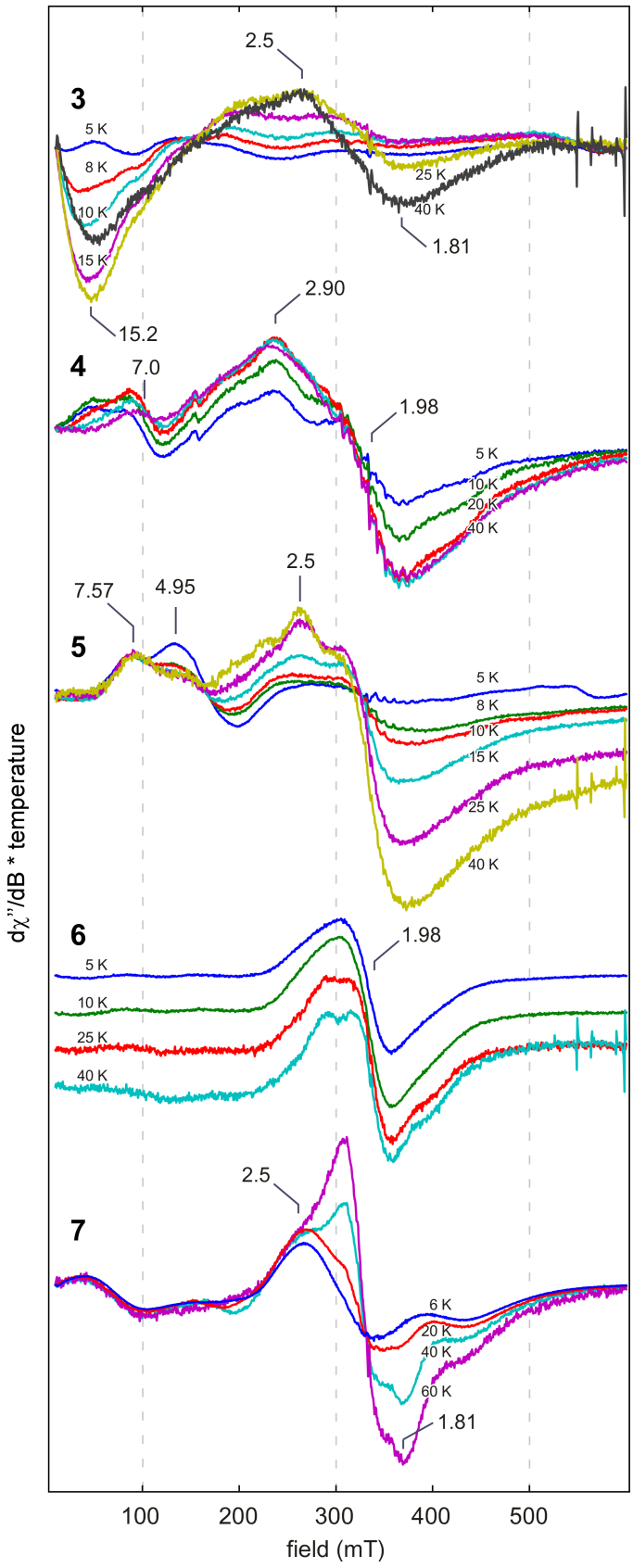

Figure 3.5 Temperature-dependent (see legends for temperatures employed) CW X-band EPR spectra of the frozen solutions of (from top to bottom) **3** (dissolved in 1:1 CH_2Cl_2/CH_3CN), **4** (dissolved in pure CH_2Cl_2),**5** & **6** (dissolved in 1:1 CH_2Cl_2/toluene), and **7** (dissolved in pure toluene). Experimental parameters: microwave frequency = 9.33 – 9.37 GHz; power = 2.0 mW for all complexes except power = 1.0 mW for complex **3**, 0.02 mW for complex **4**, and 0.5 mW for complex **7**; modulation amplitude = 10 G; modulation frequency = 100 kHz. Data for complex **6** are staggered for ease of comparison. The signal from a small amount of contaminating mononuclear Mn^{II} was subtracted from the data for complex **7**.

The spectrum of **5** collected at 5 K reveals two peaks at g = 7.57 and 4.95. The feature at g = 4.95 disappears quickly when the temperature is raised from 5 K whereas the feature at g = 7.57 exhibits Curie-type behavior (i.e. is proportional to 1/T). An additional feature appears at g = 2.5 at temperatures above 25 K. Overall, the spectrum of **5** is very reminiscent of that for a mononuclear Mn^{IV} center (cf. for example, the spectrum of Mn^{IV} 3,5-di-tert-butylquinone[33]). However, we interpret the marked increase in integrated spectral intensity with increasing temperature as being diagnostic of these resonances arising from an exchange-coupled system, not a mononuclear one.

Complex **6** yields a spectrum at 5 K that is somewhat reminiscent of the multiline signal corresponding to the S = 1/2 form of the S_2 state of the $[Mn_4CaO_5]$ cluster in PSII. Namely, there is a broad feature (spanning 250 mT) centered at g = 1.98; however, the ^{55}Mn hyperfine contributions are unresolved in the case of complex **6**. As the temperature is increased from 5 K to 20 K the g = 1.98 feature grows slightly in intensity until 20 K and then begins to decrease in intensity and split into two peaks. That this feature is similar to the multiline signal for photosystem II could suggest that some of **6** became oxidized by one electron to give a $Mn^{III,IV,IV,IV}$ complex, the oxidation state scheme employed to rationalize the S_2 EPR and X-ray absorption results. Alternatively, the spectrum can be rationalized as coming from a S = 1 or S = 2 state (these are the two lowest spin states for **6** based on the exchange couplings in Table 3.2, see Exp. Sect.) with a relatively small zero-field splitting (ZFS) parameter (D ~ 1000 and 600 MHz, respectively) and convolved by broad, unresolved ^{55}Mn hyperfine features. Such small ZFS is generally unexpected for a Mn^{III}-containing compound; however structural considerations provide a rationale. XRD data for **6** show a highly

symmetric cube especially compared to complex **3**, **4**, or **5**, and the Jahn-Teller (JT) axes of the two Mn^{III} ions are perpendicular to each other. This orthogonality effectively cancels the contributions of the two Mn^{III} site-specific ZFS tensors to the molecular ZFS tensor.[34]

The lowest-temperature EPR spectrum of complex **7** is fairly similar to that for **6**, though a bit broader, indicating a slightly larger ZFS for this lowest energy state. This behavior is not surprising given the modest difference in ligand set between the two species. However, there is a much more dramatic temperature dependence in which features at g = 2.16 and g =1.81 grow in as the temperature is raised.

3.6 Cluster Reactivity and Interconversion

The present series of clusters of varying oxidation state and oxido content provides a unique opportunity to investigate cluster reactivity conceptually related to the PSII photoactivation. PSII binds four Mn centers, photooxidizing the Mn and incorporating oxido/hydroxido ligands to stabilize the increasing Mn oxidation states up through Mn^{IV}_4. As shown in Scheme 3.2 by dashed arrows, oxidative water incorporation formally interconverts many of the complexes **2**-**6**, and thus cluster interconversion was explored here to conceptually model these key steps of photoactivation and turnover. Complex **2** formally differs from **3** by one electron and a ligand exchange from OTf^- to acetate. Complex **4** corresponds formally to water incorporation and double deprotonation from **3**. Complex **5** is the product of a formal oxygen-atom addition to **4** – a process comprised of water incorporation, a two-electron

oxidation, and double deprotonation. Complex **6** represents a similar oxygen-atom addition to **5**.

The conversion of **3** to **2** involves a one-electron reduction, without change in the oxygen content of the cluster. Cyclic voltammetry studies of **3** in CH_2Cl_2 with 0.1 M $[^nBu_4N][PF_6]$ showed two irreversible reductions at –0.2 V and –1.0 V versus the Fc/Fc^+ couple, suggesting the formation of $Mn^{II}_3Mn^{III}$ and Mn^{II}_4 species (Fc = ferrocene) (Figure 3.8). Indeed, if one equivalent of bis(pentamethylcyclopentadienyl)iron(II) was added to **3**, a new species was formed that upon isolation, dissolution in CH_3CN, and addition of excess $[^nBu_4N][OAc]$ cleanly precipitated complex **2** (^{1}H NMR).

Water incorporation/deprotonation was investigated for the conversion of **3** to **4**. However, reaction of **3** with water in the presence of amines or hydroxide as bases generated complicated mixtures that did not contain **4** by ^{1}H NMR spectroscopy. Cationic **3** is soluble in water, generating a green solution rather than purple-brown as observed in organic solvents. Removal of water *in vacuo* after 30 minutes and dissolution in CH_3CN regenerated **3** (^{1}H NMR) as a purple-brown solution. Water coordination likely occurs at the five-coordinate apical metal center rather than the six-coordinate, basal metal centers. The weakly coordinating OTf^- anion might be displaced by the incoming Lewis base; if water binds at this axial position, isomerization to the equatorial position and displacement of a κ^2-acetate must occur before bridging to the basal metal centers as in **4**. The sterically open apical manganese could be prone to oligomerization by hydroxide or acetate bridges, precluding conversion to **4**.

Oxygen-atom transfer in the context of cluster reorganization was studied for the conversion of **4** to **5**. Complex **5** was successfully generated from the reaction of **4**

with PhIO, albeit as a minor species in a mixture of products. Reaction of **4** with excess PhIO leads to the generation of complex **6** in low yield. The conversion of **4** to **5** is remarkable given the extent of reorganization that the cluster has to undergo due to the change in the binding mode of the ligand **L**. The generation of a mixture of products is consistent with an incomplete reorganization leading to unidentified species. The observed conversion of **4** to **6** corresponds to the addition of two oxygen atoms, analogous to incorporation and full reduction of one equivalent of dioxygen. Correspondingly, reaction of a dilute solution of **4** in DMF with one atmosphere of O_2 leads to the generation of complex **6** over thirteen days. This one-step conversion is notable because it involves the reduction of O_2 to two O^{2-} moieties by a tetramanganese site, which represents the microscopic reverse of the O–O bond forming reaction performed by the OEC. The low oxidation states of manganese in precursor **4** allow for the reaction to proceed in the O_2-reduction direction.

Oxido-ligand incorporation into partial cubane **5** to form **6** will be discussed in Chapter 5,[26d] with detailed mechanistic studies performed. For both oxidative water incorporation and reductive oxygen-atom transfer, μ_3-oxido migration within the Mn_4 cluster was found to be a key mechanistic step, with implications for the structure and turnover of the OEC.

3.7 Electrochemistry and Potential Leveling

The redox properties of **5**, **6**, and **7** were studied by cyclic voltammetry (Figure 3.6). Complex **5** irreversibly reduces to a proposed $Mn^{II}Mn^{III}_3$ oxidation state ca. –1.0 V vs ferrocene/ferrocenium (Fc/Fc^+) in THF with a coupled return oxidation and

oxidizes quasireversibly at +100 mV vs Fc/Fc^+ to the $Mn^{III}_3Mn^{IV}$ oxidation state. In contrast, **6** reduces to the $Mn^{III}_3Mn^{IV}$ state at –870 mV in THF. This oxidation state is ca. 1 V more negative in **6** because of the presence of the fourth oxide versus the three oxides of **5**. An oxidation of **6** was also observed at +250 mV in THF, proposed to correspond to the $Mn^{III}_2Mn^{IV}_2/Mn^{III}Mn^{IV}_3$ couple. Complex **7**, a cationic rather than neutral $Mn^{III}_2Mn^{IV}_2$ complex, quasireversibly oxidizes at +340 mV in THF and irreversibly reduces at –510 mV. The oxidation event varies little (ca. 90 mV) in potential from **6** despite the buildup of charge at the now dicationic complex. Although

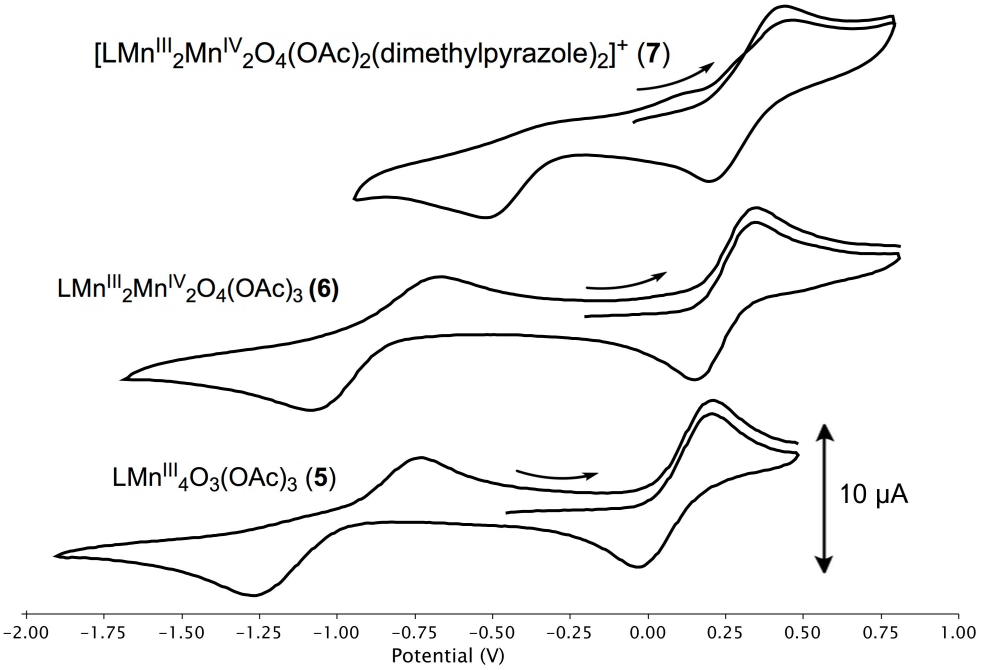

Figure 3.6 Redox properties of **5**-**7**. Cyclic voltammograms of **6** (bottom), **5** (middle), and **7** (top) referenced to Fc/Fc^+. The scan rate was 50 mV/s in the positive direction. The analyte concentration was 1.0 mM. The electrolyte was 0.1M $[^nBu_4N][PF_6]$ in THF. Open-circuit potential for **5** = – 460 mV, for **6** = – 200 mV, and for **7** = –50 mV. $E_{1/2}$ values: $\mathbf{5}^+/\mathbf{5}$ = +0.10 V; $\mathbf{5}/\mathbf{5}^-$ = –1.0 V; $\mathbf{6}^+/\mathbf{6}$ = +0.25 V; $\mathbf{6}/\mathbf{6}^-$ = –0.87 V; $\mathbf{7}/\mathbf{7}^+$ = +0.34 V; E_C of $\mathbf{7}/\mathbf{7}^-$ = –0.51 V.

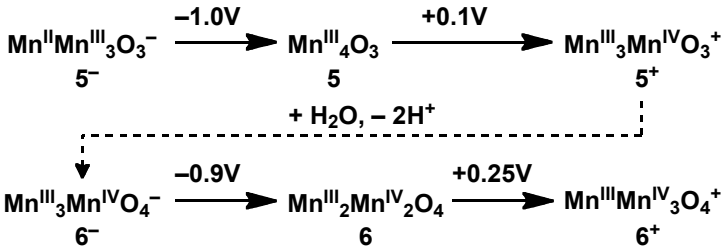

Scheme 3.4 Effect of oxidation state and oxido ligand content on leveling of reduction potentials for **5** and **6**.

the product of chemical oxidation has proven unstable (see Section 3.8 below), the electrochemical oxidation of **6** and **7** indicates that the $Mn^{III}Mn^{IV}_3$ species is accessible. Only one $Mn^{III}Mn^{IV}_3O_4$ cubane has been previously reported.[35, 36]

The reduction and oxidation events of **5** parallel those of **6**, with the reductions only differing by ca. 130 mV and the oxidations by 150 mV (Figure 3.6, Scheme 3.4). With only a slight increase in potential, a $Mn^{III}Mn^{IV}_3$ oxidation state can be accessed in **6** where only a $Mn^{III}_3Mn^{IV}$ oxidation state is accessible in **5**. This can be explained by the neutralization of charge build-up on the cluster by incorporation of an O^{2-} donor (Scheme 3.4). The water incorporated into **5** to give **6** is deprotonated twice, allowing access to oxidation states two units more oxidized at close to the same potential. Neutralization of charge buildup has been demonstrated for a dimanganese catalase model system with a terminal water/hydroxide.[37] Notably, that system was able to span four oxidation states—Mn^{II}_2 through $Mn^{III}Mn^{IV}$—with little change in the chelating ligand framework as observed herein.[38] This redox leveling of the cluster upon formal water incorporation and deprotonation is relevant to the OEC, as the oxidizing equivalents come at the same potential for all four oxidations during catalysis to generate O_2.

*3.8 Chemical Redox Reactions of $LMn^{III}_2Mn^{IV}_2O_4(OAc)_3$ (**6**)*

Based on the electrochemical potentials for oxidation and reduction of **6** (+0.25 V and –0.87 V vs Fc/Fc^+ in THF), chemical redox reagents were chosen in an attempt to isolate a series that only varied by oxidation state and not by structure to complement the structural series of **2**-**7** (Scheme 3.5). For the oxidation of **6**, Tris(4-bromophenyl)aminium hexachloroantimonate, or Magic Blue, was chosen (+0.7 V in CH_2Cl_2). The addition of the blue radical solution to the red/brown solution of **6** immediately gave a new, symmetric species $\mathbf{6}^+$ by ^{1}H NMR (See Appendix A). ESI-MS supported oxidation, with the main peak now being 1316—$[LMn^{III}Mn^{IV}_3O_4(OAc)_3]^+$—rather than the starting material's 1257 peak—$[LMn^{III}_2Mn^{IV}_2O_4(OAc)_2]^+$. Within 30 minutes, however, new peaks begin to appear in the ^{1}H NMR, and if left at room temperature over many hours, multiple species were evident. Nevertheless, frozen samples could be made of reactions either in CH_2Cl_2 for EPR or THF for XAS.

Reduction of **6** was performed with cobaltocene (–1.33 V in CH_2Cl_2). ^{1}H NMR of the reaction mixture at short reaction times showed a new, symmetric species $\mathbf{6}^-$ that also decomposed over time like $\mathbf{6}^+$. If excess cobaltocene was added, multiple species were visible by NMR. Frozen samples were made for EPR and XAS. Interestingly, a stable one-electron reduced species could be made simply by protonation of the unstable complex $\mathbf{6}^-$. *In situ* formation of $\mathbf{6}^-$ with cobaltocene followed by addition of Et_3NHOTf afforded a new ^{1}H NMR spectrum that lined up with spectra found from the reaction of **6** with H-atom donor TEMPOH. Therefore, **6H** is proposed to be $[LMn^{III}_3Mn^{IV}O_4(OAc)_3]H$, with an unknown location for the proton. **6H** cannot be cleanly made using these routes; complex **6** and the trioxide complex $LMn^{III}_4O_3(OAc)_3$

(**5**) are always present. Nevertheless, using the ratios from the ^{1}H NMR integration, subtraction can be performed for the XAS and EPR samples.

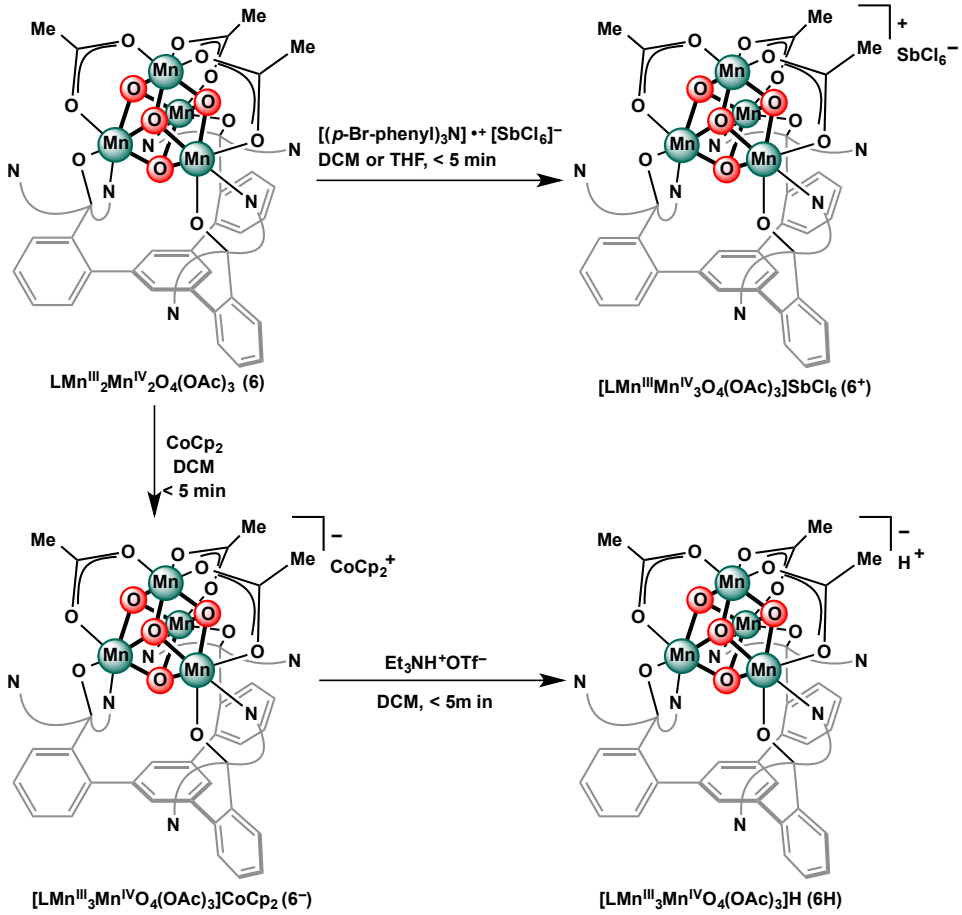

Scheme 3.5. Redox chemistry of $Mn^{III}_{2}Mn^{IV}_{2}O_4$ cubane complex **6**.

The three oxidation states for the Mn_4O_4 cubane series model S_0 ($Mn^{III}_{3}Mn^{IV}$), S_1 ($Mn^{III}_{2}Mn^{IV}_{2}$) and S_2 ($Mn^{III}Mn^{IV}_{3}$) of the S-state cycle. Although these are in the wrong geometry for a structural model of the OEC, comparison of K-edge energies from XAS and electronic states found through EPR to past model complexes and the OEC could help in corroborating the proposed oxidation states of the S-state cycle. As of writing, EPR and XAS studies are underway on **6**$^{+}$, **6**$^{-}$, and **6H**.

3.9 Ligand Flexibility as Design Element

The propensity of the present supporting multinucleating ligand to allow for different binding modes is instrumental for supporting the wide span of metal oxidation states and oxido content. The lability of the dipyridylalkoxymethyl moiety is well documented in the coordination chemistry of dipyridylketone and the *gem*-diol or hemiacetal form thereof, which chelate and bridge metal ions in a wide variety of binding modes.[39] Bridging three dipyridylalkoxymethyl units through a triarylbenzene scaffold therefore provides rich possibilities for coordination that benefit the formation of complexes **2** through **7**. Clusters rich in labile Mn^{II} are coordinated by nine donors from **L**, binding to twelve coordination sites (counting three μ-alkoxides) while the higher oxidation state species, displaying Mn^{III} and Mn^{IV}, require only six donors (Figure 3.7).

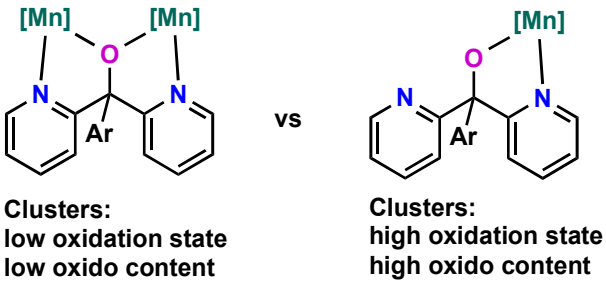

Figure 3.7 Ligand flexibility as function of cluster oxido content and oxidation state: Binding modes of dipyridylalkoxide arms in clusters **1**-**7**.

The switch in coordination mode is likely due to the strong Mn-oxido bonds that lead to the displacement of the pyridine and μ_2-alkoxide donors. The three acetates from precursor **1** complete the metal coordination spheres by bridging the $Mn_3(\mu\text{-}OR)_3$ core of **2**-**4** to the fourth manganese and the three diamond core motifs in **5**-**7**. The versatility of carboxylate ligation in manganese cluster chemistry has also been

documented.[40] The present compounds show conservation of the ancillary ligands (L and acetates) over a large set of oxidation states and oxide contents, indicating that donor flexibility is an important factor in the design of ligands for clusters in multielectron chemistry involving transfers of oxygenous moieties.

3.10 Relation to the Assembly and Turnover of the OEC; Design Implications for Metal-Oxide Clusters

PSII stabilizes four manganese centers through nine oxidation states. The present compounds comprise eight oxidation states from Mn^{II}_4 to $Mn^{III}Mn^{IV}_3$, mimicking states from the beginning of photoactivation, a hypothetical S_{-5}, through to S_2. As in PSII, the higher oxidation states are stabilized by incorporation of strong oxido ligands. Alongside three acetates, the semilabile ligand framework **L** is conserved throughout the series with a decrease in the number of coordinating donors from **L**. The type of change in coordination observed here might be relevant to the assembly of the OEC in PSII. The early biochemical intermediates in photoactivation are reported to proceed to fully assembled OEC in low yields relative to light absorption.[10c, 41] Additional nitrogen and oxygen donors are present in the protein close to the active site, such as His337 and Asp61. These do not coordinate to the fully assembled cluster, but have been proposed to be important in binding the metal centers in the low oxidation state intermediates of photoactivation ($< S_0$),[9b] although Asp170 has been shown to coordinate to the first Mn^{2+} center during assembly and remains coordinated to the full OEC.[10a, 42] A slow kinetic step after the initial binding and photooxidation of Mn^{2+} has been proposed to be a protein conformational change, which may involve ligand rearrangements.[10c, 41b]

The charge neutralization demonstrated by **5** and **6** conceptually mimics how the OEC can access high oxidation states. In PSII, the oxidizing equivalents, all with the same potential, are provided by the photooxidized chlorophyll P_{680} via a tyrosine $Y_z^{\bullet}$.[43,37,44] Therefore, as the OEC is oxidized during turnover, water is incorporated and deprotonated, neutralizing the positive charge built up from oxidation and facilitating access to high oxidation state Mn. Complexes **5** and **6** show that charge neutralization manifests in high oxidation state, tetramanganese-oxido synthetic models of the OEC.

Beyond the assembly of the OEC, the present series of compounds suggests a rational strategy for the synthesis of high oxidation state clusters from reduced precursors. Low oxidation state clusters support fewer oxido ligands due to negative charge buildup. Consequently, additional donors from the multinucleating ligands are necessary to satisfy the coordination sphere of the metal and avoid oligomerization. Upon oxidation, water incorporation and deprotonation, the clusters include additional oxido moieties. These moieties facilitate further oxidation. Increased number of oxido moieties require some supporting ligand dissociation to maintain similar coordination numbers. Labile pendant donors, such as the pyridines in the present case, facilitate not only the isolation of the reduced clusters, but also provide coordination flexibility to support the higher oxidation state, higher oxido content clusters.

CONCLUSIONS

In summary, a series of tetramanganese complexes of variable oxido-content (one through four) and oxidation state (Mn^{II}_4 through $Mn^{III}Mn^{IV}_3$) has been obtained. Six clusters in four oxidation states were crystallographically characterized, and four

further redox events were accessed electrochemically. Reduced ($Mn^{III}_3Mn^{IV}O_4$) and oxidized ($Mn^{III}Mn^{IV}_3O_4$) cubane complexes could be synthesized chemically and frozen for spectroscopic analysis before decomposition. XANES data support the assigned oxidation states, and EXAFS were consistent with XRD. Magnetism and EPR studies were performed to elucidate the electronic structures. These complexes conceptually mimic the wide range of tetramanganese-oxido species in photoactivation and the Kok cycle of the OEC in PSII. Cluster interconversion was achieved in several cases. These transformations show that the coordination environment around the metal centers changes as a function of the number of oxido moieties due to their propensity to bridge and form strong bonds. Similar to the OEC active site, several linked donors in a multinucleating ancillary ligand support the four-manganese cluster over a broad range of oxidation states and oxido content. Ligand lability was found to be instrumental for accommodating the increased number of oxido moieties. The presence of labile pendant donor groups is a design feature that is expected to apply generally to the rational synthesis of metal-oxido clusters from reduced precursors.

EXPERIMENTAL SECTION

General Considerations

Reactions performed under inert atmosphere were carried out in a glovebox under a nitrogen atmosphere. Anhydrous tetrahydrofuran (THF) was purchased from Aldrich in 18 L Pure-Pac™ containers. Anhydrous dichloromethane, diethyl ether, and THF were purified by sparging with nitrogen for 15 minutes and then passing under nitrogen pressure through a column of activated A2 alumina (Zapp's). Anhydrous *N,N*-

dimethylformamide (DMF) was purchased from Aldrich and stored over molecular sieves. NMR solvents were purchased from Cambridge Isotope Laboratories, Inc. CD_2Cl_2 was dried over calcium hydride, then degassed by three freeze-pump-thaw cycles and vacuum-transferred prior to use. ^{1}H NMR and ^{13}C NMR spectra were recorded on a Varian 300 MHz instrument, with shifts reported relative to the residual solvent peak. Elemental analyses were performed by Midwest Microlab, LLC, Indianapolis, IN. High-resolution mass spectrometry (HRMS) was performed at the California Institute of Technology Mass Spectra Facility.

Unless indicated otherwise, all commercial chemicals were used as received. Tetrabutylammonium permanganate,[45] iodosobenzene,[46] and $Mn(OTf)_2$•CH_3CN[47] were prepared according to literature procedures. **Caution!** Tetrabutylammonium permanganate and iodosobenzene are potentially explosive and should be used only in small quantities.

Synthetic Procedures

Synthesis of 1,3,5-Tris(2-di(2'-pyridyl)hydroxymethylphenyl)benzene (H_3L): See Chapter 2.

Synthesis of $LMn^{II}_3(OAc)_3$ (1). See Chapter 2.

Synthesis of $LMn^{II}_3Mn^{III}O_1(OAc)_4$ (2).

Method A from **1**: In the glovebox, yellow solid **1**•$CHCl_3$ (42 mg, 0.03 mmol) was suspended in THF (5 mL). $Mn(OAc)_2$ (5.8 mg, 0.03 mmol) was added as a solid,

followed by KO_2 (4.5 mg, 0.06 mmol). The heterogeneous mixture slowly became brown. After magnetically stirring for 4 days, the solution was brown with brown precipitate. The brown solid was collected on a frit with a bed of celite, rinsed with THF (~10 mL), the THF fraction was discarded, and the solid was solubilized and rinsed through with CH_2Cl_2. The resulting red-brown solution was concentrated *in vacuo* to afford brown solid **2** (30 mg, 70%). Recrystallization from vapor diffusion of Et_2O into a DMF solution gave crystals amenable to X-ray diffraction studies.

Method B from **3**: In the glovebox, the purple solid **3** (126.3 mg, 0.08 mmol) was dissolved in CH_2Cl_2 (8 mL). Decamethylferrocene (27.6 mg, 0.085 mmol) was added to the purple-brown solution of **3** as an orange solution in CH_2Cl_2 (1 mL). The reaction mixture turned gray-brown. Volatile materials were removed *in vacuo* after 30 minutes of stirring. The resulting solid was dissolved in minimal CH_3CN, and Et_2O was allowed to vapor diffuse into the solution to afford large green crystals ([FeCp*]OTf) and small purple crystals. The crystals were separated manually to afford 60 mg of purple crystalline material. Based on preliminary XRD studies and elemental analysis, this material was characterized as dimeric $[LMn^{II}_3Mn^{III}O_1(OAc)_3]_2$•2OTf: Anal. Calcd. for $C_{128}H_{96}F_6Mn_8N_{12}O_{26}S_2$: C, 54.21; H, 3.41; N, 5.93. Found: C, 54.29; H, 3.63; N, 5.86. A sample of this material (27 mg, 0.01 mmol) was dissolved in CH_3CN (3 mL), and a solution of $^n Bu_4NOAc$ (16 mg, 0.05 mmol) in CH_3CN (1 mL) was added. Within seconds, a brown precipitate formed. The mixture was allowed to stir for 15 minutes and then filtered through Celite. The brown solid was rinsed with ample CH_3CN. The solid was washed through with CH_2Cl_2 and volatiles were removed *in vacuo* to afford brown solid **2**. (16.2 mg, 34% from **3**). ^{1}H NMR (300 MHz, CD_2Cl_2, 25 °C) 42.1

($\Delta\nu_{1/2}$=1500 Hz), 38.3 ($\Delta\nu_{1/2}$=700 Hz), 31.9 ($\Delta\nu_{1/2}$=240 Hz), 11.3 ($\Delta\nu_{1/2}$=180 Hz), 8.6 ($\Delta\nu_{1/2}$=460 Hz), 5.0 ($\Delta\nu_{1/2}$=180 Hz), –4.2 ($\Delta\nu_{1/2}$=220 Hz), –7.5 ($\Delta\nu_{1/2}$=330 Hz) ppm. UV-Vis (λ_{max} [ε (M^{-1} cm^{-1})]): 254 ($5.2x10^4$), 418 (720), 491 (520) nm. Anal. Calcd. for $C_{66}H_{53}Cl_2Mn_4N_6O_{12}$ (**3**•CH_2Cl_2): C, 56.11; H 3.78; N, 5.95. Found: C, 56.67; H, 3.90; N, 5.98.

Synthesis of [$LMn^{II}_2Mn^{III}_2O_1(OAc)_3(OTf)$]OTf (3). In the glovebox, the yellow solid **1**•THF (523 mg, 0.41 mmol) was suspended in THF (80 mL) and $Mn(OTf)_2$•CH_3CN (170 mg, 0.43 mmol) was separately dissolved in THF (20 mL). The solution of $Mn(OTf)_2$ was added by pipette to the suspension of **1**, affording a ~4mM solution of **1**. Iodosobenzene (90 mg, 0.41 mmol) was added as a solid to this hazy, yellow solution. The heterogeneous solution turned purple, then brown and mostly homogeneous within 30 minutes at which point a brown precipitate formed. After stirring for 1 hour, the mixture was filtered through Celite to afford a purple solid and brown solution. The solid was rinsed with some THF and then rinsed through with CH_2Cl_2. Both fractions were concentrated *in vacuo* to give brown-purple powder. The powder from the THF fraction was triturated in benzene, collected by filtration, and rinsed with ~40 mL benzene to remove iodobenzene. The resulting solid **3** was pure by ^{1}H NMR (410 mg, 64%). The powder from the CH_2Cl_2 fraction—ca. 95% pure by ^{1}H NMR—was recrystallized from vapor diffusion of Et_2O into CH_3CN to afford pure **3** (180 mg, 28%, 91% total yield). Recrystallization from vapor diffusion of Et_2O into a CH_2Cl_2/dimethoxyethane solution gave crystals amenable to X-ray diffraction studies.

^{1}H NMR (300 MHz, CD_2Cl_2, 25 °C) 45.3 ($\Delta\nu_{1/2}$=800 Hz), 40.8 ($\Delta\nu_{1/2}$=410 Hz), 35.5 & 33.3 (overlapping), 11.5 ($\Delta\nu_{1/2}$=100 Hz), 8.1 ($\Delta\nu_{1/2}$=160 Hz), 7.1 ($\Delta\nu_{1/2}$=650 Hz), 5.2 ($\Delta\nu_{1/2}$=90 Hz), –9.2 ($\Delta\nu_{1/2}$=220 Hz), –11.5 ($\Delta\nu_{1/2}$=230 Hz) ppm. ^{19}F NMR (282 MHz, CD_2Cl_2, 25 °C): 60.0 ($\Delta\nu_{1/2}$=750 Hz) ppm. UV-Vis (λ_{max} [ε (M^{-1} cm^{-1})]): 251 ($5.4x10^4$), 412 (870), 489 (810) nm. Anal. Calcd. for $C_{65}H_{48}F_6Mn_4N_6O_{16}S_2$: C, 49.82; H, 3.09; N, 5.36. Found: C, 50.09; H, 3.45; N, 5.44.

Synthesis of $LMn^{II}_2Mn^{III}_2O_2(OAc)_3$ (4). In the glovebox, yellow solid **1**•THF (365 mg, 0.28 mmol) was suspended in CH_3CN (18 mL) and $Mn(OAc)_2$ (50.3 mg, 0.29 mmol) was added as a solid. KO_2 (59.0 mg, 0.83 mmol) was then added as a solid, and the heterogeneous mixture was magnetically stirred for 3.5 days to afford a tan precipitate and green/brown solution. The precipitate was collected by filtration over Celite, washed with CH_3CN, and then rinsed through with CH_2Cl_2. CH_2Cl_2 was removed *in vacuo*, affording an analytically pure tan powder **4** (225 mg, 63%). Recrystallization from vapor diffusion of Et_2O into a DMF solution gave crystals amenable to X-ray diffraction studies.^{1}H NMR (300 MHz, CD_2Cl_2, 25 °C) 61.9 ($\Delta\nu_{1/2}$=900 Hz), 54.0 ($\Delta\nu_{1/2}$=1350 Hz), 46.3 ($\Delta\nu_{1/2}$=720 Hz), 42.3 & 40.8 (overlapping), 30.8 ($\Delta\nu_{1/2}$=340 Hz), 20.4 & 19.7 (overlapping), 11.9 ($\Delta\nu_{1/2}$=130 Hz), 11.1 ($\Delta\nu_{1/2}$=420 Hz), 8.6 & 7.7 (overlapping), 6.3 ($\Delta\nu_{1/2}$=200 Hz), 4.0 ($\Delta\nu_{1/2}$=290 Hz), –4.1 ($\Delta\nu_{1/2}$=370 Hz), –7.8 ($\Delta\nu_{1/2}$=350 Hz), –15.2 & –16.0 (overlapping) ppm. All resonances are paramagnetically broadened. UV-Vis (λ_{max} [ε (M^{-1} cm^{-1})]): 254 ($8.0x10^4$) nm. Anal. Calcd. for $C_{63}H_{48}Mn_4N_6O_{11}$: C, 58.89; H, 3.77; N, 6.54. Found: C, 58.58; H, 3.86; N, 6.31.

Synthesis of $LMn^{III}_4O_3(OAc)_3$ (5).

Method A from $LMn_3(OAc)_3$ (**1**): In the glovebox, yellow solid **1**•THF (3.7 g, 2.9 mmol) was suspended in THF (200 mL) and $Mn(OTf)_2CH_3CN$ (1.15 g, 2.9 mmol) was separately dissolved in THF (90 mL). The solution of $Mn(OTf)_2$ was added by pipette to the solution of $LMn_3(OAc)_3$ (**1**). After stirring for 20 minutes, KO_2 (0.52 g, 7.3 mmol) was added as a solid. The solution was magnetically stirred for 20 hours and then concentrated *in vacuo* to afford a brown solid. This brown solid was triturated in benzene (100 mL) for 3 hours and then filtered through Celite to afford an orange-red-brown solution. Volatiles were removed *in vacuo*, affording a red-orange powder **5** (1.7 g, 45%).

Method B from **6** and PMe_3: In the glovebox, red-brown solid **6** (95.6 mg, 0.07 mmol) was dissolved in benzene (15 mL) to give a brown-red solution. PMe_3 as a 1.0M solution in THF (0.62 mL, 0.7 mmol) was added to the stirring solution. The solution was stirred for 14 hours, and volatiles were removed *in vacuo*. The resulting red-orange powder was triturated in Et_2O, collected on Celite, and rinsed with copious Et_2O to remove Me_3PO. The solid was rinsed through the Celite with benzene and volatiles were removed *in vacuo* to afford a red-orange powder **5** (88 mg, 93%). Recrystallization from vapor diffusion of hexane into a tetrahydrofuran solution gave crystals amenable to X-ray diffraction studies. $_1$H NMR (300 MHz, C_6D_6, 25 ºC) 22.4 ($\Delta\nu_{1/2}$ = 160), 14.3 ($\Delta\nu_{1/2}$ = 60), 10.1 ($\Delta\nu_{1/2}$ = 30), 8.9 ($\Delta\nu_{1/2}$ = 30 Hz), 8.7 ($\Delta\nu_{1/2}$ = 90 Hz), 7.6 ($\Delta\nu_{1/2}$ = 100 Hz), 6.6 ($\Delta\nu_{1/2}$ = 60 Hz), 5.3 ($\Delta\nu_{1/2}$ = 20 Hz), -12.9 ($\Delta\nu_{1/2}$ = 50 Hz), - 46.0 ($\Delta\nu_{1/2}$ = 1000 Hz) ppm. UV-Vis (λ_{max} [ε (M^{-1}•cm^{-1})]): 234 (7.0×10^4), 239 (6.9×10^4), 244 (6.6×10^4), 249

(6.0×10^4), 256 (5.3×10^4), 262 (4.7×10^4), 396 (2170), 497 (980) nm. Anal. Calcd. for $C_{67}H_{56}Mn_4N_6O_{13}$ ($LMn^{III}_4O_3(OAc)_3$•THF): C, 58.61; H, 4.11; N, 6.12. Found: C, 58.94; H, 4.00; N, 6.24. An X-ray diffraction study of a single crystal of $LMn^{III}_4O_3(OAc)_3$ showed that the compound crystallizes with four THF molecules.

Synthesis of $LMn^{III}_2Mn^{IV}_2O_4(OAc)_3$ (6).

Method A from $LMn^{II}_3(OAc)_3$ (**1**):In the glovebox, yellow solid **1**•$CHCl_3$ (57.8 mg, 0.045 mmol) and *n*Bu_4NMnO_4 (34.9 mg, 0.10 mmol) were separately dissolved in CH_2Cl_2 (≈4 mL) in scintillation vials. The purple solution of *n*Bu_4NMnO_4 was transferred to the stirring yellow solution of $LMn^{II}_3(OAc)_3$ (**1**). The reaction mixture was stirred at RT for 12 h, then concentrated *in vacuo* to afford a brown powder. The powder was triturated in benzene and filtered to afford a brown solution. Crystalline material was obtained by vapor diffusion of Et_2O into this benzene solution (20 mg, 30%). Recrystallization of this material from vapor diffusion of Et_2O into a CH_2Cl_2 solution gave crystals amenable to X-ray diffraction studies.

Method B from **5** and PhIO: In the glovebox, **5** (1.55 g, 1.2 mmol) was dissolved in CH_2Cl_2 (100 mL). PhIO (524 mg, 2.4 mmol) was added as a suspension in CH_2Cl_2. The solution was magnetically stirred for 5 hours and concentrated *in vacuo*. The resulting brown powder was triturated in benzene (50 ml) for 1 hour then filtered through Celite, giving a red-brown solution and brown solid. The brown solid was scraped into a flask and triturated in benzene again. This mixture was filtered through Celite, and the process repeated until no color was seen in the filtered solution. The brown solid was discarded, and the red-brown solution was concentrated *in vacuo*. Benzene was added to

this solid (15 mL) to give a red-brown solution and 250 mL of Et_2O was added to afford a red-brown precipitate **6** (770 mg, 50%), collected by filtration and rinsed with Et_2O to remove iodobenzene.

Method C from **5** and NR_4OH (R = Me, Et) and $FcPF_6$: Under an anaerobic atmosphere, **5** (18.0 mg, 0.014 mmol) was dissolved in THF (7 mL). In a separate flask, a 35 wt.% solution of NEt_4OH in H_2O (11.6 mg, 0.028 mmol) was diluted with CH_3CN (1 mL). In a third flask, $FcPF_6$ (18.3 mg, 0.055 mmol) was dissolved in CH_3CN (1 mL). While stirring the solution of **5**, the NEt_4OH solution was added by pipette followed quickly by addition of the $FcPF_6$ solution. The red-orange solution turned green-brown upon addition of the $FcPF_6$. Volatiles were removed *in vacuo* after 40 minutes of stirring. The resulting green-brown solid was triturated in Et_2O and filtered to remove ferrocene. The solid was then rinsed with benzene to afford a red-orange solution of **6** and blue solid (excess $FcPF_6$). The solution was concentrated *in vacuo* to afford the red-orange powder **6** (13 mg, 70%, ca. 90% pure by ^{1}H NMR).

Method D from **4** and O_2: In the glovebox, **4** (50 mg, 0.04 mmol, 200 μM) was dissolved in DMF (200 mL) in an oven-dried schlenk tube to give a brown and clear solution. The schlenk tube was brought out of the glovebox, connected to the schlenk line, and degassed by introducing the solution to vacuum with vigorous stirring for ~2 minutes. An atmosphere of O_2 was introduced with vigorous stirring for ~2min, and the degassing/O_2-introduction cycle was repeated four times. Aliqouts (~25 mL each) for ^{1}H NMR analysis were removed by syringe, transferred to an oven-dried schlenk tube, and concentrated *in vacuo* to give brown solids. After six aliquots over 12 days, the

remaining reaction mixture (~ 50 mL) was concentrated *in vacuo* to give the final sample at 13 days (~60% **6** by ^{1}H NMR).

Method B afforded the purest **6**: ^{1}H NMR (300 MHz, C_6D_6, 25 ºC), 17.0, 15.6 (overlapping), 10.5 ($\Delta\nu_{1/2}$ = 50 Hz), 9.8 ($\Delta\nu_{1/2}$ = 100 Hz), 8.8 ($\Delta\nu_{1/2}$ = 30 Hz), 7.5 ($\Delta\nu_{1/2}$ = 60 Hz), 5.5 ($\Delta\nu_{1/2}$ = 190),-16.0 ($\Delta\nu_{1/2}$ = 110) -64.6 ($\Delta\nu 1/2$ =2400) ppm. UV-Vis (λ_{max} [r (M^{-1} cm^{-1})]): 238 (1.0×105), 243 (1.1×105), 248 (1.3×105), 254 (1.4×105), 260 (1.1×105), 714 (200), nm. Anal. Calcd. for $C_{63}H_{48}Mn_4N_6O_{13}$: C, 57.46; H 3.67; N, 6.38. Found: C, 56.66; H, 3.70; N, 6.10. HRMS (TOF- MS): calcd. for $C_{63}H_{49}Mn_4N_6O_{13}$ (M+H): 1317.0879; found: 1317.0850.

Synthesis of $[LMn^{III}Mn^{IV}_3O_4(OAc)_3]SbCl_6$ (6^+):

a) In CH_2Cl_2: In a glovebox, **6** was dissolved (6.8 mg, 5 μmol) in CD_2Cl_2 (1.0 mL). Separately, Magic Blue (1.05 equiv) was partially dissolved in CD_2Cl_2 (0.4 mL). The Magic Blue solution was added dropwise to the Mn solution. The magic blue vial was rinsed with 2 x 0.3 mL CD_2Cl_2. The mixture was stirred for 5 minutes and then frozen in the cold well. This sample was thawed briefly to prepare NMR and EPR samples.

b) In THF: In a glovebox, **6** was dissolved (3.9 mg, 3 μmol) in THF (0.8 mL). Separately, Magic Blue (1.05 equiv) was dissolved in THF (0.4 mL), and was added dropwise to the Mn solution. The Magic Blue vial was rinsed with 2 x 0.2 mL THF. The reaction mixture was stirred for ca. 3 minutes and then frozen in the cold well. This sample was only thawed briefly to prepare NMR and XAS samples.

^{1}H NMR (300 MHz, CD_2Cl_2, 25 ºC) 13.8, 10.9, 9.2, 4.9, -18.5 ppm.

EPR, XAS, XES, AND RIXS to be reported.

Synthesis of $[LMn^{III}_3Mn^{IV}O_4(OAc)_3]CoCp_2$ (6^-): In a glovebox, **6** (11.3 mg, 8 μmol) was dissolved in CD_2Cl_2 (2.3 mL). $CoCp_2$ (1.7 mg, 9 μmol, 1.05 equiv.) was weighed into a separate vial. The Mn solution was added to the $CoCp_2$ solid quickly by pipette, taking the solution quickly between the two vials to ensure good mixing. After ca. 90 seconds, the reaction mixture was frozen and then thawed for NMR or EPR samples. For XAS, XES, and RIXS samples, an equal volume of DMA was added to the frozen sample and refroze. While thawing, the CD_2Cl_2 was removed *in vacuo*, leaving the cold DMA solution. During removal of CD_2Cl_2 the solution was re-cooled 3 times to keep the compound stable. ^{1}H NMR (300 MHz, CD_2Cl_2, 25 °C) 27.1, 20.6, 10.6, 8.5, 5.7, -19.6 ppm. EPR, XAS, XES, AND RIXS to be reported.

Synthesis of $[LMn^{III}_3Mn^{IV}O_4(OAc)_3]H$ (6H): In a glovebox, **6** (11.2 mg, 8 μmol) was dissolved in CH_2Cl_2 (ca. 4 mL). $CoCp_2$ (1.6 mg, 8 μmol, 1.0 equiv.) was separately dissolved in CH_2Cl_2 (1 mL). The later solution was transferred into the former solution. Let stir ca. 5 minutes, then $Et_3NH^+OTf^-$ (2.1 mg, 8 μmol, 1.0 equiv.) was added as a solution in CH_2Cl_2 (1 mL). Let stir 5 minutes, and then volatiles were removed *in vacuo*. The brown residue was re-dissolved in CH_2Cl_2 for EPR and NMR and in DMA for XAS, XES, and RIXS. ^{1}H NMR (300 MHz, CD_2Cl_2, 25 °C) 27.9, 24.1, 15.4, 12.0, 10.8, 7.8, -30.3 ppm. EPR, XAS, XES, AND RIXS to be reported.

Synthesis of $[LMn^{III}_2Mn^{IV}_2O_4(OAc)_2$(3,5-dimethylpyrazole)$_2]OTf$ (7): In the glovebox, **6** (71.6 mg, .055 mmol) was dissolved in CH_2Cl_2. While stirring the solution of **6**, Me_3SiOTf was added as a 0.1M solution in CH_2Cl_2 (0.57 ml, 0.057 mmol, 1.05

equiv) dropwise. The solution was stirred magnetically for 30 minutes, and then volatiles were removed *in vacuo*. The resulting brown residue was washed with hexanes to remove Me_3SiOAc byproduct. The residue was then dissolved in C_6H_6 and filtered through celite, leaving some brown solid that was discarded. The brown C_6H_6 solution was concentrated *in vacuo* to dryness, affording $LMn_4O_4(OAc)_2(OTf)$ (72 mg, 90%). A sample of this material (51.5 mg, 0.037 mmol) was dissolved in C_6H_6 (6 mL) and 3,5-dimethylpyrazole (27.0 mg, 0.3 mmol, 8 equiv) was added as a solid. The solution was stirred magnetically for 40 minutes, and then solvent was removed *in vacuo*. The resulting residue was triturated in hexanes, collected on celite, and rinsed with 8 ml hexanes to remove excess 3,5-dimethylpyrazole. The brown solid was rinsed through with CH_2Cl_2 and volatiles were removed *in vacuo*. Microcrystalline precipitate **7** was isolated by Et_2O vapor diffusion into a 1:1 CH_2Cl_2/C_6H_6 solution (20 mg, 34%). X-ray quality crystals were grown from Et_2O vapor diffusion into a C_6H_6 solution of **7**. ^1H NMR (300 MHz, CD_2Cl_2, 25 ºC) 26.6, 25.7, 22.5, 21.1, 18.1, 15.4 (overlapping), 10.4, 9.1, 8.8, 8.2, 7.6, 7.1 (overlapping), 6.1, 5.3, 4.8, 4.3, 2.7 (overlapping), –14.2, –14.7 ppm (overlapping). ^{19}F NMR (282 MHz, CD_2Cl_2, 25 ºC) –76.4 ppm. UV-Vis (λ_{max} [ε (M^{-1} cm^{-1})]): 238 ($9.3x10^4$), 310 ($2.3x10^4$), 715 (200) nm. Anal. Calcd. for $C_{79}H_{69}Cl_2F_3Mn_4N_{10}O_{14}S$ (**7**• CH_2Cl_2•C_6H_6) (sample crystallized from CH_2Cl_2/C_6H_6): C, 53.85; H, 3.95; N, 7.95. Found: C, 53.72; H, 4.05; N, 7.73.

Cyclic Voltammetry

Electrochemical measurements were recorded under a nitrogen atmosphere in a MBraun glovebox at 25 °C with a Pine Instrument Company AFCBP1 bipotentiostat.

An auxiliary Pt-coil electrode, a Ag/Ag^+ reference electrode (0.01 M $AgNO_3$ in CH_3CN), and a 3.0 mm glassy carbon electrode disc (BASI) were used. Data were recorded using the Pine Instrument Company AfterMath software package. All reported values were referenced to an internal ferrocene/ferrocenium couple. The electrolyte solutions were 0.1 M $^n Bu_4NPF_6$ in CH_2Cl_2 in the study of **3** and 0.1M $^n Bu_4NPF_6$ in THF for **5**, **6**, and **7**.

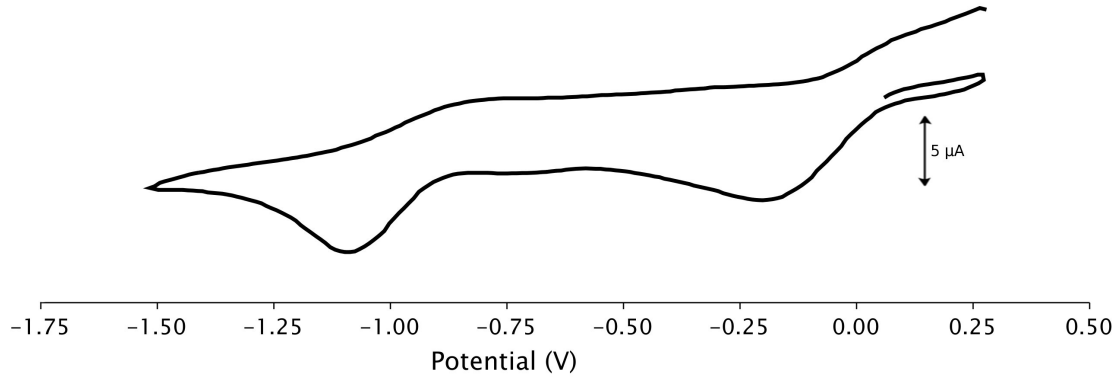

Figure 3.8. Cyclic voltammogram of **3** referenced to Fc/Fc^+. The scan rate was 100 mV/s initially in the positive direction. The analyte concentration was 1.0 mM. The electrolyte was 0.1M $^n Bu_4NPF_6$ in CH_2Cl_2. Open-circuit potential was 70 mV. E_{cat} values: -0.2 V assigned to $Mn^{II}{}_2Mn^{III}{}_2/Mn^{II}{}_3Mn^{III}$ and -1.0 V assigned to $Mn^{II}{}_3Mn^{III}/Mn^{II}{}_4$.

XAS Methods

Mn X-ray Absorption Spectroscopy (XAS) Data Collection. XAS measurements were performed at the Stanford Synchrotron Radiation Laboratory on Beamline 7-3 at an electron energy of 3.0 GeV with an average current of 350 mA. The radiation was monochromatized by a Si(220) double-crystal monochromator. An N_2-filled ion

chamber (I_0) in front of the sample was used to monitor the intensity of the incident X-ray beam. A Ge 30-element detector (Canberra) was used to collect the data as fluorescence excitation spectra. The monochromator energy was calibrated using the pre-edge peak of $KMnO_4$ (6543.3 eV). The calibration standard was placed between two N_2-filled ionization chambers (I_1 and I_2) after the sample. The X-ray flux at 6.6 keV ranged from 2 to 5 × 10^9 photons $s^{-1}mm^{-2}$ of the sample. To minimize radiation damage, samples were maintained at a temperature of 10 K in a liquid He flow cryostat.

To prepare the XAS samples, 5-10 mg of the individual complexes were finely ground with a mortar and pestle in a glovebox, and diluted with boron nitride (1% w/w). The mixture was packed anaerobically into 0.5 mm thick aluminum sample holders and sealed with Kapton tape. To ensure that no X-ray induced radiation damage occurred, the Mn K-edge was closely monitored for any reduction of manganese as seen by a shift in the K-edge inflection point energy.

Data reduction and analysis for EXAFS. Data reduction of the EXAFS spectra was performed using SamView (SixPACK software, Dr. Samuel M. Webb, SSRL). The pre-edge and post-edge backgrounds were subtracted from the XAS spectra using Athena (IFEFFIT software[48]), and the resulting spectra were normalized with respect to the edge height. The background removal in *k*-space was performed using a cubic spline function. Curve fitting was performed with Artemis and IFEFFIT software using *ab initio* calculated phases and amplitudes from the program FEFF 8.2.[48] These *ab initio* calculated phases and amplitudes were applied in the EXAFS equation:

$$\chi(k) = S_0^2 \sum_j \frac{N_j}{kR_j^2} f_{eff}(\pi,k,R_j) e^{-2\sigma_j^2 k^2} e^{-2R_j/\lambda_j(k)} \sin[2kR_j + \phi_{ij}(k)] \qquad \text{[Eq. 1]}$$

where the neighboring atoms to the central atom(s) are divided into j shells, with all atoms having the same atomic number and distance from the central atom(s) grouped into a single shell. For each shell, the coordination number N_j indicates the number of neighboring atoms in shell j at a distance of R_j from the central atom(s). $f_{eff_j}(\pi,k,R_j)$ defines the *ab initio* amplitude function for shell j, and the Debye-Waller term $e^{-2\sigma^2_j k^2}$ denotes the damping that occurs due to static and thermal disorder in absorber-scatterer distances. Losses due to inelastic scattering are defined by the mean free path term, $e^{-2R_j/\lambda_j(k)}$, where the electron mean free path is denoted as $\lambda_j(k)$. The sinusoidal term, $\sin[2kR_j + \phi_{ij}(k)]$, represents the oscillations in the EXAFS spectrum, where $\phi_{ij}(k)$ is the *ab initio* phase function for shell j. The term S_0^2 is the amplitude reduction factor due to shake-up/shake-off processes that occur at the central atom(s). This EXAFS equation was used to fit the experimental data using N, R, and the EXAFS Debye-Waller factor (σ^2) as variable parameters. For the energy (eV) to wave vector (k, Å^{-1}) axis conversion, E_0 was defined as 6561.3 eV.

Table 3.3: Mn K-edge EXAFS curve-fitting parameters for complexes **3**-**6**.[a]

Complex	Path	R (Å)		N	s^2 ($Å^2$)	R (%)
		EXAFS	XRD			
3	Mn-O	1.99 (0.03)	1.93–2.29	**3.5**	0.014 (0.005)	1.4
	Mn-O	2.18 (0.08)		**0.75**	0.002 (0.002)	DE_0=-10.6
	Mn-N	2.19 (0.04)	2.13–2.31	**1.5**	0.002 (0.002)	
	Mn-C	2.97 (0.06)	2.91–3.12	**4.75**	0.011 (0.009)	
	Mn-Mn	3.13 (0.01)	3.12–3.14	**1.5**	0.007 (0.005)	
	Mn-Mn	3.48 (0.04)	3.46–3.52	**1.5**	0.007 (0.005)	
4	Mn-O	1.86 (0.04)	1.86–2.18	**2.25**	0.005 (0.004)	1.8
	Mn-O	2.08 (0.08)		**1.75**	0.010 (0.001)	DE_0=-14.2
	Mn-N	2.18 (0.12)	2.14-2.37	**1.75**	0.010 (0.001)	
	Mn-Mn	2.74 (0.10)	2.79	**0.5**	0.010 (0.001)	
	Mn-C	2.85 (0.10)		**5.5**	0.015 (0.001)	
	Mn-Mn	3.10(0.05)	3.13–3.18	**1.5**	0.004 (0.003)	
	Mn-Mn	3.66 (0.13)	3.46, 3.63	**1.0**	0.009 (0.001)	
5	Mn-O	1.90 (0.02)	Mn-O: 1.85–2.36	**3.75**	0.006 (0.001)	0.2 DE_0=-10.5
	Mn-N/O	2.12 (0.04)	Mn-N: 2.03-2.04	**2.25**	0.014 (0.005)	
	Mn-Mn	2.81 (0.03)	2.77–2.87	**1.5**	0.005 (0.002)	
	Mn-C	2.95 (0.04)	2.82–3.03	**3.5**	0.008 (0.010)	
	Mn-Mn	3.24 (0.02)	3.20–3.23	**1.5**	0.004 (0.001)	
6	Mn-O	1.87 (0.01)	Mn-O: 1.85 – 2.20	**4.25**	0.005 (0.001)	0.7 DE_0=-12.8
	Mn-O/N	2.11 (0.01)	Mn-N: 2.03 – 2.05	**1.75**	0.020 (0.012)	
	Mn-Mn	2.83 (0.05)	2.76–3.07	**3**	0.007 (0.001)	

[a] Complex **3** was fit in the k-range of 2.0 < k (/Å) < 11.0 (1.0 < R (Å) < 3.5). Complex **4** was fit in the k-range of 2.0 < k (/Å) < 11.0 (1.0 < R (Å) < 4.0). Complex **5** was fit in the k-range of 2.2 < k (/Å) < 11.0 (1.0 < R (Å) < 3.0). Complex **6** was fit in the k-range of 2.1 < k (/Å) < 11.4 (1.0 < R (Å) < 3.3).

EPR Methods

Perpendicularly polarized CW X-band (9 GHz) spectra were collected using a Bruker model E-500 spectrometer equipped with a super-high Q resonator (SHQE). Parallel polarized CW X-band (9 GHz) spectra were collected using a dual-mode cavity (ER 4116DM). All CW X-band spectra were collected under non-saturating slow-passage conditions. Temperature control was maintained with an Oxford Instruments model ESR900 helium flow cryostat with an Oxford ITC 503temperature controller.

For complex **6**, using the coupling scheme $S_A S_C S_{AC} S_B S_D S_{BD} S_{ACBD}$, the energy levels can be calculated using this formula:[49]

$$\begin{aligned} \mathrm{H} = &-J_{33}\left[S_{AC}\left(S_{AC}+1\right)-S_A\left(S_A+1\right)-S_C\left(S_C+1\right)\right] \\ &-J_{44}\left[S_{BD}\left(S_{BD}+1\right)-S_B\left(S_B+1\right)-S_D\left(S_D+1\right)\right] \\ &-J_{34}\left[S_{ACBD}\left(S_{ACBD}+1\right)-S_{AC}\left(S_{AC}+1\right)-S_{BD}\left(S_{BD}+1\right)\right] \end{aligned}$$

Using the J values obtained from magnetic susceptibility data (Table 3.2), we expect that complex **6** has a ground spin state of $S_{ACBD}=1$ ($S_{AC}=4, S_{BD}=3$), and the first excited state is $S_{ACBD}=2$ ($S_{AC}=4, S_{BD}=2$). We cannot ascertain which state is giving rise to the low-temperature EPR signal centered at 330 mT, as we find acceptable simulations for the centermost feature using either $S = 1$ or $S = 2$ as the ground state spin quantum number. The additional spectral intensity at 270 and 400 mT in the experimental 5 K spectrum is not accounted for in our simulations. The temperature-dependent data show that these features results from transitions between levels of higher spin states that become more populated at elevated temperatures (see Figure 3.5).

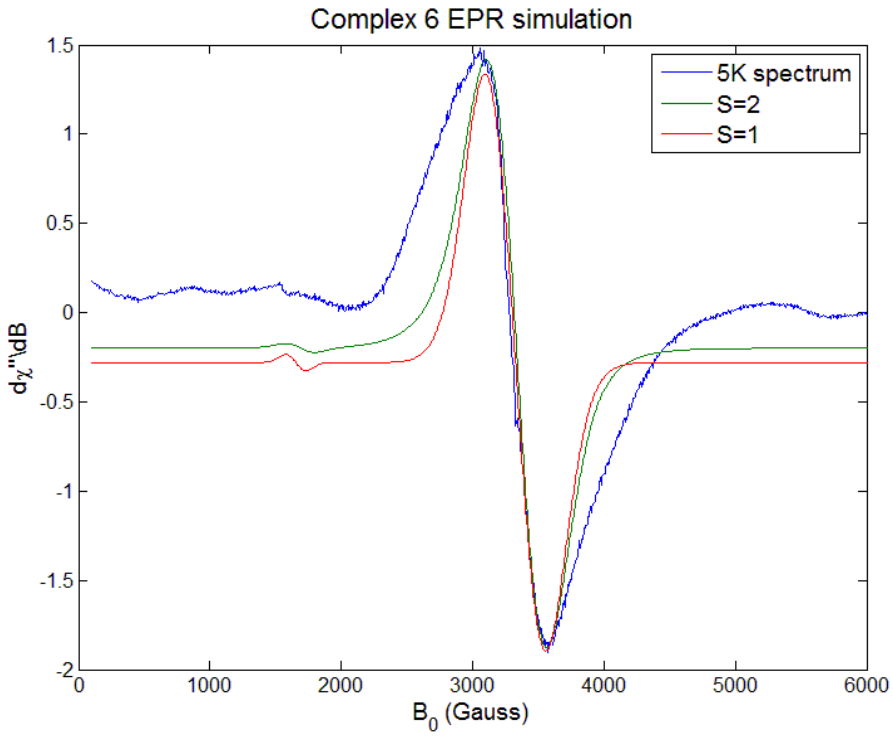

Figure 3.9. X band (9.33 GHz) CW EPR of complex **6** acquired at 5 K (blue trace). Simulations are presented for S = 1 and S = 2 ground states. Simulation parameters: (red trace) S = 1, g = 2, zero-field splitting D = 1000 MHz, E/D =0.1; (green trace) S = 2, g = 2, zero-field splitting D = 600 MHz, E/D = 0.1. Simulations were performed using Matlab R2011b and the EasySpin 4.5.0 package.[50]

Magnetism Studies

General Considerations. DC magnetic susceptibility measurements were carried out in the Molecular Materials Research Center in the Beckman Institute of the California Institute of Technology on a Quantum Design MPMS instrument running MPMS MultiVu software. Powdered samples (0.040–0.059 g) were fixed in eicosane (0.10–0.12 g) in gelatin capsules or in plastic wrap and suspended in clear plastic straws. Data were recorded at 0.5 T from 4–300 K. Diamagnetic corrections were made using the average

experimental magnetic susceptibility of **H_3L** at 0.5 T from 100–300 K (-593×10^{-6} cm^3/mol) in addition to the values of Pascal's constants for amounts of solvent quantified for each sample using elemental analysis.

For compounds **6**, the $\chi_M T$ data taken at 0.5 T were fit to the magnetic susceptibility equation derived from the isotropic spin Hamiltonian for three coupling constants, J_{34}, J_{33}, and J_{44}. Specifically, the manganese centers were modeled as an asymmetric tetrahedron (Figure 3.10), with the basal three manganese centers (Mn_B, Mn_C, and Mn_D) modeled as an isosceles triangle. The exchange interactions between the apical Mn^{III} center (Mn_A) and the two Mn^{IV} centers (Mn_B, Mn_D), J_{34}, were assumed to be the same as the interactions between the Mn^{IV} centers and the basal Mn^{III} (Mn_C) in order to allow the eigenvalues to be determined for the isotropic spin Hamiltonian [Eq. (1)].

$$\hat{H} = -2J_{34}[(\hat{S}_A \bullet \hat{S}_B) + (\hat{S}_A \bullet \hat{S}_D) + (\hat{S}_B \bullet \hat{S}_C) + (\hat{S}_C \bullet \hat{S}_D)] - 2J_{33}(\hat{S}_A \bullet \hat{S}_C) - 2J_{44}(\hat{S}_B \bullet \hat{S}_D) \quad (1)$$

The eigenvalues were determined using the Kambe method.[31] The data were fit from 10–300 K using Matlab[51] by minimizing $R = \sum |(\chi_M T)_{obs} - (\chi_M T)_{calcd}|^2 / \sum (\chi_M T)_{obs}{}^2$. Similar models were used to fit the 0.5 T $\chi_M T$ data taken of compound **3** and **4** with the concomitant change in oxidation states at the Mn centers (Figure 3.10). The Hamiltonian for **3** and **4** is Eq. (2), although note the different locations of the Mn^{II} centers and Mn^{III} centers.

$$\hat{H} = -2J_{23}[(\hat{S}_A \bullet \hat{S}_B) + (\hat{S}_A \bullet \hat{S}_D) + (\hat{S}_B \bullet \hat{S}_C) + (\hat{S}_C \bullet \hat{S}_D)] - 2J_{22}(\hat{S}_A \bullet \hat{S}_C) - 2J_{33}(\hat{S}_B \bullet \hat{S}_D) \quad (2)$$

For compound **5**, the $\chi_M T$ data taken at 0.5 T were fit to the magnetic susceptibility equation derived from the isotropic spin Hamiltonian for two coupling constants J_{TOP} and J_{BOT}. The Mn centers were modeled as an equilateral triangle interacting with a fourth metal center (Figure 3.10, right). The resulting Hamiltonian is Eq. (3). The eigenvalues were determined using the Kambe method.[31] The data were fit from 10–300 K using Matlab[51] by minimizing $R = \sum \left| (\chi_M T)_{obs} - (\chi_M T)_{calcd} \right|^2 / \sum (\chi_M T)_{obs}{}^2$.

$$\hat{H} = -2J_{TOP}[(\hat{S}_A \bullet \hat{S}_D) + (\hat{S}_B \bullet \hat{S}_D) + (\hat{S}_C \bullet \hat{S}_D)] - 2J_{BOT}[(\hat{S}_A \bullet \hat{S}_B) + (\hat{S}_B \bullet \hat{S}_C) + (\hat{S}_A \bullet \hat{S}_C)] \quad (3)$$

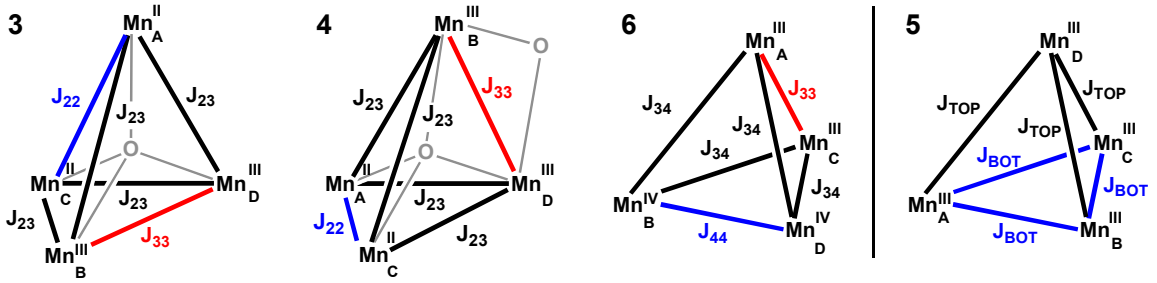

Figure 3.10. Exchange coupling models employed for **3**-**6**. For complexes **3** and **4**, the oxido ligands are shown in gray. In all cases, the Mn_4 tetrahedra are drawn such that the ligand framework $\mathbf{L}^{3-}$ is below the drawing (as in Scheme 3.2).

Crystallographic Information

Table 3.4. Crystal and refinement data for complexes **2**, **3**, and **4**.

	2	**3**	**4**
CCDC number	858642	858643	842512
empirical formula	$C_{65}H_{51}N_6O_{12}Mn_4$• 0.66($C_4H_{10}O$) • C_3H_7N • 0.43(H_2O)	0.59[$C_{64}H_{48}F_3N_6O_{13}SMn_4$]+ 0.41[$C_{65}H_{51}N_6O_{12}Mn_4$]$^+$ [CF_3O_3S]$^-$	$C_{63}H_{48}N_6O_{11}Mn_4$• 3($C_3H_7NO$)
formula wt	1456.92	1529.34	1504.12
T (K)	100(2)	100(2)	100(2)
a, Å	19.5671(8)	12.3050(6)	12.6007(5)
b, Å	12.5184(5)	15.5248(7)	13.0991(5)
c, Å	27.8828(11)	37.6815(18)	20.5699(8)
α, deg	90	90	99.263(2)
β, deg	106.461(2)	98.567(3)	95.161(2)
γ, deg	90	90	94.247(2)
V, Å^3	6549.9(5)	7118.1(6)	3323.8(2)
Z	4	4	2
cryst syst	Monoclinic	Monoclinic	Triclinic
space group	P $2_1/c$	P $2_1/n$	P-1
d_{calcd}, g/cm^3	1.477	1.427	1.503
θ range, deg	1.96 to 28.34	1.68 to 27.50	1.63 to 30.62
μ, mm^{-1}	0.826	0.819	0.817
abs cor	None	None	None
GOF	1.086	1.136	1.542
R1,[a] wR2[b] (I > 2σ(I))	0.0643, 0.1784	0.0848, 0.2042	0.0536, 0.0634

[a] $R1 = \sum||F_o| - |F_c||/\sum|F_o|$. [b] $wR2 = \{\sum[w(F_o^2 - F_c^2)^2]/\cdot[w(F_o^2)^2]\}^{1/2}$.

Table 3.4 continued. Crystal and refinement data for complexes **5**, **6**, and **7**.

	5	**6**	**7**
CCDC number	840141	817379	938750
empirical formula	$C_{63}H_{48}N_6O_{12.09}Mn_4$• 4($C_4H_8O$)	$C_{63}H_{48}N_6O_{13}Mn_4$ • 4(CH_2Cl_2)	$C_{72}H_{61}F_3Mn_4N_{10}O_{14}S$• C_6H_6
formula wt	1590.45	1656.54	1671.19
T (K)	100	100(2)	100(2)
a, Å	13.7255(6)	24.1366(10)	15.410(3)
b, Å	18.1596(7)	15.8728(7)	24.640(5)
c, Å	28.1662(11)	19.1846(8)	19.230(4)
α, deg	90	90	90
β, deg	92.620(2)	112.526(2)	103.16(3)
γ, deg	90	90	90
V, $Å^3$	7013.1(5)	6789.2(5)	7110(2)
Z	4	4	4
cryst syst	Monoclinic	Monoclinic	Monoclinic
space group	P $2_1/c$	P $2_1/c$	P $2_1/n$
d_{calcd}, g/cm^3	1.506	1621	1.561
θ range, deg	1.83 to 26.43	1.73 to 30.54	1.40 to 31.33
μ, mm^{-1}	0.780	1.111	0.807
abs cor	None	none	Empirical
GOF	1.277	2.125	1.640
R1,[a] wR2[b] (I > 2σ(I))	0.0569, 0.0549	0.0589, 0.0823	0.0572, 0.1694

[a] $R1 = \sum||F_o| - |F_c||/\sum|F_o|$. [b] $wR2 = \{\sum[w(F_o^2 - F_c^2)^2]/\cdot[w(F_o^2)^2]\}^{1/2}$.

Special Refinement Details

Refinement of F2 against ALL reflections. The weighted R-factor (wR) and goodness of fit (S) are based on F2, conventional R-factors (R) are based on F, with F set to zero for negative F2. The threshold expression of F2 > 2σ(F2) is used only for calculating R-factors(gt) etc. and is not relevant to the choice of reflections for refinement. R-factors based on F2 are statistically about twice as large as those based on F, and R-factors based on ALL data will be even larger.

All esds (except the esd in the dihedral angle between two l.s. planes) are estimated using the full covariance matrix. The cell esds are taken into account individually in the estimation of esds in distances, angles and torsion angles; correlations between esds in cell parameters are only used when they are defined by crystal symmetry. An approximate (isotropic) treatment of cell esds is used for estimating esds involving l.s. planes.

Compound **2.** Crystals were mounted on a glass fiber using Paratone oil then placed on the diffractometer under a nitrogen stream at 100K. The acetate bridging Mn3-Mn4 adopts two bridging modes: one mode is the usual κ^2(O) mode as in the other acetates and the other has a single oxygen atom forming the bridge. Both orientations were refined with geometric restraints based on similar ligands in the model. The diethyl ether solvent was refined with geometric restraints, a fixed temperature factor and variable occupancy. No restraints were placed on the DMF. The lone oxygen (presumably water) was refined with a fixed temperature factor and a variable occupancy. . The similar ADP and rigid-bond restraints were used on C2C.

Compound **3.** Crystals were mounted on a glass fiber using Paratone oil and then placed on the diffractometer under a nitrogen stream at 100K. The electron density map of the solvent area in this crystal contains a very clearly defined triflate anion and another long ill-defined chain of density, presumably arising from disordered hexane/dimethoxyethane solvents. This latter was solvent flattened using the program SQUEEZE.[7] The total potential solvent is 1203Å^3, about 17% of total unit cell volume, which required 315 electrons to adjust the observed intensities such that this area contained no electron density. This is reasonably consistent with two hexane molecules per asymmetric unit. The trifluoromethanesulfonate anion coordinating Mn4 has compositional disorder with an acetate anion, with populations at 59% and 41%, respectively. The acetate was modeled isotropically. The similar ADP and rigid-bond restraints were used on C64 and O8.

Compound **4.** Crystals were mounted on a glass fiber using Paratone oil then placed on the diffractometer under a nitrogen stream at 100K. The non-bridging acetate bound to Mn4 is disordered over two orientations.

Compound **5**. Crystals were mounted on a loop and then placed on the diffractometer under a nitrogen stream at 100K. The asymmetric unit contains four molecules of THF and the largest peaks in the final difference Fourier map are in the area of these, suggesting disorder. This was not modeled. Additionally, the Fourier map contained a peak suggesting an oxygen capping the Mn_4O_3 partial cubane structure. This oxygen was assigned a fixed temperature factor (U = 0.050) and was included in the final least squares refinement with position and occupancy free to refine. The refined occupancy was equal to 0.09.

Compound **6**. Crystals were mounted on a glass fiber using Paratone oil and then placed on the diffractometer under a nitrogen stream at 100K.

Compound **7.** Crystals were mounted on a plastic loop using Paratone oil and then placed in liquid N_2 for transport to SSRL beamline 12-2. A molecule of benzene (the crystallization solvent) was found in the lattice and could not be satisfactorily modeled anisotropically. It was thus modeled isotropically and hydrogens were not calculated for this molecule.

REFERENCES

1. McEvoy, J. P.; Brudvig, G. W. *Chem. Rev.* **2006,** *106*, 4455-4483.
2. (a) Joliot, P. *Biochim. Biophys. Acta* **1965,** *102*, 116-134.(b) Kok, B.; Forbush, B.; Mcgloin, M. *Photochem. Photobiol.* **1970,** *11*, 457-475.
3. Kolling, D. R. J.; Cox, N.; Ananyev, G. M.; Pace, R. J.; Dismukes, G. C. *Biophys J* **2012,** *103*, 313-322.
4. (a) Pecoraro, V. L.; Baldwin, M. J.; Caudle, M. T.; Hsieh, W. Y.; Law, N. A. *Pure Appl. Chem.* **1998,** *70*, 925-929.(b) Pecoraro, V. L.; Hsieh, W. Y., The use of Model Complexes to Elucidate the Structure and Function of Manganese Redox Enzymes. In *Manganese and its Role in Biological Systems*, Sigel, A.; Sigel, H., Eds. Marcel Dekker, Inc.: New York, 2000; Vol. 37, pp 429-504.(c) Sproviero, E. M.; Gascon, J. A.; McEvoy, J. P.; Brudvig, G. W.; Batista, V. S. *J. Am. Chem. Soc.* **2008,** *130*, 3428-3442.
5. Chow, W. S.; Aro, E. M., Photoinactivation and Mechanisms of Recovery. In *The Light-Driven Water: Plastoquinone Oxidoreductase*, Wydrzynski, T. J.; Satoh, K., Eds. Springer: Dordrecht, 2005; Vol. 22, pp 627-648.
6. Cheniae, G. M.; Martin, I. F. *Biochem. Bioph. Res. Co.* **1967,** *28*, 89-95.
7. (a) Miller, A. F.; Brudvig, G. W. *Biochemistry* **1989,** *28*, 8181-8190.(b) Miller, A. F.; Brudvig, G. W. *Biochemistry* **1990,** *29*, 1385-1392.(c) Burnap, R. L. *Phys. Chem. Chem. Phys.* **2004,** *6*, 4803-4809.

8. (a) Shevela, D.; Su, J. H.; Klimov, V.; Messinger, J. *Bba-Bioenergetics* **2008,** *1777*, 532-539.(b) Ulas, G.; Olack, G.; Brudvig, G. W. *Biochemistry* **2008,** *47*, 3073-3075.

9. (a) Baranov, S. V.; Tyryshkin, A. M.; Katz, D.; Dismukes, G. C.; Ananyev, G. M.; Klimov, V. V. *Biochemistry* **2004,** *43*, 2070-2079.(b) Dasgupta, J.; Tyryshkin, A. M.; Dismukes, G. C. *Angew. Chem. Int. Ed.* **2007,** *46*, 8028-8031.(c) Dasgupta, J.; Tyryshkin, A. M.; Baranov, S. V.; Dismukes, G. C. *Appl. Magn. Reson.* **2010,** *37*, 137-150.

10. (a) Campbell, K. A.; Force, D. A.; Nixon, P. J.; Dole, F.; Diner, B. A.; Britt, R. D. *J. Am. Chem. Soc.* **2000,** *122*, 3754-3761.(b) Tyryshkin, A. M.; Watt, R. K.; Baranov, S. V.; Dasgupta, J.; Hendrich, M. P.; Dismukes, G. C. *Biochemistry* **2006,** *45*, 12876-12889.(c) Zaltsman, L.; Ananyev, G. M.; Bruntrager, E.; Dismukes, G. C. *Biochemistry* **1997,** *36*, 8914-8922.(d) Dasgupta, J.; Ananyev, G. M.; Dismukes, G. C. *Coord. Chem. Rev.* **2008,** *252*, 347-360.(e) Ananyev, G. M.; Dismukes, G. C. *Biochemistry* **1997,** *36*, 11342-11350.

11. (a) Brudvig, G. W.; Beck, W. F., Oxidation-Reduction and Ligand-Substitution Reactions of The Oxygen-Evolving Center of Photosystem II. In *Manganese Redox Enzymes*, Pecoraro, V. L., Ed. VCH Publishers, Inc.: New York, 1992; pp 119-140.(b) Beck, W. F.; Brudvig, G. W. *Biochemistry* **1987,** *26*, 8285-8295.(c) Schansker, G.; Goussias, C.; Petrouleas, V.; Rutherford, A. W. *Biochemistry* **2002,** *41*, 3057-3064.(d) Messinger, J.; Seaton, G.; Wydrzynski, T.; Wacker, U.; Renger, G. *Biochemistry* **1997,** *36*, 6862-6873.

12. (a) Mukhopadhyay, S.; Mandal, S. K.; Bhaduri, S.; Armstrong, W. H. *Chem. Rev.* **2004,** *104*, 3981-4026.(b) Mullins, C. S.; Pecoraro, V. L. *Coord. Chem. Rev.* **2008,** *252*, 416-443.(c) Mukherjee, S.; Stull, J. A.; Yano, J.; Stamatatos, T. C.; Pringouri, K.; Stich, T. A.; Abboud, K. A.; Britt, R. D.; Yachandra, V. K.; Christou, G. *Proc. Natl. Acad. Sci. USA* **2012,** *109*, 2257-2262.

13. (a) Tsui, E. Y.; Day, M. W.; Agapie, T. *Angew. Chem. Int. Ed.* **2011,** *50*, 1668-1672.(b) Tsui, E. Y.; Kanady, J. S.; Day, M. W.; Agapie, T. *Chem. Commun.* **2011,** *47*, 4189-4191.(c) Kanady, J. S.; Tsui, E. Y.; Day, M. W.; Agapie, T. *Science* **2011,** *333*, 733-736.

14. Vincent, J. B.; Christmas, C.; Chang, H. R.; Li, Q. Y.; Boyd, P. D. W.; Huffman, J. C.; Hendrickson, D. N.; Christou, G. *J. Am. Chem. Soc.* **1989,** *111*, 2086-2097.

15. Kulawiec, R. J.; Crabtree, R. H.; Brudvig, G. W.; Schulte, G. K. *Inorg. Chem.* **1988,** *27*, 1309-1311.

16. Philouze, C.; Blondin, G.; Girerd, J. J.; Guilhem, J.; Pascard, C.; Lexa, D. *J. Am. Chem. Soc.* **1994,** *116*, 8557-8565.

17. (a) Bashkin, J. S.; Chang, H. R.; Streib, W. E.; Huffman, J. C.; Hendrickson, D. N.; Christou, G. *J. Am. Chem. Soc.* **1987,** *109*, 6502-6504.(b) Ruettinger, W.; Campana, C.; Dismukes, G. *J. Am. Chem. Soc.* **1997**, 6670-6671.

18. Wieghardt, K.; Bossek, U.; Gebert, W. *Angew. Chem. Int. Ed.* **1983,** *22*, 328-329.

19. (a) Chan, M. K.; Armstrong, W. H. *J. Am. Chem. Soc.* **1991,** *113*, 5055-5057.(b) Chen, H. Y.; Faller, J. W.; Crabtree, R. H.; Brudvig, G. W. *J. Am. Chem. Soc.* **2004,** *126*, 7345-7349.

20. Wang, S. Y.; Tsai, H. L.; Hagen, K. S.; Hendrickson, D. N.; Christou, G. *J. Am. Chem. Soc.* **1994,** *116*, 8376-8377.

21. Aromi, G.; Wemple, M. W.; Aubin, S. J.; Folting, K.; Hendrickson, D. N.; Christou, G. *J. Am. Chem. Soc.* **1998,** *120*, 5850-5851.

22. (a) Mckee, V.; Tandon, S. S. *J. Chem. Soc. Chem. Comm.* **1988**, 1334-1336.(b) Beagley, B.; Mcauliffe, C. A.; Macrory, P. P.; Ndifon, P. T.; Pritchard, R. G. *J. Chem. Soc. Chem. Comm.* **1990**, 309-310.(c) Gallo, E.; Solari, E.; Deangelis, S.; Floriani, C.; Re, N.; Chiesivilla, A.; Rizzoli, C. *J. Am. Chem. Soc.* **1993,** *115*, 9850-9851.(d) Cotton, F. A.; Daniels, L. M.; Falvello, L. R.; Matonic, J. H.; Murillo, C. A.; Wang, X.; Zhou, H. *Inorg. Chim. Acta* **1997,** *266*, 91-102.(e) Cotton, F. A.; Daniels, L. M.; Jordan, G. T.; Murillo, C. A.; Pascual, I. *Inorg. Chim. Acta* **2000,** *297*, 6-10.(f) Millos, C. J.; Piligkos, S.; Bell, A. R.; Laye, R. H.; Teat, S. J.; Vicente, R.; McInnes, E.; Escuer, A.; Perlepes, S. P.; Winpenny, R. E. P. *Inorg. Chem. Commun.* **2006,** *9*, 638-641.(g) Yang, C. I.; Wernsdorfer, W.; Tsai, Y. J.; Chung, G.; Kuo, T. S.; Lee, G. H.; Shieh, M.; Tsai, H. L. *Inorg. Chem.* **2008,** *47*, 1925-1939.(h) Zaleski, C. M.; Weng, T. C.; Dendrinou-Samara, C.; Alexiou, M.; Kanakaraki, P.; Hsieh, W. Y.; Kampf, J.; Penner-Hahn, J. E.; Pecoraro, V. L.; Kessissoglou, D. P. *Inorg. Chem.* **2008,** *47*, 6127-6136.

23. Mikuriya, M.; Yamato, Y.; Tokii, T. *Chem. Lett.* **1991**, 1429-1432.

24. Sanudo, E. C.; Grillo, V. A.; Knapp, M. J.; Bollinger, J. C.; Huffman, J. C.; Hendrickson, D. N.; Christou, G. *Inorg. Chem.* **2002,** *41*, 2441-2450.

25. (a) Ruettinger, W.; Ho, D.; Dismukes, G. *Inorg. Chem.* **1999,** *38*, 1036-1037.(b) Ruettinger, W.; Carrell, T.; Baesjou, P.; Boelrijk, A.; Maneiro, M.; Dismukes, G. *J. Inorg. Biochem.* **1999**, 88.

26. (a) Wang, S. Y.; Folting, K.; Streib, W. E.; Schmitt, E. A.; McCusker, J. K.; Hendrickson, D. N.; Christou, G. *Angew. Chem. Int. Ed.* **1991,** *30*, 305-306.(b) Aubin, S. M. J.; Wemple, M. W.; Adams, D. M.; Tsai, H. L.; Christou, G.; Hendrickson, D. N. *J. Am. Chem. Soc.* **1996,** *118*, 7746-7754.(c) Aliaga-Alcalde, N.; Edwards, R. S.; Hill, S. O.; Wernsdorfer, W.; Folting, K.; Christou, G. *J. Am. Chem. Soc.* **2004,** *126*, 12503-12516.(d) Kanady, J. S.; Mendoza-Cortes, J. L.; Tsui, E. Y.; Nielson, R. J.; Goddard, W. A.; Agapie, T. *J. Am. Chem. Soc.* **2013,** *135*, 1073-1082.

27. Yano, J.; Yachandra, V. K. *Photosynth Res* **2009,** *102*, 241-254.

28. (a) Visser, H.; Anxolabehere-Mallart, E.; Bergmann, U.; Glatzel, P.; Robblee, J. H.; Cramer, S. P.; Girerd, J. J.; Sauer, K.; Klein, M. P.; Yachandra, V. K. *J. Am. Chem. Soc.* **2001,** *123*, 7031-7039.(b) Pizarro, S. A.; Glatzel, P.; Visser, H.; Robblee, J. H.; Christou, G.; Bergmann, U.; Yachandra, V. K. *Phys. Chem. Chem. Phys.* **2004,** *6*, 4864-4870.

29. (a) Yachandra, V. K.; Sauer, K.; Klein, M. P. *Chem. Rev.* **1996,** *96*, 2927-2950.(b) Messinger, J.; Robblee, J. H.; Bergmann, U.; Fernandez, C.; Glatzel, P.; Visser, H.; Cinco, R. M.; McFarlane, K. L.; Bellacchio, E.; Pizarro, S. A.; Cramer, S. P.; Sauer, K.; Klein, M. P.; Yachandra, V. K. *J. Am. Chem. Soc.* **2001,** *123*, 7804-7820.(c) Glatzel, P.; Bergmann, U.; Yano, J.; Visser, H.; Robblee, J. H.; Gu, W. W.; de Groot, F. M. F.; Christou, G.; Pecoraro, V. L.; Cramer, S. P.; Yachandra, V. K. *J. Am. Chem. Soc.* **2004,** *126*, 9946-9959.

30. (a) Wemple, M. W.; Tsai, H. L.; Wang, S. Y.; Claude, J. P.; Streib, W. E.; Huffman, J. C.; Hendrickson, D. N.; Christou, G. *Inorg. Chem.* **1996,** *35*, 6437-6449.(b) Stoumpos, C. C.; Gass, I. A.; Milios, C. J.; Lalioti, N.; Terzis, A.; Aromi, G.; Teat, S. J.; Brechin, E. K.; Perlepes, S. P. *Dalton Trans.* **2009**, 307-317.(c) Stoumpos, C. C.; Stamatatos, T.

C.; Sartzi, H.; Roubeau, O.; Tasiopoulos, A. J.; Nastopoulos, V.; Teat, S. J.; Christou, G.; Perlepes, S. P. *Dalton Trans.* **2009**, 1004-1015.(d) Yang, P. P.; Song, X. Y.; Liu, R. N.; Li, L. C.; Liao, D. Z. *Dalton Trans.* **2010,** *39*, 6285-6294.(e) Yang, P. P.; Li, L. C. *Inorg. Chim. Acta* **2011,** *371*, 95-99.

31. Kambe, K. *J Phys Soc Jpn* **1950,** *5*, 48-51.
32. Hendrickson, D. N.; Christou, G.; Schmitt, E. A.; Libby, E.; Bashkin, J. S.; Wang, S. Y.; Tsai, H.-L.; Vincent, J. B.; Boyd, P. D. W.; Huffman, J. C.; Folting, K.; Li, Q.; Streib, W. E. *J. Am. Chem. Soc.* **1992,** *114*, 2455-2471.
33. Lynch, M. W.; Hendrickson, D. N.; Fitzgerald, B. J.; Pierpont, C. G. *J. Am. Chem. Soc.* **1984,** *106*, 2041-2049.
34. Stamatatos, T. C.; Christou, G. *Philos T R Soc A* **2008,** *366*, 113-125.
35. Ruettinger, W.; Ho, D.; Dismukes, G. *Inorg. Chem.* **1999**, 1036-1037.
36. Brimblecombe, R.; Bond, A. M.; Dismukes, G. C.; Swiegers, G. F.; Spiccia, L. *Phys. Chem. Chem. Phys.* **2009,** *11*, 6441-6449.
37. Caudle, M. T.; Pecoraro, V. L. *J. Am. Chem. Soc.* **1997,** *119*, 3415-3416.
38. (a) Gelasco, A.; Kirk, M. L.; Kampf, J. W.; Pecoraro, V. L. *Inorg. Chem.* **1997,** *36*, 1829-1837.(b) Gelasco, A.; Bensiek, S.; Pecoraro, V. L. *Inorg. Chem.* **1998,** *37*, 3301-3309.
39. Stamatatos, T. C.; Efthymiou, C. G.; Stoumpos, C. C.; Perlepes, S. P. *Eur. J. Inorg. Chem.* **2009**, 3361-3391.
40. Christou, G. *Acc. Chem. Res.* **1989,** *22*, 328-335.
41. (a) Radmer, R.; Cheniae, G. M. *Biochim. Biophys. Acta* **1971,** *253*, 182-186.(b) Chen, C. G.; Kazimir, J.; Cheniae, G. M. *Biochemistry* **1995,** *34*, 13511-13526.
42. Debus, R. J.; Aznar, C.; Campbell, K. A.; Gregor, W.; Diner, B. A.; Britt, R. D. *Biochemistry* **2003,** *42*, 10600-10608.
43. (a) Debus, R. J.; Barry, B. A.; Sithole, I.; Babcock, G. T.; Mcintosh, L. *Biochemistry* **1988,** *27*, 9071-9074.(b) Metz, J. G.; Nixon, P. J.; Rogner, M.; Brudvig, G. W.; Diner, B. A. *Biochemistry* **1989,** *28*, 6960-6969.(c) Baldwin, M. J.; Pecoraro, V. L. *J. Am. Chem. Soc.* **1996,** *118*, 11325-11326.

44. Diner, B. A.; Britt, R. D., The Redox-Active Tyrosines YZ and YD. In *Photosystem II: The Light-Driven Water: Plastoquinone Oxidoreductase*, Wydrzynski, T. J.; Satoh, K., Eds. Springer: Dordrecht, 2005; Vol. 22, pp 207-233.

45. Vincent, J. B.; Chang, H. R.; Folting, K.; Huffman, J. C.; Christou, G.; Hendrickson, D. N. *J. Am. Chem. Soc.* **1987,** *109*, 5703-5711.

46. Saltzman, H.; Sharefkin, J. G. *Org. Synth. Coll.* **1973,** *5*, 658.

47. Bryan, P. S.; Dabrowiak, J. C. *Inorg. Chem.* **1975,** *14*, 296-299.

48. (a) Newville, M. *J Synchrotron Radiat* **2001,** *8*, 322-324.(b) Ravel, B.; Newville, M. *J Synchrotron Radiat* **2005,** *12*, 537-541.

49. Bencini, A. G., *Electron Paramagnetic Resonance of Exchange Coupled Systems*. Springer, Verlag: Berlin, 1990.

50. Stoll, S.; Schweiger, A. *J Magn Reson* **2006,** *178*, 42-55.

51. *Matlab*, 7.10.0.499 (R2010a); The MathWorks, Inc.: Natick, MA, 2010.

CHAPTER 4

A Synthetic Model of the Mn_3Ca Subsite of the Oxygen-Evolving Complex in Photosystem II and Progress Toward more Accurate Mn_3CaM Models.

Published in part as:

Kanady, J. S.; Tsui, E. Y.; Day, M. W.; Agapie, T. *Science* **2011,** *333*, 733-736.

ABSTRACT

Within photosynthetic organisms, the oxygen-evolving complex (OEC) of photosystem II generates dioxygen from water using a catalytic Mn_4CaO_n cluster (*n* varies with the mechanism and nature of the intermediate). We report here the rational synthesis of a $[Mn_3CaO_4]^{6+}$ cubanes that structurally models the trimanganese-calcium–cubane subsite of the OEC. Structural and electrochemical comparison between Mn_3CaO_4 and a related Mn_4O_4 cubane alongside characterization of an intermediate calcium-manganese multinuclear complex reveal potential roles of calcium in facilitating high oxidation states at manganese and in the assembly of the biological cluster. Furthermore, to more accurately model the low-symmetry geometry of the OEC, low-symmetry $Mn^{IV}_3GdO_4$ and $Mn^{IV}_3CaO_4$ cubanes are synthesized in a rational, step-wise fashion through desymmetrization by ligand substitution. This asymmetry manifests in increased basicity at one of the μ_3-oxos within the Mn_3CaO_4 unit, leading to selective protonation at this position and, more importantly, coordination of a transition metal to give a Mn_3CaO_4 + dangling metal topology that structurally models the geometry of the OEC.

INTRODUCTION

Biological dioxygen generation occurs at the Oxygen Evolving Complex (OEC) of Photosystem II (PSII) in cyanobacteria and plants.[1] The active site responsible for this transformation consists of a Mn_4CaO_n cluster embedded in a large protein complex.[2] One commonly proposed arrangement of metals in the active site is three closely spaced manganese centers—part of a heteronuclear Mn_3CaO_4 cubane—bridging

via oxide or hydroxide ligands to a dangling fourth manganese.[2-3] Given broad fundamental interest and potential applications in artificial photosynthesis, the structure of this cluster and the mechanism of water splitting to make dioxygen have been the subject of many spectroscopic, computational, synthetic, crystallographic, and biochemical studies.[1, 2e, 4] Despite significant advances, the mechanism of oxygen production is not well understood. During one turnover, four oxidizing equivalents generated by light are delivered to the active site cluster leading to the stepwise formation of intermediates commonly referred to as the S-states. The sequential transitions from S_0—the most reduced state—to S_4—the most oxidized state—involve electron and proton transfer events. The highly oxidized S_4 state is unstable and evolves dioxygen to return to the S_0-state. The exact Mn oxidation states and the site of O-O bond formation in S_4 are debated; nevertheless, high-oxidation state Mn centers are required to activate a terminal or bridging oxo ligand for O_2 production. The large protein matrix has complicated direct studies of the OEC active site, and the synthesis of small molecule models has been impeded by the complexity of the cluster.

The synthesis of potentially biomimetic manganese oxide clusters has relied heavily on self-assembly due to the propensity of oxide and hydroxide ligands to bridge two or more metal centers.[5] Judicious choice of ancillary ligands has enabled synthesis of a large variety of manganese clusters.[5-6] Some of these complexes have provided valuable spectroscopic models for the OEC as well as insight into the reactivity of high oxidation state manganese species, including water oxidation.[7] The synthesis of an accurate model of the full active site cluster has been elusive, however. Many di-, tri-, and tetranuclear clusters of manganese with bridging oxides have been reported,[6c] but

incorporation of a calcium center is much less common.[8] Some reported Ca-Mn clusters, although they incorporate a cuboidal arrangement, are of much higher nuclearity than the OEC.[8a, 9] Thus, fundamental studies on the role of calcium have been hindered by a lack of well-defined, small molecule models.

In this chapter the synthetic strategies to 1) access a Mn_3CaO_4 heterometallic cubane on the $\mathbf{L}^{3-}$ framework and 2) desymmetrize said cubane to more accurately model the OEC will be discussed alongside electrochemical and spectroscopic findings. The "retrosynthetic analysis" we devised for the OEC is shown in Scheme 4.1. Starting from the preorganized Mn^{II}_3 complex **1** introduced in Chapter 2, site-differentiated functionalization is targeted as in Chapter 3, except using Ca^{2+} as the unique metal rather than a fourth Mn to afford a Mn_3CaO_4 system. From there, selective incorporation of a fifth metal to a single face of the cubane is performed by desymmetrization of the cubane followed by addition of metal equivalents. Data are included that support successful syntheses of complexes containing the Mn_3CaO_4 + dangling transition metal structure; thus the following compounds are the most accurate synthetic models of the OEC to date.

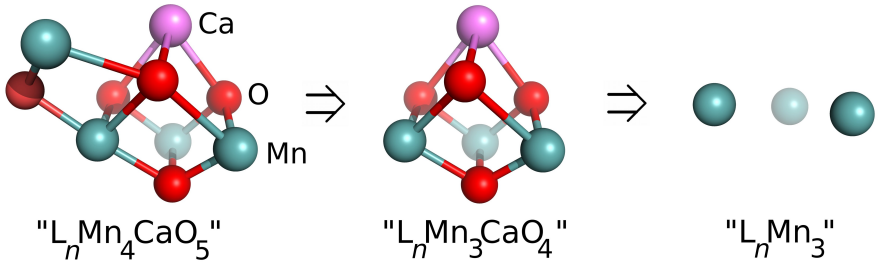

Scheme 4.1 Retrosynthetic analysis for the OEC Mn_4CaO_5 geometry.

RESULTS & DISCUSSION

*4.1 Initial and Optimized Synthesis of $LMn^{IV}_3CaO_4(OAc)_3$ (**8**)*

Targeting a heterotetranuclear complex containing calcium and manganese, we treated **1** with two equivalents of potassium superoxide as a source of both oxygen atoms and oxidizing equivalents in the presence of $Ca(OTf)_2$ (Figure 4.1, OTf = trifluoromethanesulfonate). Although **1** is insoluble in tetrahydrofuran (THF), addition

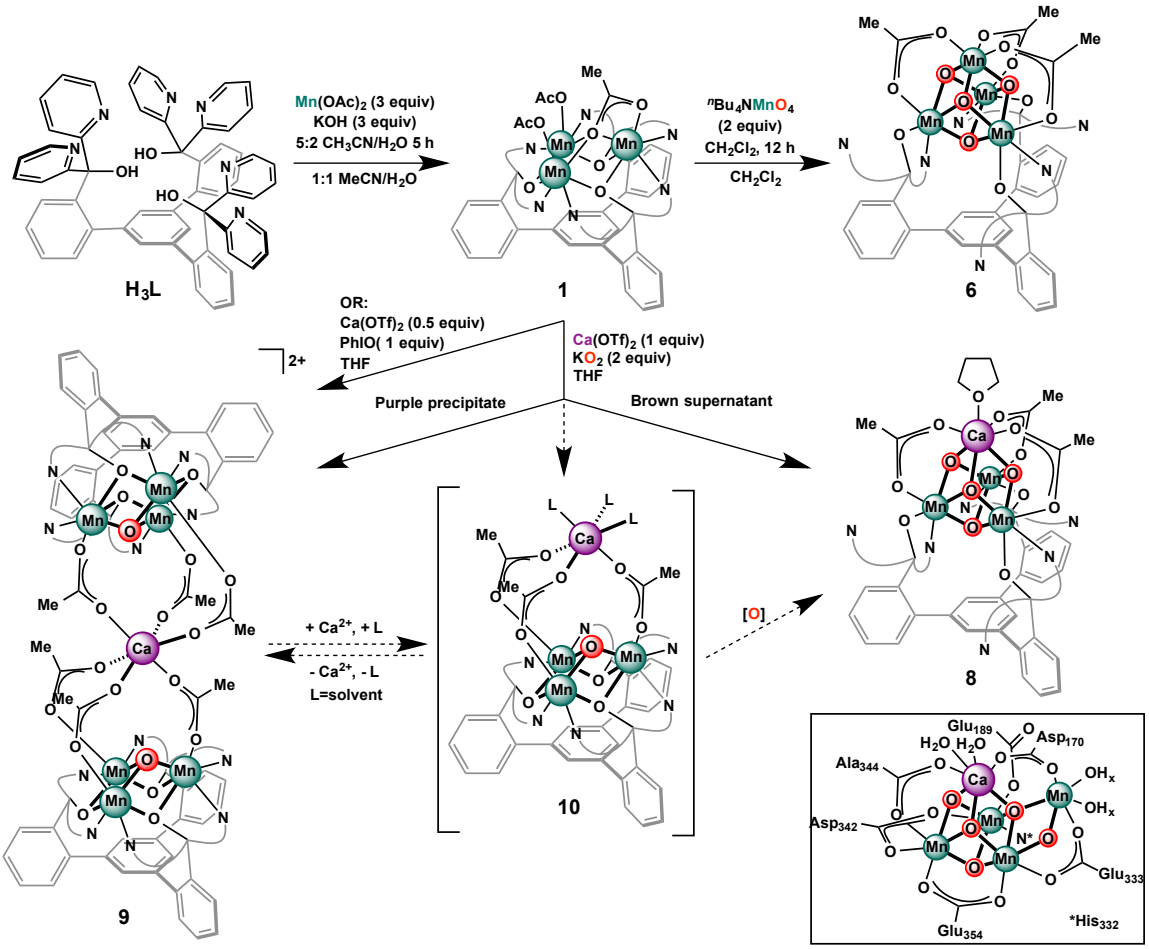

Scheme 4.1 Initial Synthesis of **1**, **6**, **8**, and **9** from **1-H$_3$** and proposed formation of an intermediate **6**. Curves schematically represent 2-pyridyl groups. A recent structure of the OEC from crystallographic studies is shown in the box.[2g]

of $Ca(OTf)_2$ leads to partial dissolution of the suspended material, suggesting the formation of a more soluble Ca-Mn intermediate. Reaction with superoxide over 24 to 48 hours leads to the formation of a brown, heterogeneous mixture with purple precipitate. Filtration affords a purple solid **9**—characterized by single crystal X-ray diffraction (XRD) as a calcium-hexamanganese cluster in which two monooxygenated Mn_3 cores are linked to Ca^{2+} via acetate bridges (Figure 4.10)—and a brown supernatant. Vapor diffusion of hexane into the THF supernatant afforded red-brown crystals of compound **8**, which was also characterized by XRD.

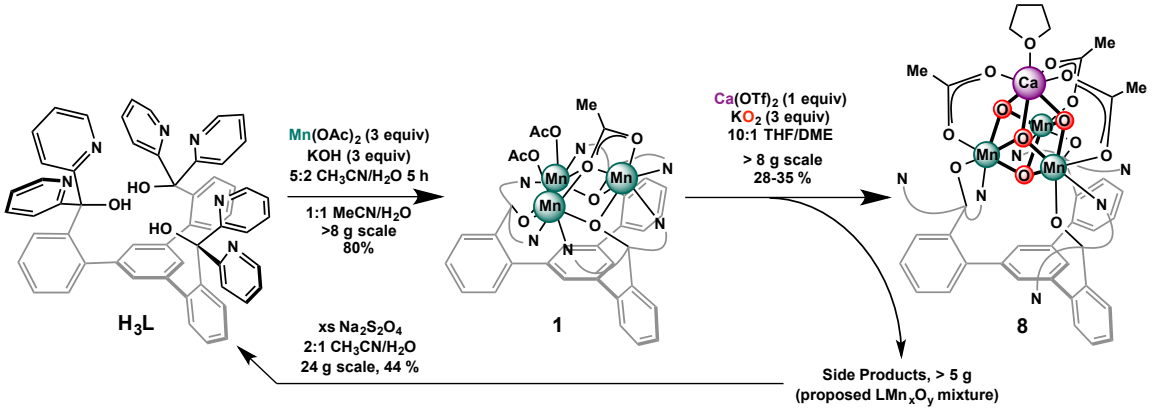

Scheme 4.2 Optimized synthesis of $LMn_3CaO_4(OAc)_3$•THF (**8**)

Although reproducible, the initially discovered procedure to synthesize **8** was quite low yielding (8-10%). This is consistent with the transformation of **1** into any cubane complex, as both the conversion of **1** to **5** and **1** to **6** were both low yielding as well (40% and 30%, respectively). Extensive reorganization within the cluster must occur, with multiple Mn–N and Mn–O bonds being broken and formed (See Ch. 3, Sect. 3.9). We believe—based on similar patterns in the ^{1}H NMR spectra—that the side products are LMn_4O_1 and LMn_4O_2 clusters similar to **2**-**4** in Chapter 3 formed from

incompletely reorganized intermediates. Nevertheless, variation of solvent, scale, reaction time, and equivalents of KO_2 have led to a procedure with a more palatable 28-35% yield (Scheme 4.2). Moreover, the side LMn_xO_y side products could be recycled in moderate yield back to free **H_3L** by reducing off the Mn centers with $Na_2S_2O_4$.

*4.2 Structural Comparison of the Mn_3CaO_4 Complex **8** and the OEC*

Compound **8** displays the desired $[Mn_3CaO_4]^{6+}$ core (FIgure 4.1A, B). The three manganese centers are supported by framework **1**, with each manganese binding to one alkoxide and one pyridyl group. Three pyridyl groups from **1** remain unbound. The manganese centers are pseudo-octahedral. The calcium center is supported by three oxide ligands and three acetates that bridge across different faces of the cube. The calcium coordination sphere is completed by a THF molecule, consistent with a large heptacoordinate calcium center. Modeling all four metal sites as manganese centers does not fit the XRD data and the Ca–O distances are all significantly longer than would be expected for Mn–O bonds (Table 4.2). Analysis of the Mn–oxo distances in **8** reveals short average bond lengths of 1.83, 1.87, and 1.87 Å, consistent with three Mn^{IV} centers. In agreement with this oxidation state assignment, the standard deviation of the Mn-oxo bond lengths is small, as expected for a d^3 electronic configuration.

The discrete $[Mn_3CaO_4]$ core matches the proposed structure of PSII without the dangler manganese. The Mn–Mn distances and Mn–Ca distances of **8** parallel those found in extended X-ray absorption fine structure (EXAFS) and crystallographic studies of PSII.[2e-g, 10] The average Mn–Mn distance in **8** is 2.834 Å and the average Mn–Ca distance is 3.231 Å. A recent crystallographic study gave Mn–Mn distances of 2.8, 2.9,

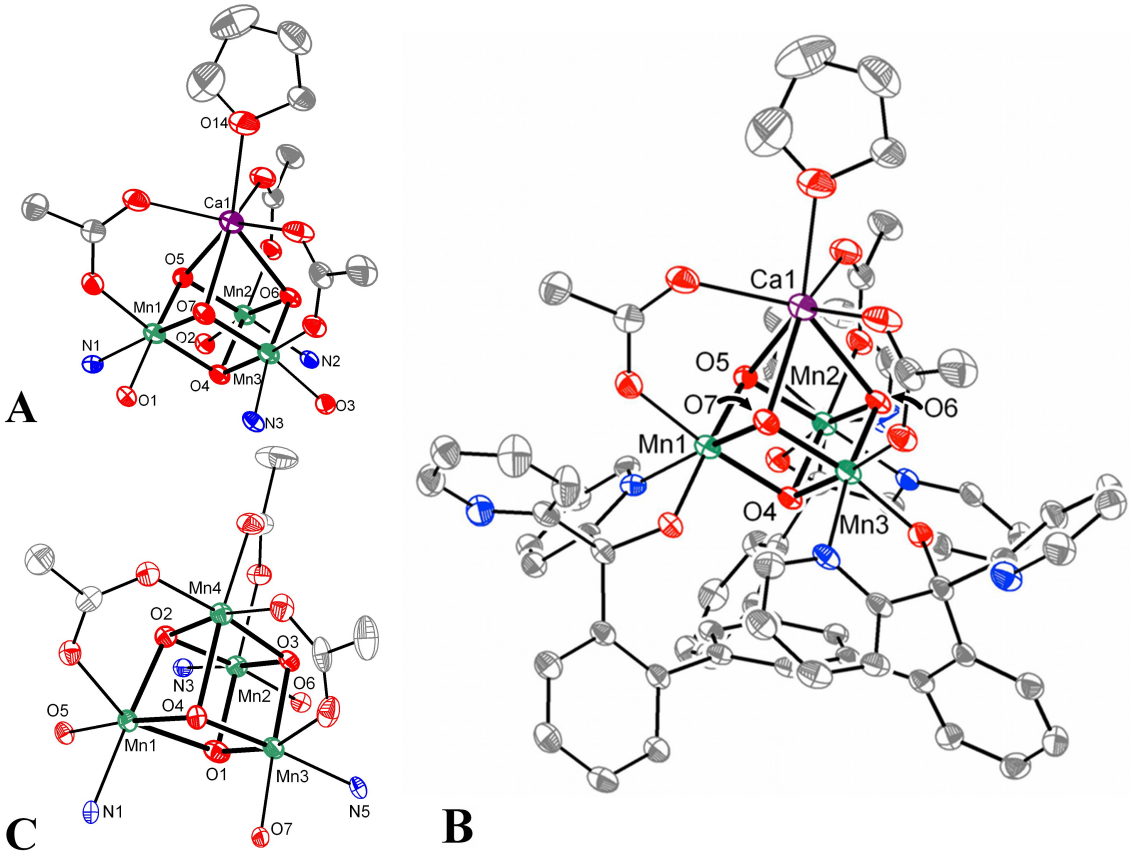

Figure 4.1 Solid-state structures of (**A**) truncated Mn_3CaO_4 cubane in **8**, (**B**) full structure of **8**, and (**C**) truncated Mn_4O_4 cubane in **6**. Thermal ellipsoids are drawn at 50% probability. Hydrogen atoms and solvent molecules are not shown for clarity. Metal–oxo average distance (Å) and the corresponding standard deviation (in parenthesis) for each specific metal center in **6** and **8** are as follows. **6**: Mn1 2.036 (0.187); Mn2 1.864 (0.016); Mn3 1.926 (0.074); Mn4 2.012 (0.165). **8**: Mn1 1.873 (0.038); Mn2 1.872 (0.048); Mn3 1.869 (0.043); Ca1 2.417 (0.023). See Table 4.2 for a complete list of metal-oxo and M–M distances.

and 3.3 Å and Mn–Ca distances of 3.3, 3.4, and 3.5 Å within the cubane subsite.[2g] The corresponding EXAFS-derived distances in PSII are 2.7 to 3.2 Å and 3.3 to 3.4 Å in the S_1-state.[2e, f, 10-11] The shorter Mn–Ca distance observed in **8** may be a consequence of bridging constraints caused by three acetate bridges, whereas in proposed structures of

the OEC the Ca^{2+} has more open coordination.[2g] There has been debate over the oxidation states of the manganese centers in the OEC.[1, 12]. The three Mn centers of the cubane subsite have been proposed to be in the +IV oxidation state in the S_2, S_3, and S_4-states.[12] The three manganese centers in **8** are all in the oxidation state +IV (vide supra), supporting $[Mn^{IV}_3CaO_4]$ as a feasible structure in the latter stages of the S-state cycle. The isolation of **8** in the solid-state at room temperature suggests that the heteronuclear cubane motif is stable and does not require a fully encapsulating ligand like that provided by the protein environment.

Our collaborators have used multiple spectroscopic techniques—XAS, XES, RIXS, and EPR—to analyze complex **8** and to compare to the wealth of spectroscopic data on the OEC. However, the data on complex **8** are yet to be finalized and are thus not included herein.

*4.3 Electrochemistry of **6** and **8***

Comparison to the related Mn_4O_4 cubane (**6**, introduced in Chapter 3), with a core analogous to **8**, could give insight into the distinct properties calcium elicits from a multinuclear manganese cluster. Complexes **6** and **8** were investigated by cyclic voltammetry in dimethylacetamide (DMA) and dimethylformamide (DMF) with 0.1M $^{n}Bu_4NPF_6$ electrolyte. Complex **8** displays a quasireversible reduction at -940 mV versus ferrocene/ferrocenium (Fc/Fc^+) in DMA (-890 mV v. Fc/Fc^+ in DMF) assigned to the $[Mn^{IV}_2\ Mn^{III}CaO_4]$ / $[Mn^{IV}_3CaO_4]$ couple (Figure 4.2). Complex **6** shows a quasireversible oxidation at +380 mV versus Fc/Fc^+ assigned to the $[Mn^{IV}_2\ Mn^{III}_2O_4]$ / $[Mn^{IV}_3Mn^{III}O_4]$ couple and a quasireversible reduction at -600 mV in DMA assigned to

the $[Mn^{IV}Mn^{III}_3O_4]$ / $[Mn^{IV}_2Mn^{III}_2O_4]$ couple (Figure 4.2). The calcium-containing $Mn^{IV}_3CaO_4$ cubane reduces at potentials more than 1 V more negative compared to the all-manganese $Mn^{IV}_3Mn^{III}O_4$ cluster. These data suggest that the presence of a non-redox active calcium center instead of manganese facilitates the formation of a species containing more highly oxidized manganese centers at lower potentials.

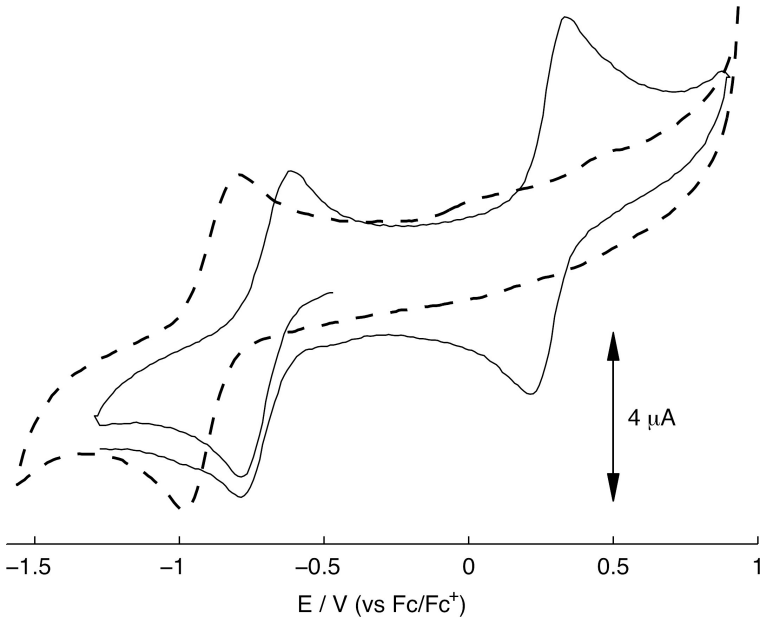

Figure 4.2 Cyclic voltammograms of **6** (—, DMA solution) and **8** (- -, DMF solution) with 0.1 M ^{n}Bu$_4$NPF$_6$. Scan rates: 50 mV/s (3) and 100 mV/s (4).

In an unoptimized procedure, complex **8** could be reduced chemically by cobaltocene in CH_2Cl_2 (Scheme 4.3). Complex **8**$^-$ was targeted, as mixed $Mn^{III/IV}$ clusters are pertinent to the lower oxidation state S states of the Kok cycle. Crystallization in dimethylacetamide (DMA)/Et_2O afforded crystals amenable to XRD. The complex is similar to **8**, but a $[CoCp_2]^+$ counterion is located nearby in the lattice. Furthermore, a localized Mn^{III} is clearly visible by the elongated axis expected in a d^4, *pseudo*-octahedral metal: Mn1–O1 at 2.168(8) Å *vs.* Mn1–O3 at 1.865(6) Å and Mn1–O4 at 1.887(5) Å.

Further study of $\mathbf{8}^{-}$ has been hampered by its seeming instability and lack of ^{1}H NMR signal.

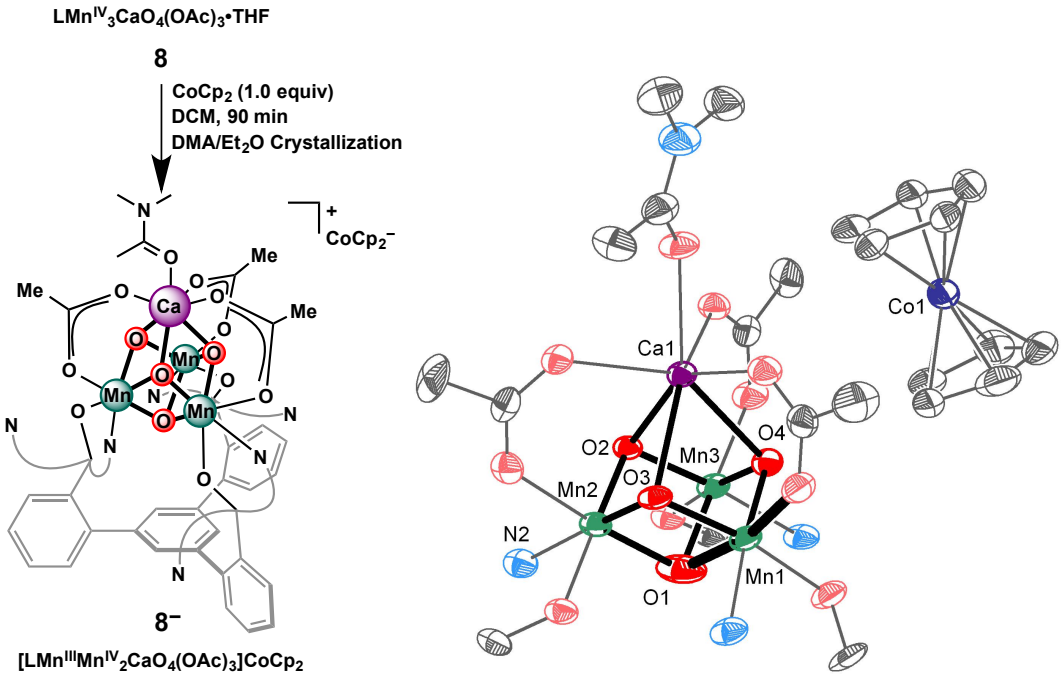

Scheme 4.3 Synthesis (left) and solid-state structure (right) of $[LMn^{III}Mn^{IV}_2CaO_4(OAc)_3]CoCp_2$ ($\mathbf{8}^{-}$). The elongated axis is emphasized, and hydrogen atoms and solvent molecules are not shown for clarity. Thermal ellipsoids are drawn at 50% probability. This dataset is not fully refined.

4.4 The Charge Localization Effect of Ca^{2+}

Recent studies of iron-oxo species interacting with Ca^{2+} and Sc^{3+} have suggested that the redox inactive metal plays a role in facilitating reduction chemistry at iron.[13] The present study suggests a complementary role of Ca^{2+}. The overall charges of the cubanes in **6** and **8** are the same: $[Mn_4O_4]^{6+}$ vs $[Mn_3CaO_4]^{6+}$. The redox inactive Ca^{2+} allows the buildup of localized positive charge, resulting in the higher oxidation state +IV at the three manganese centers in cluster **8**. When four redox active metal centers

are present in the same unit in **6**, the higher oxidation state is partially quenched by the formation of two Mn^{III} centers by the formal comproportionation of one Mn^{II} and one Mn^{IV}. This intriguing difference suggests calcium may be involved in the modulation of the reduction potentials of the manganese centers in the OEC, localizing the charge and thus facilitating access to the higher oxidation states necessary for efficient O_2 production. This notion is supported by our electrochemical data showing that the calcium-containing cluster accesses the state with three Mn^{IV} centers at a significantly more negative potential compared to the all-manganese cubane. The charge-localization effect described above has been observed in high-oxidation state nickel oxides: ternary $BaNi^{IV}O_3$ is stable whereas simple binary Ni^{IV} oxides are unstable and generally contain Ni^{III}.[14] More recently, a heterogeneous cobalt-oxide catalyst for water oxidation has been proposed to contain alkaline metals (albeit not detected by XAS)[15] as part of Co_3O_4 cubane moieties.[16] The alkaline metal in this species could facilitate access to high oxidation state cobalt species as described above. Furthermore, studies of manganese-oxide vs manganese-calcium-oxide electrocatalysts for O_2 generation from water revealed that the mixed oxide is a faster catalyst, although the exact role of calcium remained unclear.[17]

4.5 Proposed Formation Intermediates and Relation to Photoactivation of the OEC

Isolation of compound **9** in the transformation of **1** to **8** offers insight into a potential mechanism of heterometallic cubane formation. Calcium could associate to the trimanganese core via acetate bridges, explaining the mutual dissolution upon mixing in THF and opening coordination sites on the manganese centers for reaction with the

oxygenation agent. Transfer of the first oxygen atom equivalent could afford proposed species **10**, which in turn could disproportionate to generate **9** and free Ca^{2+} (Scheme 4.1). Complexes **9** and **10** contain mixed-valence Mn^{II}-Mn^{III} sites that are located an appropriate distance from calcium for the formation of a cubane upon further reaction with oxygen-atom equivalents. This mechanism is similar to proposals based on biochemical studies for the assembly of the OEC.[18] Mn^{2+} and Ca^{2+} are required for the biosynthesis of a functional cluster in PSII. These labile precursors are proposed to assemble in a geometry that allows for gradual hydration and photooxidation to the final cluster. In the absence of Ca^{2+}, excessive incorporation of manganese was reported, presumably due to uncontrolled oligomerization of manganese oxide species; [18-19] recovery of activity can be achieved, however, by subsequent addition of Ca^{2+}.[20] Without Ca^{2+} the assembled manganese-oxide cluster is less prone to oxidation beyond the S_2 state, further supporting a role for the redox inactive metal in facilitating access to the higher oxidation-state cluster.[20]

4.6 Design Elements for Functionalizing Mn_3CaO_4 Toward a Full OEC Model

The Mn_3CaO_4 cubane subsite of the OEC has been accurately modeled, as shown herein and by Christou and coworkers.[21] Based on EPR and magnetism measurements, Christou and coworkers posit that asymmetry, or distortion, in the Mn_3CaO_4 unit—manifested in their case by coordination of a cubane oxo to a second Ca^{2+}—affects its electronic structure and thus its chemical reactivity.[21] Low symmetry, heterometallic Mn_3MO_4 cubane complexes are thus desirable synthetic targets for

further electronic structure studies and as synthetic precursors to full Mn_4CaO_n models of the OEC.

However, the 1,3,5-triphenylbenzene-based ligand scaffold **H_3L** results in Mn_3MO_4 cubanes that have high, *pseudo-C_3* symmetry and an apical metal M labile to substitution by more Lewis acidic metals.[22] For example, Mn_3CaO_4 cubane complex **8** reacts quantitatively with $Mn^{II}(OTf)_2$•$2CH_3CN$ to yield the reported Mn_4O_4 cubane complex **6** and $Ca^{II}(OTf)_2$ rapidly upon mixing (Scheme 4.4). Simply appending a fourth Mn to **8** to achieve an accurate OEC model is therefore unlikely. In order to synthesize distorted Mn_3MO_4 and, more importantly, pentametallic $Mn_3MM'O_4$ complexes in the desired cubane + dangling M′ geometry, the high symmetry of our cubane complexes must be broken and the apical metal must be stabilized to substitution.

We posited that substitution of the solvent molecules and acetates on the "top" of the complex with a multidentante ligand could 1) stabilize the top metal to substitution by a fifth metal equivalent, 2) distort the cubane, and 3) change the reactivity of the cubane unit to allow incorporation of a fifth metal (Scheme 4.4). The acetates of the Mn_3MO_4 cubanes are known to be substitutionally labile, as scrambling experiments with acetate-*d_3* mentioned in Chapter 5 show.[23] Therefore, ligands were chosen that coordinated not only to M but also to at least one Mn^{IV} of the cubane through substitution of at least one of the acetates, stabilizing the ligand to dissociation in solution by the chelate effect. This synthetic sequence is modular at the anionic/neutral donors of the capping ligand, the length of the bridge, the number of donors, and the source of the fourth Mn equivalent.

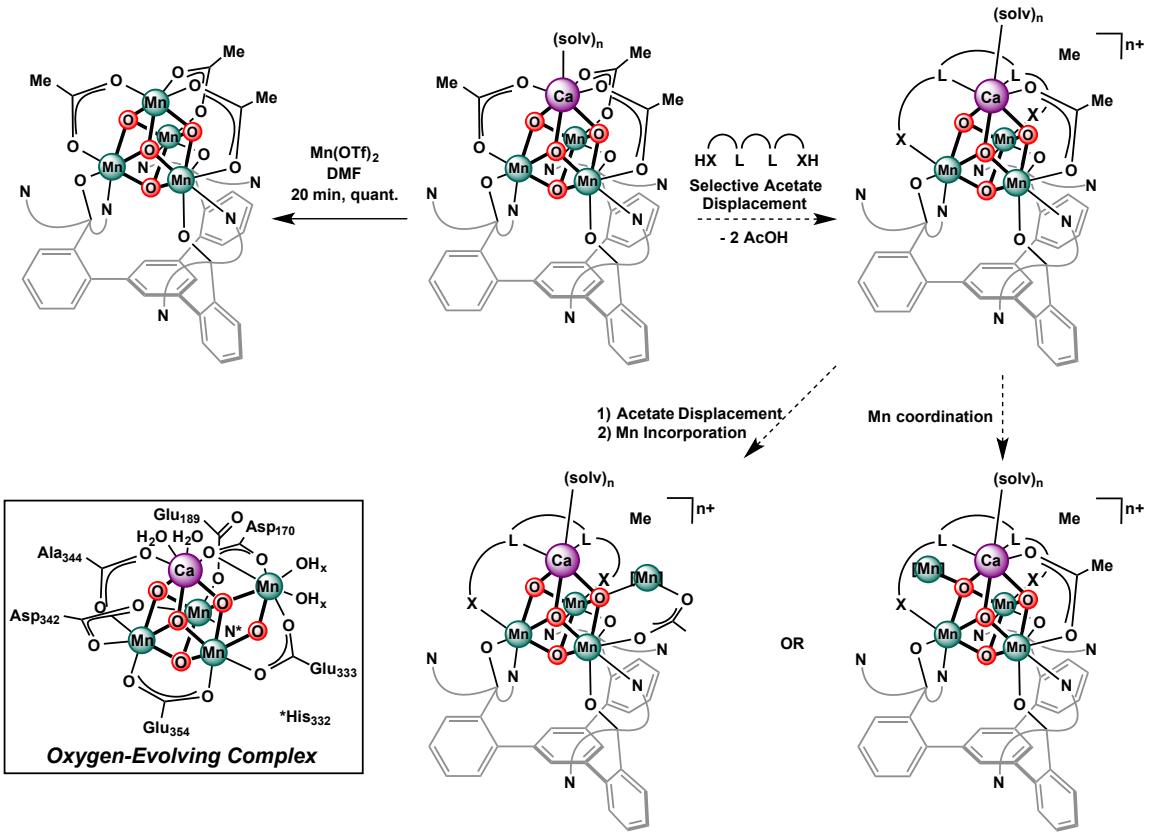

Scheme 4.4 Synthetic strategies to stabilize the top metal to substitution and desymmetrize the cubane to access Mn_3CaMO_n models of the OEC, shown in the box.

4.7 Synthesis of Asymmetric Mn_3CaO_4 Complexes

Others in the group have shown that oximates could bridge the $MnMO_2$ face of a cubane, so the initial ligands used contained two oximates bridged by variable L donors. The initial ligand tried was *N*-*n*-Propyl-*N,N*-bis(1-propan-2-onyl oxime)-amine (**PRABOH$_2$**),[24] which we initially believed could substitute two acetates, with the three nitrogens coordinated to the Ca^{2+} with two favorable five-membered chelate rings. The high-symmetry cubane complex **8** does successfully react with **PRABOH$_2$**, becoming substantially more soluble and giving distinct ^{1}H NMR and ESI spectra consistent with

PRABOH$_2$ binding (ESI) and affording lower symmetry (^{1}H NMR). However, a low quality crystal structure showed that the single N-donor bridge was too short, and instead the singly deprotonated oximate/oxime complex **11** was formed (Scheme 4.5). With one oximate bridged across a face of the cubane, only the N of the second oxime can bind to the Ca^{2+}, leaving the oxime O protonated directly over, and H-bonding to, one of the remaining acetates. **11** is the first low-symmetry Mn_3CaO_4 cubane synthesized

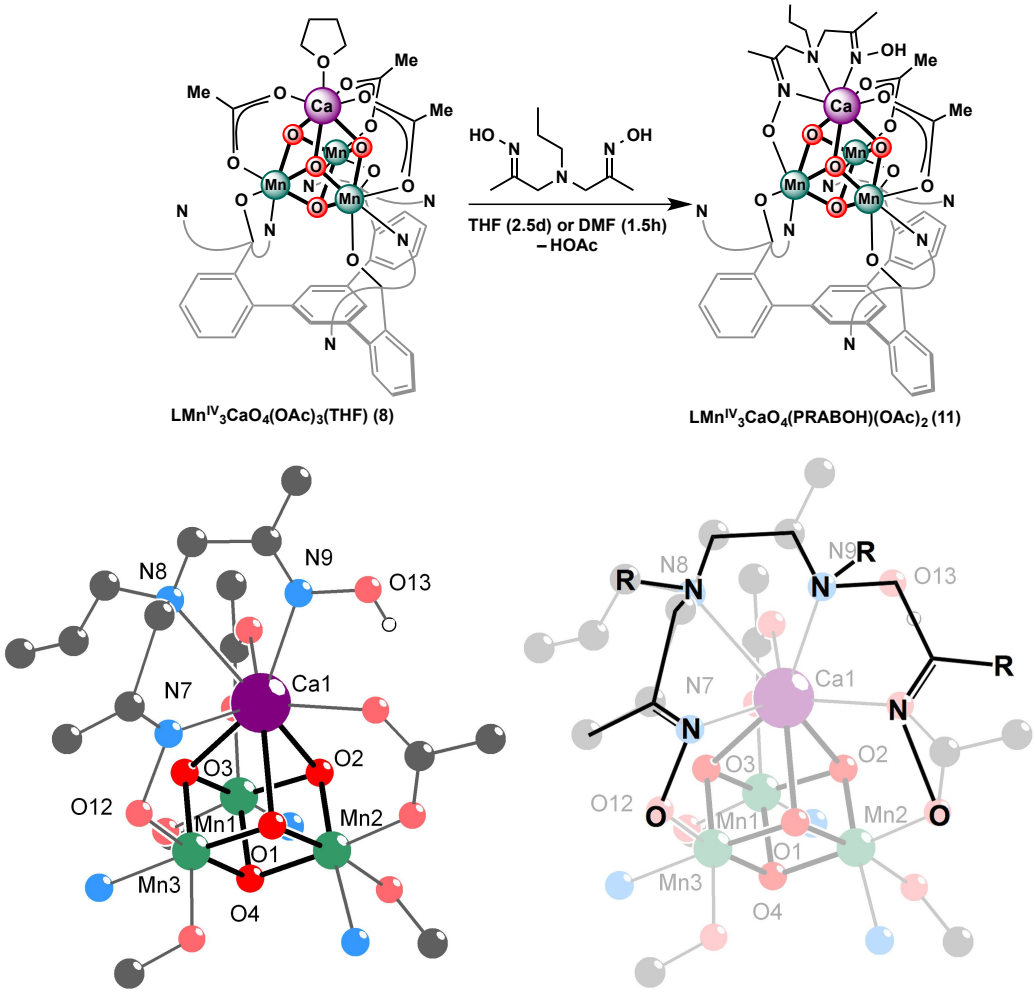

Scheme 4.5 Synthesis of low symmetry Mn_3CaO_4 cubane complex **11** (top), Ball-and-stick solid-state structure of **11** with hydrogens and disorded solvent not shown for clarity (bottom left), and the ligand design changes implemented (bottom right). The refinement shown is not complete.

on the triarylbenzene framework, and although the structure was not as hypothesized, the successful coordination of **PRABOH$_2$** acted as a proof-of-principle that capping ligands can displace acetate without chelating and removing the Ca^{2+} center and/or decomposing the cubane.

The structure of **11** also revealed the next step forward: extension of the bridge to include an ethylenediamine unit to give four nitrogens bound to Ca in a series of three five-membered chelate rings (Scheme 4.5, bottom right). Somewhat surprisingly, a simple ethylenediamine bisoxime molecule had not been synthesized in the literature, although Ioffe and coworkers had synthesized very similar chelate molecules through the reaction of nitrogen nucleophiles with *N,N*-bis(siloxy)enamine electrophiles.[25] Using their method, *N,N′*-dimethyl-*N,N′*-bis(propanone-oxime)-ethylenediamine (**HON$_4$OH**) could be synthesized on gram scale (Scheme 4.6).

Modification of the coordination sphere was achieved with **HON$_4$OH**: addition of HON$_4$OH to **8** in DMF followed by heating to 80 ºC precipitates complex **14** after a short time. Complex **14**'s low solubility has precluded structural determination, but the ^{1}H NMR spectra of **14** shows an increase in the number of peaks relative to **8** and the ESI-MS masses support bound **ON$_4$O** and loss of two acetates, both consistent with the low symmetry hypothesized. The analogous Mn_3GdO_4 complex **13** could be synthesized from the parent, high symmetry complex **12** (work done by Dr. Po-heng Lin), and shows the parallel ESI-MS signal for two lost acetates and bound **ON$_4$O**. Unlike **14**, **13** crystallized well and does display the hypothesized coordination mode, suggesting that **14** may also have the desired structure. The dioxime substitutes two of the acetates, giving two oximate bridged $MnGdO_2$ faces, four N-donors to Gd, and an

open 9th coordination site on Gd filled by a DMF in the solid state (Figure 4.2). The coordination sphere of the Gd engendered by ON_4O is reminiscent of a crown ether, with multiple five-membered rings. The coordination of ON_4O creates a low symmetry cubane core, with a unique μ_3-oxo opposite the remaining acetate (O3, Figure 4.2).

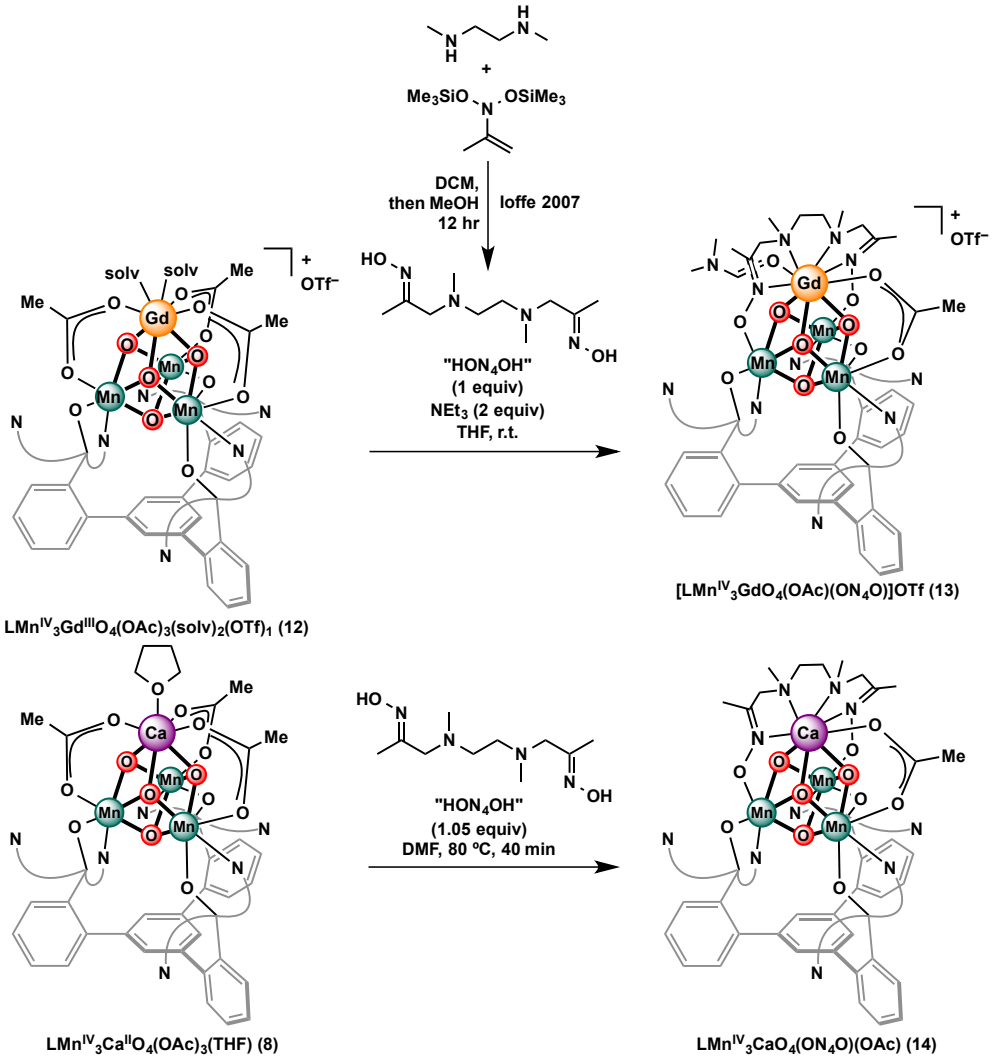

Scheme 4.6 Synthesis of asymmetric Mn_3GdO_4 and Mn_3CaO_4 cubane complexes. Work on the Gd system was performed by Dr. Po-Heng Lin.

Reactivity studies on complex **14** give more evidence that **14** is indeed the proposed $LMn_3CaO_4(ON_4O)(OAc)$ structure. Addition of an acid, 2,6-lutidinium

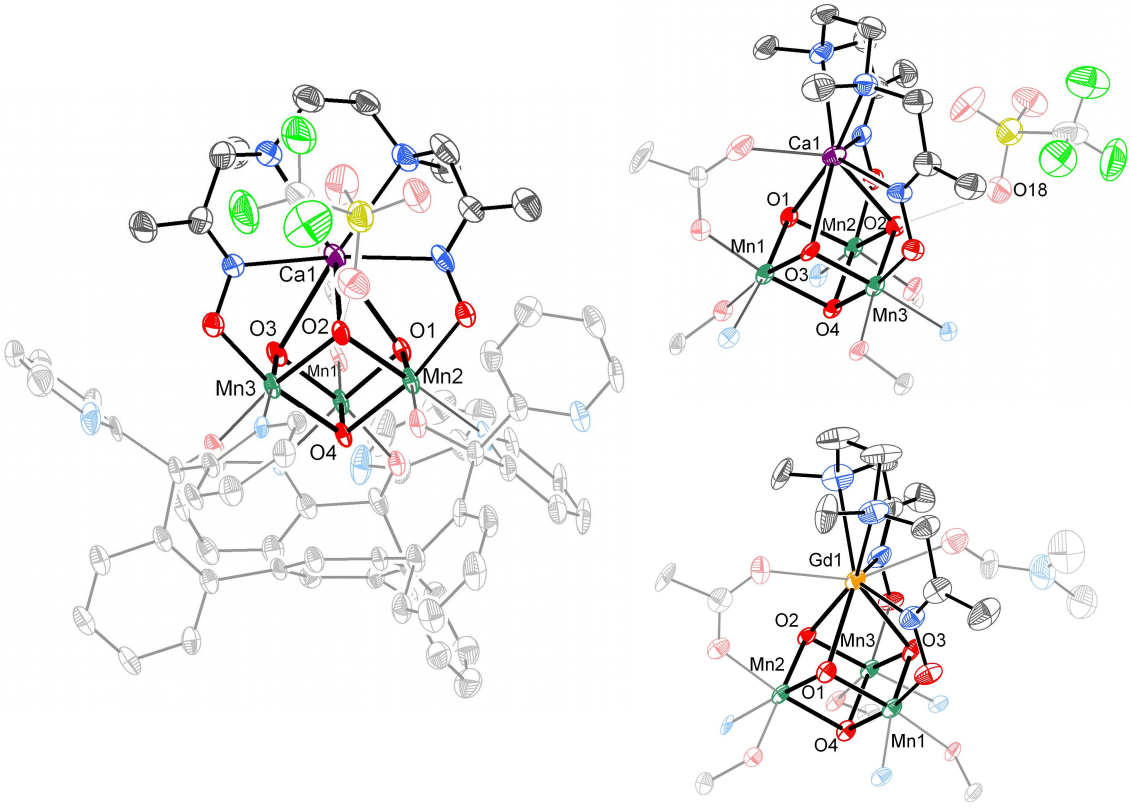

Figure 4.2 Solid-state structure of **15** (left), the primary coordination sphere of **15** rotated ca. 120° (top right), and the primary coordination **13** (bottom right) which was synthesized by Dr. Po-Heng Lin. Hydrogen atoms and solvent molecules are not shown for clarity. Thermal ellipsoids are drawn at 50% probability.

trifluoromethanesulfonate (LutHOTf) gives new paramagnetic signals and disappearance of the acidic proton of LutH at 15 ppm in the ^{1}H NMR spectrum, a similar mass to **14** by ESI, and increased solubility. Crystallization revealed the structure of complex **15**: ON_4O has substituted two acetates as proposed for **14**, the Ca^{2+} is 8-coordinate, and most notably the unique μ_3-oxo of the cubane opposite the acetate is protonated as demonstrated by the hydrogen-bonding triflate counterion (O18–O2: ca. 2.65 Å) (Scheme 4.7; Figure 4.2). This μ_3-oxo basicity is not present in the symmetric parent complex **1**, which does not react with LutHOTf in DCM. Shifting to a weaker

acid, Et_3NHOTf (pKa = 18.8 in CH_3CN *vs.* 14.3 for LutHOTf in CH_3CN), showed no reactivity with **14** in DCM. The addition of further equivalents of LutHOTf did cause further change in the ^1H NMR spectra, consistent with further protonation.

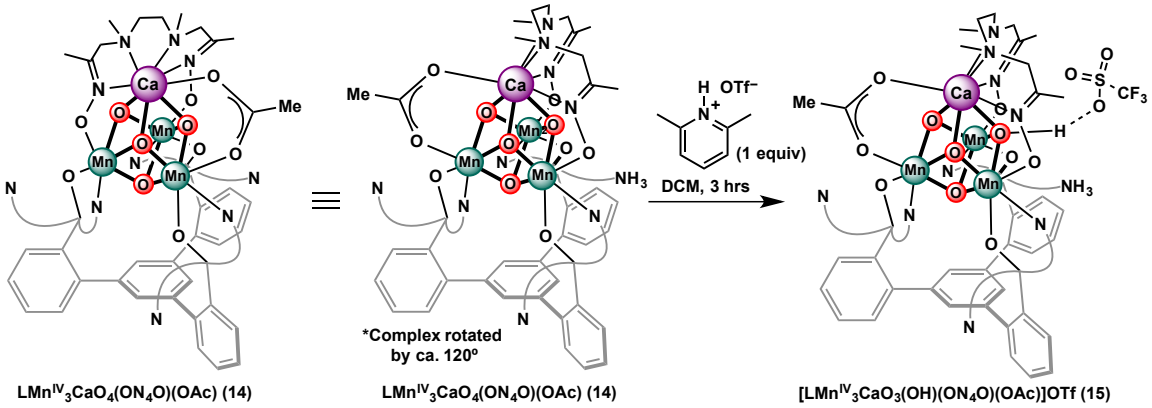

Scheme 4.7 Synthesis of protonated, low symmetry Mn_3CaO_4 complex **15**.

The first compelling evidence for the formation of a Mn_3CaO_4 + dangling transition metal complex came from adding one equivalent of $ZnEt_2$ to **15**; we posited **15** could protonate off an ethyl, losing ethane to give a dangling ZnEt. The ESI

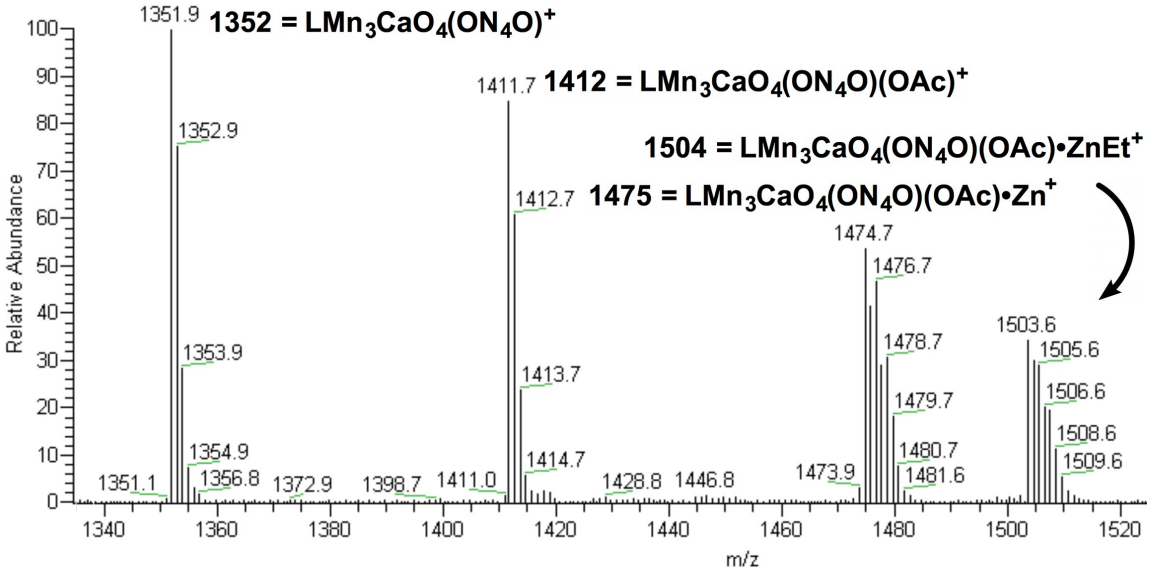

Figure 4.3 ESI mass spectrum of the reaction of $ZnEt_2$ with **15**.

spectrum strongly suggests Zn coordination to the Mn_3CaO_4 core, with peak position and isotope patterns accurate for Mn_3CaO_4Zn stoichiometries (Figure 4.3). However, also clear in the ESI spectrum are peaks for unprotonated cubane (namely **14**). One explanation is that the resulting Zn(Et)(OTf) is not bound tightly and dissociates.

With the Lewis basicity of the μ_3-oxo established by the protonation of **14** to give **15**, the addition of metal salts was attempted to see if the μ_3-oxo could act as a ligand to give a Mn_3CaO_4 + dangling metal geometry like the OEC. While a number of metal triflate salts led to changes in the ^{1}H NMR and ESI spectra upon addition to **14**, *none show substitution of* Ca^{2+}, suggesting that ON_4O stabilizes the Ca^{2+} to metal substitution as compared to **8** and thus fulfills all of our design criteria delineated above. Only AgOTf has reacted to give crystals suitable for X-ray analysis (Scheme 4.8). The quality of the dataset is quite low, and therefore only connectivity can be discussed. As shown in Figure 4.4, Ag^+ is coordinated to the μ_3-oxo of the cubane (now μ_4), one alkoxide from **L** (now bridging Mn2 and Ag), and one of the originally unbound pyridines of **L**. The fourth coordination site is filled by triflate. Ca^{2+} is in a very similar geometry as in **15**, and the overall low symmetry structure models that of the OEC well.

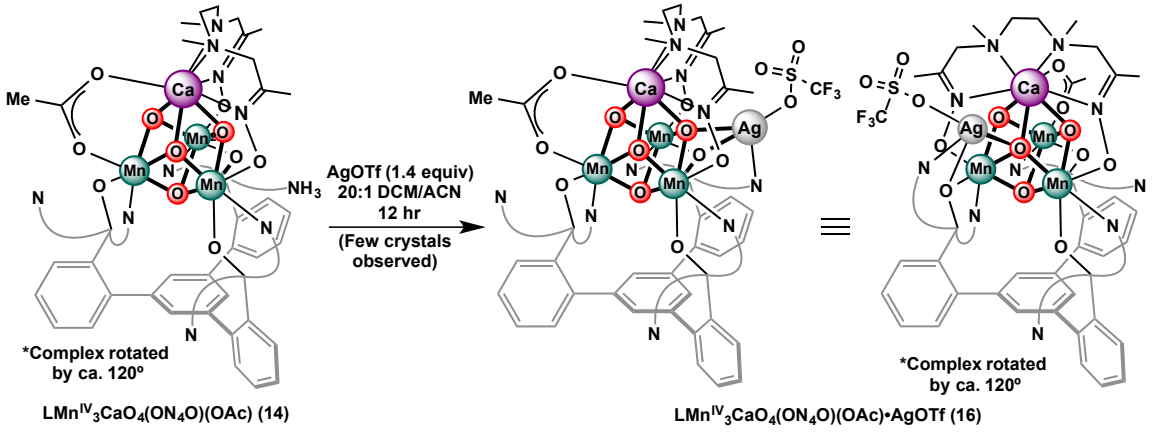

Scheme 4.8 Synthesis of the Mn_3CaO_4•Ag complex **16**.

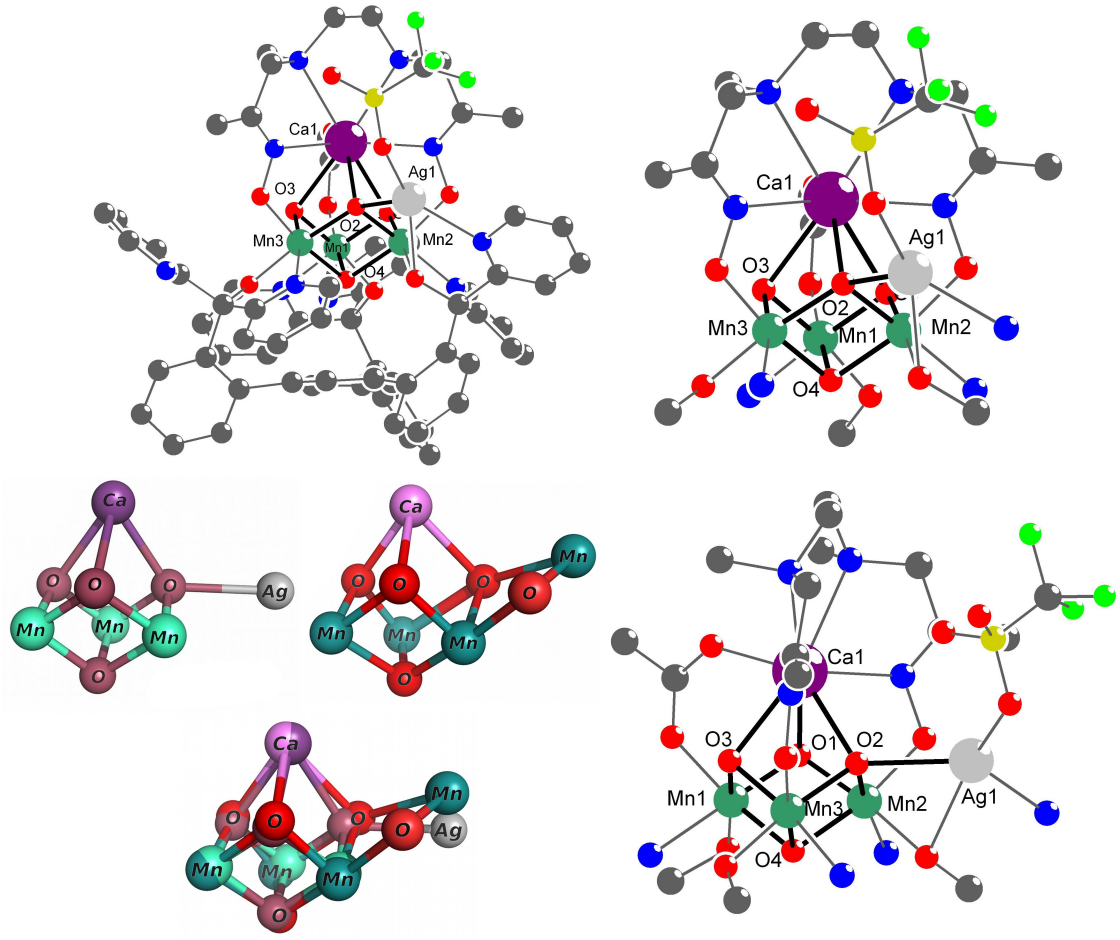

Figure 4.4 Clockwise from top left: Ball-and-stick representation of the solid-state structure of **16** (the dataset quality is low.). Hydrogen atoms and solvent molecules are not shown for clarity; primary coordination sphere in **16**, with clear view of **ON_4O** coordination; primary coordination sphere with clear view of Ag ligand sphere; Comparison of the Mn_3CaAgO_4 cluster of **16** to the OEC geometry found in the 1.9 Å resolution structure.[2g]

Although reactions with more relevant metals like cobalt and manganese did not provide crystals amenable to XRD, ESI data support the formation of Mn_3CaO_4•M (M = Mn, Co) complexes (Figure 4.5). Complex **14** was mixed with either $Mn(OTf)_2$ or

$Co(OTf)_2$ in DCM/CH_3CN mixtures, and ESI samples were removed and diluted. The masses are consistent with a fourth Mn bound to the cubane with variable ancillary ligands such as water (m/z = 1501), acetate (m/z = 1525), and triflate (m/z = 1615). With cobalt, the expected relative increase in mass by four units is observed, lending more credence to the Mn_3CaO_4•M stoichiometry proposed. Nevertheless, more work is needed to isolate and crystallize these complexes in order to do the detailed analysis desired for comparison to the OEC.

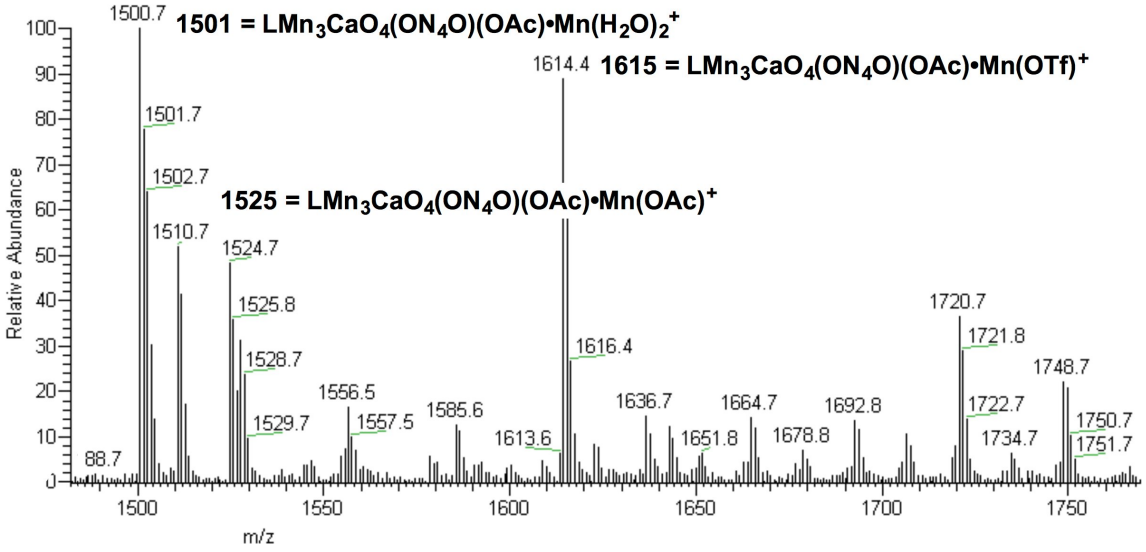

Figure 4.5 ESI spectrum from the mixture of **14** and $Mn(OTf)_2$. Each of the labeled peaks also have fragmentation patterns consistent with the proposed stoichiometries.

CONCLUSIONS

Our work establishes that the discrete [Mn_3CaO_4] core is synthetically accessible using a trinucleating ligand architecture and a bioinspired protocol. The structure of complex **8** parallels the Mn_3CaO_4 subsite of the OEC. Electrochemical comparison to Mn_4O_4 cubane **6** suggests that Ca^{2+} helps facilitate high oxidation state at Mn at a much lower potential than if a fourth Mn were present through localization of charge.

Coordination of a multidentate ligand to the cubane complexes has broken the high symmetry engendered by ligand scaffold **L**, yielding low symmetry $Mn^{IV}_3GdO_4$ and $Mn^{IV}_3CaO_4$ cubane complexes that are stable to apical metal substitution. The low symmetry distorts the cubane unit, producing a reactive μ_3-oxo that can be selectively protonated or metallated with a transition metal, namely Ag^+. The Mn_3CaAgO_4 complex structurally models the cubane + dangling M geometry of the OEC, and Mn_3CaO_4•M (M = Zn, Co, and Mn) stoichiometries are observed by ESI. Overall, the capping bisoximate ligand has engendered reactivity with the cubane towards coordinating a fifth metal. It just remains to optimize and isolate.

EXPERIMENTAL SECTION

Synthetic Procedures

General Considerations. Reactions performed under inert atmosphere were carried out in a glovebox under a nitrogen atmosphere. Anhydrous tetrahydrofuran (THF) was purchased from Aldrich in 18 L Pure-Pac™ containers. Anhydrous dichloromethane, diethyl ether, and THF were purified by sparging with nitrogen for 15 minutes and then passing under nitrogen pressure through a column of activated A2 alumina (Zapp's). Anhydrous DMA was purchased from Aldrich and stored over molecular sieves. NMR solvents were purchased from Cambridge Isotope Laboratories, Inc. CD_2Cl_2 was dried over calcium hydride, then degassed by three freeze-pump-thaw cycles and vacuum-transferred prior to use. ^{1}H NMR and ^{13}C NMR spectra were recorded on a Varian 300 MHz instrument, with shifts reported relative to the residual solvent peak. Elemental analyses were performed by Midwest Microlab, LLC, Indianapolis, IN or Robertson Microlit Laboratories, Ledgewood, NJ. Electrospray Ionization Mass Spectrometry was performed in the positive ion mode using an LCQ ion trap mass spectrometer (Thermo)

and High resolution mass spectrometry (HRMS) was performed at the California Institute of Technology Mass Spectrometry Facility.

Unless indicated otherwise, all commercial chemicals were used as received. 1,3,5-Tris(2-di(2'-pyridyl)hydroxymethylphenyl)benzene (**H_3L**) and $LMn_3(OAc)_3$ (**1**) were prepared as in Chapter 2. **PRABOH$_2$** was synthesized as published.[24] 2-[*N,N*-Bis(trimethylsilyloxy)]aminopropene was synthesized following a literature procedure.[26] In our hands, slow addition of the reaction mixture into the cold $NaHSO_4$ solution during work up was crucial in keeping the product from decomposing. *N,N'*-dimethylethylenediamine was distilled from KOH at atmospheric pressure, then distilled from Na^0. $Mn(OTf)_2$•CH_3CN was synthesized by literature procedures.[27] $[LMn^{IV}_3GdO_4(OAc)_3(DMF)_2]OTf$ (**3**) was synthesized as recently reported.(Lin 2014 submitted). Tetrabutylammonium permanganate[28] and iodosobenzene[29] were prepared according to literature procedures. **Caution!** Both these compounds are potentially explosive and should be used only in small quantities. The Gd cubanes **12** and **13** were synthesized by Dr. Po-Heng Lin.

Synthesis of $LMn_4O_4(OAc)_3$ (6). See Chapter 3.

Synthesis of $LMn_3CaO_4(OAc)_3$•THF (8). (JK_IV_110) $LMn_3(OAc)_3$ (10.89 g, 8.6 mmol) and $Ca(OTf)_2$ (3.05 g, 9.0 mmol, 1.05 equiv) were mixed as solids in a 2 L round bottom flask with a stir bar inside a glovebox. THF (ca. 830 mL) and DME (ca. 70 mL) were added and the solution was stirred for 15-20 minutes before well-powdered KO_2 (1.83 g, 25.7 mmol, 3 equiv) was added slowly over 5-10 minutes. THF (ca. 30 mL) and DME (ca. 16 mL) were added to rinse down any KO_2 on the walls and to bring the final concentration to 9 mM and a ratio of 10:1 THF/DME. The round bottom was sealed

with a 180º joint, taken out of the glovebox, and magnetically stirred. The solution changed colors from tan at 20 minutes, to brown at 45 minutes, grey-purple at 2 hours, and dark brown at 20 hours. At four days, red, crystalline precipitate can be seen, and by seven days the solution also has a reddish hue. On the eighth day, the pressure was reduced inside the flask to more safely bring it back into the glovebox, where the red crystalline precipitate was collected by filtration of the reaction mixture through a celite pad on a 150 mL frit. The solid was rinsed with 100-150 mL CH_3CN (until no color is visible in the CH_3CN). The remaining solid was scraped into a 500 mL round bottom flask, residual CH_3CN was removed *in vacuo*, and the solid was triturated in a mixture of THF (150 mL) and benzene (20 mL) for ca. 20 minutes. The resulting mixture was filtered through a pad of celite, giving a red solution and red solid, which was scraped back into the 500 mL flask and re-triturated in THF/C_6H_6 to extract more product. This process of trituration and filtration was repeated until little to no color was observed in the filtered solution (ca. 3 x 200 mL THF/C_6H_6). The remaining solid was triturated in DMF (ca. 80 mL) and filtered to give a red solution separate from the THF/C_6H_6 fraction. At this point three solutions exist: the THF/DME/CH_3CN solution from filtration of the reaction mixture, the THF/C_6H_6 fraction, and the DMF fraction. All were taken out of the glovebox and volatiles were removed by vacuum distillation. The red residue from the THF/C_6H_6 fraction is pure **8** (2.3 g, 20% yield), while the red residue from the DMF fraction (0.7 g, 6%) may contain some potassium salts. The residue from the THF/DME/CH_3CN fraction was brought back into the glovebox, triturated in CH_3CN, and collected on a pad of celite. The solid was rinsed with CH_3CN until no more color came through, and then proceeded with the THF/C_6H_6 trituration and filtration cycle performed above. The red solution was concentrated *in vacuo* to give more red powder **8** (1 g, 9%). Total yield is approximately

35%. ^{1}H NMR (300 MHz, C_6D_6 with a drop of THF for solubility, 25 ºC): 21.4, 11.3, 10.0, 8.6, 5.9, 5.1, -16.9 ppm. Anal. Calcd. for $C_{67}H_{55}CaMn_3N_6O_{14}$: C, 58.61; H, 4.04; N, 6.12. Found: C, 58.33; H, 3.90; N, 6.23. HRMS (TOF–MS): calcd. for $C_{67}H_{55}CaMn_3N_6O_{14}$: 1372.1543; found: 1375.0087. This discrepancy is consistent with probable gas-phase decomposition and protonation of the basic pyridyl and oxo sites.

Synthesis of $[LMn_3CaO_4(OAc)_3(DMA)]CoCp_2$ ($\mathbf{8^-}$): In the glovebox, cobaltocene (6.2m g, 0.03 mmol, 1 equiv) was dissolved in CH_2Cl_2 (1 mL). **8** (45 mg, 0.03 mmol) was partially dissolved in CH_2Cl_2 (3.5 mL), followed quickly (within 1 minute) by the solution of $CoCp_2$. The $CoCp_2$ vial was rinsed with CH_2Cl_2, bringing the total volume to 5 mL. The solution stays red/brown and homogeneous (unlike **8** in CH_2Cl_2, which will eventually precipitate). The solution was allowed to stir for 90 minutes, at which point it was filtered to remove any remaining **8**, and concentrated to dryness *in vacuo*. The resulting brown solid was washed with Et_2O and then extracted with C_6H_6 to give a red/brown solution that was filtered and concentrated to dryness. Vapor diffusion of Et_2O into a DMA solution of the resulting solid afforded scarce block crystals of $\mathbf{8^-}$. As this procedure is unoptimized and isolation on preparatory scale has been unfruitful, no characterization data has been collected. The most up-to-date refinement can be found on RecipricalNet (http://reciprocalnet.caltech.edu), code jsk64.

Synthesis of $[(LMn_3O(OAc)_3)_2Ca]_2(OTf)_2$ (9).

Method A: The DCM fraction isolated during the synthesis of **8** was concentrated in vacuo to a purple solid. Recrystallization from CH_2Cl_2/diethyl ether afforded the product as purple crystals

Method B: In the glovebox, a scintillation vial equipped with a stir bar was charged with a suspension of **2** (0.050 g, 0.042 mmol) in THF (3 mL). While stirring, $Ca(OTf)_2$ (0.007 g, 0.021 mmol) was added with the aid of THF (2 mL). Iodosobenzene (0.009 g, 0.042 mmol) was added as a solid to the stirring mixture, which darkened to purple-brown within minutes. After stirring for 15 min. at room temperature, the mixture was filtered over Celite. The purple solid was washed with THF, then extracted with CH_2Cl_2. The purple CH_2Cl_2 solution was concentrated in vacuo to afford a purple solid that was recrystallized from CH_2Cl_2/diethyl ether to afford the product as purple crystals that are identical by ^{1}H NMR spectroscopy to the product prepared using Method A (0.017 g, 29%). ^{1}H NMR (300 MHz, CD_2Cl_2, 25 °C): δ 54.58, 50.54, 36.41, 29.04, 12.90, 8.68, 4.39, –12.10, –13.81 ppm. All resonances are broad. Anal. Calcd. for $C_{128}H_{96}CaF_6Mn_6N_{12}O_{26}S_2$: C, 55.58; H, 3.50; N, 6.08. Found: C, 55.37; H, 3.65; N, 6.00. HRMS (TOF–MS): calcd. for $C_{126}H_{96}CaMn_6N_{12}O_{20}$ ($[LMn_3O(OAc)_3]_2Ca$): 1234.6440 $[MH]^{2+}$; found: 1234.6409.

***N,N′*-dimethyl-*N,N′*-bis(propanone-oxime)-ethylenediamine (HON_4OH)** (JK_IV_71)**:** Following the work of Ioffe *et al.*,[7] 2-[*N,N*-bis(trimethylsilyloxy)]aminopropene (75 wt% with pentane, 7.29 g, 23.42 mmol, 2.2 equiv) was added to an oven-dried 100 mL round bottom with a stirbar sealed with a septum under N_2 by syringe and needle. *N,N′*-dimethylethylenediamine (0.94 g, 10.6 mmol) was transferred to oven-dried 25 mL round bottom sealed with a septum under N_2 by syringe and needle. Both compounds were diluted with dry dichloromethane (23 mL & 10.6 mL, respectively, 1 M each). The diamine solution was then cannula transferred to the bis(trimethylsilyloxy)]aminopropene solution. Dichloromethane (3 mL) was used to rinse the 25 mL round bottom and cannula. The homogeneous yellow

solution was stirred at room temperature for 8 hours, at which point the reaction mixture was poured into MeOH (*ca.* 250 mL). This yellow solution sat unstirred for 6 hours, at which point volatiles were removed *in vacuo* to give an orange oil. Trituration in hexane caused the oil to solidify, and after decanting the hexane, trituration in Et_2O and decanting again, an orange powder produced. The orange powder was then triturated in CH_3CN, giving an orange solution and white powder that was collected on a medium frit. The powder was rinsed with CH_3CN until all color was lost from the powder, which was then dried *in vacuo* for 8 hours (1.7 g, 69.6%). To further dry, the powder was rinsed on a frit with dry CH_3CN in the glovebox and any remaining CH_3CN was removed *in vacuo* (1.6 g, 65.5%).^{1}H NMR (300 MHz, DMSO-d_6, 25 °C): δ 10.47 (s, 2H, NO*H*), 2.90 (s, 4H, N–CH_2–C=N) , 2.38 (s, 4H, N–CH_2–), 2.07 (s, 6H, H_3C–N), 1.72 (s, 6H, H_3C–C=NOH). ^{13}C{^{1}H} NMR (126 MHz, DMSO-d_6, 25 °C): δ 154.66 (*C*=NOH), 61.95 (N–CH_2–C=N), 55.11 (N–CH_2), 42.60 (H_3C–N), 12.57 (H_3C–C=NOH). HRMS (FAB+): calcd. for $C_{10}H_{23}N_4O_2$ [M+H]: 231.1821; found: 231.1826.

$LMn^{III}_2Mn^{IV}_2O_4(OAc)_3$ (6) from $LMn^{IV}_3CaO_4(OAc)_3$•THF (8): Complex **8** (6.8 mg, 5 μmol) was dissolved in DMF (*ca.* 1.5 mL) to give a red/brown, homogeneous solution. $Mn(OTf)_2$•CH_3CN (2.0 mg, 5 μmol) was separately dissolved in DMF (*ca.* 0.5 mL) to give a clear and colorless solution, which was then added to the solution of **8**. The solution turns from red/brown to brown within 30 seconds of addition. The solution was allowed to stir ca. 30 minutes, then volatiles were removed *in vacuo*. The resulting brown residue was extracted with benzene, which was filtered and concentrated to dryness to afford **6** (6.5 mg, *ca.* 100%). Spectral features match those found for **6** as synthesized in Chapter 3.

$LMn^{IV}_3CaO_4(PRABOH)(OAc)_2$ (11):

a) In THF (JK_IV_21): In a glovebox, partially dissolved $LMn^{IV}_3CaO_4(OAc)_3$•THF (27.3 mg, 0.02 mmol) in THF (ca. 7 mL) to give a brick-red suspension. **$PRABOH_2$** (4.2 mg, 0.021 mmol, 1.05 equiv.) was dissolved in THF (ca. 2 mL) and added to the reaction vessel, which was stirred for 2.5 days to afford a dark brown solution with brown precipitate. The volatiles were removed by vacuum to give a brown residue, which was then extracted with Et_2O. The resulting red/brown solution was filtered through Celite and concentrated to dryness (15 mg).

b) In DMF (JK_IV_35): In a glovebox, $LMn^{IV}_3CaO_4(OAc)_3$•THF (98.7 mg, 0.07 mmol) was dissolved in DMF (ca.13 mL) in an oven-dried Schlenk tube to give a brick-red solution. $PRABOH_2$ (15.2 mg, 0.07 mmol, 1.05 equiv.) was dissolved in DMF (ca. 2 mL) and added to the reaction vessel. There was no obvious color or solubility change. The Schlenk tube was removed from the glovebox and connected to the Schlenk line. The reation was stirred for 45 minutes, then concentrated to dryness *in vacuo* at 40 ºC over ca. 20 minutes. 5 mL of DMF was added and removed *in vacuo* to further remove acetic acid. Back in the glovebox, the resulting red/brown residue was then extracted with Et_2O and then C_6H_6. Both fractions were concentrated to dryness to give two samples of product (Et_2O: 23.3 mg, C_6H_6: 65 mg), with the Et_2O fraction containing a slight $PRABOH_2$ impurity. XRD quality crystals could be grown from vapor diffusion of Et_2O into a toluene solution of **2**. ^1H NMR (300 MHz, C_6D_6, 25 ºC): 63.1, 58.1, 33.0, 22.1, 19.4, 11.9, 11.1, 10.9, 10, -14.7, -15.5, -16.6, -17.7, -60.8, -71.1 ppm.

$LMn^{IV}_3CaO_4(ON_4O)(OAc)$ (14): (JK_IV_ 68&79) In a N_2 glovebox, an oven-dried Schlenk tube with stirbar was charged with **8** (301 mg, 0.22 mmol) and dry DMF (50 mL). **HON_4OH** (53 mg, 0.23 mmol, 1.05 equiv) was separately dissolved in dry DMF

(5 mL) and the resulting clear and colorless solution was added to the red/brown and clear solution of **8**. The Schlenk tube was sealed, brought out of the glovebox and heated to 80 ºC in an oil bath for 40 minutes during which precipitate appeared in the solution. The volatiles were removed *in vacuo*. Back inside the glovebox, the red/brown residue was suspended in dry CH_3CN and volatiles were removed *in vacuo* again to remove any remaining DMF. After further trituration with CH_3CN (15-20 mL), the solids were collected on Celite and rinsed with CH_3CN until it ran colorless. The solids, along with some Celite from the filtration, were triturated in CH_2Cl_2 to extract the product and filtered through Celite. Any undissolved solid was re-triturated until the CH_2Cl_2 runs colorless (*ca.* 3 cycles or 10-30 mL). Removed volatiles *in vacuo* to afford red/brown **14** as a powder (130 mg, 42%). ^{1}H NMR (300 MHz, CD_2Cl_2, 25 ºC) 59.9, 22.6, 11.4, 10.8, 10.3, 8.6, 8.5, 8.1, 8.0, 7.0, 6.8, 4.9, 4.7, -13.2 ppm. Anal. Calcd. for $C_{75.5}H_{78}N_{10}O_{12.5}Mn_3CaCl$ (**14**•1.5E_2O•0.5CH_2Cl_2: C, 57.91; H, 5.02; N, 8.95. Found: C, 57.73; H, 4.78; N, 8.69. *__14__ was triturated in Et_2O and concentrated to dryness three times in an attempt to remove the CH_2Cl_2. UV-Vis (λ_{max} (nm) [ε (M^{-1} cm^{-1})]): 240 ($7.3x10^4$), 315 ($1.8x10^4$), 500 ($1.8x10^3$), 705 ($7.0x10^1$).

[$LMn^{IV}_3CaO_3(OH)(ON_4O)(OAc)$]OTf (15): (JK_IV_132) In the glovebox, to partially dissolved **14** (30.4 mg, 0.022 mmol) in CH_2Cl_2 (*ca.* 9 mL) was added dropwise LutHOTf (5.8 mg, 0.023 mmol, 1.05 equiv) as a clear and colorless solution in CH_2Cl_2 (*ca.* 2 mL). As the LutHOTf was added to the stirred solution of **14**, the solution becomes red/brown and heterogenous to darker red/brown and homogeneous. The LutHOTf vial was rinsed three times to ensure the full equivalent was added (total reaction volume is *ca.* 13 mL). The solution was filtered after 3 hours and removed volatiles *in vacuo*. The resulting red/brown solid was extracted with hexane followed by

Et_2O to remove the resulting lutidine. The remaining material was extracted into C_6H_6, filtered through Celite, and concentrated to dryness to afford red/brown solid **15** (34 mg, *ca.* 100%). Crystals amenable to XRD analysis were grown from vapor diffusion of Et_2O into a C_6H_6 solution of **15**. ^{1}H NMR (300 MHz, CD_2Cl_2, 25 ºC) 59.7, 51.3, 34.9, 22.5, 16.9, 11.3, 10.4, 10.0, 8.8, 6.8, -4.4, -8.4, -13.2, -18.3 ppm . ^{19}F NMR (282 MHz, CD_2Cl_2, 25 ºC): -76.5 ppm. UV-Vis (λ_{max} [ε (M^{-1} cm^{-1})]): 307 ($2.4x10^4$) nm. Anal. Calcd. for $C_{70}H_{63}CaF_3Mn_3N_{10}O_{14}S$: C, 53.82; H, 4.06; N, 8.97. Found: C, 53.57; H, 4.31; N, 8.65.

$LMn^{IV}_3CaO_4(ON_4O)(OAc)$•Ag(OTf) (16): (JK_IV_92) In the glovebox, **14** (13.0 mg, 9 μmol) was partially dissolved in CH_2Cl_2 (ca. 12 mL). AgOTf (2.6 mg, 10 μmol, 1.1 equiv) was dissolved in CH_3CN (ca. 0.3 mL) and diluted with CH_2Cl_2 (*ca.* 1 mL). The clear and colorless AgOTf solution to the red/brown and heterogeneous solution of **14** dropwise. Within 5 minutes, the reaction mixture was clear and orange. At 11 hours the mixture was concentrated *in vacuo*. **14** was visible by ^{1}H NMR spectroscopy; therefore, excess AgOTf (1 mg, 4 μmol, *ca.* 0.4 equiv) was added as a solution in CH_3CN/CH_2Cl_2 and the resulting mixture was stirred for 15 hours and concentrated *in vacuo* to afford **16** as a red/brown solid. Crystals amenable to XRD analysis were grown from vapor diffusion of Et_2O into a CH_2Cl_2 solution of **16**. Upon repeating the procedure, 1.5-2.0 equivalents of AgOTf were found to be necessary to push the reaction to completion. ^{1}H NMR (300 MHz, CD_2Cl_2, 25 ºC) 46.1, 29.5, 26.9, 20.3, 14.0, 13.3, 11.2, 8.8, 8.5, 7.9, 6.7, 5.9, 4.0, -5.3, -9.1, -12.7 ppm. ^{19}F NMR (282 MHz, CD_2Cl_2, 25 ºC): -76.5 ppm Anal. Calcd. for $C_{72}H_{64}Ag_2CaCl_2F_6Mn_3N_{10}O_{17}S_2$ (**16**•AgOTf•CH_2Cl_2): C, 43.00; H, 3.21; N, 6.97. Found: C, 43.32; H, 3.05; N, 6.96. *The excess AgOTf necessary to push the reaction to completion precipitated alongside **16** upon vapor diffusion of Et_2O into the

CH_2Cl_2 solution of **16** and was difficult to remove by washing, as polar solvents that would extract AgOTf decompose **16**. These were therefore analyzed together, giving the extra equivalent of AgOTf in the analysis. **16** is known to crystallize with solvents in the lattice, so a CH_2Cl_2 molecule is also observed. UV-Vis (λ_{max} [ε (M^{-1} cm^{-1})]): 240 ($7.1x10^4$), 310 ($2.0x10^4$), 710 ($1.5x10^2$) nm.

Reaction of $LMn^{IV}_3CaO_4(OAc)_3$•THF (8) with LutHOTf: In the glovebox, **8** (13.9 mg, 0.01 mmol) was partially dissolved in CH_2Cl_2 (4 mL) to give a red/brown, heterogeneous mixture. A solution of LutHOTf (2.7 mg, 0.01 mmol, 1.05 equiv) in CH_2Cl_2 (1 ml) was added, and the LutHOTf vial was rinsed three times to ensure the full equivalent was added (total reaction volume is *ca.* 6 mL). The solution was stirred 6 hours, and did not homogenize like the reaction of **14** with LutHOTf. Volatiles were removed *in vacuo*, and the residue was extracted with CH_2Cl_2, which contained LutHOTf (Figure S9, bottom), and then C_6D_6 with a drop of THF (Figure S9, top), which contained pure, unreacted **8**.

Cyclic Voltammetry

Electrochemical measurements were recorded under a nitrogen atmosphere in a MBraun glovebox at 25 °C with a Pine Instrument Company AFCBP1 bipotentiostat. An auxiliary Pt-coil electrode, a Ag/Ag+ reference electrode (0.01 M $AgNO_3$ in CH_3CN), and a 3.0 mm glassy carbon electrode disc (BASI) were used. Data were recorded using the Pine Instrument Company AfterMath software package. All reported values were referenced to an internal ferrocene/ferrocenium couple. The electrolyte solutions were 0.1 M $^n Bu_4NPF_6$ in DMA or DMF.

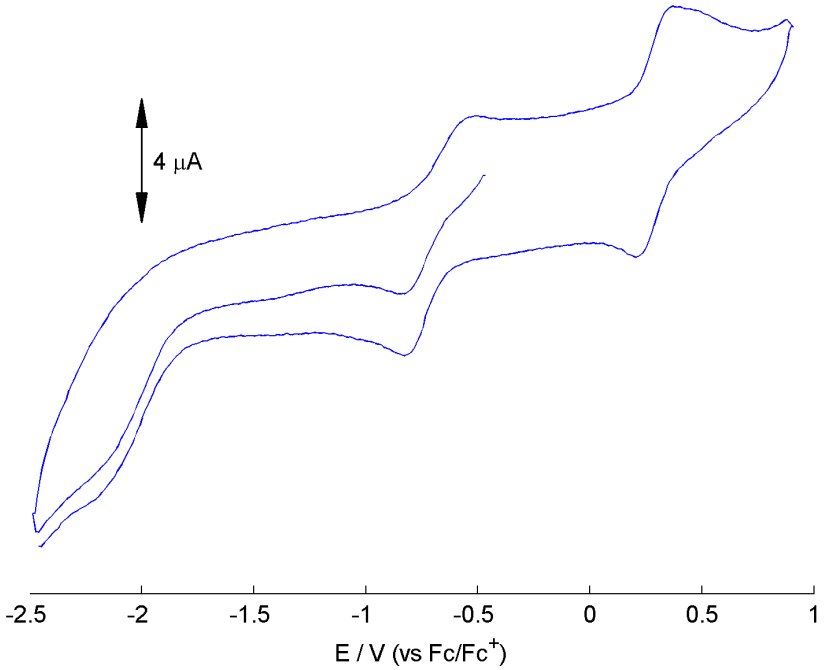

Figure 4.6 Cyclic voltammogram of **6** in DMA at 50 mV/s. Open circuit potential: –470 mV.

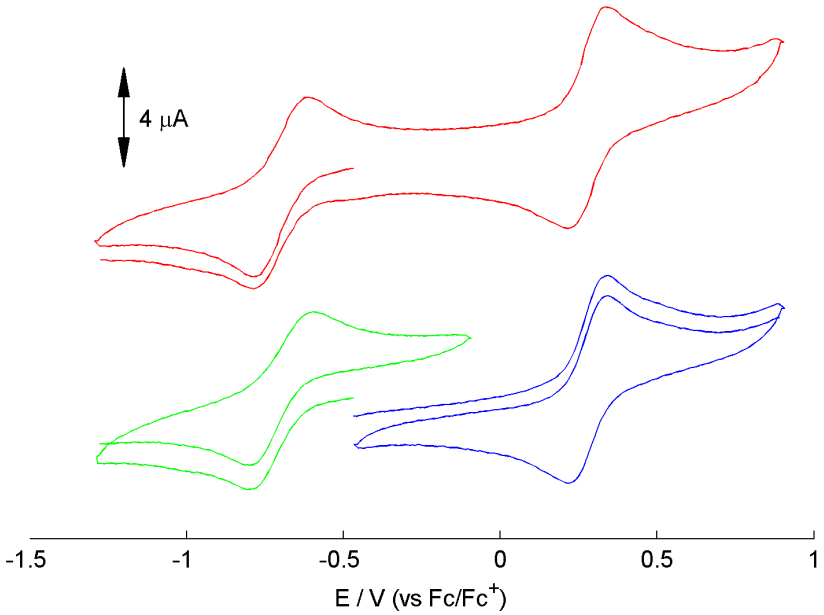

Figure 4.7 Cyclic voltammograms of quasireversible redox processes of **6** in DMA at 50 mV/s. Open circuit potential: –470 mV.

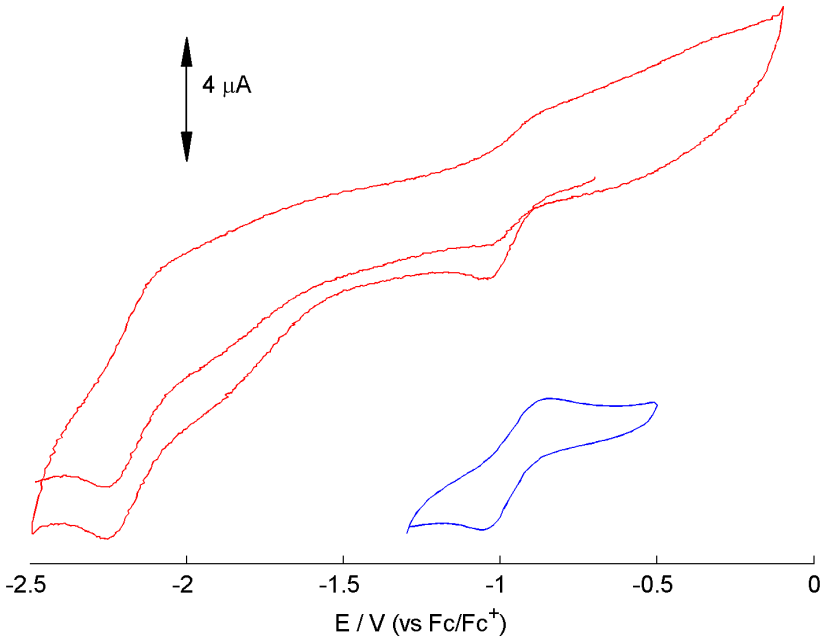

Figure 4.8 Cyclic voltammograms of **8** in DMA at 50 mV/s. Open circuit potential: –700 mV.

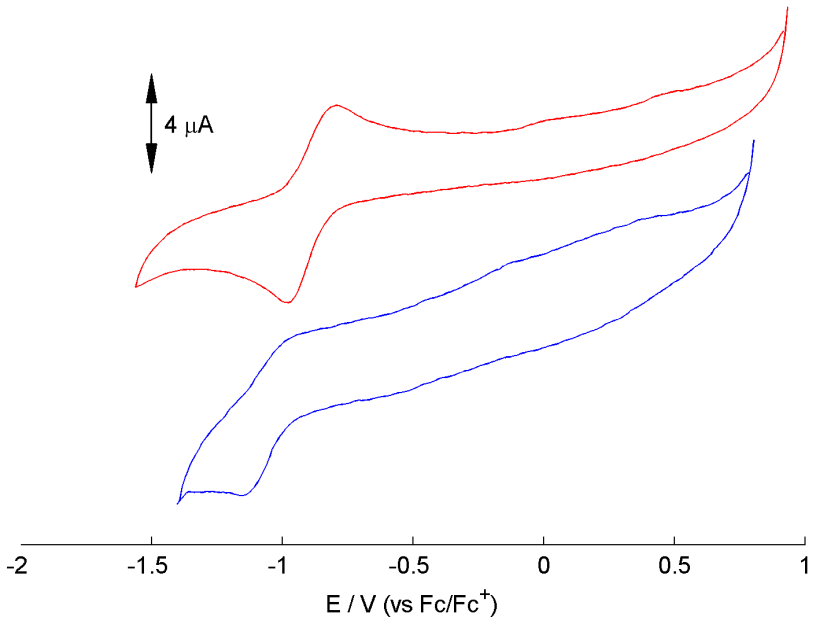

Figure 4.9 Oxidative cyclic voltammograms of **8** in DMF (top) and DMA (bottom) at 100 mV/s. Open circuit potentials: –540 mV (DMF), –700 mV (DMA).

Crystallographic Information

Table 4.1 Crystal and refinement data for complexes **8**, **9**, and **15**.

	8	**9**	**15**
CCDC Number	817683	817924	N/A
empirical formula	$C_{67}H_{56}N_6O_{14}CaMn_3 \bullet 1.21(C_6H_{12}) \bullet 2.79(C_4H_8O)$	$[C_{126}H_{96}N_{12}O_{20}CaMn_6]^{2+} 2[CF_3O_3S]^-$	$[C_{69}H_{62}CaMn_3N_{10}O_{11}]^+ [CF_3O_3S]^- \bullet 0.57(C_4H_{10}O) \bullet 1.96(C_6H_6) \bullet 1.5(C_6) \bullet 0.36(H_2O)$
formula wt	1677.05	2766.01	1871.8
T (K)	100(2)	100(2)	100
a, Å	17.8558(7)	13.606(7)	13.9463(15)
b, Å	15.7376(6)	12.148(5)	16.9456(18)
c, Å	27.5276(10)	38.306(16)	21.456(2)
α, deg	90	90	101.260(3)
β, deg	99.438(2)	97.308(13)	102.405(3)
γ, deg	90	90	102.535(3)
V, Å^3	7630.7(5)	6280(5)	4673.2(8)
Z	4	2	2
cryst syst	Monoclinic	Monoclinic	Triclinic
space group	P $2_1/c$	P $2/n$	P -1
d_{calcd}, g/cm^3	1460	1463	1329
θ range, deg	1.81 to 30.56	1.54 to 23.54	1.553 to 25.102
μ, mm^{-1}	0.632	0.745	.549
abs cor	none	Semi-empirical from equivalents TWINABS	multi-scan
GOF	2.949	1.794	1.017
R1,[a] wR2[b] (I > 2σ(I))	0.0665, 0.0926	0.1423, 0.2718	0.0897, 0.2270

[a] $R1 = \sum||F_o| - |F_c||/\sum|F_o|$. [b] $wR2 = \{\sum[w(F_o^2 - F_c^2)^2]/\sum[w(F_o^2)^2]\}^{1/2}$.

Table 4.2. Selected distances (Å) for **6** and **8**.

	$LMn^{III}_2Mn^{IV}_2O_4(OAc)_3$ (**6**)				$LMn^{IV}_3Ca^{II}O_4(OAc)_3$ (**8**)			
	$Mn1^{III}$	$Mn2^{IV}$	$Mn3^{IV}$	$Mn4^{III}$	$Mn1^{IV}$	$Mn2^{IV}$	$Mn3^{IV}$	Ca1
M–Oxo								
O_A	2.233(2)	1.869(2)	1.994(2)	--	1.916(2)	1.923(2)	1.912(2)	--
O_B	2.012(2)	1.877(2)	--	1.898(2)	1.862(2)	1.829(2)	--	2.431(2)
O_C	1.862(2)	--	1.848(2)	2.201(2)	1.842(2)	--	1.871(2)	2.391(2)
O_D	--	1.847(2)	1.936(2)	1.937(2)	--	1.864(2)	1.825(2)	2.430(2)
Avg.	2.036	1.864	1.926	2.012	1.873	1.872	1.869	2.417
Std. Dev.	0.187	0.016	0.074	0.165	0.038	0.048	0.043	0.023
M–M								
Mn2	3.0724(6)	--	--	--	2.8327(7)	--	--	--
Mn3	2.9921(6)	2.9174(6)	--	--	2.8385(7)	2.8301(7)	--	--
Mn4 / Ca1	2.9134(6)	2.7663(6)	2.8809(6)	--	3.2305(8)	3.2376(9)	3.2245(9)	--

Special Refinement Details

Refinement of F^2 against ALL reflections. The weighted R-factor (*w*R) and goodness of fit (S) are based on F^2, conventional R-factors (R) are based on F, with F set to zero for negative F^2. The threshold expression of $F^2 > 2s(F^2)$ is used only for calculating R-factors(gt) etc. and is not relevant to the choice of reflections for refinement. R-factors based on F^2 are statistically about twice as large as those based on F, and R-factors based on ALL data will be even larger.

All esds (except the esd in the dihedral angle between two l.s. planes) are estimated using the full covariance matrix. The cell esds are taken into account individually in the estimation of esds in distances, angles and torsion angles; correlations between esds in cell parameters are only used when they are defined by crystal symmetry. An approximate (isotropic) treatment of cell esds is used for estimating esds involving l.s. planes.

Compound **8**

Crystals were mounted on a glass fiber using Paratone oil and then placed on the diffractometer under a nitrogen stream at 100K.

Disorder is observed in the THF coordinated to calcium. This was modeled with common sites for the oxygen and the carbon atom across the ring. The crystal contains solvent of crystallization distributed over four sites in the asymmetric unit. Two sites contain THF, one site contains cyclohexane, and the fourth site contains a mixture of THF and cyclohexane. The cyclohexanes were restrained to a chair configuration and the THF were restrained to be similar in geometry.

Compound **9**

Crystals were mounted on a glass fiber using Paratone oil and then placed on the diffractometer under a nitrogen stream at 100K.

The crystal is twinned with a refined twin ratio of 0.531:0.469. The twin law was defined with cell_now as shown below and when the twin law was applied all violations of systematic absences were accounted for. The p4p file was recycled through successive iterations of integration three times to produce the final set of intensities. TWINABS was used to produce the HKLF5 format file used in refinement.

```
------------------------------------------------------------------------------
 1253 reflections within tolerance assigned to domain  1,
 1253 of them exclusively;   393 reflections not yet assigned to a domain
------------------------------------------------------------------------------
Rotated from first domain by 179.6 degrees about
reciprocal axis  1.000  0.001 -0.358  and real axis  1.000  0.001  0.000
Twin law to convert hkl from first to              1.000   0.002   0.001
this domain (SHELXL TWIN matrix):                  0.002  -1.000  -0.002
                                                  -0.716   0.019  -1.000
 1231 reflections within tolerance assigned to domain  2,
  392 of them exclusively;     1 reflections not yet assigned to a domain
------------------------------------------------------------------------------
 2 twin components present
==============================================
    2360 data (    476 unique ) involve domain  1 only,  mean I/sigma   9.0
    2394 data (    482 unique ) involve domain  2 only,  mean I/sigma   9.8
   42960 data (   8575 unique ) involve   2 domains,  mean I/sigma   3.5
       1 data (      1 unique ) involve   3 domains,  mean I/sigma   1.3
==============================================
```

The solvent region was modeled as triflate and the two sites were refined as rigid bodies, with Ueq=0.10. One site spans a two-fold axis and was included at half occupancy. The other site is a general position and its occupancy was allowed to refine to a final occ=0.500.

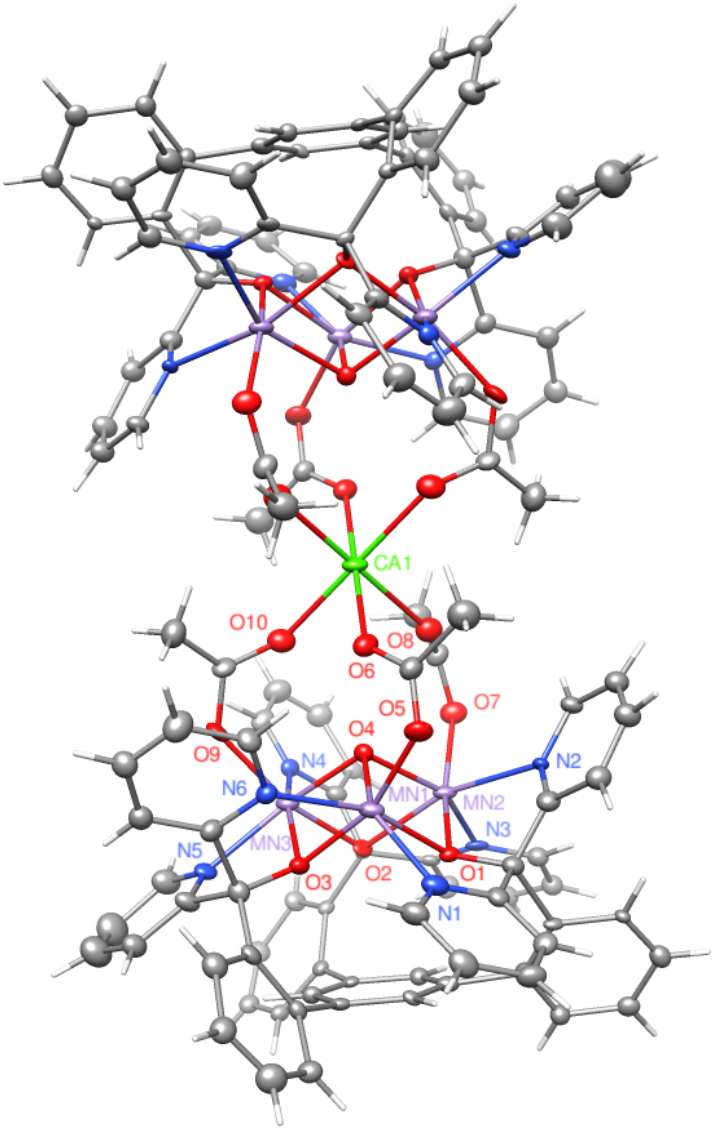

Figure 4.10. Structural drawing of **9**.

Compound **15**

Crystals were mounted on a loop using Paratone oil and then placed on the diffractometer under a nitrogen stream at 100K.

The data loses intensity quickly at higher resolution, and therefore was cut off below 0.8 Å (although data is weak below 1.0 Å). Disorder in the solvent molecules was

fit with benzenes and diethyl ethers, with restrained geometries applied. Much of the solvent was left anisotropic. C71 had to be tightly restrained with a SIMU card with O14 or it would become NPD. A water molecule is present ca. 40% of the time within H-bonding distance of the acetate and one μ_3-oxo.

REFERENCES

1. McEvoy, J. P.; Brudvig, G. W. *Chem. Rev.* **2006,** *106*, 4455-4483.
2. (a) Ferreira, K. N.; Iverson, T. M.; Maghlaoui, K.; Barber, J.; Iwata, S. *Science* **2004,** *303*, 1831-1838.(b) Guskov, A.; Kern, J.; Gabdulkhakov, A.; Broser, M.; Zouni, A.; Saenger, W. *Nat. Struct. Mol. Biol.* **2009,** *16*, 334-342.(c) Loll, B.; Kern, J.; Saenger, W.; Zouni, A.; Biesiadka, J. *Nature* **2005,** *438*, 1040-1044.(d) Zouni, A.; Witt, H. T.; Kern, J.; Fromme, P.; Krauss, N.; Saenger, W.; Orth, P. *Nature* **2001,** *409*, 739-743.(e) Dau, H.; Grundmeier, A.; Loja, P.; Haumann, M. *Philos. Trans. R. Soc. B-Biol. Sci.* **2008,** *363*, 1237-1243.(f) Yano, J.; Kern, J.; Sauer, K.; Latimer, M. J.; Pushkar, Y.; Biesiadka, J.; Loll, B.; Saenger, W.; Messinger, J.; Zouni, A.; Yachandra, V. K. *Science* **2006,** *314*, 821-825.(g) Umena, Y.; Kawakami, K.; Shen, J.-R.; Kamiya, N. *Nature* **2011,** *473*, 55-U65.
3. Peloquin, J. M.; Campbell, K. A.; Randall, D. W.; Evanchik, M. A.; Pecoraro, V. L.; Armstrong, W. H.; Britt, R. D. *J. Am. Chem. Soc.* **2000,** *122*, 10926-10942.
4. (a) Cady, C. W.; Crabtree, R. H.; Brudvig, G. W. *Coordin. Chem. Rev.* **2008,** *252*, 444-455.(b) Barber, J.; Murray, J. W. *Coordin. Chem. Rev.* **2008,** *252*, 233-243.(c) Yano, J.; Yachandra, V. *Chem. Rev.* **2014,** *114*, 4175-4205.
5. Armstrong, F. A. *Philos. Trans. R. Soc. B-Biol. Sci.* **2008,** *363*, 1263-1270.
6. (a) Mullins, C. S.; Pecoraro, V. L. *Coordin. Chem. Rev.* **2008,** *252*, 416-443.(b) Dismukes, G. C.; Brimblecombe, R.; Felton, G. A. N.; Pryadun, R. S.; Sheats, J. E.; Spiccia, L.; Swiegers, G. F. *Acc. Chem. Res.* **2009,** *42*, 1935-1943.(c) Christou, G. *Acc. Chem. Res.* **1989,** *22*, 328-335.
7. (a) Yagi, M.; Kaneko, M. *Chem. Rev.* **2001,** *101*, 21-35.(b) Mukhopadhyay, S.; Mandal, S. K.; Bhaduri, S.; Armstrong, W. H. *Chem. Rev.* **2004,** *104*, 3981-4026.

8. (a) Mishra, A.; Wernsdorfer, W.; Abboud, K. A.; Christou, G. *Chem. Commun.* **2005**, 54-56.(b) Kotzabasaki, V.; Siczek, M.; Lis, T.; Milios, C. J. *Inorg. Chem. Commun.* **2011,** *14*, 213-216.(c) Milios, C. J.; Prescimone, A.; Mishra, A.; Parsons, S.; Wernsdorfer, W.; Christou, G.; Perlepes, S. P.; Brechin, E. K. *Chem. Commun.* **2007**, 153-155.(d) Hewitt, I. J.; Tang, J. K.; Madhu, N. T.; Clerac, R.; Buth, G.; Anson, C. E.; Powell, A. K. *Chem. Commun.* **2006**, 2650-2652.(e) Nayak, S.; Nayek, H. P.; Dehnen, S.; Powell, A. K.; Reedijk, J. *Dalton Trans.* **2011,** *40*, 2699-2702.(f) Park, Y. J.; Ziller, J. W.; Borovik, A. S. *J. Am. Chem. Soc.* **2011,** *133*, 9258-2961.

9. Mishra, A.; Yano, J.; Pushkar, Y.; Yachandra, V. K.; Abboud, K. A.; Christou, G. *Chem. Commun.* **2007**, 1538-1540.

10. Yano, J.; Yachandra, V. K. *Inorg. Chem.* **2008,** *47*, 1711-1726.

11. Yano, J.; Kern, J.; Pushkar, Y.; Sauer, K.; Glatzel, P.; Bergmann, U.; Messinger, J.; Zouni, A.; Yachandra, V. K. *Philos. Trans. R. Soc. B-Biol. Sci.* **2008,** *363*, 1139-1147.

12. (a) McEvoy, J. P.; Gascon, J. A.; Batista, V.; Brudvig, G. W. *Photochem. Photobiol. Sci.* **2005,** *4*, 940-949.(b) Messinger, J. *Phys. Chem. Chem. Phys.* **2004,** *6*, 4764-4771.

13. Fukuzumi, S.; Morimoto, Y.; Kotani, H.; Naumov, P.; Lee, Y. M.; Nam, W. *Nat. Chem.* **2010,** *2*, 756-759.

14. (a) Arjomand, M.; Machin, D. J. *J. Chem. Soc. Dalton Trans.* **1975**, 1055-1061.(b) Levason, W.; Mcauliff.Ca *Coordin. Chem. Rev.* **1974,** *12*, 151-184.

15. Kanan, M. W.; Yano, J.; Surendranath, Y.; Dinca, M.; Yachandra, V. K.; Nocera, D. G. *J. Am. Chem. Soc.* **2010,** *132*, 13692-13701.

16. (a) Symes, M. D.; Surendranath, Y.; Lutterman, D. A.; Nocera, D. G. *J. Am. Chem. Soc.* **2011,** *133*, 5174-5177.(b) Kanan, M. W.; Nocera, D. G. *Science* **2008,** *321*, 1072-1075.

17. Najafpour, M. M.; Ehrenberg, T.; Wiechen, M.; Kurz, P. *Angew. Chem. Int. Edit.* **2010,** *49*, 2233-2237.

18. Bartlett, J. E.; Baranov, S. V.; Ananyev, G. M.; Dismukes, G. C. *Philos. Trans. R. Soc. B-Biol. Sci.* **2008,** *363*, 1253-1261.

19. (a) Chen, C. G.; Kazimir, J.; Cheniae, G. M. *Biochemistry* **1995,** *34*, 13511-13526.(b) Tyryshkin, A. M.; Watt, R. K.; Baranov, S. V.; Dasgupta, J.; Hendrich, M. P.; Dismukes, G. C. *Biochemistry* **2006,** *45*, 12876-12889.
20. Tamura, N.; Inoue, Y.; Cheniae, G. M. *Biochim. Biophys. Acta* **1989,** *976*, 173-181.
21. Mukherjee, S.; Stull, J. A.; Yano, J.; Stamatatos, T. C.; Pringouri, K.; Stich, T. A.; Abboud, K. A.; Britt, R. D.; Yachandra, V. K.; Christou, G. *Proc. Natl. Acad. Sci. USA* **2012,** *109*, 2257-2262.
22. Tsui, E. Y.; Agapie, T. *Proc. Natl. Acad. Sci. USA* **2013,** *110*, 10084-10088.
23. Kanady, J. S.; Mendoza-Cortes, J. L.; Tsui, E. Y.; Nielsen, R. J.; Goddard III, W. A.; Agapie, T. *J. Am. Chem. Soc.* **2013,** *135*, 1073-1082.
24. Goldcamp, M. J.; Edison, S. E.; Squires, L. N.; Rosa, D. T.; Vowels, N. K.; Coker, N. L.; Bauer, J. A. K.; Baldwin, M. J. *Inorg. Chem.* **2003,** *42*, 717-728.
25. Semakin, A. N.; Sukhorukov, A. Y.; Lesiv, A. V.; Khomutova, Y. A.; Ioffe, S. L.; Lyssenko, K. A. *Synthesis-Stuttgart* **2007**, 2862-2866.
26. Dilman, A. D.; Tishkov, A. A.; Lyapkalo, I. M.; Ioffe, S. L.; Strelenko, Y. A.; Tartakovsky, V. A. *Synthesis-Stuttgart* **1998**, 181-185.
27. Bryan, P. S.; Dabrowiak, J. C. *Inorg. Chem.* **1975,** *14*, 299-302.
28. Vincent, J. B.; Chang, H. R.; Folting, K.; Huffman, J. C.; Christou, G.; Hendrickson, D. N. *J. Am. Chem. Soc.* **1987,** *109*, 5703-5711.
29. Saltzman, H.; Sharefkin, J. G. *Org. Synth.* **1973,** *5*, 658.

CHAPTER 5

Oxygen Atom Transfer and Oxidative Water Incorporation in Cuboidal Mn_3MO_n Complexes Based on Synthetic, Isotopic Labeling, and Computational Studies

Published in part as:

Kanady, J. S.; Mendoza-Cortes, J. L.; Tsui, E. Y.; Nielsen, R. J.; Goddard III, W. A.; Agapie, T. *J. Am. Chem. Soc.* **2013,** *135*, 1073-1082.

ABSTRACT

The oxygen-evolving complex (OEC) of photosystem II contains a Mn_4CaO_n catalytic site, in which reactivity of bridging oxidos is fundamental to OEC function. We synthesized structurally relevant cuboidal Mn_3MO_n complexes (M=Mn, Ca, Sc; *n*=3,4) to enable mechanistic studies of reactivity and incorporation of μ_3-oxido moieties. We found that $Mn^{IV}{}_3CaO_4$ and $Mn^{IV}{}_3ScO_4$ were unreactive toward trimethylphosphine (PMe_3). In contrast, our $Mn^{III}{}_2Mn^{IV}{}_2O_4$ cubane reacts with this phosphine within minutes to generate a $Mn^{III}{}_4O_3$ partial cubane plus Me_3PO (discussed briefly in Chapter 3). We used quantum mechanics to investigate the reaction paths for oxygen atom transfer to phosphine from $Mn^{III}{}_2Mn^{IV}{}_2O_4$ and $Mn^{IV}{}_3CaO_4$. We found that the most favorable reaction path leads to partial detachment of the CH_3COO^- ligand, which is energetically feasible only when Mn(III) is present. Experimentally, the lability of metal-bound acetates is greatest for $Mn^{III}{}_2Mn^{IV}{}_2O_4$. These results indicate that even with a strong oxygen atom acceptor such as PMe_3, the oxygen atom transfer chemistry from Mn_3MO_4 cubanes is controlled by ligand lability, with the $Mn^{IV}{}_3CaO_4$ OEC model being unreactive. The oxidative oxide incorporation into the partial cubane, $Mn^{III}{}_4O_3$, was observed experimentally upon treatment with water, base, and oxidizing equivalents. ^{18}O-labeling experiments provided mechanistic insight into the position of incorporation in the partial cubane structure, consistent with mechanisms involving migration of oxide moieties within the cluster but not consistent with selective incorporation at the site available in the starting species. These results support recent proposals for the mechanism of the OEC, involving oxido migration between distinct positions within the cluster.

INTRODUCTION

Artificial photosynthesis schemes generally involve water as the terminal source of electrons and protons, forming dioxygen as a byproduct.[1] In biological systems, the oxidation of water is performed by the oxygen-evolving center (OEC) of photosystem II (PSII).[2] The OEC consists of a Mn_4Ca cluster supported by bridging oxidos or hydroxidos and carboxylate and histidine side chains from the protein. Early crystallographic, XAS, and EPR studies[3] supported a tetranuclear 3+1 arrangement of the four manganese centers, with more recent crystallographic studies proposing a Mn_3CaO_4 heterometallic cubane with a fourth manganese "dangler" bound by a bridging oxide.[4] The exact structure of the cluster remains under debate, with quantum mechanics studies suggesting that the recent crystal structure corresponds to a more reduced cluster[5] and that a more open structure is more consistent with spectroscopic data.[6]

In the catalytic cycle, or Kok cycle, four photogenerated oxidizing equivalents sequentially oxidize the OEC.[7] Although the oxidation states are still debated,[8] a common assignment of the intermediates, denoted as S_n states (n = 0–4), range in oxidation state from S_0, $Mn^{III}_3Mn^{IV}$, to S_4, a putative $Mn^{IV}_3Mn^{V}$ or Mn^{IV}_4-ligand radical that promotes O–O bond formation and O_2 release.[2, 9] O–O bond formation has been proposed to involve metal-bound terminal oxo/oxyl, μ_2- or μ_3-oxido moieties (Scheme 5.1).[2, 6, 9-10] Quantum mechanics investigations of the mechanism and spectroscopy have been performed in recent years. Quantum mechanics/molecular mechanics (QM/MM) studies support a cubane Mn_3CaO_4 with a Mn dangler arrangement.[9c] A computational comparison of this[9c] and more open structures[11] favors an open-cuboidal

arrangement.[10d, 11-12] Mechanistic and spectroscopic studies were recently interpreted as being most consistent with a mechanism of O-O bond formation involving such an open structure (Scheme 5.1b).[6]

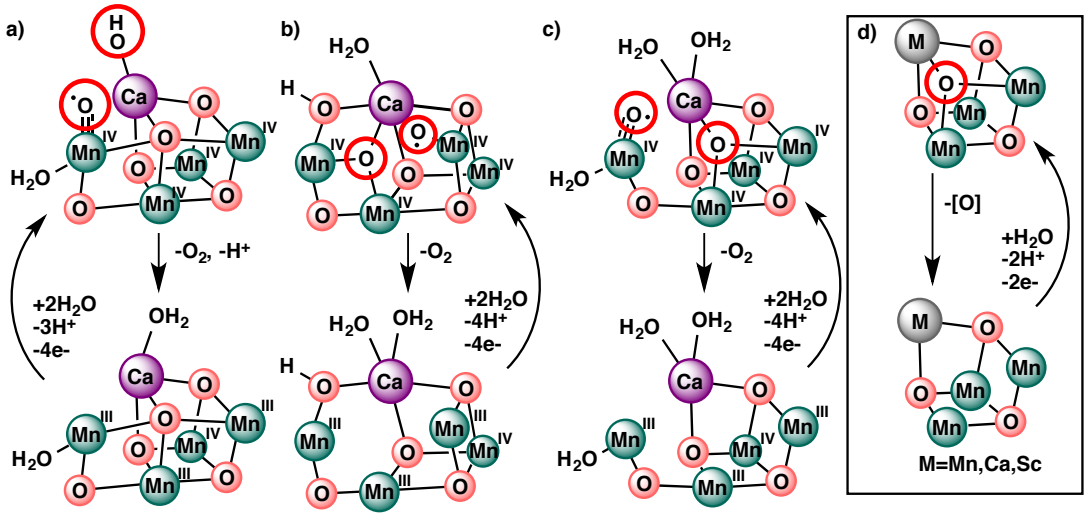

Scheme 5.1. Proposed mechanisms for O–O bond formation at the OEC of PSII (a, b, and c) and oxygen atom transfer and incorporation studies reported here (d). Bolded, red circles highlight the substrate oxygens.

During the catalytic cycle subsequent to O-O bond formation, new substrate water coordinates to the cluster and is deprotonated.[13] For the latter mechanisms (Scheme 5.1b,c), the water must be deprotonated, incorporated into a μ_3-site, and the cluster must be oxidized. Heterogeneous catalysts for water oxidation based on Ca/Mn mixed oxides displaying structural motifs related to the biological active site have been reported,[14] showing that these elementary reaction steps are relevant to practical applications. Thus, systematic studies of well-defined model clusters are an important avenue toward uncovering the reactivity of bridging oxido moieties. Additionally, the requisite oxidative incorporation of water as bridging oxido ligands into complex

multimetallic structures is key to fully understanding the mechanism of the OEC and heterogeneous metal oxides.

In addition to studies of the complex biological and heterogeneous systems, synthetic metal-oxido models have provided insight into the reactivity and spectroscopy of high-oxidation state manganese clusters.[15] Tetramanganese cubanes have been invoked in water oxidation catalysis,[16] but more recent reports assign the heterogeneous manganese oxide deposited on the electrode as the active electrocatalyst.[17] Although many varieties of tetramanganese-oxido clusters have been characterized,[15] access to structurally related clusters of controlled metal and oxido content able to selectively probe oxygen atom incorporation and transfer has been hindered by challenges related to the method of synthesis by self-assembly. Also, access to calcium-containing manganese clusters was limited to a small number of examples, restricting investigations of the effect of the calcium center.[18] Chapter 4 discussed a Mn_3CaO_4 cubane supported by a trinucleating ligand and Christou *et al.* reported a $Mn_3Ca_2O_4$ cluster, both demonstrating that heteronuclear Mn_3CaO_4 cubanes are synthetically attainable.[19]

Utilization of a trinucleating ligand framework—1,3,5-tris(2-di(2'-pyridyl)hydroxymethylphenyl)benzene (**H_3L**, Scheme 5.2) —has allowed us to prepare a trimanganese complex (**1**) as a useful precursor to site-differentiated manganese-oxido cubanes.[19a,20] Synthetic access to structurally related heteronuclear Mn_3CaO_4 (**8**) and homonuclear Mn_4O_4 (**6**) cubanes has allowed a direct comparison, showing that replacing manganese with calcium leads to a large shift (>1 V) in the reduction potential for accessing a high oxidation state, catalytically relevant, Mn^{IV}_3 species (See Chapter 4). Given the structural accuracy of these models for the OEC, the chemical reactivities of

these and related clusters are of great interest. A series of Mn_3MO_4 complexes (M = Mn^{3+}, Ca^{2+}, Sc^{3+}), and more specifically **5** and **6**, only differing by an oxygen atom with all ancillary ligands identical, allows a unique opportunity to systematically study oxygen atom transfer from and water incorporation into a cuboidal moiety. Ligand exchange was also studied to better understand the fluxionality of the Mn_3MO_4 cluster, and detailed mechanistic understanding for each process was achieved through isotope labeling, electrochemical, and QM studies.

RESULTS & DISCUSSION

5.1 O-atom Transfer to Phosphine as Comparative Probe of Mn_3MO_4 Reactivity.

With $Mn^{III}_2Mn^{IV}_2O_4$ complex **6** (Chapter 3), $Mn^{IV}_3CaO_4$ complex **8**, and $Mn^{IV}_3ScO_4$ coomplex **17** (characterized by Dr. Emily Tsui) in hand, we investigated the reaction with phosphine as a mechanistic tool, measuring propensity of the oxide for oxygen atom transfer chemistry in these cubanes. The addition of excess (2-10 equiv.) trimethylphosphine (PMe_3) to complex **6** produced a color change from red-brown to orange-red. Removal of volatiles *in vacuo* and extraction of Me_3PO with Et_2O afforded **5** as a red-orange powder in near quantitative yield (Scheme 5.2). In the ^{31}P NMR, ca. one equivalent of PMe_3 was converted within fifteen minutes with respect to a tetraphenylphosphonium internal standard. The ^{31}P NMR signal corresponding to trimethylphosphine oxide (Me_3PO) was not observed in the reaction mixture of **6** and PMe_3, but could be observed when the PMe_3O was extracted away from the paramagnetic product into diethyl ether (Et_2O). Me_3PO was also observed by ESI-MS of the Et_2O fraction as the Me_3POH^+ cation at m/z 93.1. The protonated cation mass

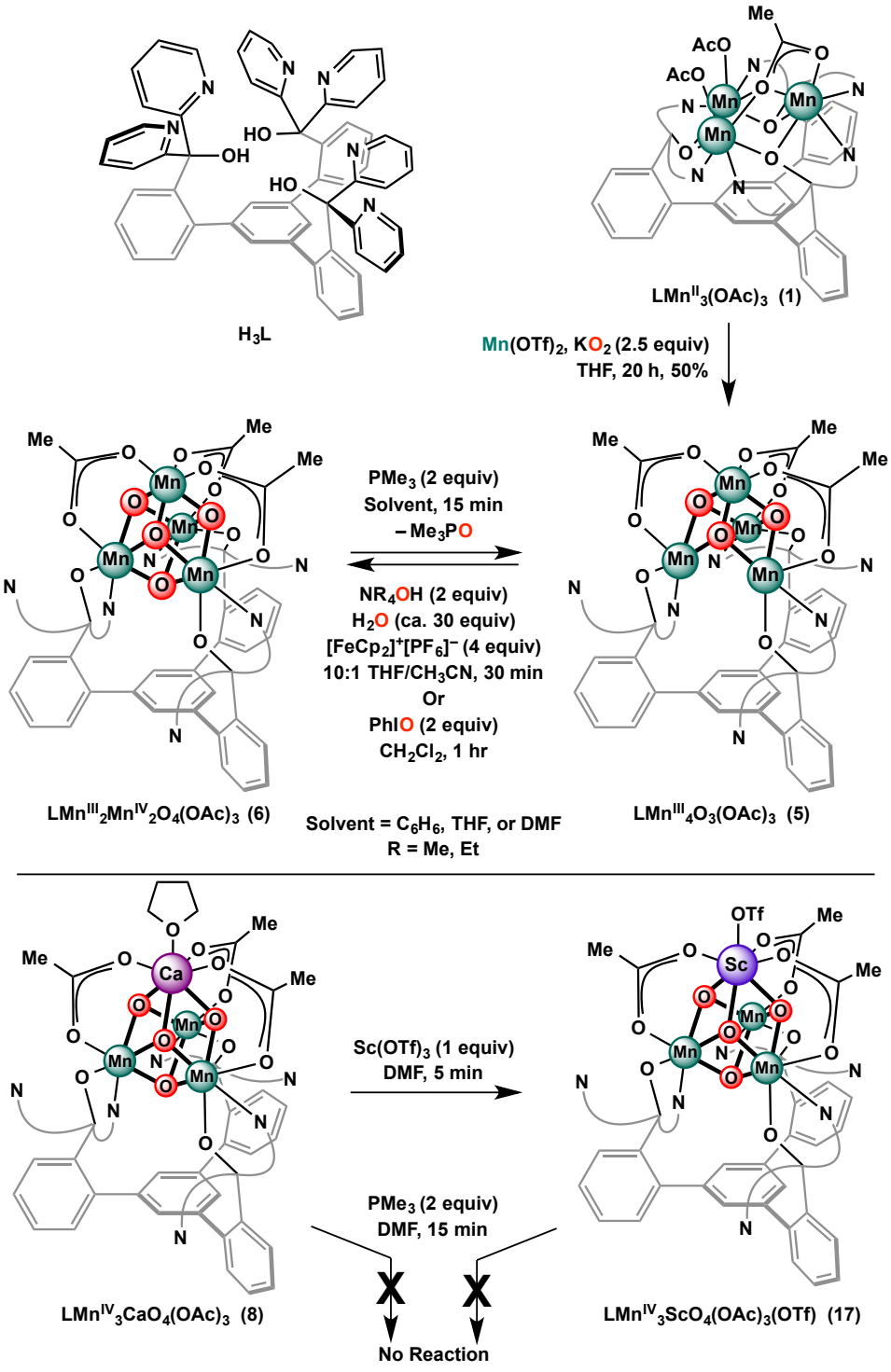

Scheme 5.2. Reactivity and synthesis of cubanes **6**, **8**, and **17** and partial cubane **5**. Curved lines represent 2-pyridyl groups.

was also observed for an authentic sample of Me_3PO. Complex **6** also reacts with PEt_3 to give **5**, albeit much slower—50% conversion over 24 hours. In contrast to the fast oxygen atom transfer reaction of **6**, $Mn^{IV}_3CaO_4$ and $Mn^{IV}_3ScO_4$ cubane complexes **8** and **17** do not show consumption of PMe_3 within fifteen minutes at room temperature (Scheme 5.2). The calcium-containing cluster **8** (in the same oxidation states as the S_2, S_3, and S_4 state of the OEC)[9c] does not perform oxygen atom transfer to PMe_3, a potent acceptor. The biological system has been interrogated with alternate reducing agents such as NH_2OH, N_2H_4 and NO, which provided access to reduced forms of the OEC (S_{-n} states).[23] These reagents generate complex mixtures of products with **6**. In contrast, our phosphine surrogate provides clean reductive chemistry and generates a Mn^{III}_4 complex corresponding to a putative S_{-1} state during OEC photoactivation.[24]

The oxidizing power of the clusters was investigated by cyclic voltammetry as a measure of oxygen atom transfer propensity. As reported in Chapter 4, the calcium cluster **8** (E_{red} = –0.94 V vs. Fc/Fc^+ in DMA) is less oxidizing than the all-manganese cluster **6** (E_{red} = –0.70 V vs. Fc/Fc^+ in DMA).[19a] Cyclic voltammetry experiments revealed that reduction of **17** (E_{red} = –0.24 V vs. Fc/Fc^+ in DMF) occurs at a much more positive potential than that of **6** and **8** (Figure 5.3), indicating that thermodynamically **17** is more oxidizing. Despite the significantly higher oxidizing power, **17** does not form trimethylphosphine oxide upon treatment with trimethyl phosphine, suggesting that the difference in reactivity is due to the kinetics, which is also consistent with the much slower reactivity of **6** with PEt_3 versus PMe_3.

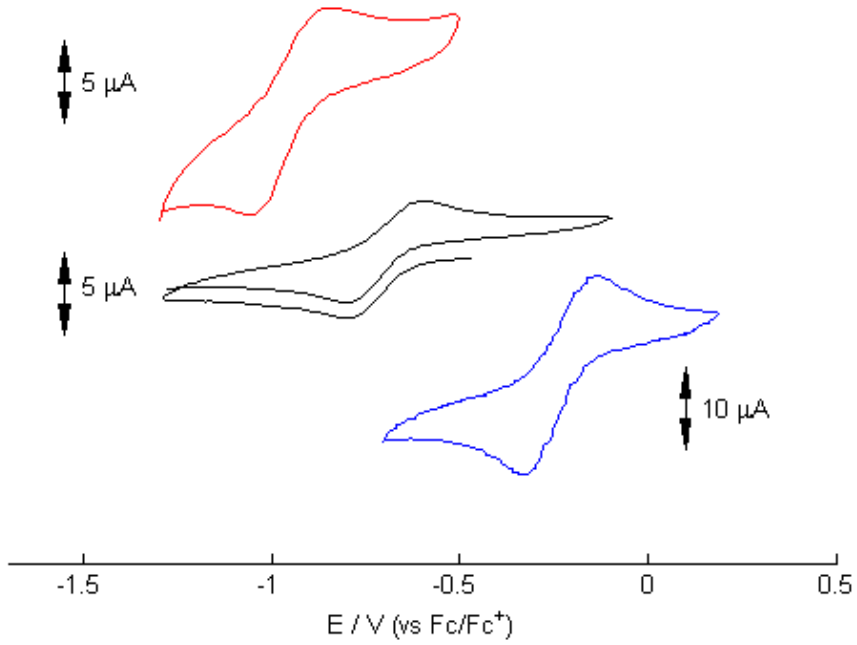

Figure 5.3. Cyclic voltammograms of **6** (middle), **8** (top), and **17** (bottom) referenced to Fc/Fc^+. The scan rate was 50 mV/s for **6** and 100 mV/s for **8** and **17** at an analyte concentration of 1 mM and electrolyte of 0.1 M $^n Bu_4NPF_6$ in dimethylacetamide (**6** and **8**) and DMF (**17**). $E_{1/2}$ values: –0.70 V for **6**, –0.94 V for **8**, –0.24 V for **17**.

5.2 QM studies of O-atom Transfer from Mn_3MO_4 to PMe_3.

Dr. José Mendoza-Cortés and Dr. Robert J. Nielson carried out QM studies to interrogate the differences in reactivity for oxygen atom transfer to phosphine. The QM studies are included here as they complete the story for oxygen atom transfer and water incorporation. As described in the Supporting Information (SI) of the published work,[25] they used the B3LYP flavor of Density Functional Theory (DFT) with Poisson Boltzmann Solvation.

In order to validate this level of DFT for predicting the structures and properties of these compounds, we compare the XRD coordinates, reduction potentials,

and electronic states with the minimized structures obtained from QM. The optimization of the structures was carried out for the high spin configuration of each compound. Using this structure, we also calculated the lower spin wavefunctions. We found a very small splitting, <0.1 kcal, for both **6** and **8**, which suggests that the coupling between high-spin manganese centers is a minor contributor to the ambient-temperature free energy surfaces computed (magnetism studies support this small splitting; see Chapter 3 for complex **6** and the Exp. Section herein for complex **8**). For the current level of DFT the difference is too small to be significant and hence we consider only the high spin configuration through this discussion.

The QM optimized structure of **8** (147 atoms) is shown in Figure 5.4a, which differs from the XRD mainly in the THF bound to the Ca, with some small differences in the nonbonded pyridines. Considering only the core Mn_3CaO_4 and the first coordination shell (21 atoms), the DFT differs from the XRD study by root mean square (RMS) of 0.007 Å for bonds, and 0.384° for bond angles. This indicates that our level of QM reproduces the geometry of **8**.

We then calculated the structure of **6** (134 atoms; Figure 5.4b) with the main difference involving the nonbonded pyridines with respect to the structure from XRD. Comparing only the Mn_4O_4 cluster and the first coordination shell (20 atoms) the QM agrees with XRD with RMS = 0.012 Å for bonds, and 0.060° for angles. Thus the computational model again accurately describes the experimental system for the Mn_4 core.

Using this level of QM, we determined the transition state for the reaction with PMe_3 at various sites of both the Mn_4O_4 and Mn_3CaO_4 clusters. A similar QM study

with smaller basis set for geometries was used for other mechanistic studies involving transition metal complexes in enzymes (including O-O formation), leading to a typical accuracy of within 3-5 kcal/mol of experiment, with the barriers usually overestimated.[26] This difference is systematic, not random, giving a potential energy surface similar to the exact one. Also, others have shown that DFT methods are able to accurately reproduce the crystal structures of oxo-manganese complexes.[27]

5.2.1. Distributions of Mn^{III} and Mn^{IV} sites and redox potentials. Comparison of the current QM methodology for single electron redox potentials in well-characterized early transition-metal metallocenes shows an absolute error deviation of 0.179 V. This is equivalent to an error of 4.1 kcal/mol, which is in the range of accuracy for B3LYP. The current B3LYP methodology systematically gives more negative potentials than experiment for the Mn_4O_4 and Mn_3CaO_4 cubanes by almost 0.2 V, an error of 4.6 kcal/mol. This is similar to the error for single transition metal complexes in well characterized metallocenes.[28] For each structure optimization of the redox compounds, we used the high spin state as in the neutral case. Thus we validated our level of QM by reproducing the experimental redox potential for these systems. We were also able to determine how the redox processes affects the geometry of the structure by reducing the Mn^{IV} atoms to Mn^{III}.

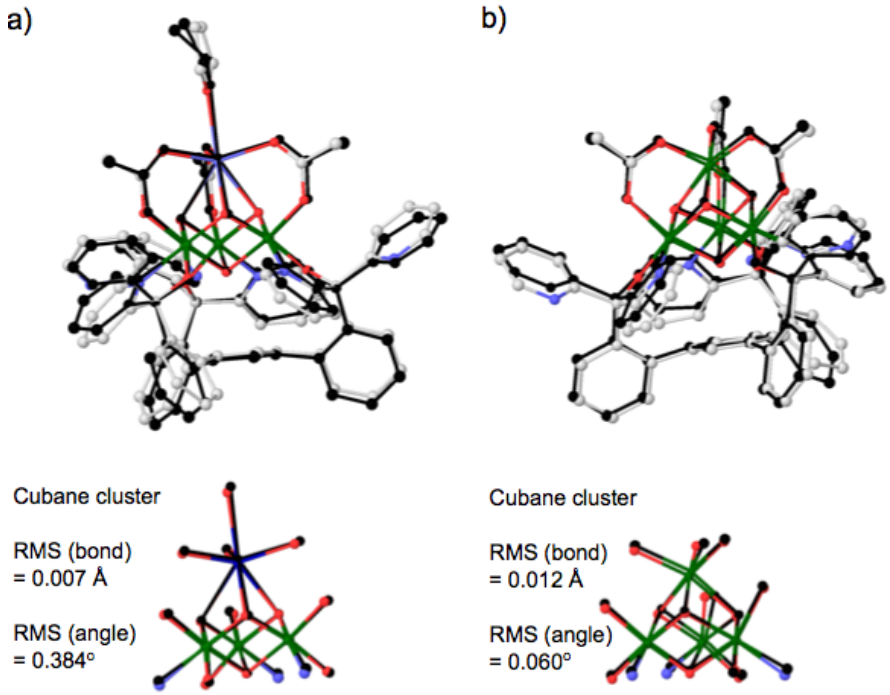

Figure 5.4. Comparison of geometries of a) **8** and b) **6** obtained from experiment (colored: Ca; dark blue, Mn; green, O; red, N; blue, C; grey) and QM (black). H is not shown for clarity.

5.2.2 QM reaction profiles for reaction with PMe_3 to form $OPMe_3$.

5.2.2a PMe_3 attacking the Mn_3CaO_4. We consider first the reaction profile for PMe_3 attacking the Mn_3CaO_4 compound **8.** We found that reacting away any of the three 'top' oxygens has a barrier of 28.7 kcal/mol while reacting with the 'bottom' oxygen leads to a barrier of 90.2 kcal/mol (pathways $\mathbf{A}^{\ddagger}$ and $\mathbf{B}^{\ddagger}$, respectively; Figure 5.5a). The attack of 'bottom' oxygen is very unfavorable due to the presence of the trinucleating ligand **L**. Removing a 'top' oxygen gives the most stable product **B**. On the other hand, removing the 'bottom' oxygen leads to a product, **A**, that is 13.2 kcal/mol less stable because the

Mn^{IV} is forced to be five coordinate. Also, the O vacancy at the top is likely stabilized by the trans axial alkoxide and pyridine ligands.

5.2.2b PMe_3 attacking the Mn_4O_4. We found that attacking the 'top' oxygens leads to three distinct barriers of 23.7, 24.5, and 28.4 kcal/mol, giving the products **D**, **C** and **E**, respectively (Figure 5.5b). These results are very similar to the lowest barrier $\mathbf{B}^{\ddagger}$ (28.7 kcal/mol) of the Mn_3CaO_4 complex. However, for the Mn_4O_4 complex we found a new lower barrier reaction path **G** involving partial detachment of the CH_3COO^-. This new path leads to a transition state $\mathbf{G}^{\ddagger}$ (Figure 5.5b) with a barrier of 18.3 kcal/mol. This barrier is 5-10 kcal/mol lower than the any of the barriers for direct PMe_3 attack on Mn_4O_4 and Mn_3CaO_4. In contrast, reacting with the 'bottom' oxygen gives product **F** (equivalent to the experimentally observed compound **5**) with a high activation barrier $\mathbf{F}^{\ddagger}$ (63.6 kcal/mol) due to the presence of the trinucleating ligand **L**, similar to results for the $CaMn_3O_4$ cubane. We found that **F** (or **5**) is the lowest energy product, as is consistent with experiment. The products of removing 'top' oxygen atoms are less energetically favorable by 30.5, 23.9 and 15.8 kcal/mol for **C**, **D**, and **E**, respectively, with respect to **F**, (Figure 5.5b). These differences arise because the Mn^{III} centers prefer to have the elongated axis along the empty coordination site and away from the electron rich alkoxide donors (as is the case for **F**).

Based on these results, we propose the following reaction mechanism for oxygen atom transfer from Mn_4O_4 cubane **6** to PMe_3 (Figure 5.6). First, partial detachment of CH_3COO-Mn^{III} and CH_3COO-Mn^{IV} involves barriers of 13.2 and 18.6 kcal/mol, respectively. This partial detachment is not observed for the CH_3COO-Mn^{IV} of Mn_3CaO_4 complex **8** because the barrier is 27.1 kcal/mol. That indicates that the

CH_3COO-Mn^{III} and CH_3COO-Mn^{IV} bonds in the Mn_4O_4 system are more labile than in **8**. This leads to the transition state $\mathbf{G}^{\ddagger}$, giving mainly products **E** and $OPMe_3$ with minor contributions of **C** and **D.** This is followed by migration of the 'bottom' oxygen to a 'top' position with a barrier of 7.5 kcal/mol, leaving behind the vacancy at the bottom which is the product observed experimentally **F** (or **5**).

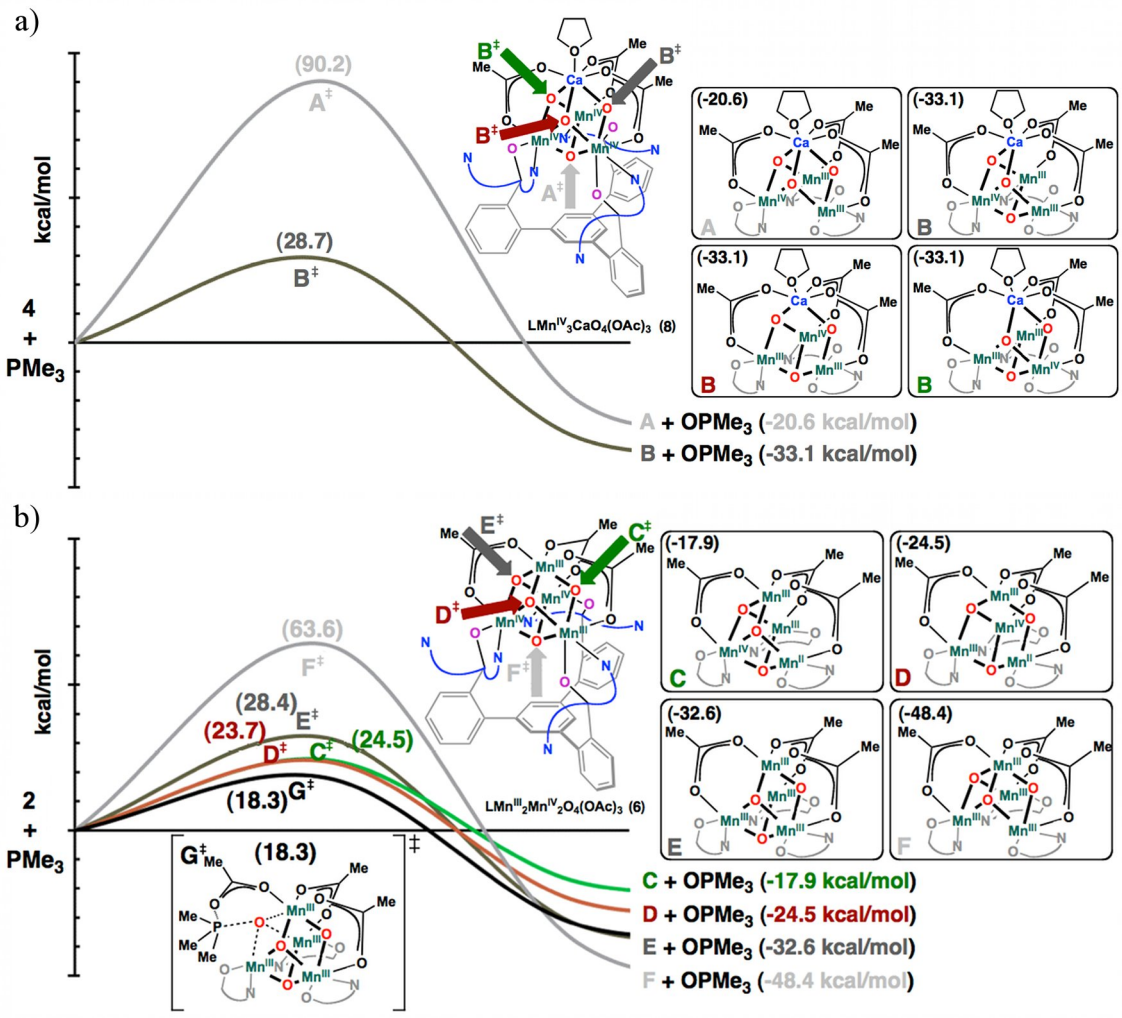

Figure 5.5. a) The QM reaction profile of **8** + PMe_3. The possible products **A** and **B** are given in the upper right. The numbers in parenthesis are the relative energies with respect to starting materials **8** and PMe_3. b) The reaction profile of **6** + PMe_3. Transition state $\mathbf{G}^{\ddagger}$ is the transition state found when partial CH_3COO^- detachment is allowed. The

possible products **C**-**F** are given in the upper right, with product **F** equivalent to compound **5** isolated experimentally. The numbers in parenthesis are the relative energies with respect to starting materials **6** and PMe_3.

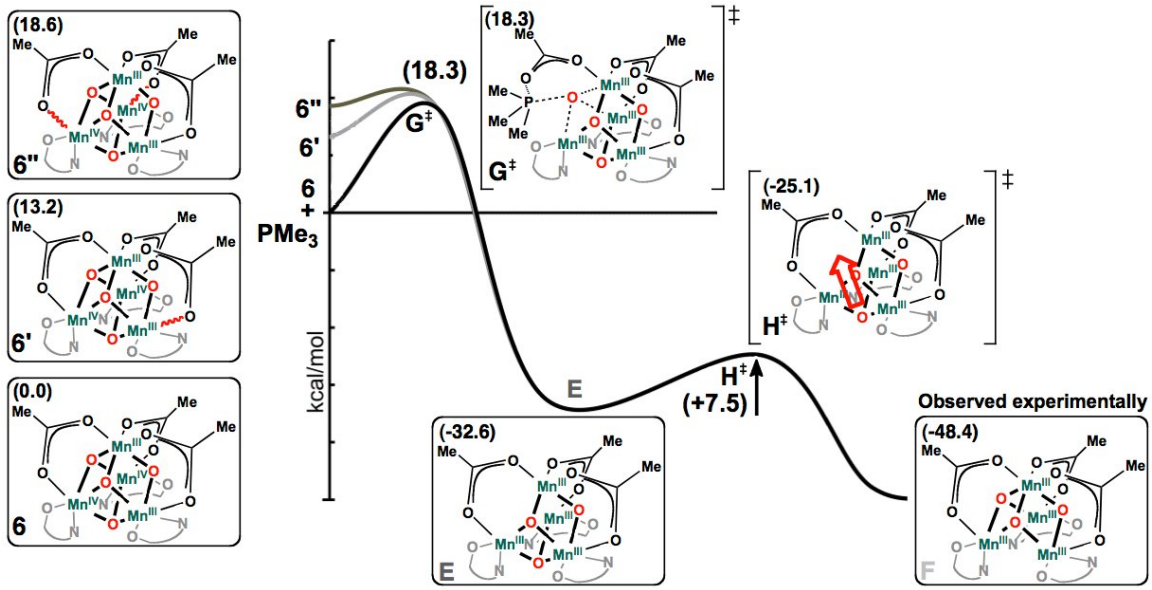

Figure 5.6. QM based mechanism proposed for the reaction of PMe_3 and the Mn_4O_4 cubane model **6**.

5.3 Carboxylate exchange studies.

The difference in the dissociation energies of acetate oxygen from Mn predicted by QM was further explored experimentally by comparison of exchange properties. Solutions of complexes **6**, **8,** and **17** were treated with deuterated acetate ([*n*Bu_4N][CD_3COO]) in 10:1 THF/CH_3CN while the incorporation of isotopic label into the complexes was monitored by ESI-MS. In agreement with QM, we found rapid equilibration (<1 min) to a statistical mixture of isotopologues for complex **6**, whereas **8** and **17** did not reach equilibrium within 50 minutes (Figure 5.23). These results are

consistent with the Mn^{III} sites of **6** being more labile due to electrons in the M-O sigma-antibonding orbital leading to weaker metal-ligand bonds.

*5.4 Oxidative incorporation of H_2O into **5***

Incorporation of water into the OEC during turnover is fundamental to the catalysis. Therefore, we studied conversion of partial cubane **5** to **6** to elucidate the mechanism for such oxido-ligand incorporation into multinuclear manganese-oxido systems. This transformation corresponds formally to low S-state (S_{-1} to S_1) conversion. The metal oxidation states (Mn^{III} and Mn^{IV}), the nature of the bridging oxido moiety, and the complexity of the cluster are all relevant to the mode of action of the OEC during catalysis. Preliminary studies found that trimethylamine-N-oxide, tert-butylhydroperoxide and cumene hydroperoxide did not react with **5** over days, whereas exposure to iodosobenzene generated **6** in one hour (Scheme 5.2). Treatment of **5** with a stoichiometric amount of water resulted in no reaction (^{1}H NMR spectroscopy). In the presence of hydroxide and water (ca. 30 equiv. H_2O and **6** equiv. NR_4OH, R = Me, Et) in THF/CH_3CN, we observed decomposition of complex **5** over hours. Ferrocenium matches the potential window for the oxidation of **5** but not of the desired product, **6** (See Chapter 3, Figure 3.6). Addition of ferrocenium hexafluorophosphate to **5** in the presence of water in THF/CH_3CN (10:1) led to formation of **6** but in low yield and in a mixture with unidentified products. Finally, when we added an excess of ferrocenium hexafluorophosphate (4 equiv.) alongside water (20-30 equiv.) and hydroxide (2 equiv.), we found that **6** was generated as the major product within

minutes (Scheme 5.2). *These experiments indicate that both base and oxidant are necessary for incorporation of oxygen from water in this system.*

Oxidative incorporation of water has been demonstrated for a dimanganese system; if dissolved in water and exposed to air, a Mn^{III}–(μ-O)–Mn^{III} complex turned into a Mn^{III}–$(\mu\text{-O})_2$–Mn^{IV} complex.[29] Also, addition of chloride to a $Mn^{III}_4O_2$ 'butterfly' complex facilitated a disproportionation that gave a one-electron oxidized $Mn^{III}_3Mn^{IV}O_3Cl$ cubane.[22a] *The present protocol mimics the biological incorporation of an oxido ligand into the OEC: water, oxidizing equivalents, and base are all necessary in this two-electron, two proton process with a tetramanganese cluster.* This reaction is important both to OEC turnover and to assembly. Although highly efficient, the OEC must be reassembled frequently under full solar flux due to photooxidative damage to the inorganic cluster and D1 peptide.[30] The process by which the OEC is assembled, called photoactivation,[24] uses Mn^{2+}, Ca^{2+}, Cl^-, bicarbonate, water, and oxidizing equivalents generated by light absorption.[31] Significant advances have defined kinetically distinct species in photoactivation,[32] and the current transformation corresponds conceptually to the putative final steps, the conversion of S_{-1} to S_1.

5.5 Isotopic labeling studies of H_2O incorporation.

The above results illustrate a synthetic cycle between Mn_4O_3 **5** and Mn_4O_4 **6** by oxidative incorporation of water and μ_3-oxygen atom transfer. With an understanding of the oxygen atom transfer mechanism (Figure 5.6), an ^{18}O-labeling study was devised to determine where the water oxygen atom is incorporated into the cluster with respect to the ligand framework (i.e., at one of the three 'top' positions or at the central, 'bottom'

position close to the central arene of the ligand). The location of ^{18}O once incorporated provides information about the extent of oxido reorganization during water incorporation into these Mn_4O_n systems, which is relevant to the OEC. We interrogated the regiochemistry of incorporation by subsequent oxygen atom abstraction with phosphine and evaluation of $^{18}O/^{16}O$ distribution in the products.

Labelled base and water ($NMe_4{}^{18}OH$ and $H_2{}^{18}O$) were utilized in the water incorporation conditions (Scheme 5.3, in box). ESI-MS analysis of the products shows a shift by two units of m/z vs. the experiment with natural abundance water and base (Figure 5.7a). This indicates generation of the $Mn_4{}^{16}O_3{}^{18}O$ isotopologue, **6***, as the major product in a mixture of higher isotopologues (labelled $\mathbf{6^T*}$ and $\mathbf{6^B*}$ in Scheme 5.3 for ^{18}O incorporation at the "top" and "bottom" positions, respectively) (see the Experimental Section for quantification of isotopologue ratios and ESI-MS data).[33] Higher ^{18}O-content isotopologues of **6*** could form from water exchange in the starting material **5**, product **6**, or from an intermediate species under the oxidizing water incorporation conditions. Control experiments showed no exchange of ^{18}O from water into either **5** or **6** over the time frame of the water incorporation reaction (< 1 hour; Scheme 5.3). This is consistent with the slow rate of scrambling in Mn_2O_2 complexes and in another Mn_4O_4 cubane system.[34] We found that Complex **6** did not incorporate ^{18}O under the same reaction conditions, showing that the Mn_4O_4 product did not further exchange once fully formed. These experiments taken together suggest that an intermediate species in the conversion of **6** to **5** is responsible for the incorporation of any additional ^{18}O from water. Attempts to isolate intermediate species—for example, a singly oxidized, singly protonated $Mn^{III}{}_3Mn^{IV}O_3(OH)$ species—have been unsuccessful

thus far. The Mn_3CaO_4 and Mn_3ScO_4 cubanes **8** and **17** were also subjected to excess $H_2{}^{18}O$, and showed no exchange over 1 hour.

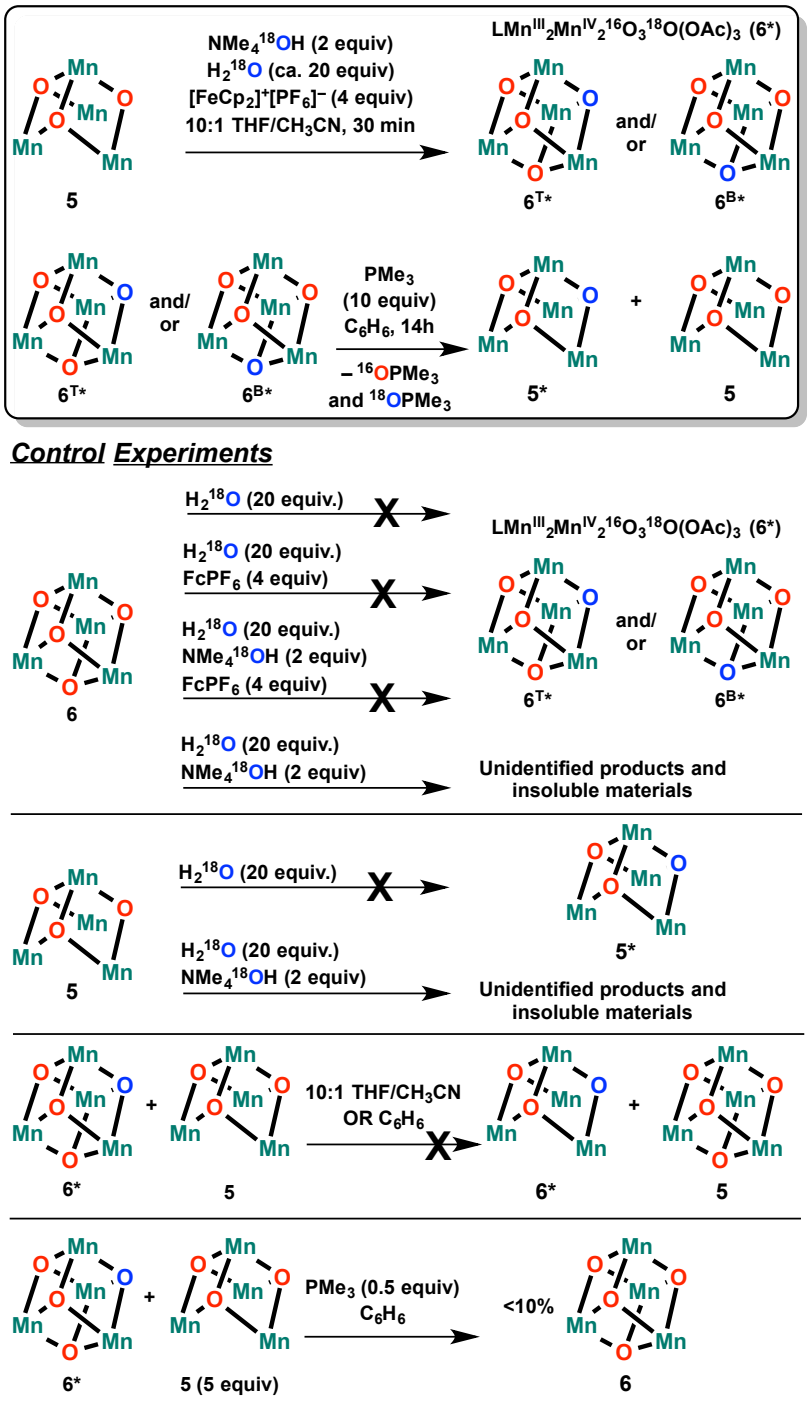

Scheme 5.3. ^{18}O-labeling experiments and controls. All experiments performed in duplicate or greater. Ligand framework **L** is below Mn_4O_n units as drawn in Scheme 5.2.

Complex **6*** was subjected to an excess of PMe_3 in C_6H_6, producing **5*** as major product in mixture with isotopologues (Figure 5.7b; Scheme 5.3).[33a] Labeled $Me_3P^{18}O$ was observed at 95.1 *m/z* along with natural abundance $Me_3P^{16}O$ at 93.1 *m/z* in a ratio of ca. 3:1 $Me_3P^{16}O/Me_3P^{18}O$. To test for the generation of lower nuclearity manganese-oxido species capable of isotopic scrambling, we mixed **5** and **6*** in various solvents and found no isotopic scrambling. Additionally, we treated a mixture of **5** (5 equiv.) and **6*** with substoichiometric amounts of PMe_3 (0.5 equiv) in benzene to test for lower nuclearity species under oxygen atom transfer conditions. Less than 10% increase of unlabelled **6** was observed by ESI-MS (close to our detection limit). These results are consistent with clusters **6** and **5** being robust in solution supporting the direct O-atom transfer from **6** to phosphine, without lower nuclearity intermediates.

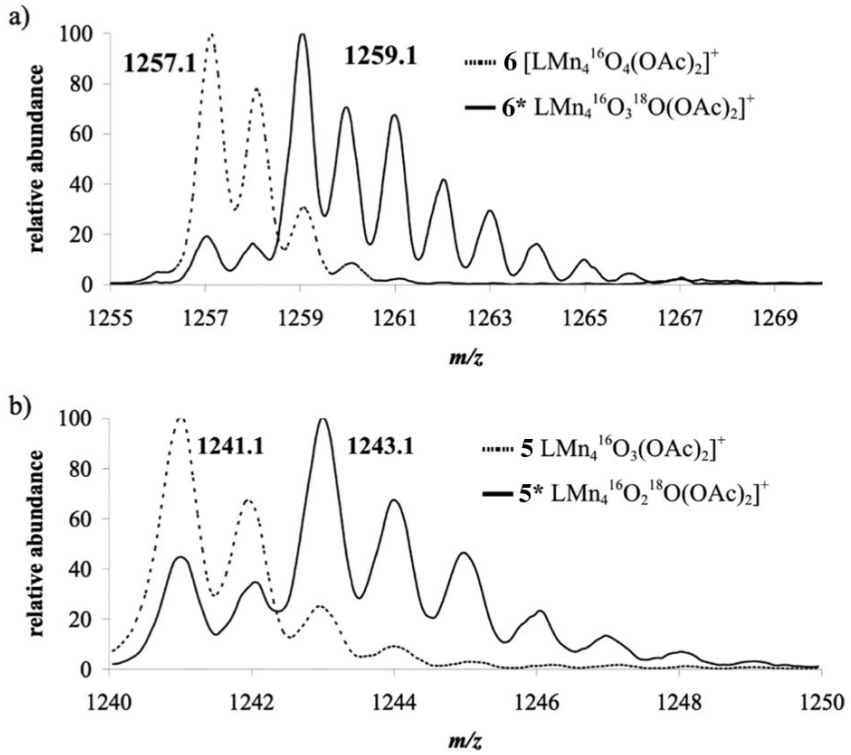

Figure 5.7. Positive ion ESI mass spectrum of labeled and unlabaled **6** (a) and **5** (b). Both fly as cations with one lost acetate.

We analyzed the isotopologue distribution of **5*** and **5** in the context of various mechanistic possibilities for water incorporation and oxygen atom removal (Scheme 5.4). In the first step of the study, water could be incorporated at the bottom, the top, or both positions. These incorporation mechanisms give the isotopomers $\mathbf{6^{B}*}$, $\mathbf{6^{T}*}$, or a mixture of the two. In the second step—oxygen atom transfer—an oxygen atom could hypothetically be removed from top, bottom, or both sites. These removal mechanisms afford a ratio of **5**/**5*** and $^{18}OPMe_3/^{16}OPMe_3$ that is correlated to the mechanism of the first step: incorporation (Scheme 5.4, bottom).

The deceivingly simple mechanism of selective ^{18}O incorporation at the bottom position, which is open, followed by selective removal by PMe_3 from the bottom would be consistent with the observed products/starting materials. However this would give solely unlabeled, natural abundance **5** and fully labeled $Me_3P^{18}O$, which is not observed (Scheme 5.3). If the water were incorporated solely at the top and the bottom oxygen atom was transferred to phosphine, the label location would be opposite: 100% mono-^{18}O labelled **5*** and natural abundance $Me_3P^{16}O$. Because mixtures of **5** and **5*** were observed—as well as Me_3PO and $Me_3P^{18}O$—these two mechanisms can be ruled out, in agreement with the top selective mechanism for oxygen atom transfer to phosphine suggested by the QM studies.[33b] Another mechanism inconsistent with experiment involves water incorporation at the bottom position, followed by selective removal of any of the top three oxidos by PMe_3. This mechanism could be plausible if the lower site were accessible by water and not PMe_3. However, this mechanism would lead to solely **5*** after cluster rearrangement and natural abundance $Me_3P^{16}O$, which again is not observed (Scheme 5.4, right-hand pathway).[33b]

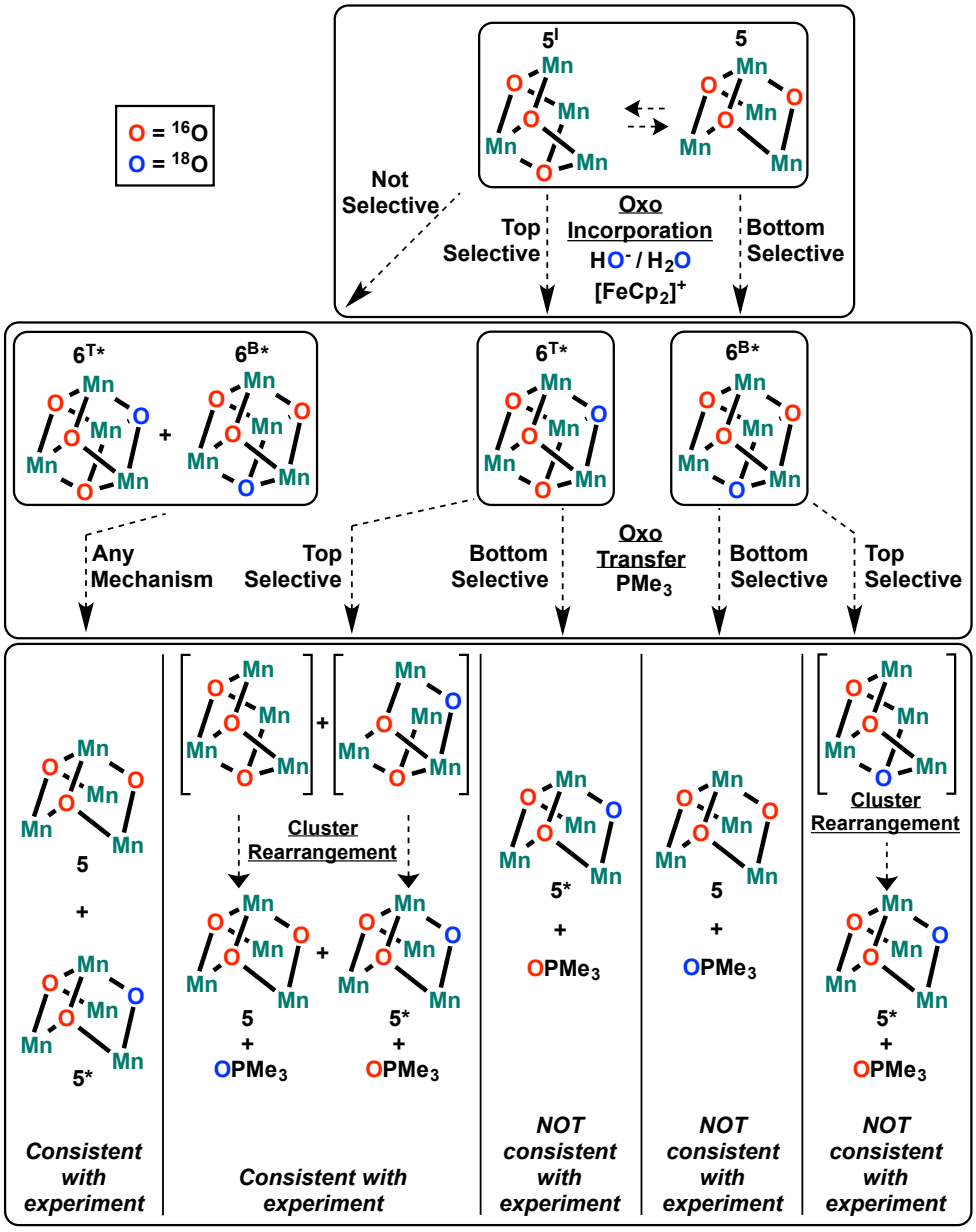

Scheme 5.4. Mechanistic possibilities of water incorporation and removal. Ligand framework **L** is below Mn_4O_n units, as drawn in Scheme 5.2.

A number of mechanisms are consistent with the experimental distributions. If water is selectively incorporated into the top positions, **6^{T}*** is the sole isotopomer of **6*** formed. Selective transfer from the top oxygen sites would then give a 2:1 mixture of

5*/5. If the water incorporation is not selective, then a 3:1 mixture of $\mathbf{6^{T}*/6^{B}*}$ is expected. Any mechanism of oxygen atom transfer would then give a 3:1 mixture of **5*/5** (Scheme 5.5 in the Exp. Sect.). Both mechanisms are roughly consistent with the experimental ratio of ca. 2:1. Intramolecular scrambling after incorporation also predicts isotopologue mixtures for both **5** and Me_3PO, and cannot be distinguished based on the present data.

Given the steric constraints of the ligand framework, the phosphine cannot access directly the bottom oxido of compound **6**, as supported by the high-energy barriers calculated above. Hence, the observed mixture of $Me_3P^{18}O$ and $Me_3P^{16}O$ upon treatment of **6*** with Me_3P suggests that a significant amount of $\mathbf{6^{T}*}$ must be generated upon ^{18}O incorporation from $H_2{}^{18}O$. Isotopomer $\mathbf{6^{T}*}$ may be generated by direct ^{18}O incorporation at the top position upon isomerization of **5** to transfer an oxido to the bottom position or migration within $\mathbf{6^{B}*}$. Either mechanism for ^{18}O-incorporation at the top position involves intramolecular migration of oxido moieties in **6** or **5**. Intermolecular versions of this scrambling process are not supported by our control experiments. Hence, although there is more than one mechanism consistent with the present studies, *all pathways invoke migration of oxido ligands within the clusters during the process of oxidative water incorporation*.

Interestingly, recent computational work suggests that the OEC interconverts between two "sub-state" structures in both the S_1-state[12b] and S_2-state[12c]. Both studies involve μ-O-migration: a μ_3-oxido or hydroxido bonds more strongly to either a Mn in the cubane subsite or to the dangling Mn to form the open-cuboidal structure mentioned above. One report posits that this fluxionality could engender a higher

exchange rate to this oxygen consistent with one of the substrate waters as observed in experimental kinetics studies[35] and ^{17}O Electron–Electron Double Resonance-Detected NMR Spectroscopy[6] studies.

CONCLUSIONS

Oxygen atom transfer reactivity and incorporation was explored for cuboidal Mn_3MO_n complexes (M=Mn, Ca, Sc; n=3,4) displaying μ_3-oxido moieties relevant to the OEC in PSII. High oxidation state heterometallic cubanes $Mn^{IV}{}_3CaO_4$ and $Mn^{IV}{}_3ScO_4$ did not show oxygen atom transfer to trimethylphosphine. In contrast, the $Mn^{III}{}_2Mn^{IV}{}_2O_4$ cubane reacts with this phosphine within minutes to generate a $Mn^{III}{}_4O_3$ partial cubane and trimethylphosphine oxide. Reaction paths were interrogated by QM for oxygen atom transfer from $Mn^{III}{}_2Mn^{IV}{}_2O_4$ and $Mn^{IV}{}_3CaO_4$ (Dr. Mendoza-Cortés and Dr. Nielson). We found that the preferred mechanism involves partial CH_3COO^- ligand dissociation and coordination with PMe_3. This leads to a five-coordinated phosphorous transition state that is 5 to 10 kcal/mol lower than when all CH_3COO^- ligands are attached. This partial dissociation of the CH_3COO^- ligand is accessible only when Mn(III) is present. Experimentally, the rate of exchange between metal-bound acetates and CD_3COO^- was highest for $Mn^{III}{}_2Mn^{IV}{}_2O_4$, in agreement with the QM. These results indicate that even with a strong oxygen atom acceptor such as trimethylphosphine, the oxygen atom transfer chemistry from Mn_3MO_4 cubanes is controlled by ligand lability, with the $Mn^{IV}{}_3CaO_4$ OEC model being unreactive.

The $Mn^{III}{}_4O_3$ partial cubane **5** was isolated cleanly upon oxygen atom transfer, without overreduction. This species was converted back to the full cubane

$Mn^{III}_2Mn^{IV}_2O_4$ with water as oxygen source, base, and oxidant, mimicking the biological incorporation of an oxido ligand in the OEC. ^{18}O-labeling experiments were performed via two-step conversions, from $Mn^{III}_4O_3$ to $Mn^{III}_2Mn^{IV}_2O_4$ (with $H_2{}^{18}O$) and back to $Mn^{III}_4O_3$ (with phosphine). Following the extent of $^{18}O/^{16}O$ distribution in the products provided mechanistic insight into this two-electron, two-proton process with respect to the position of incorporation into the partial cubane structure. These isotopic labeling experiments support reaction mechanisms involving migration of oxide moieties within the cluster and are not consistent with selective oxide incorporation at the site available in the starting species, thus supporting the possibility of such migration processes during water incorporation into the OEC during photoactivation and turnover.

EXPERIMENTAL SECTION

Theory/Computation

As the QM studies were performed by Dr. José Mendoza-Cortés and Dr. Robert J. Neilson from the group of Prof. William A. Goddard III, the experimental section was not included here, although their contribution to the story was included above for the sake of completeness. It can be found in the supplemental information of the published paper.[25]

General Considerations

Reactions performed under inert atmosphere were carried out in a glovebox under a nitrogen atmosphere. Anhydrous tetrahydrofuran (THF) was purchased from Aldrich in 18 L Pure-PacTM containers. Anhydrous dichloromethane, diethyl ether, and

THF were purified by sparging with nitrogen for 15 minutes and then passing under nitrogen pressure through a column of activated A2 alumina (Zapp's). Anhydrous N,N-dimethylformamide (DMF) was purchased from Aldrich and stored over molecular sieves. 97% $H_2{}^{18}O$ was purchased from Aldrich and degassed by three freeze-pump-thaw cycles or sparging with N_2 for 10 minutes. NMR solvents were purchased from Cambridge Isotope Laboratories, Inc. Benzene-d_6 was vacuum distilled from sodium benzophenone ketyl. CD_2Cl_2 was dried over calcium hydride, then degassed by three freeze-pump-thaw cycles and vacuum-transferred prior to use. Celite was activated by heating under vacuum at 200 ºC for 12 hours. ^{1}H NMR and ^{31}P NMR spectra were recorded on a Varian 300 MHz instrument, with shifts reported relative to the residual solvent peak (^{1}H) or a phosphoric acid external standard (^{31}P). Elemental analyses were performed by Midwest Microlab, LLC, Indianapolis, IN. Electrospray Ionization Mass Spectrometry was performed in the positive ion mode using an LCQ ion trap mass spectrometer (Thermo) at the California Institute of Technology Mass Spectra Facility.

Unless indicated otherwise, all commercial chemicals were used as received. Tetrabutylammonium permanganate,[36] iodosobenzene,[37] and $Mn(OTf)_2{\bullet}CH_3CN$[38] were prepared according to literature procedures. Tetrabutylammonium acetate-d_3 (nBu$_4$N$^+$O$_2$CCD$_3^-$) was made by neutralization of a 1.0M nBu$_4$NOH solution in methanol (Sigma-Aldrich) with d_4-acetic acid (Cambridge) and removal of volatiles under vacuum at 40-50 ºC over 6 hours. *Caution*! Tetrabutylammonium permanganate and iodosobenzene are potentially explosive and should be used only in small quantities.

Synthetic procedures

Synthesis of 1,3,5-Tris(2-di(2'-pyridyl)hydroxymethylphenyl)benzene (H_3L): See Chapter 2.

Synthesis of $LMn^{II}_3(OAc)_3$ (1). See Chapter 2.

Synthesis of $LMn^{III}_2Mn^{IV}_2O_4(OAc)_3$ (6). See Chapter 3.

Synthesis of $LMn^{III}_4O_3(OAc)_3$ (5). See Chapter 3.

Synthesis of $LMn^{IV}_3CaO_4(OAc)_3$•THF (8). See Chapter 4.

Synthesis of $LMn^{IV}_3ScO_4(OAc)_3(OTf)$ (17). (performed by Dr. Emily Tsui) In the glovebox, a scintillation vial equipped with a stir bar was charged with **8** (0.101 g, 0.073 mmol) and $Sc(OTf)_3$ (0.036 g, 0.073 mmol, 1.0 equiv). DMF (3 mL) was added, and the dark red-brown solution was stirred at room temperature for 5 minutes. Diethyl ether (35 mL) was added to precipitate a dark red-brown solid. The precipitate was collected by filtration, then recrystallized from acetonitrile/diethyl ether to afford the product as dark brown crystals (0.069 g, 65 %). ^{1}H NMR (CD_2Cl_2, 300 MHz): δ 12.1, 11.8, 9.5, 8.0, 6.2, 4.4, -1.1, -23.8 ppm. ^{19}F NMR (CD_2Cl_2): δ -77.5 ppm. UV-Vis (CH_2Cl_2, λ_{max} [ε (M^{-1} cm^{-1})]): 243 (6.6×10^4), 350 (shoulder, 1.2×10^4). Anal. Calcd. for $C_{64}H_{48}F_3Mn_3N_6O_{16}SSc$: C, 52.80; H, 3.32; N, 5.77. Found: C, 53.07; H, 3.41; N, 5.65.

*Reactivity comparison of **6** and **8** and **17** with PMe_3*

In the glovebox, **6** (0.0091 g, 0.0069 mmol), **8** (0.0095 g, 0.0069 mmol), and **17** (0.0079 g, 0.0054 mmol), respectively, were dissolved in 0.8 mL (0.7 mL for **17**) of a DMF solution of $[PPh_4][BF_4]$ (3.4 mg, 0.0079 mmol, 1.14 equiv for **6** and **8**; 2.3 mg, 0.0054 mmol, 1.0 equiv for **17**) and transferred to separate J. Young NMR tubes (PPh_4^+ serves

as an internal standard). A solution of PMe_3 (18 μL, 0.78 M in THF, 0.014 mmol, 2.0 equiv for **6** and **8**; 20 μL, 0.78 M in THF, 0.015 mmol, 2.9 equiv for **17**) was added via syringe to both mixtures, and the tubes were sealed with Teflon caps. The reactions were monitored using ^{31}P NMR spectroscopy referenced to an external standard of 85% H_3PO_4.

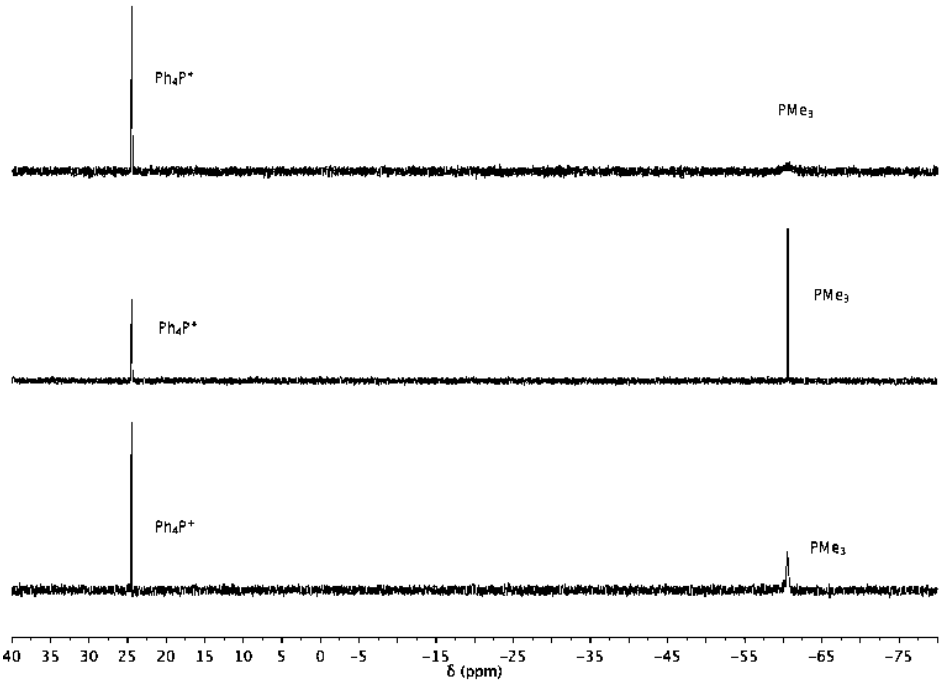

Figure 5.8. ^{31}P NMR spectra of the reaction of **6** and PMe_3 (top), **8** and PMe_3 (middle), and **17** and PMe_3 (bottom) in DMF after 15 minutes at RT. $[PPh_4][BF_4]$ (1 equiv) is present as an internal standard.

Within 15 minutes at RT, ^{31}P NMR spectroscopy of the reaction with **6** indicates consumption of one equivalent of PMe_3 as well as a broadened PMe_3 signal (Figure 5.8). No signal corresponding to $OPMe_3$ is observed. ^{31}P NMR spectroscopy of the solutions of **8** and **17** show no consumption of PMe_3 (Figure 5.8). No changes in the ^{31}P NMR

spectra of the mixtures containing **6** and **8** are observed after 18 hours at RT (Figure 5.9). Approximately one equivalent of PMe_3 has been consumed in the reaction containing **17**, though no $OPMe_3$ is detected by GC-MS, likely indicating an alternate decomposition route not involving oxygen-atom transfer.

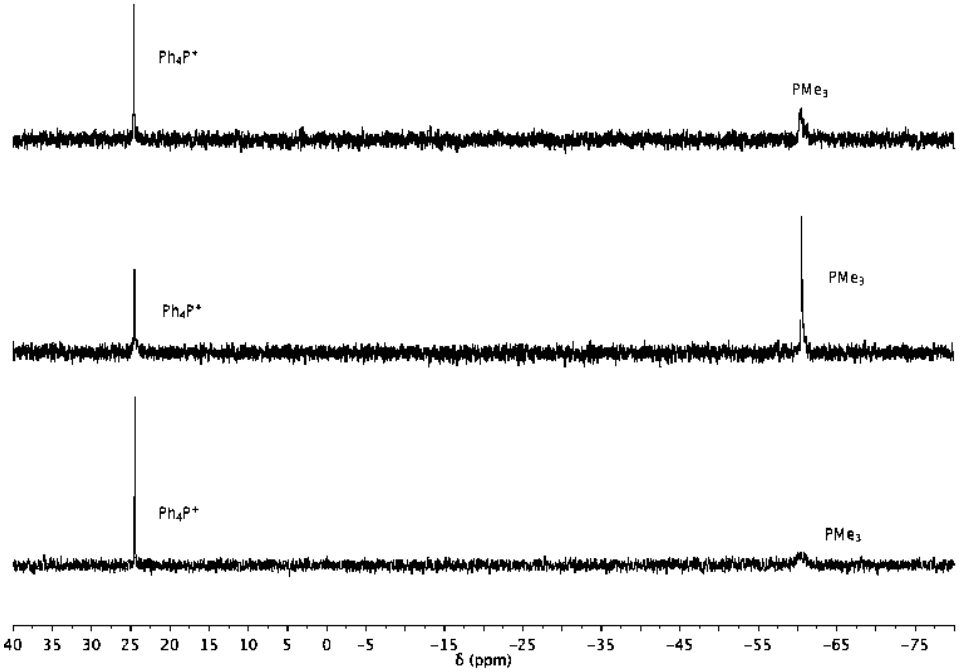

Figure 5.9. ^{31}P NMR spectra of the reaction of **6** and PMe_3 (top), **8** and PMe_3 (middle), and **17** and PMe_3 (bottom) in DMF after 18 hours at RT. $[PPh_4][BF_4]$ (1 equiv) is present as an internal standard.

Cyclic Voltammetry

Electrochemical measurements were recorded under a nitrogen atmosphere in an MBraun glovebox at 25 °C with a Pine Instrument Company AFCBP1 bipotentiostat. An auxiliary Pt-coil electrode, a Ag/Ag^+ reference electrode (0.01 M $AgNO_3$ in CH_3CN), and a 3.0 mm glassy carbon electrode disc (BASI) were used. Data were

recorded using the Pine Instrument Company AfterMath software package. All reported values were referenced to an internal ferrocene/ferrocenium couple. The electrolyte solutions were 0.1 M $^{n}Bu_4NPF_6$ in DMF, dimethylacetamide (DMA) or THF.

Magnetism Studies

General Considerations. DC magnetic susceptibility measurements were carried out in the Molecular Materials Research Center in the Beckman Institute of the California Institute of Technology on a Quantum Design MPMS instrument running MPMS MultiVu software. Powdered samples (0.040–0.059 g) were fixed in eicosane (0.10–0.12 g) in gelatin capsules or in plastic wrap and suspended in clear plastic straws. Data were recorded at 0.5 T from 4–300 K. Diamagnetic corrections were made using the average experimental magnetic susceptibility of **H_3L** at 0.5 T from 100–300 K (-593×10^{-6} cm^3/mol) in addition to the values of Pascal's constants for amounts of solvent quantified for each sample using elemental analysis.

Discussion. See Chapter 3 for magnetic studies of complex **6**.

For **8**, dominant ferromagnetic coupling between Mn ions is observed (Figure 5.10); at 6 K, the $\chi_M T$ value increases to a maximum of 7.5 cm^3 mol^{-1} K, which is slightly lower than the expected spin-only value of a S = 9/2 system (10.0 cm^3 mol^{-1} K, g = 1.8), but greater than the expected spin-only value of a S = 7/2 system (6.4 cm^3 mol^{-1} K, g = 1.8). The $\chi_M T$ value decreases from the maximum below 6 K, likely due to low temperature effects such as intermolecular exchange interactions. At 300 K, the $\chi_M T$

value approaches 4.7 cm^3 mol^{-1} K, which is close to the expected spin-only value of three uncoupled Mn^{IV} ions (S = 3/2, 1.5 cm^3 mol^{-1} K, g = 1.8).

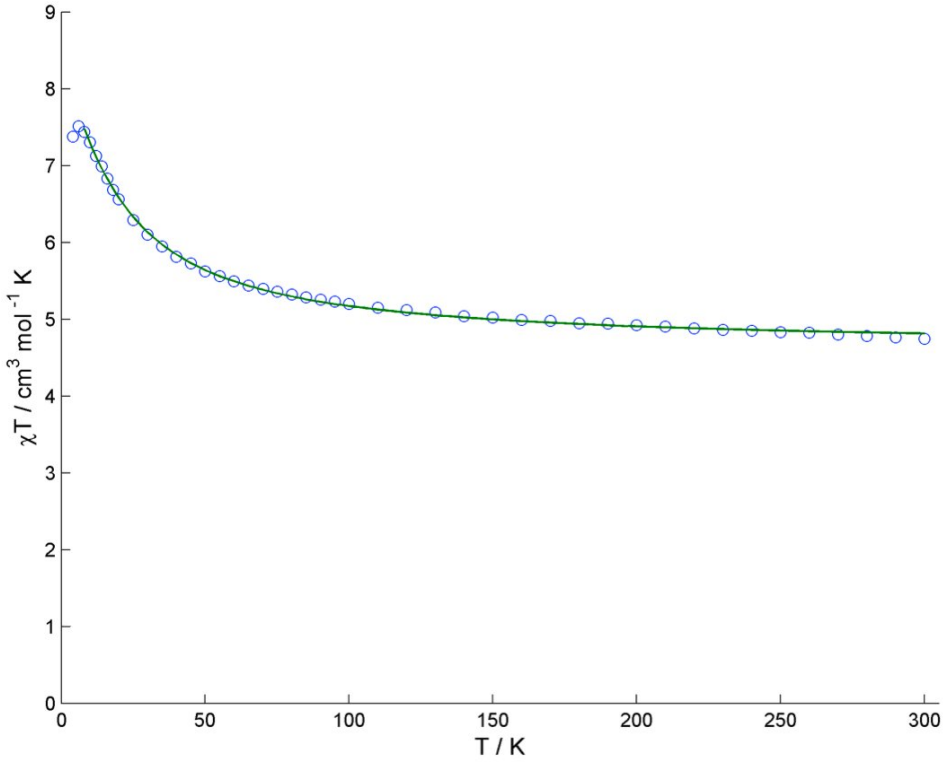

Figure 5.10: $\chi_M T$ vs. T data (circles) and fit (line) for compound **8** (See Chapter 3 for compound **6**). See Table 5.1 for fit parameters.

The $\chi_M T$ data taken at 0.5 T of **8** were fit to the magnetic susceptibility equation derived from the isotropic spin Hamiltonian for two coupling constants, J_1 and J_2 [Eq. (1)], where the exchange pathways between the three Mn^{IV} centers are modeled as an isosceles triangle (Figure 5.11).

$$\hat{H} = -2J_1[(\hat{S}_A \bullet \hat{S}_B) + (\hat{S}_A \bullet \hat{S}_C)] - 2J_2(\hat{S}_B \bullet \hat{S}_C) \quad (1)$$

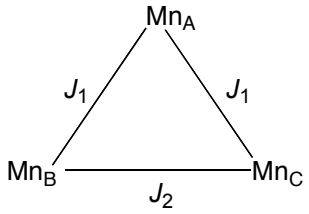

Figure 5.11. Exchange coupling model employed for **8**. The spins used were three S = 3/2.

Table 5.1. Magnetic susceptibility fitting parameters.

Compound	Diamagnetic Correction ($\times 10^{-6}$ cm^3/mol)	J_1 (cm^{-1})	J_2 (cm^{-1})	g	R ($\times 10^{-5}$)
$LMn^{IV}_3CaO_4(OAc)_3$•3DMF (**8**)	–721	3.5	-1.8	1.81	2.2

The eigenvalues were determined using the Kambe method.[39] and the data were fit from 10–300 K using Matlab[40] by minimizing $R = \sum |(\chi_M T)_{obs} - (\chi_M T)_{calc}|^2 / \sum (\chi_M T)^2_{obs}$ (Table 5.1) to give J_1 = 3.5 cm^{-1} and J_2 = –1.8 cm^{-1}. The larger absolute value of J_1 leads to the dominant ferromagnetic interactions observed in the low temperature susceptibility data, but the relatively weak coupling observed may lead to population of higher energy lower spin states even at low temperatures. A related [$Ca_2Mn^{IV}_3O_4$] cluster prepared by Christou and co-workers showed similar exchange interactions, with J_1 = 40.5 cm^{-1} and J_2 = –10.8 cm^{-1}.[19b] The stronger coupling observed between the Mn^{IV} centers of the latter complex may be due to the more acute Mn-O-Mn angles [92.11(11)-96.81(12)º] compared to the greater Mn-O-Mn angles [95.09(9) -100.25(10)º] of complex **8**, since exchange interactions are known to be greatly affected by angle changes.[19b]

Note: More recent magnetism data was collected and analyzed by Dr. Emily Tsui and can be found on page 117 in Chapter 4 of her thesis. The parameters change slightly, but the main conclusions herein still hold true.

^{18}O Labeling Studies

ESI-MS Procedures. In a nitrogen glovebox, samples were dissolved in anhydrous, degassed CH_2Cl_2 and diluted to ~10 μM in M.S. vials. These vials were then transferred to 20 mL vials that were then capped and taped shut with electrical tape. Separately, a small sample of anhydrous, degassed CH_2Cl_2 in a 4 mL vial was capped and taped. These were removed from the glovebox and taken immediately to the instrument. After rinsing the line and inlet with wet, aerobic CH_2Cl_2, the line was rinsed quickly with the anhydrous, degassed CH_2Cl_2 followed immediately by the sample. The spectra shown are averages of ≥70 scans.

Synthetic/Control Procedures. All experiments performed in duplicate or greater. Mass spectra corresponding to each experiment are included directly below said experiment.

Enrichment of NR_4OH with ^{18}O. In an anaerobic, water-containing glovebox, the desired amount (generally <10μmol) of $NMe_4OH•5H_2O$ (solid) or 35 wt. % NEt_4OH in H_2O (solution) was weighed out. For NEt_4OH, excess H_2O was removed first *in vacuo*. Ca. 10 μL 97% $H_2{}^{18}O$ was added, full dissolution of the white solid was observed, and

then volatiles were removed *in vacuo*. This procedure was repeated a total of three times to afford ca. 96% 18-labelled $NR_4{}^{18}OH$.

Synthesis of $LMn^{III}{}_2Mn^{IV}{}_2{}^{16}O_3{}^{18}O(OAc)_3$ (6*). In an anaerobic, water-containing glovebox, **5** (3.8 mg, 0.003 mmol) was dissolved in THF (1.2 mL). In a separate flask, $NMe_4OH{\bullet}5H_2O$ (1.1 mg, 0.006 mmol) was enriched with ^{18}O by the method above. $H_2{}^{18}O$ (1.1μL, 0.060 mmol) was added to the $NMe_4{}^{18}OH$, followed by CH_3CN (0.07 mL) and THF (0.2 mL). In a third flask, $FcPF_6$ (3.9 mg, 0.012 mmol) was dissolved in CH_3CN (0.07 mL) and THF (0.2 mL). While stirring the solution of $NMe_4{}^{18}OH$ and $H_2{}^{18}O$, the solution of **5** was added by syringe, followed by a rinse of the syringe with THF (0.2 mL). One minute after addition of **5**, the $FcPF_6$ solution was added, and the syringe was again rinsed with THF (0.2 mL) and CH_3CN (0.06 mL). The final concentration is 1.33mM in 10:1 THF/CH_3CN. The red-orange solution turns green-brown upon addition of the dark blue $FcPF_6$. Volatiles were removed *in vacuo* after 35 minutes of stirring. The resulting green-brown solid was triturated in Et_2O and filtered to remove ferrocene. The solid was then rinsed with benzene to afford a red-orange solution of **6*** and blue solid (excess $FcPF_6$). The solution was concentrated *in vacuo* to afford the red-orange powder **6***.

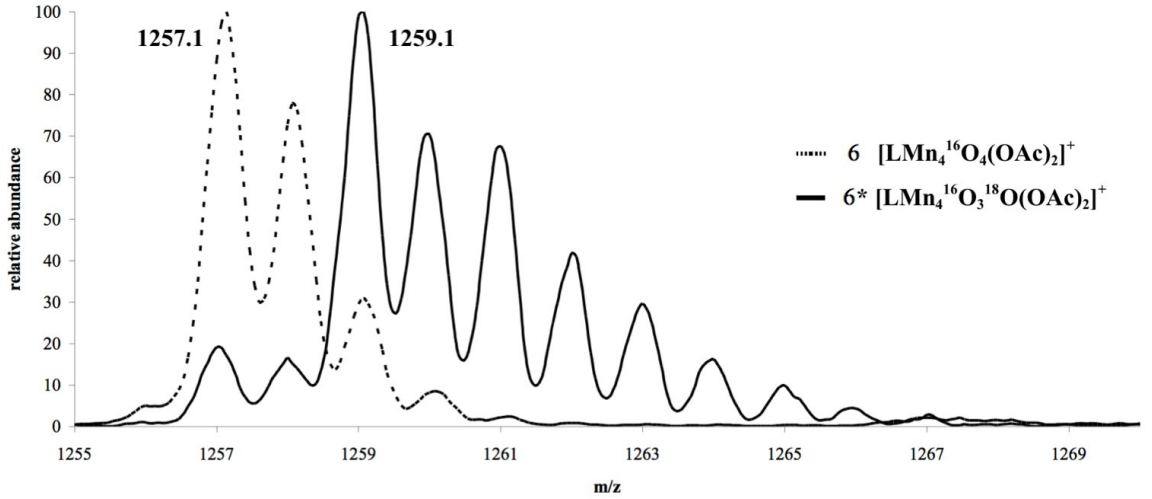

Figure 5.12. Electrospray Ionization Mass Spectra of compound **6** (solid line) isolated from the labeling experiments and natural abundance compound **6** (dashed line). The 1257.1 and 1259.1 peaks correspond to the unlabeled and labeled mass with one acetate lost from the parent ion—$LMn_4O_4(OAc)_2^+$. Conditions: **5** (1 equiv.), $NMe_4{}^{18}OH$ (2 equiv.), $H_2{}^{18}O$ (ca. 20 equiv.), $FcPF_6$ (4 equiv.), 10:1 THF/CH_3CN, RT, 35 minutes.

Synthesis of $LMn^{III}{}_4{}^{16}O_2{}^{18}O(OAc_3$ (3*). See Method B in the synthesis of **5** (labeled **5**) in Chapter 3.

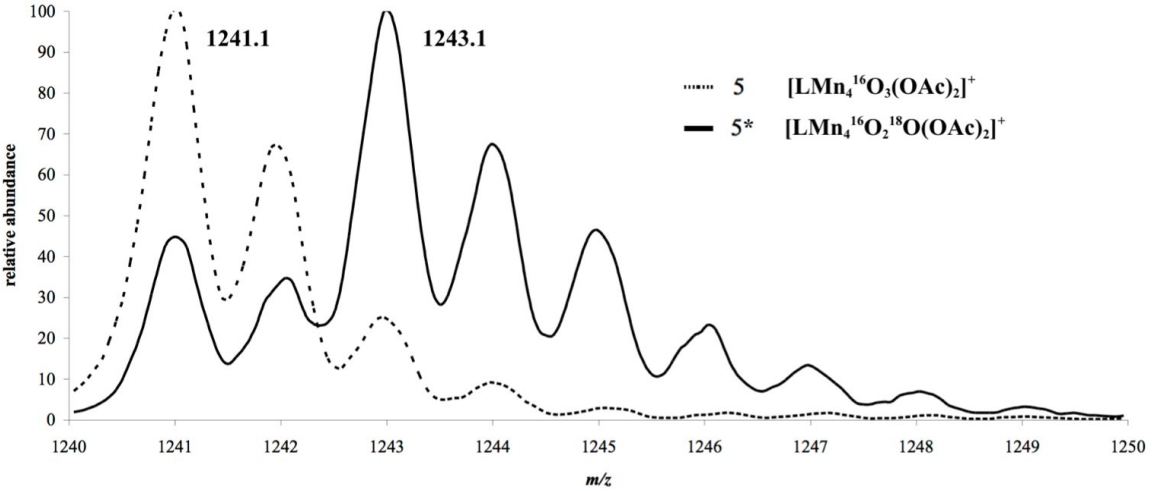

Figure 5.13. Electrospray Ionization Mass Spectra of natural abundance **5** (dashed lines) isolated from the reaction of unlabeled **6** and compound **5*** (solid line) isolated

from the reaction of labeled **6*** with PMe_3. The 1241.1 and 1243.1 peaks correspond to the unlabeled and labeled mass with one acetate lost from the parent ion—$LMn_4O_3(OAc)_2^+$. Reaction Conditions: **6*** (1 equiv.), PMe_3 (10 equiv.), C_6H_6, RT, 24 hours.

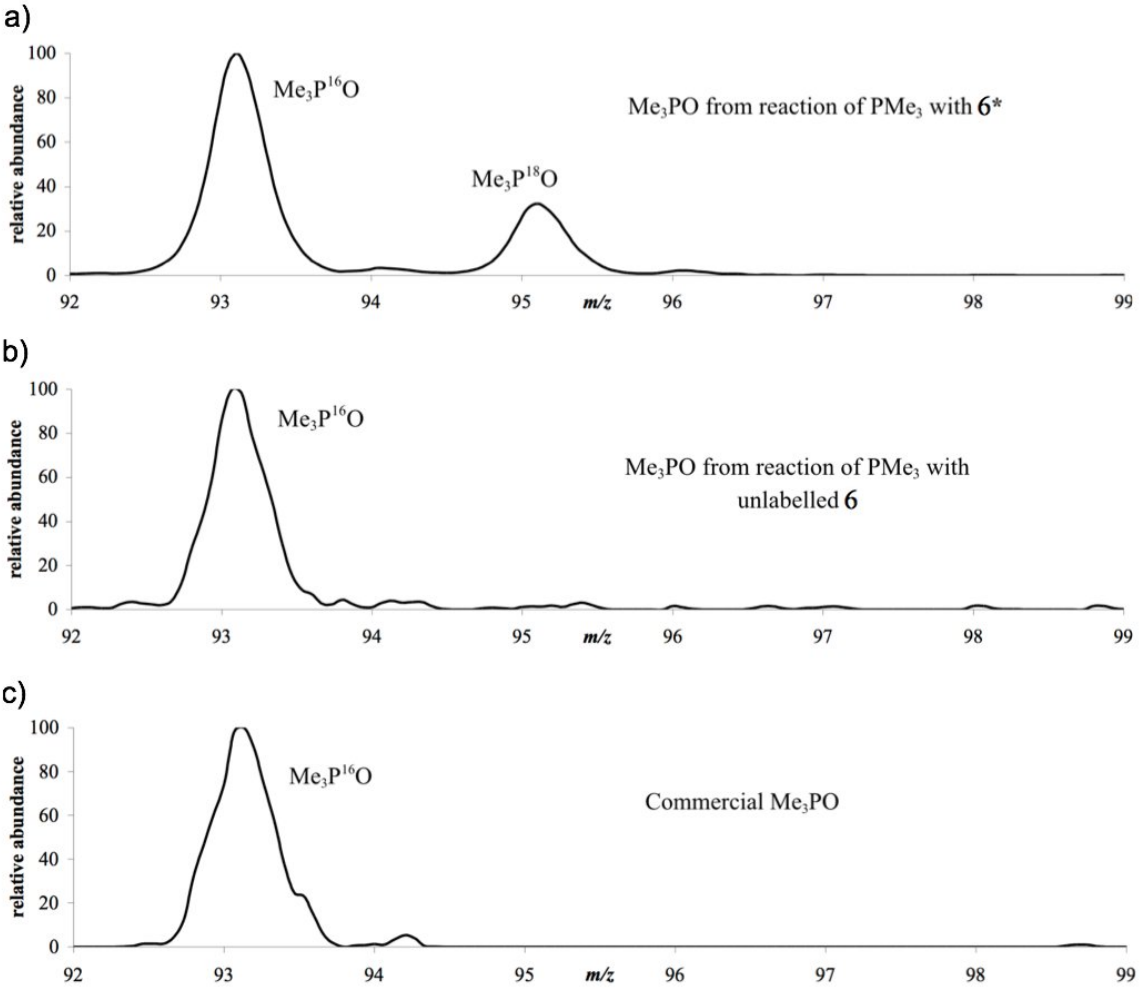

Figure 5.14: Electrospray Ionization Mass Spectra of a) trimethylphosphine oxide isolated from the reaction of PMe_3 with **6***, b) trimethylphosphine oxide isolated from the reaction of PMe_3 with unlabeled **6**, and c) commercial trimethylphosphine oxide (Alfa Aesar).

6 + $H_2^{18}O$ Control. In an anaerobic, water-containing glovebox, **6** (4 mg, 0.003 mmol) was dissolved in 10:1 THF/CH_3CN (2.3 mL) to give a 1.33 mM solution (the

concentration used in the water incorporation experiments). $H_2{}^{18}O$ (1.1 μL, 0.060 mmol) was added by syringe and the solution was stirred for 35 minutes (the time course of the water incorporation experiments). Volatiles were removed *in vacuo*. The resulting solid was rinsed with dry Et_2O and rinsed through with C_6H_6 and concentrated *in vacuo*.

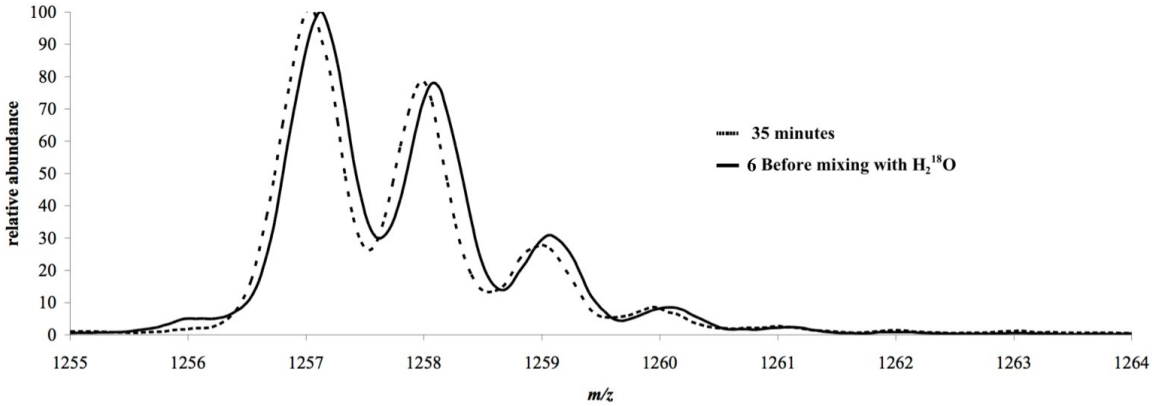

Figure 5.15. Electrospray Ionization Mass Spectra of natural abundance **6** (solid line) and compound **6** (dashed line) after stirring for 35 minutes in the presence of $H_2{}^{18}O$. Conditions: **6** (1 equiv.), $H_2{}^{18}O$ (20 equiv.), 10:1 THF/CH_3CN, 35 minutes, RT.

5 + $H_2{}^{18}O$ Control. In an anaerobic, water-containing glovebox, **5** (3.9 mg, 0.003 mmol) was dissolved in 10:1 THF/CH_3CN (2.3 mL) to give a 1.33 mM solution. $H_2{}^{18}O$ (1.1 μL, 0.060 mmol) was added by syringe and the solution was stirred for 35 minutes. Volatiles were removed *in vacuo*. The resulting solid was rinsed with dry Et_2O and rinsed through with C_6H_6 and concentrated *in vacuo*.

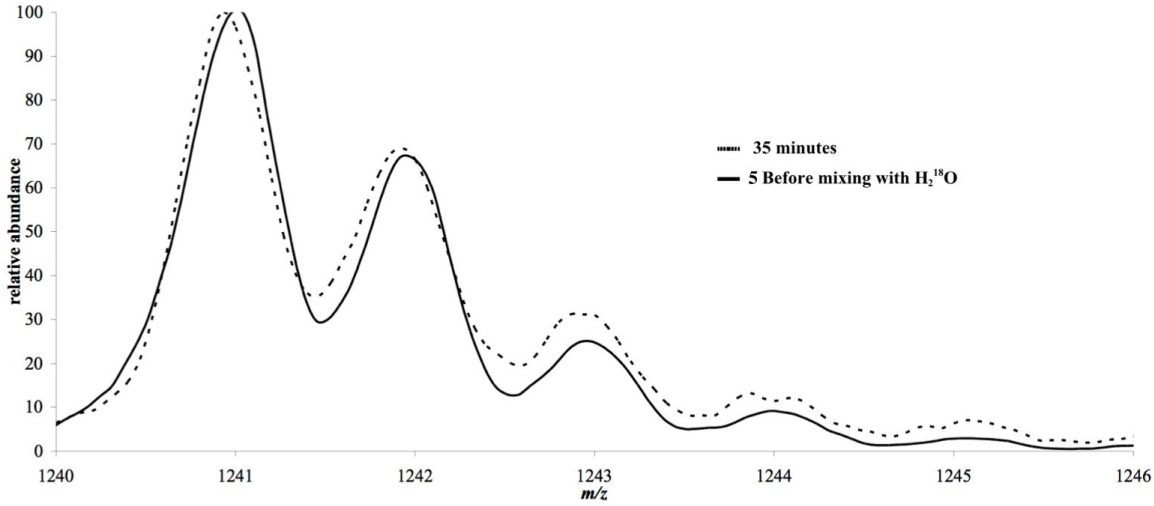

Figure 5.16: Electrospray Ionization Mass Spectra of natural abundance **5** (solid lines) and compound **5** (dashed lines) after stirring for 35 minutes in the presence of $H_2{}^{18}O$. Conditions: **5** (1 equiv.), $H_2{}^{18}O$ (20 equiv.), 10:1 THF/CH_3CN, 35 minutes, RT.

6 + $H_2{}^{18}O$ + $FcPF_6$ Control. In an anaerobic, water-containing glovebox, **6** (3.8 mg, 0.003 mmol) was dissolved in THF (1.6 mL). In a second flask, $FcPF_6$ (3.8 mg, 0.012 mmol) was dissolved in CH_3CN (0.10 mL) and THF (0.2 mL). $H_2{}^{18}O$ (1.0 μL, 0.060 mmol) was added to the solution of **6**, followed one minute later by the $FcPF_6$ solution. The syringe was rinsed with THF (0.2 mL) and CH_3CN (0.10 mL). The final concentration is 1.33 mM in 10:1 THF/CH_3CN. The red-orange solution turns green-blue upon addition of the dark blue $FcPF_6$. Volatiles were removed *in vacuo* after 35 minutes of stirring. The resulting green-brown solid was triturated in dry Et_2O and filtered. The solid was then rinsed with benzene to afford a red-orange solution of **6** and blue solid (excess $FcPF_6$). The solution was concentrated *in vacuo* to afford a red-orange powder of **6**.

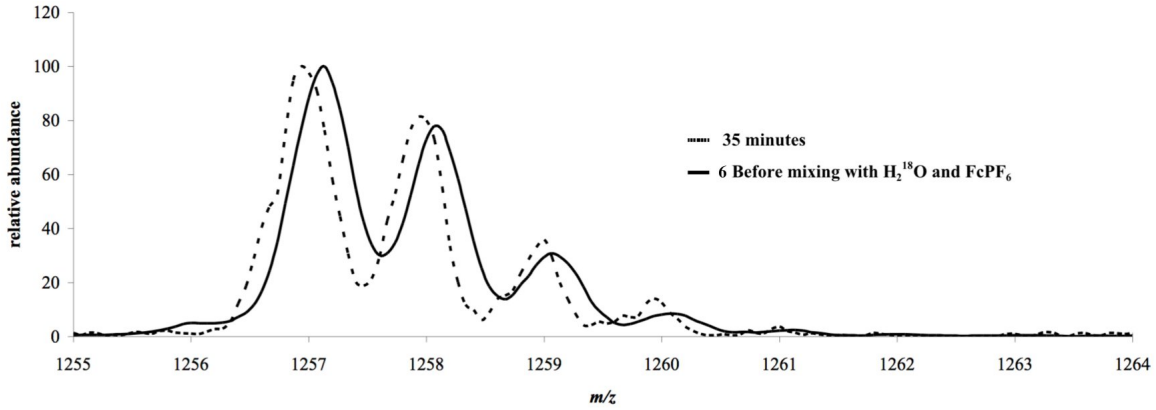

Figure 5.17. Electrospray Ionization Mass Spectra of natural abundance **6** (dashed lines) and compound **6** (solid lines) after stirring for 35 minutes in the presence of $H_2{}^{18}O$ and $FcPF_6$. Conditions: $H_2{}^{18}O$ (20 equiv.), $FcPF_6$ (4 equiv.), 10:1 THF/CH_3CN, 35 minutes, RT.

6 + $H_2{}^{18}O$ + $NMe_4{}^{18}OH$ + $FcPF_6$ Control. In an anaerobic, water-containing glovebox, **6** (3.9 mg, 0.003 mmol) was dissolved in THF (1.3 mL). In a separate flask, $NMe_4OH \cdot 5H_2O$ (1.1 mg, 0.006 mmol) was enriched with ^{18}O by the method above. $H_2{}^{18}O$ (1.1μL, 0.060 mmol) was added to the $NMe_4{}^{18}OH$, followed by CH_3CN (0.07 mL) and THF (0.2 mL). In a third flask, $FcPF_6$ (3.9 mg, 0.012 mmol) was dissolved in CH_3CN (0.07 mL) and THF (0.2 mL). While stirring the solution of $NMe_4{}^{18}OH$ and $H_2{}^{18}O$, the solution of **6** was added by syringe, followed by a rinse of the syringe with THF (0.2 mL). One minute after addition of **6**, the $FcPF_6$ solution was added, and the syringe was again rinsed with THF (0.2 mL) and CH_3CN (0.07 mL). The final concentration is 1.33mM in 10:1 THF/CH_3CN. The red-orange solution turns green-brown upon addition of the dark blue $FcPF_6$. Volatiles were removed *in vacuo* after 35 minutes of stirring. The resulting green-brown solid was triturated in dry Et_2O and filtered to remove any ferrocene formed. The solid was then rinsed with benzene to

afford a red-orange solution of **6** and blue solid (excess $FcPF_6$). The solution was concentrated *in vacuo* to afford a red-orange powder of **6**.

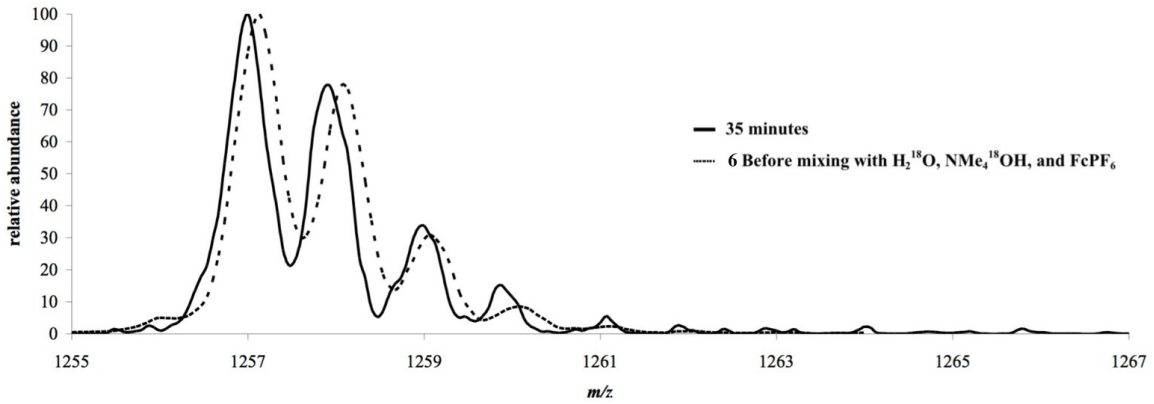

Figure 5.18. Electrospray Ionization Mass Spectra of natural abundance **6** (dashed lines) and compound **6** after stirring for 35 minutes (solid lines) in the presence of $H_2{}^{18}O$, $NMe_4{}^{18}OH$ and $FcPF_6$. Conditions: **6** (1 equiv.), $H_2{}^{18}O$ (20 equiv.), $NMe_4{}^{18}OH$ (2 equiv.), $FcPF_6$ (4 equiv.), 10:1 THF/CH_3CN, 35 minutes, RT.

6* + 5 + PMe_3 Control. In a nitrogen glovebox, **6*** (1.2 mg, 9x10−4 mmol) was mixed with **5** (5.9 mg, 0.005 mmol) as solids. These were dissolved in C_6H_6 (2.7 mL) and PMe_3 was added (10 μL, 50 mM in THF). This solution was allowed to stir, and aliquots were taken and pumped down.

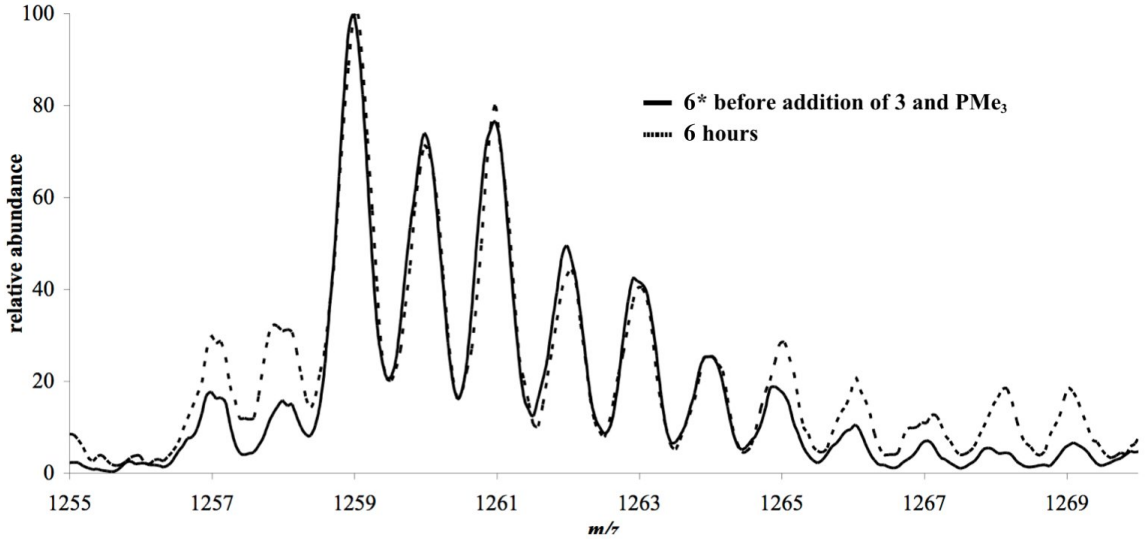

Figure 5.19. Electrospray Ionization Mass Spectra of **6*** before addition of **5** and PMe_3 (solid line) and 2 hours after addition (dashed line). Conditions: **6*** (1 equiv.), **5** (5 equiv.), PMe_3 (0.5 equiv.), C_6H_6, RT.

6* + 5 Control. In a nitrogen glovebox, **6*** (1.0 mg, 0.002 mmol) and **5** (1.0 mg, 0.002 mmol) were mixed as solids. This solid mixture was then dissolved in: 10:1 THF/CH_3CN (1.2 mL to give a solution 1.33 mM in **6***+**5** (0.67 mM in each)); C_6H_6 (0.75 mL to give a solution **6** mM in **6***+**5**). Volatiles were removed *in vacuo* after 35 minutes. The resulting solid was rinsed with dry Et_2O and rinsed through with C_6H_6 and concentrated *in vacuo*.

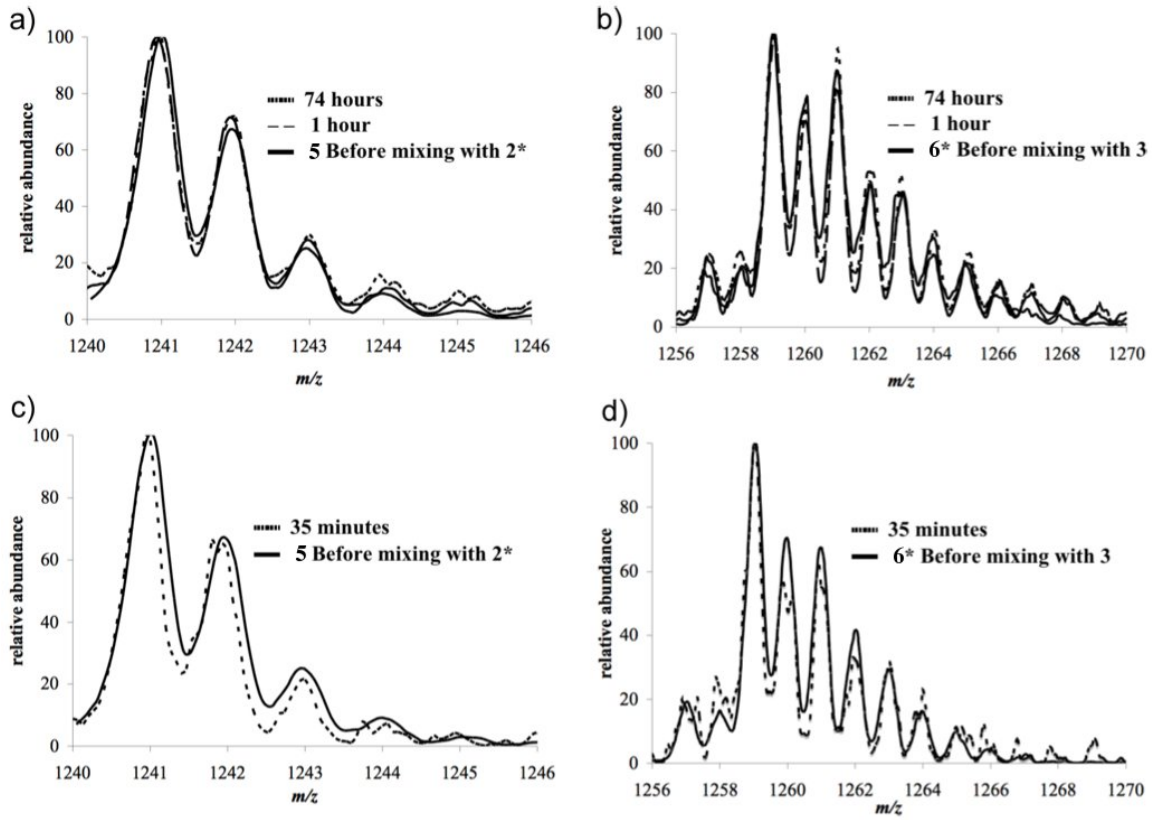

Figure 5.20. Electrospray Ionization Mass Spectra of **5** and **6*** from their mixture in benzene and 10:1 THF/CH_3CN. a) Natural abundance **5** (solid line) before mixture with **6*** and 1 hour (large-dashed line) and 74 hours (short-dashed line) after mixture with **6*** in benzene. b) Labeled **6*** (solid line) before mixture with **5** and 1 hour (large-dashed line) and 74 hours (short-dashed line) after mixture with **5** in benzene. c) Natural abundance **5** (solid line) before mixture with **6*** and 35 minutes (short-dashed line) after mixture with **6*** in 10:1 THF/CH_3CN. d) Labeled **6*** (solid line) before mixture with **5** and 35 minutes (short-dashed line) after mixture with **5** in 10:1 THF/CH_3CN.

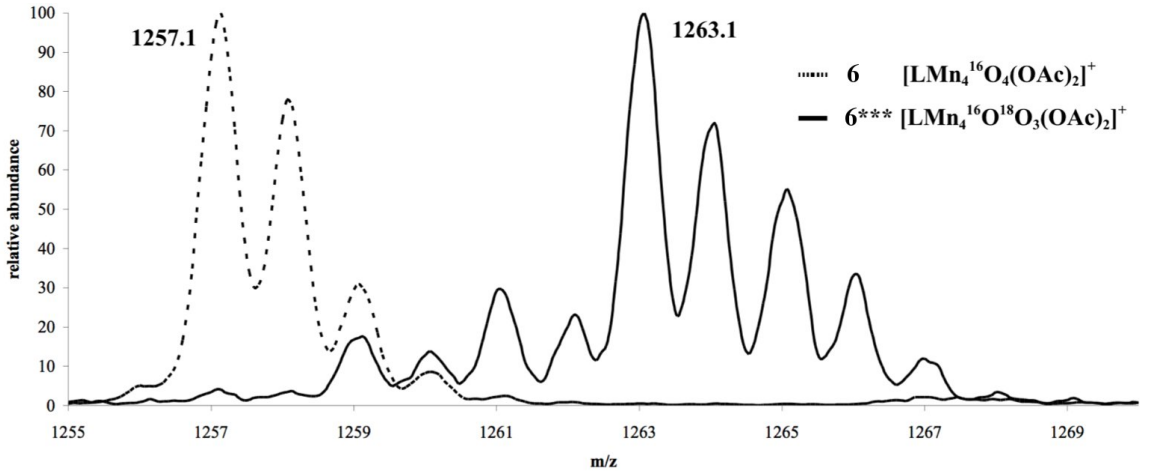

Figure 5.21. Electrospray Ionization Mass Spectra of compound **6** (solid line) isolated from the 2:1 THF/CH_3CN labeling experiment and natural abundance compound **6** (dashed line). The result of majority triple ^{18}O incorporation conditions: **5** (1 equiv.), $NEt_4{}^{18}OH$ (2 equiv.), $H_2{}^{18}O$ (ca. 60 equiv.), $FcPF_6$ (4 equiv.), 2:1 THF/CH_3CN, r.t., 35 minutes.

Quantification of Isotopologue Ratio

For a similar ESI-MS analysis, see ref. 34a. The peak assignments for natural abundance **6** (1257.1 m/z = $LMn_4O_4(OAc)_2^+$ and **5** (1241.1 m/z = $LMn_4O_3(OAc)_2^+$) were based on m/z values and theoretical isotope distribution. The theoretical isotope distribution was obtained by inputting the molecular formulas into the isotope distribution calculator program at http://www.sisweb.com/mstools/isotope.htm. For natural abundance **6**, the distributation is: 1257.1–100% relative abundance, 1258.1–69%, 1259.1–26%, 1260.1–7%, and 1261.1–1%. The same distribution is found for **5**. Therefore, for ^{18}O enriched samples, overlap of the expected isotope distributions for each ^{18}O isotopologue (separated by two m/z units) is expected. Moreover, both the parent (1257.1 m/z) and protonated (1258.1 m/z) species for **6** are observed in the ESI-MS spectrum with variable amounts of protonation from sample to sample (Figure

5.22). If crude **6** was taken from the water incorporation reaction, more protonation was observed; after fractionation with Et_2O and C_6H_6 less protonated **6** was observed. However, a small amount of adventitious protons in the ESI-MS line gave a variable amount of protonated complex and therefore both **6** and $\mathbf{6_{H+}}$ had to be taken into account in the isotopologue ratio calculations. From this, ten masses are expected: **6** at 1257.1, $\mathbf{6_{H+}}$ at 1258.1, **6*** at 1259.1, $\mathbf{6^*_{H+}}$ at 1260.1 through to $\mathbf{6^{****}_{H+}}$ at 1266.1 *m/z*.

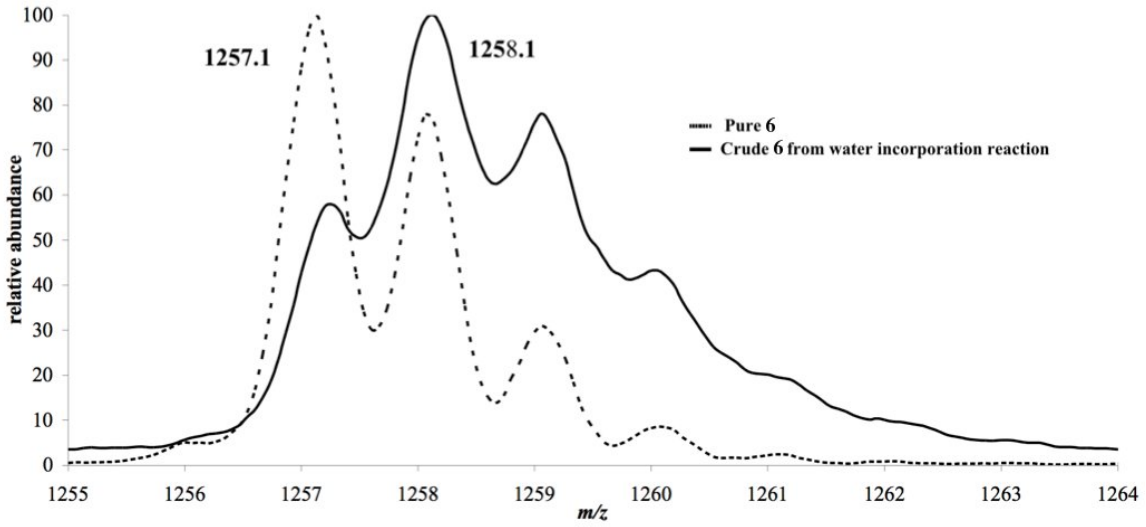

Figure 5.22. Electrospray Ionization Mass Spectra of pure compound **6** (dashed lines) and crude compound **6** isolated from the natural abundance H_2O control experiment (solid line). The 1257.1 and 1258.1 peaks correspond to the unprotonated and protonated mass with one acetate lost from the parent ion - $LMn_4O_4(OAc)_2^+$and $[LMn_4O_4(OAc)_2]H^+$. Natural abundance control experiment conditions: **5** (1 equiv.), NMe_4OH (2 equiv.), H_2O (ca. 30 equiv.), $FcPF_6$ (4 equiv.), THF/CH_3CN, RT, 30 minutes.

To quantify the amount of each isotopologue of **6** and $\mathbf{6_{H+}}$, let p_i represent the theoretical isotope distribution, with $p_1 = 0.69$, $p_2 = 0.26$ … $p_4 = 0.01$. Let T_{m+n} represent the observed relative abundance (total peak height observed in the spectrum) at mass $m+n$, with m representing the first mass (1257.1) and n = 0,1,2…9. Thus each value of

$m+n$ represents one of the ten masses from **6** to **6****$_{H+}$**. Therefore, the relative abundance, or intensity, of each isotopologue of **6** and **6$_{H+}$**, denoted I_{m+n}, is given by the equation:

$$I_{m+n} = T_{m+n} - \sum_{i=1}^{n} p_i \bullet I_{m+n-i}$$

From this equation, the intensity of each of the ten species can be calculated. For example, the intensity of **6*** (I_{m+2}) is the total, observed relative abundance at 1259.1 m/z (T_{m+2}) minus the 69% peak for **6$_{H+}$** ($p_1 \bullet I_{m+1}$), and the 26% peak for **6** ($p_2 \bullet I_m$):

$$I_{m+2} = T_{m+2} - (p_1 \bullet I_{m+1} + p_2 \bullet I_m)$$

These ten intensities were converted to mole fraction by dividing each intensity by the overall sum:

$$\chi_{m+n} = \frac{I_{m+n}}{\sum_{n=0}^{9} I_{m+n}}$$

The mole fraction of each isotopologue (**6**, **6***,…,**6******) is the sum of the mole fraction of each of the unprotonated isotopologues and their corresponding protonated isotopologue, with y = 0,1,2,3, and 4, representing the number of ^{18}O:

$$\chi_y = \chi_{m+n} + \chi_{m+n+1}$$

So the five mole fractions of **6** through **6****** are:

$$\chi_0 = \chi_m + \chi_{m+1} \qquad \chi_1 = \chi_{m+2} + \chi_{m+3} \qquad \chi_2 = \chi_{m+4} + \chi_{m+5} \qquad \chi_3 = \chi_{m+6} + \chi_{m+7}$$

$$\chi_4 = \chi_{m+8} + \chi_{m+9}$$

The same is applicable to **5**, with n = 0,1,2,…7 for **5** at 1241.1 m/z through **5***$_{H+}$** at 1248.1 m/z.

Table 5.2. Isotopologue mole fractions for **6** and **5** isolated from the water incorporation and removal reactions, respectively.

χ_y	**6***[a]	**5***[b]
χ_0	0.09	0.28
χ_1	0.61	0.52
χ_2	0.17	0.15
χ_3	0.09	0.05
χ_4	0.04	--

[a] Conditions: **5**, $NMe_4{}^{18}OH$ (2 equiv.), $H_2{}^{18}O$ (20 equiv.), $FcPF_6$ (4 equiv.), 10:1 THF/CH_3CN, RT 35 minutes.

[b] Conditions: **6***, PMe_3 (10 equiv.), C_6H_6, RT ≥6 hours.

*Calculation of Theoretical Isotopologue Distribution of **5**.*

By applying the expected statistical outcome of a specific water incorporation/O-atom transfer pathway to the experimental isotopologue distribution of **6** from the ESI-MS analysis above, one can determine if a certain mechanism of incorporation/removal is consistent with the experimentally observed isotopologue ratio of **5** (Scheme 5.5). Starting at the left side of Scheme 5.5, there are three possible mechanisms of incorporation: top selective, bottom selective, or not selective. Each gives its own isotopomer mixture of each isotopologue (isotopomer is used to denote the location of ^{18}O within the cubane, whereas isotopologue is used to denote the number of ^{18}O's).

For example, the singly labeled **6*** (61% of the distribution), will be 75% $\mathbf{6^{T}*}$ and 25% $\mathbf{6^{B}*}$ for a random water incorporation mechanism—three top positions to one bottom position. Applying this statistical outcome to the 61% of **6*** gives 15.25% $\mathbf{6^{T}*}$ and 45.75% $\mathbf{6^{B}*}$ for the whole distribution of species. Taking these hypothetical

distributions of **6** on to the O-atom transfer reaction gives five possible pathways: top/top, top/bottom, bot- tom/bottom, bottom/top, and random. The first term refers to water incorporation and the second term refers to O-atom transfer. "Bottom" refers to the central, basal oxido position closest to the ligand framework. "Top" refers to the three other oxido sites on the cubane (those further from the ligand framework and therefore on the 'top'). "Random" represents random incorporation, random removal, or both; the calculated mole fractions are the same for all three cases. Applying each statistical outcome to all eight possible species of **6** gives the distribution of the four possible isotopologues of **5**. Summing up the percentages of each isotopologue gives the theoretical distribution of **5** that can be directly compared to the distribution of **5** experimentally determined from ESI-MS (Table 5.3).

Table 5.3. Experimental and calculated isotopologue percentages for various possible water incorporation/O-atom transfer mechanisms.

χ_y	Experimental	Bottom/Bottom	Top/Bottom	Bottom/Top	Top/Top	Random
χ_0	28%	70%	9%	9%	29.33%	24.25%
χ_1	52%	17%	61%	66.67%	52%	54.25%
χ_2	15%	9%	17%	17.33%	14.67%	15.25%
χ_3	5%	4%	13%	7%	4%	6.25%
Consistent	--	No	No	No	Yes	Yes

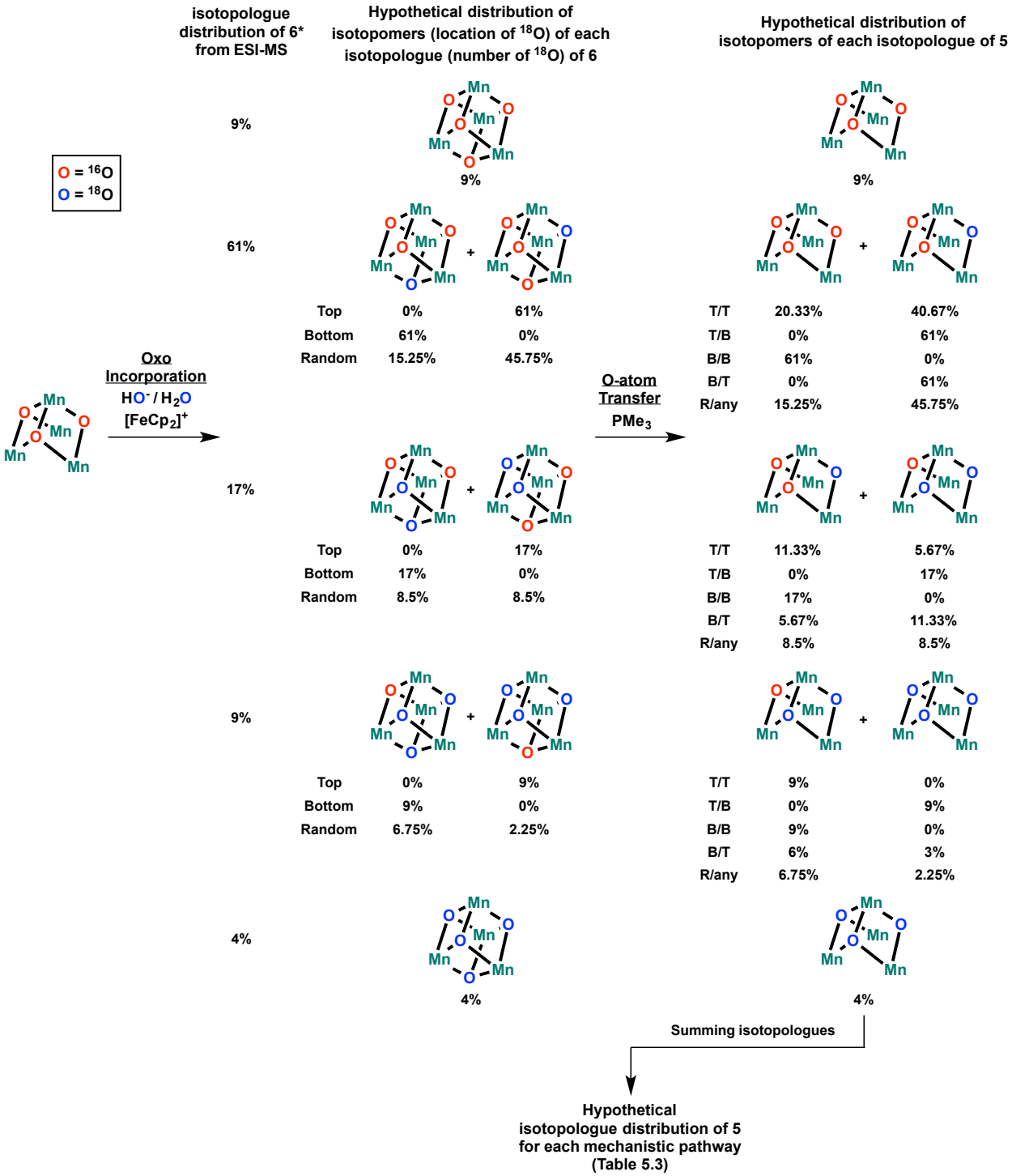

Scheme 5.5. Calculation of theoretical isotopologue distribution of **5** for each possible pathway of water incorporation and O-atom transfer. T=Top, B=Bottom, R=Random.

d_3-acetate Labeling Studies

8 + nBu_4NOAc-d_3. In a glovebox, **8** (1.0 mg, $7.0x10^{-4}$ mmol) was dissolved in 10:1 THF/CH_3CN (1.0 mL) in a septum-capped 10 mL round-bottom flask. Separately, a 0.35 mM solution of nBu_4NOAc-d_3 in 10:1 THF/CH_3CN was prepared and 6 mL was taken up in a syringe. The solution of **8** in the flask and the syringe of acetate solution were taken to the ESI-MS room. The 6 mL of acetate solution was injected into the solution of **8** to give a 100 μM solution of **8** with 3 equivalents of d_3-acetate. Samples were taken directly from this flask and injected into the spectrometer.

6 + nBu_4NOAc-d_3. In a glovebox, **6** (0.5 mg, $3.8x10^{-4}$ mmol) was dissolved in 10:1 THF/CH_3CN (1.9 mL) in a septum-capped 10 mL round-bottom flask. Separately, a 0.60 mM solution of nBu_4NOAc-d_3 in 10:1 THF/CH_3CN was prepared and 1.9 mL was taken up in a syringe. The solution of **6** in the flask and the syringe of acetate solution were taken to the ESI-MS room. The acetate solution was injected into the solution of **6** to give a 100 μM solution of **6** with 3 equivalents of d_3-acetate. Samples were taken directly from this flask and injected into the spectrometer.

17 + nBu_4NOAc-d_3. In a glovebox, **17** (1.2 mg, $8.2x10^{-4}$ mmol) was dissolved in 10:1 THF/CH_3CN (1.2 mL) in a septum-capped 10 mL round-bottom flask. Separately, a 0.35 mM solution of nBu_4NOAc-d_3 in 10:1 THF/CH_3CN was prepared and 6 mL was taken up in a syringe. The solution of **17** in the flask and the syringe of acetate solution were taken to the ESI-MS room. The acetate solution was injected into the solution of **17** to give a 100 μM solution of **17** with 3 equivalents of d_3-acetate. Samples were taken directly from this flask and injected into the spectrometer.

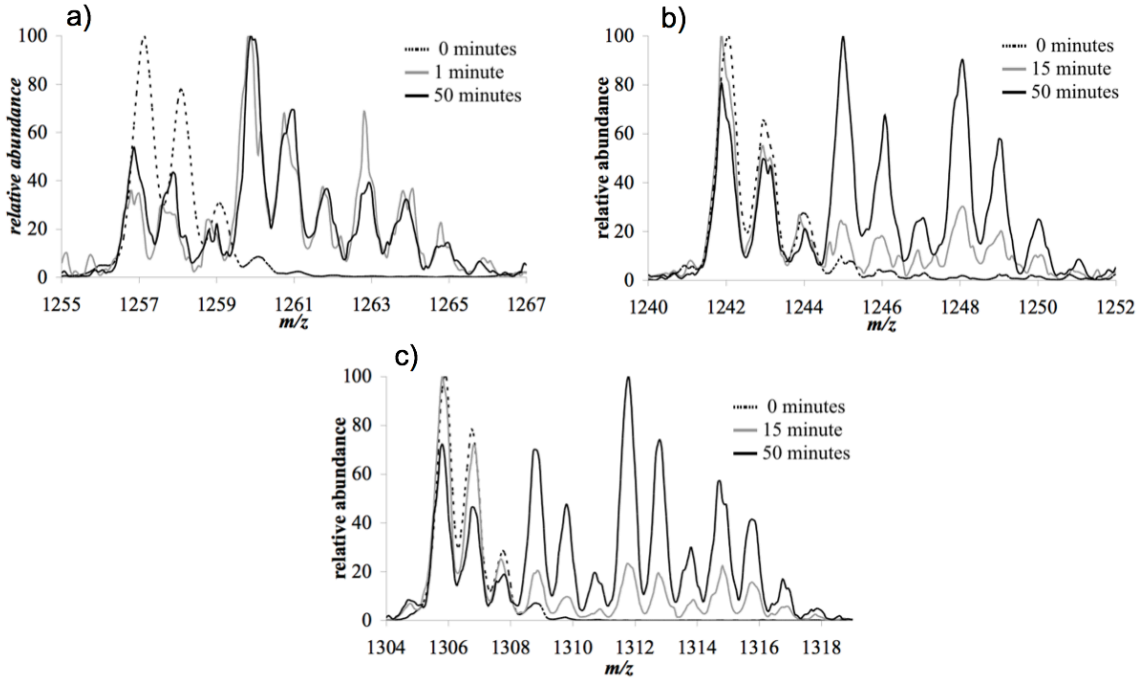

Figure 5.23. Electrospray Ionization Mass Spectra of 100 μM **6** (a), **8** (b), and **17** (c) after mixture with nBu_4NOAc-d_3 at 15 minutes (grey line; 1 minute for **6**) and 50 minutes (black line). The unscrambled starting complexes are shown as '0 minute' spectra (dotted lines). Conditions: **6**, **8**, or **17** (100 μM in 10:1 THF/CH_3CN), nBu_4NOAc-d_3 (3 equiv.), RT.

REFERENCES

1. (a) Gray, H. B. *Nat. Chem.* **2009,** *1*, 7-7.(b) Lewis, N. S.; Nocera, D. G. *Proc. Natl. Acad. Sci. USA* **2006,** *103*, 15729-15735.
2. McEvoy, J. P.; Brudvig, G. W. *Chem. Rev.* **2006,** *106*, 4455-4483.
3. (a) Yano, J.; Kern, J.; Sauer, K.; Latimer, M. J.; Pushkar, Y.; Biesiadka, J.; Loll, B.; Saenger, W.; Messinger, J.; Zouni, A.; Yachandra, V. K. *Science* **2006,** *314*, 821-825.(b) Peloquin, J. M.; Campbell, K. A.; Randall, D. W.; Evanchik, M. A.; Pecoraro, V. L.; Armstrong, W. H.; Britt, R. D. *J. Am. Chem. Soc.* **2000,** *122*, 10926-10942.(c) Zouni, A.; Witt, H. T.; Kern, J.; Fromme, P.; Krauss, N.; Saenger, W.; Orth, P. *Nature* **2001,** *409*, 739-743.

4. (a) Ferreira, K. N.; Iverson, T. M.; Maghlaoui, K.; Barber, J.; Iwata, S. *Science* **2004,** *303*, 1831-1838.(b) Umena, Y.; Kawakami, K.; Shen, J. R.; Kamiya, N. *Nature* **2011,** *473*, 55-U65.

5. Luber, S.; Rivalta, I.; Umena, Y.; Kawakami, K.; Shen, J. R.; Kamiya, N.; Brudvig, G. W.; Batista, V. S. *Biochemistry* **2011,** *50*, 6308-6311.

6. Rapatskiy, L.; Cox, N.; Savitsky, A.; Ames, W. M.; Sander, J.; Nowaczyk, M. M.; Rögner, M.; Boussac, A.; Neese, F.; Messinger, J.; Lubitz, W. *J. Am. Chem. Soc.* **2012,** *134*, 16619-16634.

7. (a) Joliot, P. *Biochim. Biophys. Acta* **1965,** *102*, 116-134.(b) Kok, B.; Forbush, B.; Mcgloin, M. *Photochem. Photobiol.* **1970,** *11*, 457-475.

8. Kolling, D. R. J.; Cox, N.; Ananyev, G. M.; Pace, R. J.; Dismukes, G. C. *Biophys. J.* **2012,** *103*, 313-322.

9. (a) Pecoraro, V. L.; Baldwin, M. J.; Caudle, M. T.; Hsieh, W. Y.; Law, N. A. *Pure Appl. Chem.* **1998,** *70*, 925-929.(b) Pecoraro, V. L.; Hsieh, W. Y., The use of Model Complexes to Elucidate the Structure and Function of Manganese Redox Enzymes. In *Manganese and its Role in Biological Systems*, Sigel, A.; Sigel, H., Eds. Marcel Dekker, Inc.: New York, 2000; Vol. 37, pp 429-504.(c) Sproviero, E. M.; Gascon, J. A.; McEvoy, J. P.; Brudvig, G. W.; Batista, V. S. *J. Am. Chem. Soc.* **2008,** *130*, 3428-3442.

10. (a) McEvoy, J. P.; Gascon, J. A.; Batista, V. S.; Brudvig, G. W. *Photochem. Photobiol. Sci.* **2005,** *4*, 940-949.(b) Yachandra, V. K.; Sauer, K.; Klein, M. P. *Chem. Rev.* **1996,** *96*, 2927-2950.(c) Messinger, J. *Phys. Chem. Chem. Phys.* **2004,** *6*, 4764-4771.(d) Siegbahn, P. E. M. *Chem. Eur. J.* **2008,** *14*, 8290-8302.(e) Siegbahn, P. E. M. *Acc. Chem. Res.* **2009,** *42*, 1871-1880.(f) Siegbahn, P. E. M. *Chemphyschem* **2011,** *12*, 3274-3280.(g) Siegbahn, P. E. M. *Phys. Chem. Chem. Phys.* **2012,** *14*, 4849-4856.

11. Ames, W.; Pantazis, D. A.; Krewald, V.; Cox, N.; Messinger, J.; Lubitz, W.; Neese, F. *J. Am. Chem. Soc.* **2011,** *133*, 19743-19757.

12. (a) Siegbahn, P. E. M. *J. Am. Chem. Soc.* **2009,** *131*, 18238-18239.(b) Kusunoki, M. *J. Photochem. Photobio. B* **2011,** *104*, 100-110.(c) Pantazis, D. A.; Ames, W.; Cox, N.; Lubitz, W.; Neese, F. *Angew. Chem. Int. Ed.* **2012,** *51*, 9935-9940.

13. (a) McEvoy, J. P.; Brudvig, G. W. *Phys. Chem. Chem. Phys.* **2004,** *6*, 4754-4763.(b) Haumann, M.; Liebisch, P.; Muller, C.; Barra, M.; Grabolle, M.; Dau, H. *Science* **2005,** *310*, 1019-1021.

14. (a) Najafpour, M. M.; Ehrenberg, T.; Wiechen, M.; Kurz, P. *Angew. Chem. Int. Ed.* **2010,** *49*, 2233-2237.(b) Shevela, D.; Koroidov, S.; Najafpour, M. M.; Messinger, J.; Kurz, P. *Chem. Eur. J.* **2011,** *17*, 5414-5422.(c) Zaharieva, I.; Najafpour, M. M.; Wiechen, M.; Haumann, M.; Kurz, P.; Dau, H. *Energ. Environ. Sci.* **2011,** *4*, 2400-2408.

15. (a) Mukhopadhyay, S.; Mandal, S. K.; Bhaduri, S.; Armstrong, W. H. *Chem. Rev.* **2004,** *104*, 3981-4026.(b) Mullins, C. S.; Pecoraro, V. L. *Coordin. Chem. Rev.* **2008,** *252*, 416-443.

16. Brimblecombe, R.; Swiegers, G. F.; Dismukes, G. C.; Spiccia, L. *Angew. Chem. Int. Ed.* **2008,** *47*, 7335-7338.

17. Hocking, R. K.; Brimblecombe, R.; Chang, L. Y.; Singh, A.; Cheah, M. H.; Glover, C.; Casey, W. H.; Spiccia, L. *Nat. Chem.* **2011,** *3*, 461-466.

18. (a) Mishra, A.; Wernsdorfer, W.; Abboud, K. A.; Christou, G. *Chem. Commun.* **2005**, 54-56.(b) Hewitt, I. J.; Tang, J. K.; Madhu, N. T.; Clerac, R.; Buth, G.; Anson, C. E.; Powell, A. K. *Chem. Commun.* **2006**, 2650-2652.(c) Kotzabasaki, V.; Siczek, M.; Lis, T.; Milios, C. J. *Inorg. Chem. Commun.* **2011,** *14*, 213-216.(d) Koumousi, E. S.; Mukherjee, S.; Beavers, C. M.; Teat, S. J.; Christou, G.; Stamatatos, T. C. *Chem. Commun.* **2011,** *47*, 11128-11130.(e) Nayak, S.; Nayek, H. P.; Dehnen, S.; Powell, A. K.; Reedijk, J. *Dalton Trans.* **2011,** *40*, 2699-2702.(f) Park, Y. J.; Ziller, J. W.; Borovik, A. S. *J. Am. Chem. Soc.* **2011,** *133*, 9258-2961.

19. (a) Kanady, J. S.; Tsui, E. Y.; Day, M. W.; Agapie, T. *Science* **2011,** *333*, 733-736.(b) Mukherjee, S.; Stull, J. A.; Yano, J.; Stamatatos, T. C.; Pringouri, K.; Stich, T. A.; Abboud, K. A.; Britt, R. D.; Yachandra, V. K.; Christou, G. *Proc. Natl. Acad. Sci. USA* **2012,** *109*, 2257-2262.

20. (a) Tsui, E. Y.; Day, M. W.; Agapie, T. *Angew. Chem. Int. Ed.* **2011,** *50*, 1668-1672.(b) Tsui, E. Y.; Kanady, J. S.; Day, M. W.; Agapie, T. *Chem. Commun.* **2011,** *47*, 4189-4191.

21. (a) Ruettinger, W.; Ho, D.; Dismukes, G. *Inorg. Chem.* **1999,** *38*, 1036-1037.(b) Ruettinger, W.; Carrell, T.; Baesjou, P.; Boelrijk, A.; Maneiro, M.; Dismukes, G. *J. Inorg. Biochem.* **1999,** *74*, 88-88.

22. (a) Wang, S. Y.; Folting, K.; Streib, W. E.; Schmitt, E. A.; McCusker, J. K.; Hendrickson, D. N.; Christou, G. *Angew. Chem. Int. Ed.* **1991,** *30*, 305-306.(b) Wang, S. Y.; Tsai, H. L.; Hagen, K. S.; Hendrickson, D. N.; Christou, G. *J. Am. Chem. Soc.* **1994,** *116*, 8376-8377.(c) Aubin, S. M. J.; Wemple, M. W.; Adams, D. M.; Tsai, H. L.; Christou, G.; Hendrickson, D. N. *J. Am. Chem. Soc.* **1996,** *118*, 7746-7754.(d) Aromi, G.; Wemple, M. W.; Aubin, S. J.; Folting, K.; Hendrickson, D. N.; Christou, G. *J. Am. Chem. Soc.* **1998,** *120*, 5850-5851.(e) Aliaga-Alcalde, N.; Edwards, R. S.; Hill, S. O.; Wernsdorfer, W.; Folting, K.; Christou, G. *J. Am. Chem. Soc.* **2004,** *126*, 12503-12516.

23. (a) Beck, W. F.; Brudvig, G. W. *Biochemistry* **1987,** *26*, 8285-8295.(b) Brudvig, G. W.; Beck, W. F., Oxidation-Reduction and Ligand-Substitution Reactions of The Oxygen-Evolving Center of Photosystem II. In *Manganese Redox Enzymes*, Pecoraro, V. L., Ed. VCH Publishers, Inc.: New York, 1992; pp 119-140.(c) Messinger, J.; Seaton, G.; Wydrzynski, T.; Wacker, U.; Renger, G. *Biochemistry* **1997,** *36*, 6862-6873.(d) Schansker, G.; Goussias, C.; Petrouleas, V.; Rutherford, A. W. *Biochemistry* **2002,** *41*, 3057-3064.

24. Cheniae, G. M.; Martin, I. F. *Biochem. Bioph. Res. Co.* **1967,** *28*, 89-95.

25. Kanady, J. S.; Mendoza-Cortes, J. L.; Tsui, E. Y.; Nielson, R. J.; Goddard, W. A.; Agapie, T. *J. Am. Chem. Soc.* **2013,** *135*, 1073-1082.

26. Siegbahn, P. E. M. *J. Biol. Inorg. Chem.* **2006,** *11*, 695-701.

27. (a) Lundberg, M.; Blomberg, M. R. A.; Siegbahn, P. E. M. *Inorg. Chem.* **2004,** *43*, 264-274.(b) Lundberg, M.; Siegbahn, P. E. M. *J. Comput. Chem.* **2005,** *26*, 661-667.(c) Sproviero, E. M.; Gascon, J. A.; McEvoy, J. P.; Brudvig, G. W.; Batista, V. S. *J. Inorg. Biochem.* **2006,** *100*, 786-800.(d) Orio, M.; Pantazis, D. A.; Petrenko, T.; Neese, F. *Inorg. Chem.* **2009,** *48*, 7251-7260.

28. Baik, M. H.; Friesner, R. A. *J. Phys. Chem. A* **2002,** *106*, 7407-7412.

29. Wieghardt, K.; Bossek, U.; Zsolnai, L.; Huttner, G.; Blondin, G.; Girerd, J. J.; Babonneau, F. *J. Chem. Soc., Chem. Commun.* **1987**, 651-653.

30. Chow, W. S.; Aro, E. M., Photoinactivation and Mechanisms of Recovery. In *The Light-Driven Water: Plastoquinone Oxidoreductase*, Wydrzynski, T. J.; Satoh, K., Eds. Springer: Dordrecht, 2005; Vol. 22, pp 627-648.

31. (a) Miller, A. F.; Brudvig, G. W. *Biochemistry* **1989,** *28*, 8181-8190.(b) Miller, A. F.; Brudvig, G. W. *Biochemistry* **1990,** *29*, 1385-1392.(c) Burnap, R. L. *Phys. Chem. Chem. Phys.* **2004,** *6*, 4803-4809.

32. (a) Campbell, K. A.; Force, D. A.; Nixon, P. J.; Dole, F.; Diner, B. A.; Britt, R. D. *J. Am. Chem. Soc.* **2000,** *122*, 3754-3761.(b) Tyryshkin, A. M.; Watt, R. K.; Baranov, S. V.; Dasgupta, J.; Hendrich, M. P.; Dismukes, G. C. *Biochemistry* **2006,** *45*, 12876-12889.(c) Dasgupta, J.; Tyryshkin, A. M.; Baranov, S. V.; Dismukes, G. C. *Appl. Magn. Reson.* **2010,** *37*, 137-150.(d) Zaltsman, L.; Ananyev, G. M.; Bruntrager, E.; Dismukes, G. C. *Biochemistry* **1997,** *36*, 8914-8922.(e) Dasgupta, J.; Ananyev, G. M.; Dismukes, G. C. *Coordin. Chem. Rev.* **2008,** *252*, 347-360.(f) Ananyev, G. M.; Dismukes, G. C. *Biochemistry* **1997,** *36*, 11342-11350.

33. (a) Isotopologue percentages of **6*** (#^{18}O; %): 0; 9%, 1; 61%, 2; 17%, 3; 9%, 4: 4%; isotopologue percentages of **5***: 0; 28%, 1; 52%, 2; 15%, 3; 5%. .(b) Complex **6*** was 9% unlabelled, 61% singly labelled, and 30% higher isotopologues. Higher solvent polarity resulted in increased ^{18}O incorporation: 2:1 THF/CH_3CN rather than 10:1 afforded **6*** with three ^{18}O as the major isotopologue (Figure 5.19). As a polar solvent was necessary for dissolution of the ferrocenium salt and tetraalkyl hydroxides, some excess ^{18}O incorporation was unavoidable. A 10:1 THF/CH_3CN was utilized throughout the study. Calculations of expected isotope distribution for different mechanisms takes into account the incorporation percentage in **6*** and **5***.

34. (a) Tagore, R.; Chen, H. Y.; Crabtree, R. H.; Brudvig, G. W. *J. Am. Chem. Soc.* **2006,** *128*, 9457-9465.(b) Ohlin, C. A.; Brimblecombe, R.; Spiccia, L.; Casey, W. H. *Dalton Trans.* **2009**, 5278-5280.

35. (a) Messinger, J.; Badger, M.; Wydrzynski, T. *Proc. Natl. Acad. Sci. USA* **1995,** *92*, 3209-3213.(b) Hillier, W.; Messinger, J.; Wydrzynski, T. *Biochemistry* **1998,** *37*, 16908-

16914.(c) Hillier, W.; Messinger, J.; Wydrzynski, T. *Photosynthesis: Mechanisms and Effects, Vols I-V* **1998**, 1307-1310.(d) Hillier, W.; Wydrzynski, T. *Biochemistry* **2000,** *39*, 4399-4405.(e) Hillier, W.; Wydrzynski, T. *Phys. Chem. Chem. Phys.* **2004,** *6*, 4882-4889.(f) Hillier, W.; Wydrzynski, T. *Coordin. Chem. Rev.* **2008,** *252*, 306-317.

36. Vincent, J. B.; Chang, H. R.; Folting, K.; Huffman, J. C.; Christou, G.; Hendrickson, D. N. *J. Am. Chem. Soc.* **1987,** *109*, 5703-5711.
37. Saltzman, H.; Sharefkin, J. G. *Organic Synthesis Collective Volumes* **1973,** *5*, 658.
38. Bryan, P. S.; Dabrowiak, J. C. *Inorg. Chem.* **1975,** *14*, 296-299.
39. Kambe, K. *J. Phys. Soc. Jpn.* **1950,** *5*, 48-51.
40. *Matlab*, 7.10.0.499 (R2010a); The MathWorks, Inc.: Natick, MA, 2010.

APPENDIX A

Side Products and Other Structures

INTRODUCTION

The synthetic strategies of the above chapters have afforded predictive power in the synthesis of homo- and heterometallic, multinuclear complexes with the **H_3L** ligand framework. Nevertheless, as shown in Chapter 3, small changes in solvent, oxidant, and metal salt can strongly affect the structure produced; thus, over the last five years of work a number of complexes have been observed that were unexpected. This appendix describes these complexes and some others that did not fit in the stories given above. Most of these complexes are not fully characterized, and many only have a crystal structure. They are included to add to the overall picture of our framework's reactivity, and to show other possibilities for those carrying the work on.

RESULTS & DISCUSSION

A.1 Trinuclear Complexes

As described in Chapter 2, trinuclear complexes could be formed by the addition of three equivalents of Mn^{2+}, Co^{2+}, or Ni^{2+} salts to **H_3L**. Here, two complexes are described that were only characterized by poor XRD data sets. Addition of $Co_3(PO_4)_2$ to **H_3L** in the presence of three equivalents of NaOH affords $LCo_3(PO_4)$ (Scheme A.1). The complex is homologous to the $LCu_3(PO_4)$ complex synthesized by Dr. Emily Tsui, with three oxygens of the phosphate capping the $Co^{II}{}_3(\mu\text{-OR})_3$ core to give a neutral complex.

Next, while exploring the reactivity of metal salts of less-coordinating anions—like the $Mn(ClO_4)_2$ and $Co(BF_4)_2$ work in Chapter 2—$Ni(ClO_4)_2 \cdot 6H_2O$ was mixed with **H_3L** in CH_3CN. Before base was added, however, a homogeneous, blue solution was

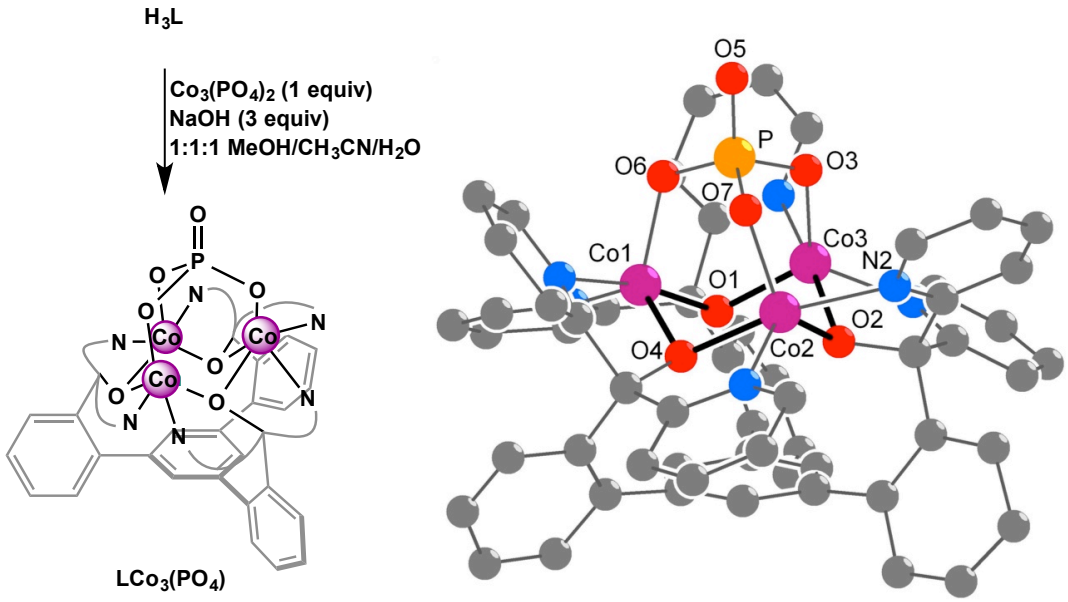

Scheme A.1 Synthesis (left) and ball-and-stick solid-state structure (right) of $LCo_3(PO_4)$. Hydrogen atoms and solvent molecules are not shown for clarity.

observed. Layering of Et_2O onto the CH_3CN afforded purple crystals that diffracted to show the complex $[H_3LNi_3(CH_3CN)_{10}(H_2O)](ClO_4)_6$ (Scheme A.2). Without deprotonation of the alcohols the ligand framework cannot make the $M_3(\mu\text{-}OR)_3$ core generally observed, and thus the Ni centers are in isolated coordination environments quite far apart. Two of the Ni^{II} centers are coordinated in a N,O,N pincer, with the three remaining coordination sites filled by acetonitriles. The other Ni^{II} is coordinated by the alcohol and one pyridine of an arm, with three acetonitriles and one monoatomic ligand, likely water, completing the octahedral coordination sphere. The ligand framework is neutral in this protonation state, so six outer-sphere perchlorates are expected and observed. Addition of base to the blue solution in CH_3CN changed the color to green, as observed in the other $Ni^{II}(\mu\text{-}OR)_3$ complexes, so structures similar to

the one observed in $[H_3LNi_3(CH_3CN)_{10}(H_2O)](ClO_4)_6$ may be intermediate in the synthesis of many of the trinuclear complexes synthesized in the above chapters.

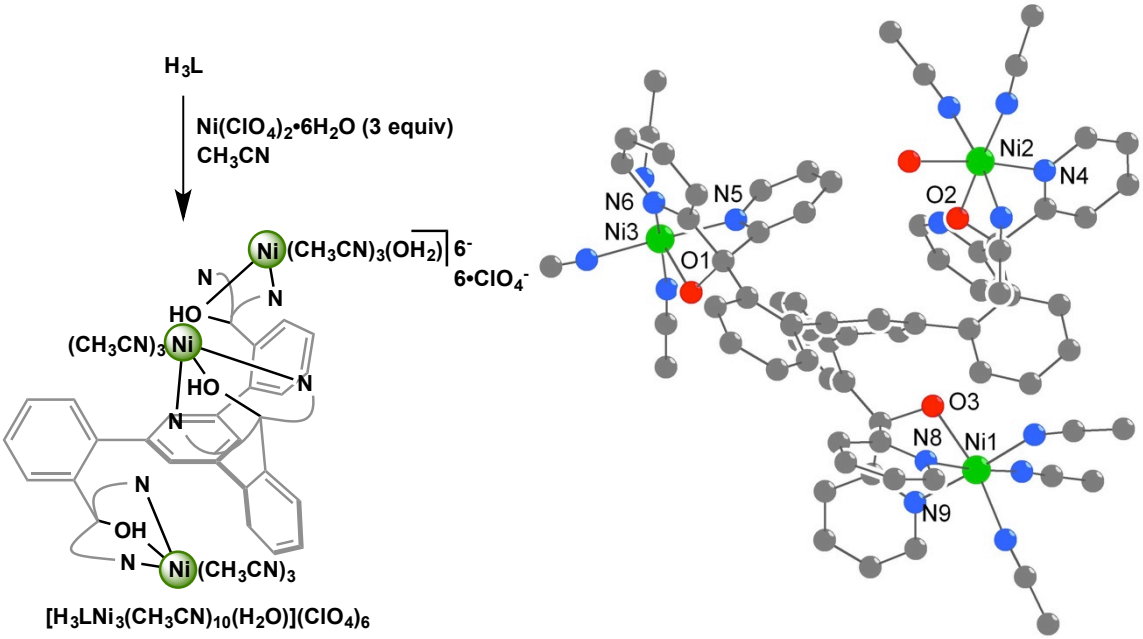

Scheme A.2 Synthesis (left) and ball-and-stick solid-state structure (right) of $[H_3LNi_3(CH_3CN)_{10}(H_2O)](ClO_4)_6$. Hydrogen atoms, disordered counterions, and solvent molecules are not shown for clarity.

A.2 Mono-oxo Complexes

While exploring the chemistry of $[LMn^{II}_2Mn^{III}_2O(OAc)_3(OTf)]OTf$ (**3**; discussed in Chapter 3), it was found that **3** dissolved in polar, protic solvents. As mentioned in Chapter 3, dissolution of **3** in water afforded a green solution from which a complex could not be isolated cleanly. However, dissolution of **3** in MeOH led to a yellow/brown solution that afforded crystals upon Et_2O vapor diffusion (Scheme A.3). In the structure, one κ^2-acetate has been replaced with a μ_2-methoxide, giving a core structure analogous to the dioxo complex **4**. The apical Mn still has triflate coordinated

to it, and there is an outer-sphere triflate, consistent with the $Mn^{II}_2Mn^{III}_2$ oxidation state. The observation of a μ-methoxide for **3** in MeOH suggests that the core may include a μ-hydroxide upon dissolution of **3** in water.

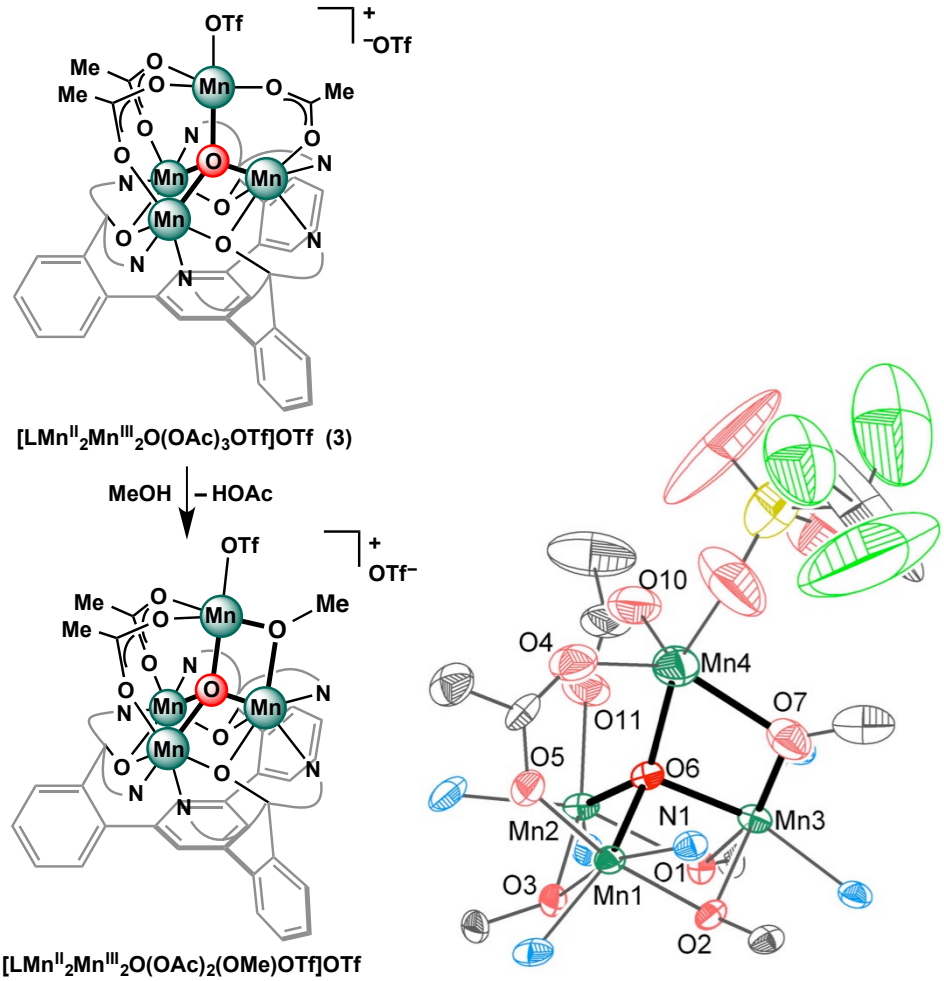

Scheme A.3 Synthesis (left) and solid-state, core structure (right) of $[LMn^{II}_2Mn^{III}_2O(OAc)_2(OMe)(OTf)]OTf$. Hydrogen atoms, disordered counterions, and solvent molecules are not shown for clarity.

Another compound relating to the chemistry of mono-oxo complex **3** was isolated and fully characterized. As mentioned briefly in Chapter 3 with respect to conversion of $Mn^{II}_2Mn^{III}_2$ complex **3** to $Mn^{II}_3Mn^{III}$ complex **2**, addition of $Fe(Cp^*)_2$ to **3**,

followed by addition of $^{n}Bu_4NOAc$, gave **2** cleanly (Scheme 3.2). However, if the $^{n}Bu_4NOAc$ was not added, an intermediate species $[LMn^{II}_3Mn^{III}O(OAc)_3]_2[OTf]_2$ could be isolated and crystallized (Scheme A.4). Upon reduction, the weakly bound triflate of **3** is displaced by an acetate of a second Mn_4O unit, giving a dimer structure through two κ^3-acetates. The observation of two outer-sphere triflates is consistent with the reduced $[Mn^{III}_3Mn^{III}O]_2$ oxidation state.

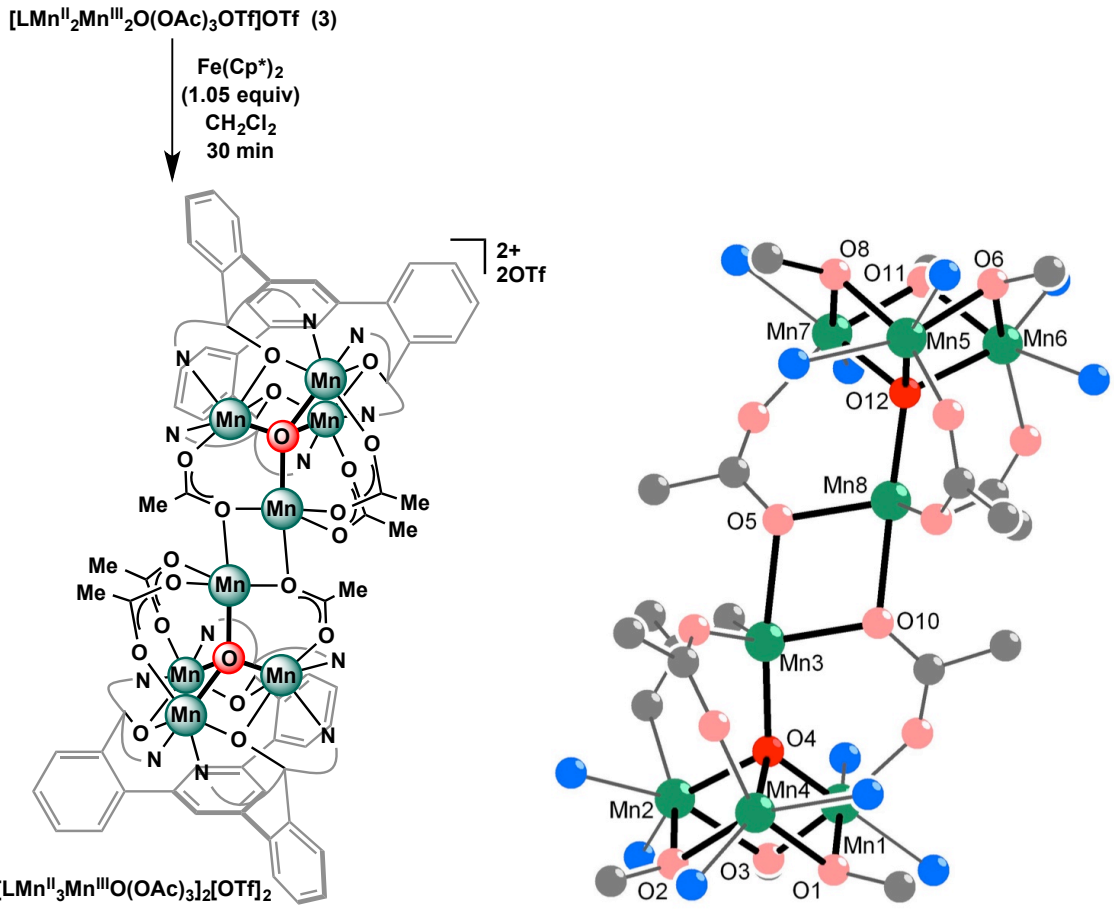

Scheme A.4 Synthesis (left) and ball-and-stick, solid-state, core structure (right) of $[LMn^{II}_3Mn^{III}O(OAc)_3]_2[OTf]_2$. Hydrogen atoms, disordered counterions, and solvent molecules are not shown for clarity.

While exploring the parameter space for site-differentiated functionalization of **1** with a fourth equivalent of Mn, modifying the solvent for the synthesis of **2** from THF to CH_2Cl_2 afforded another $Mn^{II}_3Mn^{III}O$ complex; however, the apical Mn is coordinated by a chloride rather than an acetate (Scheme A.5). $LMn^{II}_3Mn^{III}O(OAc)_3Cl$ is structurally analogous to **2** and **3**, with a tetrahedral $Mn_4(\mu_4\text{-}O)$ core structure, and the apical metal is *pseudo*-trigonal bipyramidal, with Cl^- in an equatorial position. The chloride likely came from the CH_2Cl_2; radical chemistry initiated by KO_2 could be responsible.

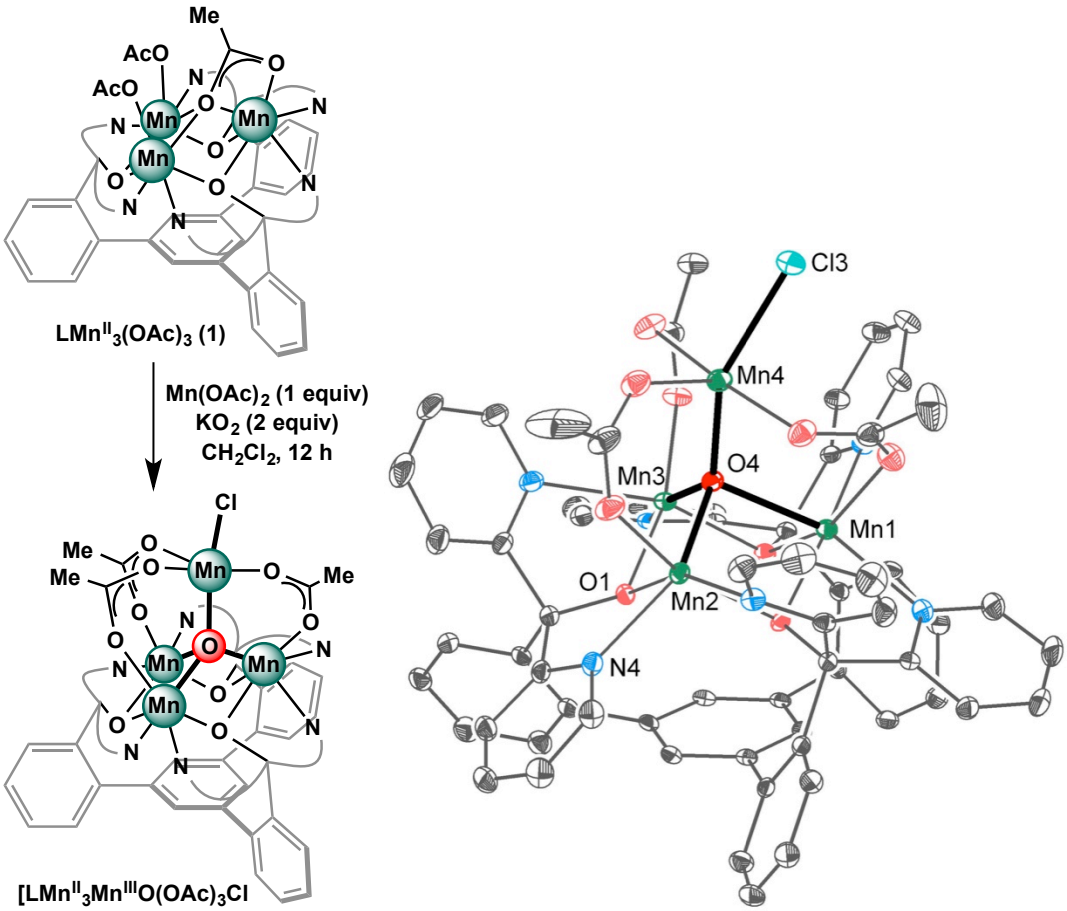

Scheme A.5 Synthesis (left) and solid-state structure (right) of $LMn^{II}_3Mn^{III}O(OAc)_3Cl$. Hydrogen atoms and solvent molecules are not shown for clarity.

A structural motif has been found many times in the chemistry of $\mathbf{L}^{3-}$: two $LM_3(\mu_3\text{-}O)(OAc)_3$ motifs bridged through the acetates by an octahedral metal M′. The first example was the $[Mn_3O]_2$•Ca compound **9** discussed in Chapter 4, while others have synthesized a number of homologous $[Co_3O]_2$•M compounds. Here, three other complexes of this type are reported. $Sc(OTf)_3$, KO_2, and a catalytic amount of 18-crown-6 were added to **1** in CH_2Cl_2. Et_2O vapor diffusion afforded crystals of $[[LMn_3O(OAc)_3]_2Sc][OTf]_n$, where Sc^{3+} is in the central, octahedral site (Schemes A.6 & B7, left). The diffraction data set was poor, so the number of triflates—and therefore the oxidation state—could not be determined.

Next, decomposition of complex **3** dissolved in a wet, aerobic CH_2Cl_2/THF mixture in the presence of excess H_2O afforded crystals of a $[Mn_3O]_2$•Mn compound in an unknown oxidation state, again because the triflates could not be located (Schemes A.6 & A.7, center). As a possible explanation, the apical Mn^{II} of **3** becomes labile in the presence of excess water. The now μ_3-O is more donating, allowing the basal Mn to be oxidized by the air in the reaction. Once the basal Mn are oxidized, the bridging oxo is not coordinating enough to coordinate the Mn^{II}, and thus the $[Mn_3O]_2$•Mn structure is observed. Consistent with this, another $[Mn_3O]_2$•Mn could be isolated by the reaction of **1** following Dr. Emily Tsui's procedure for the formation of the Mn_3MO_2 'dioxo' compounds (Schemes A.6 & A.7, right). The crystal data was good enough to locate the triflates, which gives an oxidation state of $[LMn^{III}{}_3O(OAc)_3]_2Mn^{II}[OTf]_4$. Again, as the basal Mn become more oxidized, the bridging oxo is less donating and cannot coordinate the fourth Mn.

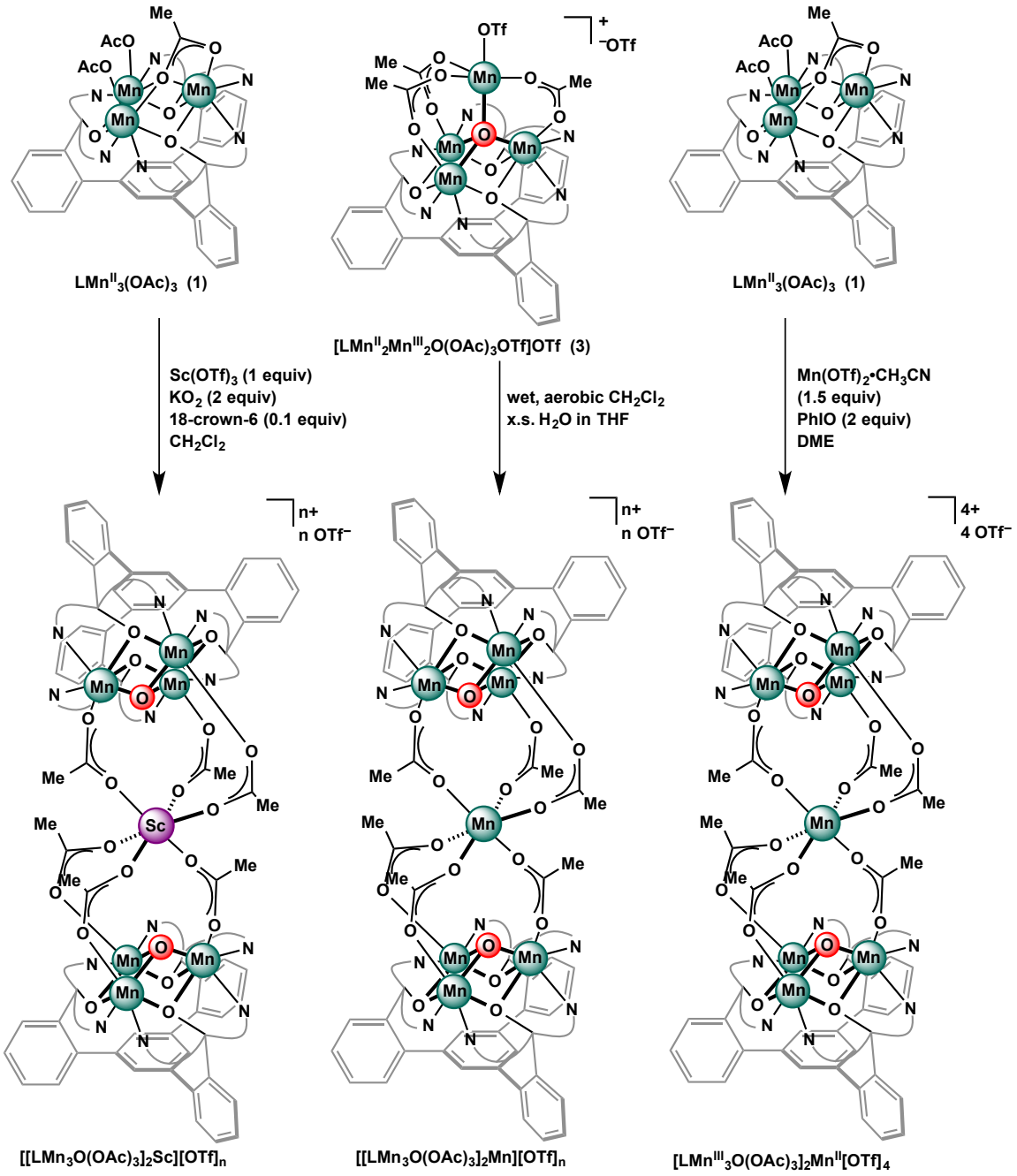

Scheme A.6 Synthesis of heptametallic compounds of the type $[Mn_3O]_2$•M: $[[LMn_3O(OAc)_3]_2Sc][OTf]_n$ (left), $[[LMn_3O(OAc)_3]_2Mn][OTf]_n$ (center), and $[LMn^{III}{}_3O(OAc)_3]_2Mn^{II}[OTf]_4$ (right).

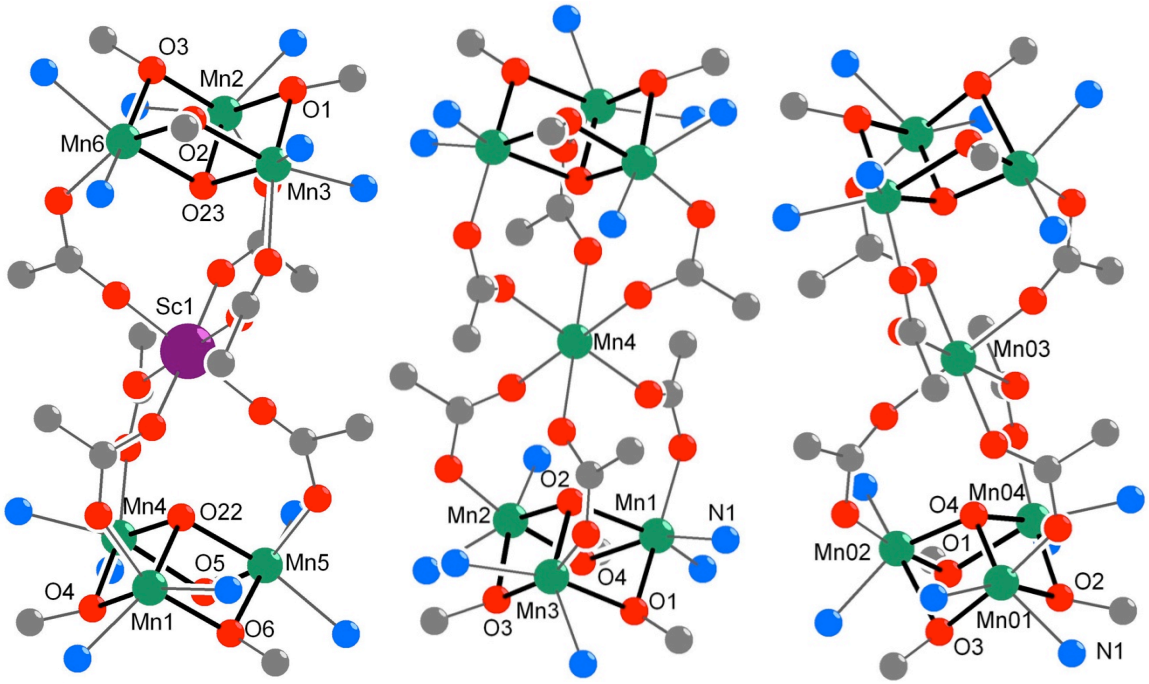

Scheme A.7 Ball-and-stick, solid-state, core structures of $[[LMn_3O(OAc)_3]_2Sc][OTf]_n$ (left), $[[LMn_3O(OAc)_3]_2Mn][OTf]_n$ (center), and $[LMn^{III}{}_3O(OAc)_3]_2Mn^{II}[OTf]_4$ (right). H atoms, disordered counterions, and solvent molecules are not shown for clarity.

While targeting more accurate Mn_3CaO_4+Mn dangler models of the OEC, reactions of $Mn(O_2CCF_3)_2$ with the asymmetric Mn_3CaO_4 cubane **14** were attempted. Reaction of **14** with an excess (three equivalents) of $Mn(O_2CCF_3)_2$ over 40 hours led to decomposition of the cubane core, as shown by crystals isolated from the reaction. From the very preliminary data set, a mono-oxo $Mn_4O(O_2CCF_3)_4$ compound could be observed co-crystallized with a mononuclear Mn complex $Mn(HON_4OH)(O_2CCF_3)_2$ (Scheme A.8). Decomposition of the Mn_3MO_4 cubanes to Mn_4O complexes has been observed in the presence of desymmetrizing, chelating ligands in a number of cases. It is unclear how three oxidos are lost. The conditions for successful formation of a dangling Mn complex must be carefully chosen.

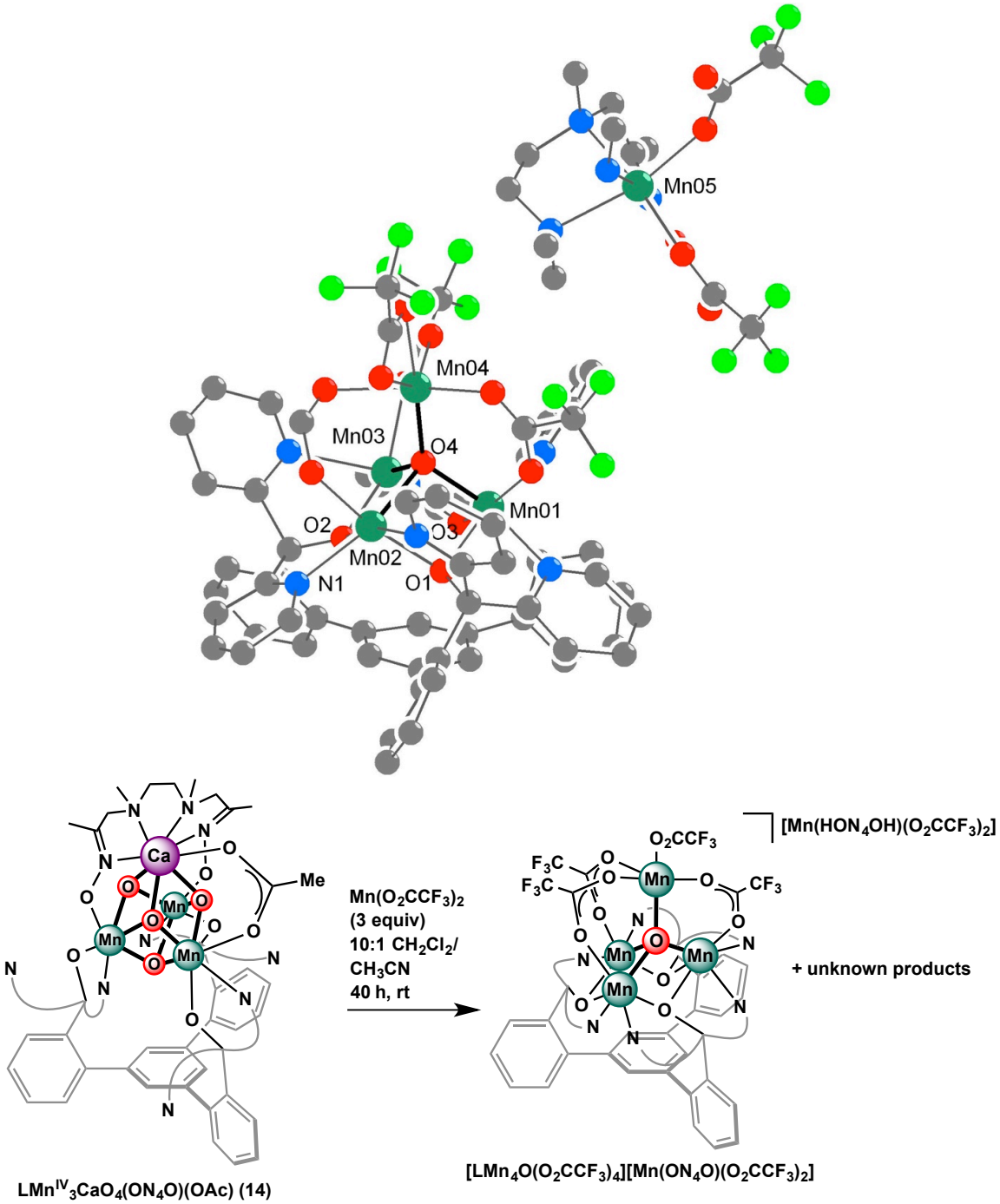

Scheme A.8 Synthesis (bottom) and preliminary ball-and-stick solid-state structure (top) of $[LMn_4O(O_2CCF_3)_4][Mn(ON_4O)(O_2CCF_3)_2]$. Hydrogen atoms, disordered counterions, and solvent molecules are not shown for clarity. Some moieties are incomplete in this refinement, such as the HON_4OH ligand and the $^{-}O_2CCF_3$ bridging Mn02 and Mn04.

A.3 Other Mn_4O_4 Cubane Complexes

The ligand framework **H_3L** was not initially designed to coordinate M_4O_4 cubanes. The first, serendipitous discovery of a cubane complex came from substituting $Mn(OAc)_2$ for Co^{II} or Ni^{II} in the original conditions for formation of $LCo_3(OAc)_3$ and $LNi_3(OAc)_3$. Under aerobic conditions, the solution turned from yellow to dark brown, suggesting oxidation of Mn^{II}, which did not occur in the case of Co^{II} or Ni^{II} (See Chapter 2). After collecting a poor data set that suggested a cubane unit, the equivalents of $Mn(OAc)_2$ was increased from three to four to give a balanced reaction to afford what we propose to be $[LMn^{III}_3Mn^{IV}O_4(OAc)_3]H$ (Scheme A.9). In the solid-state, the Mn bond distances are consistent with the oxidation state $Mn^{III}_3Mn^{IV}$; however, no counterions are present, so we posit a proton is balancing the charge. A water is hydrogen bonding to the cubane core, and therefore the final stoichiometry is $[LMn^{III}_3Mn^{IV}O_4(OAc)_3]H{\bullet}H_2O$. Complete characterization could not be achieved, as the reaction was not always reproducible and the ^{1}H NMR spectra reaction to reaction were not consistent. The complex $LMn^{III}_2Mn^{IV}_2O_4(OAc)_3$ (**6**) could be made much more reliably and therefore its chemistry was explored in great detail (See Chapters 3, 4, and 5). When **6** was reacted with TEMPOH, the mixture of species formed could be co-crystallized, and seem to be consistent with a major constituent being an analogous $Mn^{III}_3Mn^{IV}O_4H$ complex; however, as with $[LMn^{III}_3Mn^{IV}O_4(OAc)_3]H{\bullet}H_2O$, isolation of pure material was never achieved.

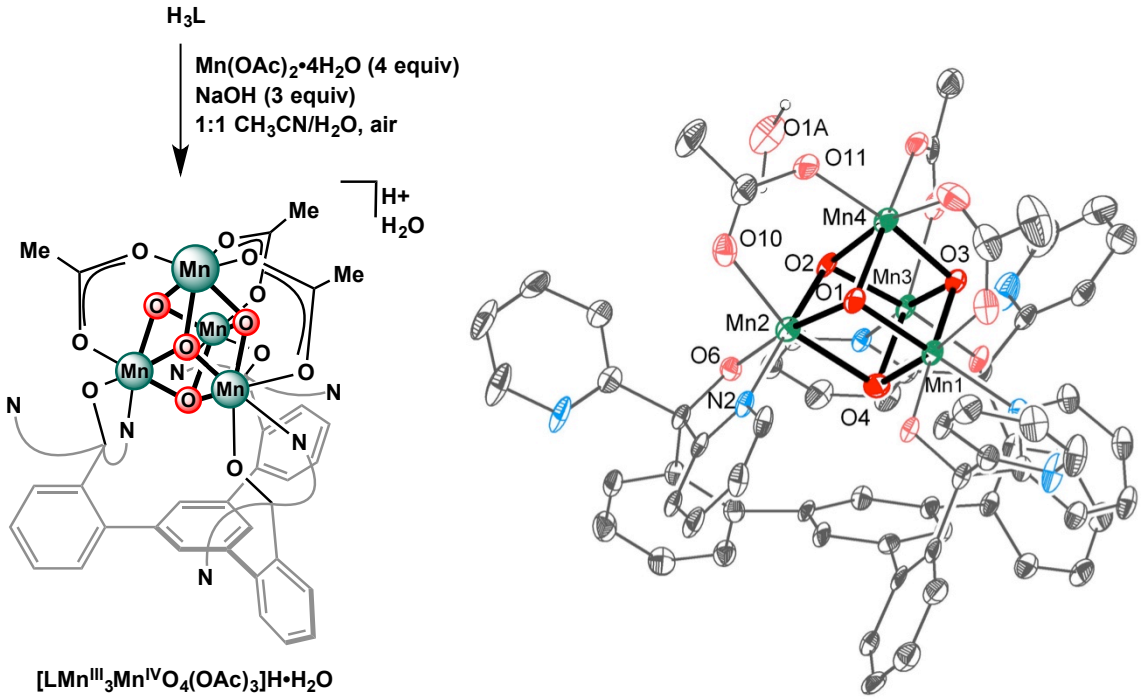

Scheme A.9 Synthesis (left) and solid-state structure (right) of $[LMn^{III}_3Mn^{IV}O_4(OAc)_3]H•H_2O$. Hydrogen atoms solvent molecules (other than the H-bonding water molecule) are not shown for clarity.

Our initial attempts to synthesize Mn_3M+M' dangler type complexes included desymmetrization of the *pseudo-*C_3 symmetric Mn_4O_4 cubane complexes. The simplest way to break the symmetry without re-engineering the multidentate ligand framework is selective removal of one (or two) of the bridging acetates. Initially, we hypothesized protonation of one of the bridging acetates of $LMn^{III}_2Mn^{IV}_2O_4(OAc)_3$ (**6**) could afford an asymmetric cubane and an equivalent of acetic acid. Attempts with *p*-cyanoanilinium triflate and pyridinium triflate afforded new species reproducibly; however, these did not appear asymmetric in the ^{1}H NMR spectra (too few peaks) and could not be isolated. The unbound pyridines of the ligand framework may have been interfering, although acetate is more basic in organic media. Nevertheless, trimethylsilyltriflate

(TMSOTf) proved much more successful (Scheme A.10; see also Chapter 3). Addition of one equivalent of TMSOTf to **6** in CH_2Cl_2, removal of volatiles *in vacuo*, and rinsing the resulting red/brown powder with Et_2O to remove trimethylsilylacetate (TMSOAc) afforded pure $LMn^{III}_2Mn^{IV}_2O_4(OAc)_2(OTf)$ in 90% yield. The ^1H NMR spectrum contained 23 peaks as compared to nine for **6**, consistent with decreased symmetry. The ^{19}F NMR spectrum contains a single peak, but rather than at ca. –78 ppm expected for an outer-sphere triflate the peak is at –37 ppm. A preliminary XRD structure confirms that a single acetate has been replaced with a κ^2-triflate (Figure B..11), consistent with the above solution spectra. Attempts with trimethylsilylperrhenate to produce a pentametallic complex gave a similar ^1H NMR to that found from TMSOTf; however, the resulting species postulated as $LMn_4O_4(OAc)_2(ReO_4)$ was only stable over hours in solution.

With the weakly bound triflate now in place, L-type donors were added to $LMn^{III}_2Mn^{IV}_2O_4(OAc)_2(OTf)$ as a proof of concept for selective functionalization of one face of the cubane unit. Addition of excess pyridine or 3,5-dimethylpyrazole (ca. 8 equiv.) to $LMn^{III}_2Mn^{IV}_2O_4(OAc)_2(OTf)$ afforded new species by ^1H NMR consistent with asymmetric species and a signal at –78 ppm in the ^{19}F NMR consistent with an outer-sphere triflate. Preliminary XRD studies showed two L donors bound to the sixth coordination sight of the two Mn on the open face ($[LMn^{III}_2Mn^{IV}_2O_4(OAc)_2(pyr)_2][OTf]$ for L=pyridine and **7** for L=3,5-dimethylpyrazole; Scheme A.10; see Chapter 3 for discussion of complex **7**). The pyridines and 3,5-dimethylpyrazoles π-stack with an unbound pyridine of the ligand framework. For the pyrazole complex, the two N–H units hydrogen bond to two of the oxygens of the triflate counterion.

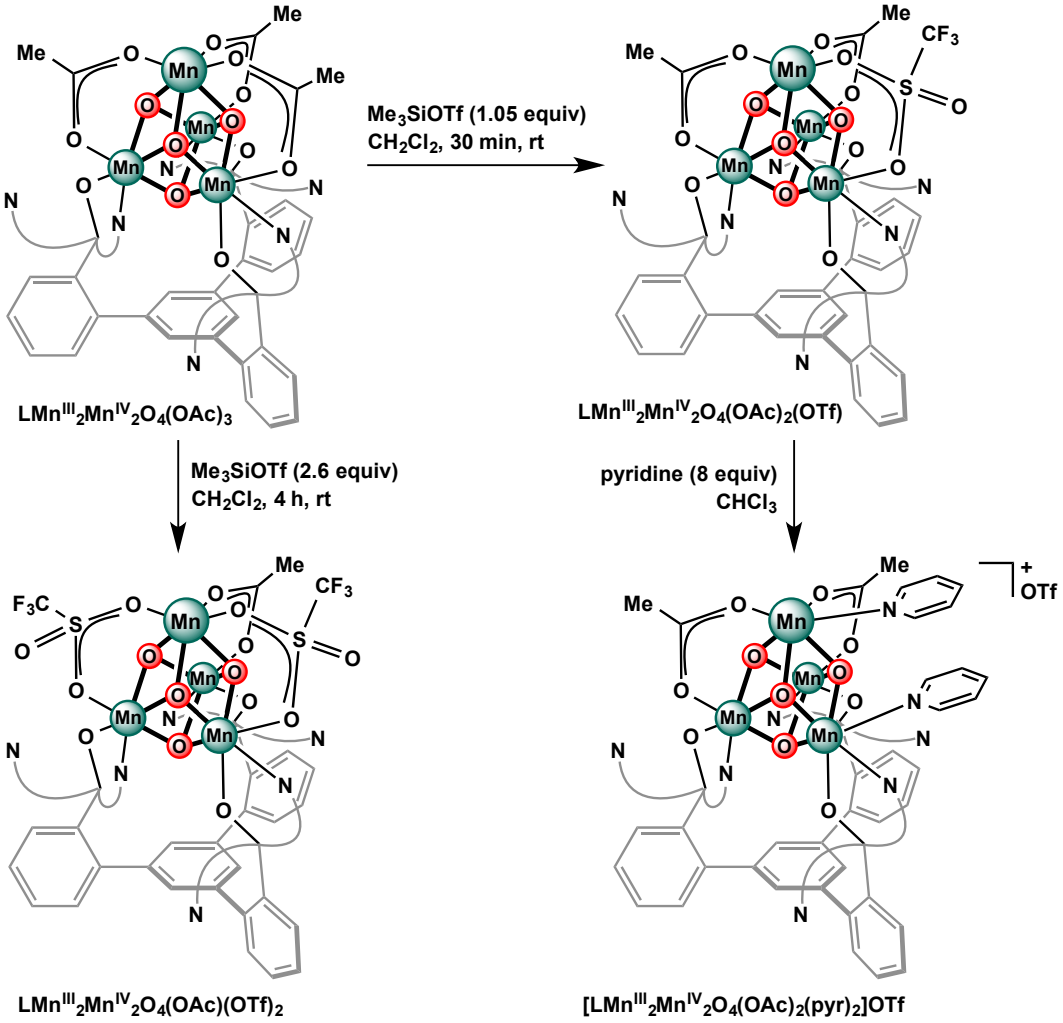

Scheme A.10 Synthesis of desymmetrized Mn_4O_4 cubane complexes.

The structural parameters and location of the manganese(IV) ions in the $Mn^{III}_2Mn^{IV}_2O_4$ unit varies depending on the ligand(s) bound to the unique face of the cubane. For example, in $LMn^{III}_2Mn^{IV}_2O_4(OAc)_2(OTf)$ the two Mn^{IV} are bound to the acetate bridges (Mn1 and Mn2) while in ($[LMn^{III}_2Mn^{IV}_2O_4(OAc)_2(pyr)_2][OTf]$ and **7** one of the Mn^{IV} is bound to the L-type donor (Mn2 in $[LMn^{III}_2Mn^{IV}_2O_4(OAc)_2(pyr)_2][OTf]$ and Mn1 in **7**). This is not surprising because triflate is a much worse donor than the aromatic N-donors pyridine and pyrazole. Thus it seems that donor variation could be

used to control Mn^{IV} location, possibly interesting in electronic structure studies especially if the ancillary donor set could be ligated to a fifth metal. Also, the Mn–Mn distance across the unique face elongates once a bridging ligand is absent: ca. 3.0 Å for $[LMn^{III}_2Mn^{IV}_2O_4(OAc)_2(pyr)_2][OTf]$ and **7** versus ca. 2.85 Å for **6** and $LMn^{III}_2Mn^{IV}_2O_4(OAc)_2(OTf)$. However, the elongation of the Mn–Mn distance does not cause a shortening of the O–O distance across the same face.

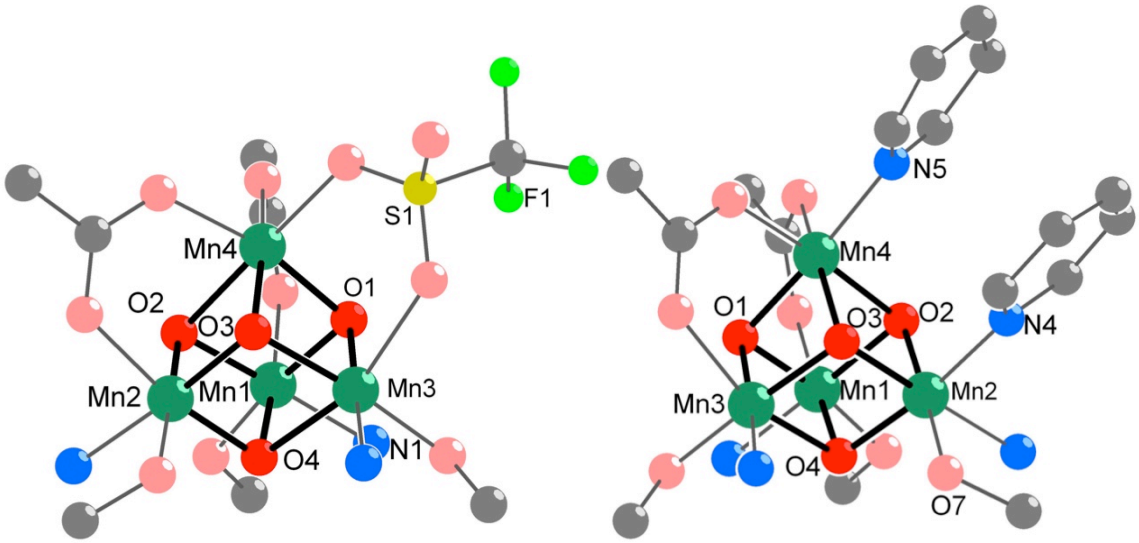

Scheme A.11 Ball-and-stick, solid-state, core structures of $LMn^{III}_2Mn^{IV}_2O_4(OAc)_2(OTf)$ (left) and $[LMn^{III}_2Mn^{IV}_2O_4(OAc)_2(pyr)_2][OTf]$ (right). Hydrogen atoms, disordered counterions, and solvent molecules are not shown for clarity.

Next, we posited that if one acetate could be removed, maybe two (or all three) could be removed by adding further equivalents of TMSOTf. This could allow more favorable reaction with bipy, terpy, or other more bulky ligands if two faces were more open to coordination. Mixture of **6** with 2.6 equivalents of TMSOTf affords a mixture of $LMn_4O_4(OAc)_2(OTf)$ and another asymmetric species within 10 minutes. Over four hours, the second species becomes major. After removal of volatiles *in vacuo* and rinsing

with hexanes, Et_2O and benzene, $LMn_4O_4(OAc)(OTf)_2$ was isolated in the CH_2Cl_2 fraction (Scheme A.10). The ^{19}F NMR spectrum contained two peaks (–42 and –48 ppm), consistent with two κ^2-triflates on two of the faces of the cubane. Disappointingly, reaction with bipy showed starting material and decomposition to the monotriflate complex. Although unsuccessful with bipy, $LMn_4O_4(OAc)(OTf)_2$ is still an interesting complex with the possibility of further functionalization complimentary to $LMn_4O_4(OAc)_2(OTf)$.

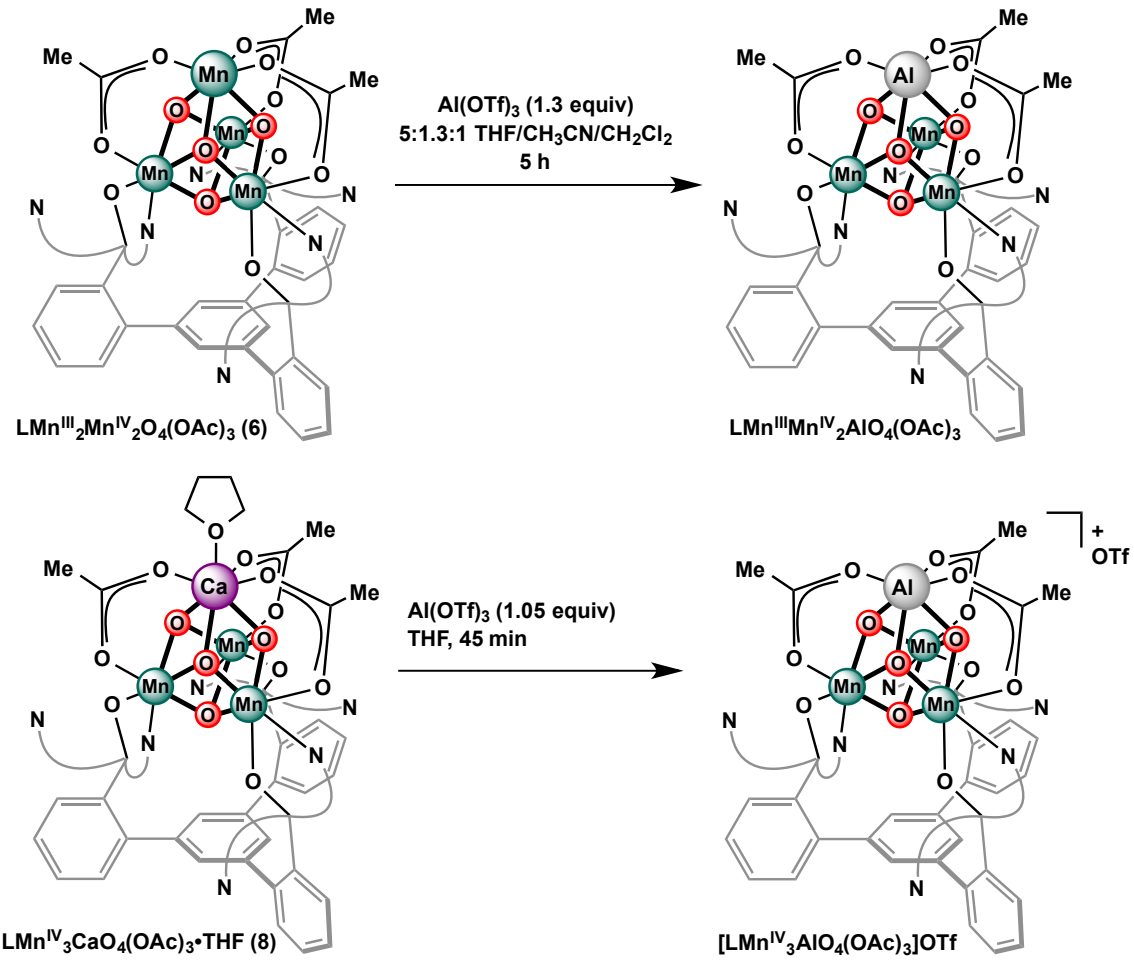

Scheme A.12 Synthesis of Mn_3AlO_4 cubane complexes.

A.4 Other Mn_3MO_4 Cubane Complexes

Site-differentiated functionalization of our Mn_3MO_4 cubane complexes has been successful for a wide range of metals M. In general, the metals have been larger than Mn^{III} (Ca^{2+}, Ln^{3+}, etc.); therefore, aluminum was tried, as it is smaller than Mn^{III}. We posited that the Al^{3+} could be a diamagnetic control for Mn^{III} while still allowing facile acetate substitution as observed above for the Mn_4O_4 cubanes as a path to Mn_3Al+Mn models of the OEC. Mn_3AlO_4 cubanes were successfully crystallized in two oxidation states, but in both cases the Al site had substantial populations of Mn and could not be synthesized cleanly. In the first case, **6** was reacted with $Al(OTf)_3$ in a mixture of polar, aprotic solvents to give $LMn^{III}Mn^{IV}{}_2AlO_4(OAc)_3$ (Scheme A.12). The bond lengths to the apical metal do not show distortion along one of the axes and are thus consistent with Al^{3+}; however, the displacement parameters refine to 90% Al and 10% Mn. The

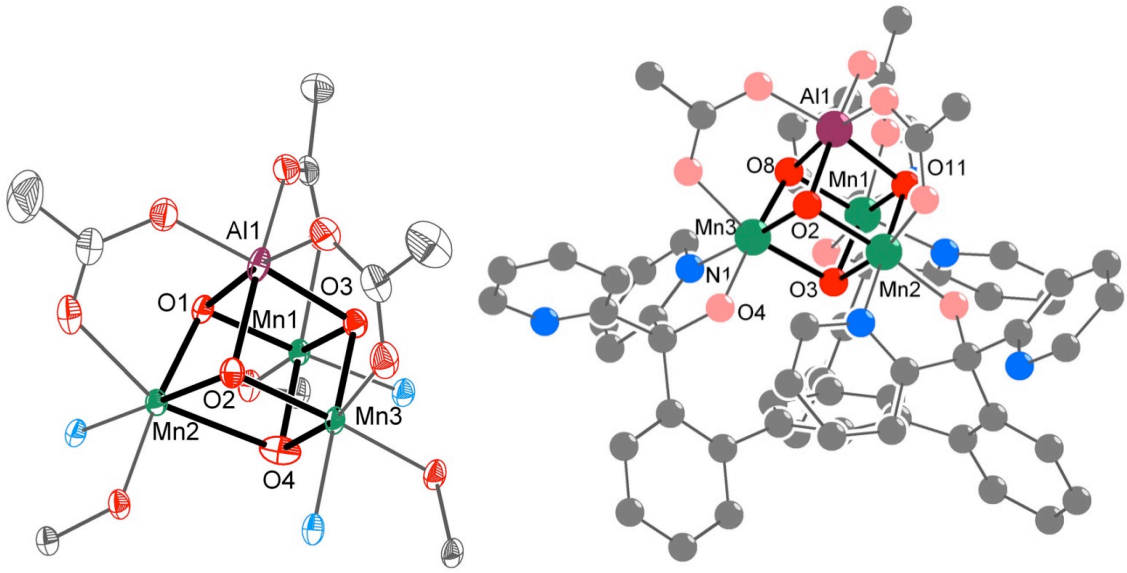

Scheme A.13 Solid-state, core structure of $LMn^{III}Mn^{IV}{}_2AlO_4(OAc)_3$ (left), and ball-and-stick solid-state structure of $[LMn^{iV}{}_3AlO_4(OAc)_3]OTf$ (right). Hydrogen atoms, disordered counterions, and solvent molecules are not shown for clarity.

one electron oxidized complex $[LMn^{IV}_3AlO_4(OAc)_3]OTf$ could be synthesized from salt metathesis of $Al(OTf)_3$ with **8** (Scheme A.12). A disordered, outer-sphere triflate was observed—consistent with the $Mn^{IV}_3AlO_4$ oxidation state—however, axial distortions are observed in the cubane core, consistent with the presence of Mn^{III}. This discrepancy, alongside the mixing of Al and Mn in the apical position made the Mn_3AlO_4 complexes intractable for further studies.

CymCOOH (cym = cymantrene = cyclopentadienylmanganesetricarbonyl), was found to substitute for acetate on the Mn_3MO_4 cubane complexes. Thus, a fully substituted $LMn_3MO_4(cymCOO)_3$ complex was targeted to show the geometry of $cymCOO^-$ binding and to prove the feasibility of utilizing cymCOO as a dangler precursor. Reaction of $LMn_3ScO_4(OAc)_3(OTf)$ (**17**) with excess cymCOOH produced an NMR very similar to that of starting material with only slight differences, and the ESI showed masses consistent with all combinations of $LMn_3ScO_4(OAc)_x(cymCOO)_{3-x}$ (1306, 1494, 1682, and 1870 *m*/*z*). To push the full substitution to completion, the reaction was instead run in DMF. After stirring **17** with three equivalents of cymCOOH in DMF, DMF was removed *in vacuo* with heating to also remove the byproduct acetic acid (Scheme A.14). This was repeated three times, and the excess cymCOOH was removed by extraction with Et_2O to give $Mn^{I}_3Mn^{IV}_3ScO_4$ complex $LMn^{IV}_3ScO_4(cymCOO)_3(OTf)$.

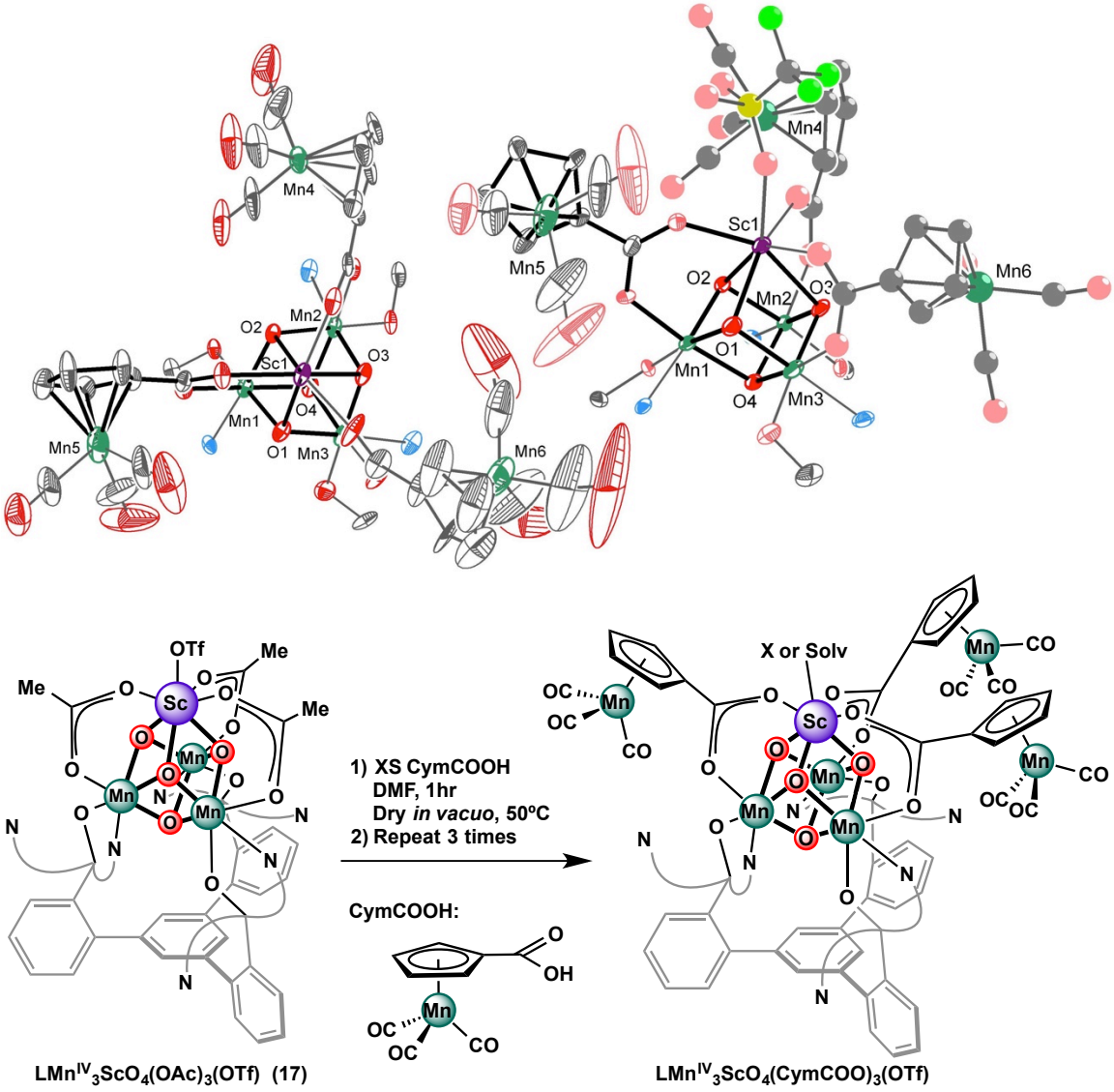

Scheme A.14 Synthesis (bottom) and solid-state, core structure (left, top view; right, side view) of $LMn^{IV}_3ScO_4(cymCOO)_3(OTf)$. In the top view, the triflate bound to Sc is not shown for clarity, and in the side view, two CymCOO motifs are drawn as ball-and-stick to highlight one dangling unit. Hydrogen atoms and solvent molecules are not shown for clarity.

In the solid-state structure of $LMn^{IV}_3ScO_4(cymCOO)_3(OTf)$, the three acetates of **17** have been replaced by $cymCOO^-$, while the triflate remains in scandium's seventh

coordination site (Scheme A.14). Although the diffraction data is poor, the Mn distances are still consistent with Mn^{IV}, with Mn-μ_3-O distances between 1.839 and 1.904 Å. The $Mn^{I}_3Mn^{IV}_3$ oxidation state is consistent with the number of anions as well. The Cp rings are approximately perpendicular to the basal, central benzene, such that the Mn^{I} centers are about the same distance from the closest Mn^{IV} and the Sc (ca. 5.5 Å). The Mn^{I} centers face away from the unbound pyridine rings, likely because of the steric clash that would occur with the carbonyls. The Mn^{I} centers are also ca. 5 Å away from the nearest μ_3-O, suggesting substantial rearrangement upon oxidation to $Mn^{II/III}$ would be necessary to give an OEC-like dangler motif.

CONCLUSIONS

This appendix briefly outlined complexes that were either not fully characterized or did not fit into one of the chapters above. They were included such that all of the complexes observed over the last five years of work are fully disclosed in this thesis.

EXPERIMENTAL SECTION

Synthetic Procedures

Synthesis of $LCo_3(PO_4)$: H_3L powder (80.2 mg, 0.093 mmol) and $Co_3(PO_4)_2$ (34.2 mg, 0.093 mmol, 1 equiv) were weighed into a 20 mL scintillation vial, and MeOH (2 mL) was added. No dissolution of the tan/purple heterogeneous mixture was observed after 15 minutes, so NaOH (11 mg, 0.279 mmol, 3 equiv) were added as a 0.56 M solution in MeOH (0.5 mL). After 5 hours, homogeneity was not observed; therefore an equal

volume (2.5 mL) of CH_3CN was added. As no change to solubility occurred, H_2O (2.5 mL) was added. The solution became red/brown and cloudy. The solution was stirred for 12 hours, and then concentrated *in vacuo* to dryness. The resulting residue was extracted with CH_3CN to afford a red/brown solution and tan solid that was filtered off. Vapor diffusion of Et_2O into a CH_3CN solution afforded red/brown crystals of $LCo_3(PO_4)$.

Synthesis of $[H_3LNi_3(CH_3CN)_{10}(H_2O)](ClO_4)_6$: H_3L (229 mg, 0.27 mmol) was suspended in CH_3CN (4 mL), and $Ni(ClO_4)_2 \cdot 6H_2O$ (292.5 mg, 0.8 mmol, 3 equiv) was added as a crystalline solid. The solution immediately turned blue and homogeneous. 3 mL of the reaction mixture was taken on to a reaction with NaOH, but 1 mL was kept unbasified. Et_2O was carefully layered onto this CH_3CN solution, and liquid diffusion over weeks afforded light purple crystals of $[H_3LNi_3(CH_3CN)_{10}(H_2O)](ClO_4)_6$.

Synthesis of $[LMn^{II}_2Mn^{III}_2O(OAc)_2(OMe)(OTf)]OTf$: Under an anaerobic atmosphere, purple powder $[LMn^{II}_2Mn^{III}_2O(OAc)_3(OTf)]OTf$ (**3**) (~10 mg, 6μmol) was dissolved in degassed methanol (~0.6 mL) to give a yellow/brown, homogeneous solution. Diethyl ether was allowed to vapor diffuse into the solution, giving brown crystals. ^{1}H NMR (300 MHz, CD_3OD, 25 ºC). 79.1 ($\Delta\nu_{1/2}$=300 Hz), 70.3 ($\Delta\nu_{1/2}$=300 Hz), 65.9 ($\Delta\nu_{1/2}$=70 Hz), 54.8 ($\Delta\nu_{1/2}$=140 Hz), 44.2 ($\Delta\nu_{1/2}$=300 Hz), 40.6 ($\Delta\nu_{1/2}$=100 Hz), 36.9 ($\Delta\nu_{1/2}$=520 Hz), 33.3 ($\Delta\nu_{1/2}$=260 Hz), 26.6 ($\Delta\nu_{1/2}$=360 Hz), 15.7 ($\Delta\nu_{1/2}$=40 Hz), 14.0 ($\Delta\nu_{1/2}$=50 Hz), 8.2 & 7.0 (overlapping), 5.4 & 4.7 & 4.2 (overlapping), –16.3 & –17.1 (overlapping), –20.5 ($\Delta\nu_{1/2}$=250 Hz), –23.5 ($\Delta\nu_{1/2}$=170 Hz), –36.6 ($\Delta\nu_{1/2}$=180 Hz). ^{19}F NMR (282 MHz, CD_2Cl_2, 25 ºC): 79.5 ($\Delta\nu_{1/2}$=140 Hz) ppm

Synthesis of $[LMn^{II}_3Mn^{III}O(OAc)_3]_2$•2OTf$^-$. In the glovebox, the purple solid **3** (126.3 mg, 0.08 mmol) was dissolved in CH_2Cl_2 (8 mL). Decamethylferrocene (27.6 mg, 0.085 mmol) was added to the purple-brown solution of **3** as an orange solution in CH_2Cl_2 (1 mL). The reaction mixture turned gray-brown. Volatile materials were removed *in vacuo* after 30 minutes of stirring. The resulting solid was dissolved in minimal CH_3CN and Et_2O was allowed to vapor diffuse into the solution to afford large green crystals ([FeCp*]OTf) and small purple crystals. The crystals were separated manually to afford 60 mg of purple, crystalline material. ^{1}H NMR (300 MHz, $CDCl_3$, 25 ºC) 54.2 ($\Delta\nu_{1/2}$=920 Hz), 42.0 & 37.2 & 34.5 (overlapping), 28.1 ($\Delta\nu_{1/2}$=220 Hz), 10.8 ($\Delta\nu_{1/2}$=150 Hz), 8.6 ($\Delta\nu_{1/2}$=340 Hz), 5.6 ($\Delta\nu_{1/2}$=170 Hz), –5.3 ($\Delta\nu_{1/2}$=250 Hz), –7.2 ($\Delta\nu_{1/2}$=200 Hz) ppm. ^{19}F NMR (282 MHz, CD_2Cl_2, 25 ºC): 76.5 ($\Delta\nu_{1/2}$=230 Hz) ppm. Anal. Calcd. for $C_{128}H_{96}F_6Mn_8N_{12}O_{26}S_2$: C, 54.21; H, 3.41; N, 5.93. Found: C, 54.29; H, 3.63; N, 5.86.

Synthesis of $LMn^{II}_3Mn^{III}O(OAc)_3Cl$: In a $LMn_3(OAc)_3$ (**1**) (30.45 mg, 0.023 mmol) was dissolved in CH_2Cl_2 (unknown volume). $Mn(OAc)_2$ (4 mg, 0.023 mmol, 1 equiv) was added as a suspension in CH_2Cl_2. KO_2 (3.3 mg, 0.046 mmol, 2 equiv) was added as a solid. No fast change in appearance was obsvered from the yellow solution with tan and yellow solids. After 12 hours, the solution is orange/brown. A small amount of yellow powder was filtered off, and the resulting clear solution was concentrated to dryness. The resulting residue was fractioned with C_6H_6 (which contained some free **H_3L** and other paramagnetic species by ^{1}H NMR spectroscopy) and CH_2Cl_2. The CH_2Cl_2 fraction was concentrated, and vapor diffusion of Et_2O into the solution afforded spike crystals of $LMn^{II}_3Mn^{III}O(OAc)_3Cl$.

Synthesis of $[[LMn_3O(OAc)_3]_2Sc][OTf]_n$: In the glovebox, $LMn_3(OAc)_3$ (**1**) (18.7 mg, 0.015 mmol) and $Sc(OTf)_3$ (7.7 mg, 0.015 mmol, 1 equiv) were weighed into a 20 mL vial and CH_2Cl_2 (unknown volume) was added. $Sc(OTf)_3$ did not dissolve readily. KO_2 (2.2 mg, 0.03 mmol, 2 equiv) was added as a yellow solid, with no obvious change to the heterogeneous mixture. 18-crown-6 (< 1 mg, <0.1 equiv) was added in an attempt to increase solubility. The solution became brown over time, and was concentrated to dryness at 1 hour. The residue was washed with C_6H_6, which took a small amount of color, and then extracted with CH_2Cl_2, filtered, and concentrated. Vapor diffusion of pentane into the CH_2Cl_2 solution afforded crystals of $[LMn_3O(OAc)_3]_2Sc][OTf]_n$.

Synthesis of $[[LMn_3O(OAc)_3]_2Mn][OTf]_n$: The purple solid **3** (25 mg, 0.016 mmol) was dissolved in wet, aerobic CH_2Cl_2 on the benchtop. Two drops of H_2O were added while stirring the solution, followed a few minutes later by THF to increase the miscibility of the H_2O and CH_2Cl_2. Let stir until precipitation of a dark brown solid is complete. The mixture was filtered to give an army green/brown solution, which was then concentrated to dryness. Dissolution in $CDCl_3$ and standing for 2 days afforded dark brown crystals of $[[LMn_3O(OAc)_3]_2Mn][OTf]_n$.

Synthesis of $[LMn^{III}_3O(OAc)_3]_2Mn^{II}[OTf]_4$: Following Dr. Emily Tsui's procedure for the formation of the Mn_3MO_2 'dioxo' compounds, $LMn_3(OAc)_3$ (**1**) (42.4 mg, 0.03 mmol) was suspended in DME in the glovebox. $Mn(OTf)_2 \bullet 2CH_3CN$ (19.7 mg, 0.05 mmol, 1.5 equiv) was added as a solution in DME (total reaction volume=4 mL). After stirring for 5 minutes, PhIO (14.7 mg, 0.07 mmol, 2 equiv) was added as a solid. The solution turned brown quickly, then red/purple at 30 minutes, and after stirring 12

hours had red/purple precipitate. The mixture was filtered, the solids were rinsed with DME, and then extracted with CH_2Cl_2 into a solution kept separate from the DME solution. The CH_2Cl_2 fraction was concentrated, and vapor diffusion of Et_2O into it afforded crystals of $[LMn^{III}_3O(OAc)_3]_2Mn^{II}[OTf]_4$.

Synthesis of $[LMn_4O(O_2CCF_3)_4][Mn(ON_4O)(O_2CCF_3)_2]$: In the glovebox, $LMn_3CaO_4(ON_4O)(OAc)$ (**14**) (37.4 mg, 0.027 mmol) was partially dissolved in CH_2Cl_2 (12 mL). $Mn(O_2CCF_3)_2$ (22.3 mg, 0.08 mmol, 3 equiv) was dissolved in CH_3CN (1-2 mL) and added to the solution of **14** under stirring dropwise over 5 minutes. The solution becomes homogeneous by half addition of $Mn(O_2CCF_3)_2$. After stirring 40 hours, volatiles were removed *in vacuo*. The resulting residue was rinsed with Et_2O and extracted with C_6H_6. This solution was filtered and concentrated to dryness. Vapor diffusion of Et_2O into a $CHCl_3$ solution of the C_6H_6 fraction afforded crystals of $[LMn_4O(O_2CCF_3)_4][Mn(ON_4O)(O_2CCF_3)_2]$.

Synthesis of $[LMn^{III}_3Mn^{IV}O_4(OAc)_3]H•H_2O$: H_3L (131.3 mg, 0.15 mmol) was weighed into a vial and suspended in H_2O (1.5 mL) and CH_3CN (1.5 mL). $Mn(OAc)_2•4H_2O$ (150 mg, 0.6 mmol, 4 equiv) was added as a solid, followed by NaOH (0.46 mmol, 3 equiv) as a 1.0 M solution in H_2O. The mixture turns golden brown and almost fully homogeneous within two minutes, then turns darker brown as the Mn is oxidized. At 20 hours, the solution was concentrated *in vacuo*, giving a milky green solution when mostly H_2O was left and then returned to brown once fully dry. The resulting brown powder was triturated in Et_2O, and $CHCl_3$ was added until mostly off-

white solids were left undissolved. The solids were filtered away, and the resulting brown solution was concentrated *in vacuo*. The residue was re-dissolved in CH_2Cl_2, and vapor diffusion of Et_2O into the solution afforded brown crystals of $[LMn^{III}_3Mn^{IV}O_4(OAc)_3]H•H_2O$.

Synthesis of $LMn^{III}_2Mn^{IV}_2O_4(OAc)_2(OTf)$: In the glovebox, $LMn_4O_4(OAc)_3$ (**6**) (225 mg, 0.18 mmole) was dissolved in CH_2Cl_2 (35 mL) to give a red/brown and clear solution. Separately, a clear and colorless 0.1 M solution of TMSOTf (50 μL, 0.28 mmole) in DCM (2.8 mL) was prepared. 1.8 mL of the 0.1 M TMSOTf solution (0.18 mmole, 1.05 equiv) was transferred by syringe to the solution of **6**. No color change occurred, the solution was stirred magnetically for 25 minutes, and volatiles were then removed *in vacuo*. To the resulting red/brown solid, Et_2O (3 mL) was added and removed *in vacuo* to remove any remaining CH_2Cl_2. The solid was triturated in Et_2O (10 mL), loaded onto a celite plug and rinsed with Et_2O to remove the TMSOAc side product. The solid was rinsed through with C_6H_6 and concentrated *in vacuo* to give $LMn^{III}_2Mn^{IV}_2O_4(OAc)_2(OTf)$ as a red/brown powder (224 mg, 93%) that was stored in the freezer. Crystals amenable to structural determination were grown from vapor diffusion of Et_2O into a solution in C_6H_6 or toluene. ^{1}H NMR (300 MHz, CD2Cl2, 25 oC) –66.0 (Δν1/2=1500 Hz), – 42.0 (Δν1/2=1500 Hz), –15.5 (Δν1/2=90 Hz), –10.8 (Δν1/2=100 Hz), –9.9 (Δν1/2=90 Hz), 2.8 (Δν1/2=200 Hz), 5.5, 5.7, 5.8, 6.3 (overlapping), 7.5, 8.2, 8.5, 8.6, 9.1, 9.8, 9.9, 10.3, 10.4, 11.2, 12.3, 12.9 (overlapping), 15.8 (Δν1/2=250 Hz) ppm. 19F NMR (282 MHz, CD2Cl2, 25 oC): –37 (Δν1/2=460 Hz) ppm.

Synthesis of $[LMn^{III}_2Mn^{IV}_2O_4(OAc)_2(pyr)_2][OTf]$: 6 (18 mg, 13 μmol) was dissolved in CH_2Cl_2. Pyridine (8.2 μL, 0.1 mmole, 8 equiv) was added with a 25 μL syringe. Volatiles were removed *in vacuo* after stirring for 10 minutes. The resulting solid was triturated in hexane and filtered to remove any remaining pyridine. The solid was rinsed through with CH_2Cl_2 and concentrated *in vacuo* to afford a brown solid $[LMn^{III}_2Mn^{IV}_2O_4(OAc)_2(pyr)_2][OTf]$ (17 mg, 84%) that was stored in the freezer. Crystals amenable to structural determination were grown from vapor diffusion of pentane into a solution in $CHCl_3$. ^{1}H NMR (300 MHz, CD_2Cl_2, 25 ºC) –15.1, –13.5, –12.2 (overlapping), –1.1 ($\Delta\nu_{1/2}$=700 Hz), 4.5, 6.6, 7.1, 7.2, 7.3, 7.9, 8.8, 9.1, 9.8, 10.5, 10.8, 14.3, 15.8, 17.5, 17.5 (overlapping), 21.7, 23.4 (overlapping) ppm. ^{19}F NMR (282 MHz, CD_2Cl_2, 25 ºC): –78 ($\Delta\nu_{1/2}$=100 Hz) ppm.

Synthesis of $LMn_4O_4(OAc)(OTf)_2$: 6 (53.1 mg, 0.04 mmol) was dissolved in CH_2Cl_2. 1.05 mL of a 0.1 M solution of TMSOTf in CH_2Cl_2 (0.105 mmol, 2.6 equiv) was added to the solution of **6** and the mixture was stirred for four hours. The volatiles were removed *in vacuo*, and the resulting solid was loaded onto glass filter paper and fractioned with hexanes, Et_2O, benzene, and CH_2Cl_2. The benzene fractioned contained a mixture of $LMn^{III}_2Mn^{IV}_2O_4(OAc)_2(OTf)$ and $LMn_4O_4(OAc)(OTf)_2$, whereas the CH_2Cl_2 contained solely $LMn_4O_4(OAc)(OTf)_2$ by ^{1}H NMR. Removal of solvent *in vacuo* afforded $LMn_4O_4(OAc)(OTf)_2$ as a red/brown solid (41 mg, 68%) that must be stored in the freezer and should be used quickly, as it decomposes. ^{1}H NMR (300 MHz, CD_2Cl_2, 25 ºC) –16.9 ($\Delta\nu_{1/2}$=100 Hz), –14.4 ($\Delta\nu_{1/2}$=110 Hz),–12.0 ($\Delta\nu_{1/2}$=90 Hz), 4.7,

5.6, 6.1, 6.3, 7.6, 8.2, 8.6, 9.1, 9.5, 9.8, 10.3, 10.9, 11.1, 11.8, 12.7, 13.6, 15.3 (overlapping) ppm. ^{19}F NMR (282 MHz, CD_2Cl_2, 25 °C): –47.6, –41.9 ppm.

Synthesis of $LMn^{III}Mn^{IV}_2AlO_4(OAc)_3$: In the glovebox, **6** (13.6 mg, 0.01 mmol) was dissolved in THF (5 mL) and CH_2Cl_2 (1 mL). **6** was further diluted with CH_3CN (1.3 mL) and then $Al(OTf)_3$ (6.4 mg, 0.013 mmol, 1.3 equiv) was added as a solid. No obvious color or solubility changes occurred. Volatiles were removed *in vacuo* after 5 hours of stirring. The resulting residue was rinsed with Et_2O and C_6H_6, then extracted with CH_2Cl_2, filtered, and concentrated to give a brown solid. Vapor diffusion of Et_2O into a CH_2Cl_2 solution of the brown solid afforded crystals of $LMn^{III}Mn^{IV}_2AlO_4(OAc)_3$.

Synthesis of $[LMn^{IV}_3AlO_4(OAc)_3]OTf$: In the glovebox, $LMn_3CaO_4(OAc)_3$•THF (**8**) (33 mg, 0.024 mmol) was partially dissolved in THF. $Al(OTf)_3$ (11.9 mg, 0.025 mmol, 1.05 equiv) was added as a suspension in THF. The solution became darker and more homogeneous within 2 minutes of addition. The reaction was stirred for 45 minutes, and then concentrated to dryness. The resulting residue was dissolved in CH_2Cl_2, and vapor diffusion of Et_2O afforded crystals of $[LMn^{IV}_3AlO_4(OAc)_3]OTf$.

Synthesis of $LMn^{IV}_3ScO_4(cymCOO)_3(OTf)$: In the glovebox, $LMn_3ScO_4(OAc)_3(OTf)$ (**17**) (29.8 mg, 0.02 mmol) was dissolved in DMF, and then cymantrenecarboxylic acid (20 mg, 0.08 mmol, 4 equiv) was added as a solution in DMF. The mixture was stirred for 1 hour, and then volatiles were removed *in vacuo* at *ca.* 40 °C. More DMF and cymantrenecarboxylic acid (8 mg, 0.03 mmol, 1.5 equiv) was added, the solution was

stirred 40 minutes, and then concentrated to dryness at 40 ºC. Again, more DMF and cymantrenecarboxylic acid (15 mg, 0.06 mmol, 3 equiv) was added, the solution was stirred 16 hours, and then concentrated to dryness at 40 ºC. The resulting residue was rinsed with hexane and Et_2O, then extracted with C_6H_6, filtered, and concentrated to dryness to afford $LMn^{IV}_3ScO_4(cymCOO)_3(OTf)$ (26 mg, 63%). Crystals amenable to structural determination were grown from vapor diffusion of pentane into a CH_2Cl_2 solution. ^{1}H NMR (300 MHz, CD_2Cl_2, 25 ºC) 13.2, 12.3, 9.4, 8.5, 6.9, 4.5, 3.2, –0.7, –23.9 ppm. ^{19}F NMR (282 MHz, CD_2Cl_2, 25 ºC): –78.5 ppm.

Crystallographic Information

The refinements for all of these complexes were never finalized. As such, their refinement data is not included. All of the most up-to-date refinements and notes on their quality as of this writing can be found on ReciprocalNet (http://reciprocalnet.caltech.edu) with the appropriate jskXX, syncjskXX, or aXXXX code, which can be found in the file "JSKanady XRD structure list.pdf" on the Agapie Group server in the directory LANGLEYSERVER/group/Structures/JacobKanady.

APPENDIX B

NMR SPECTRA

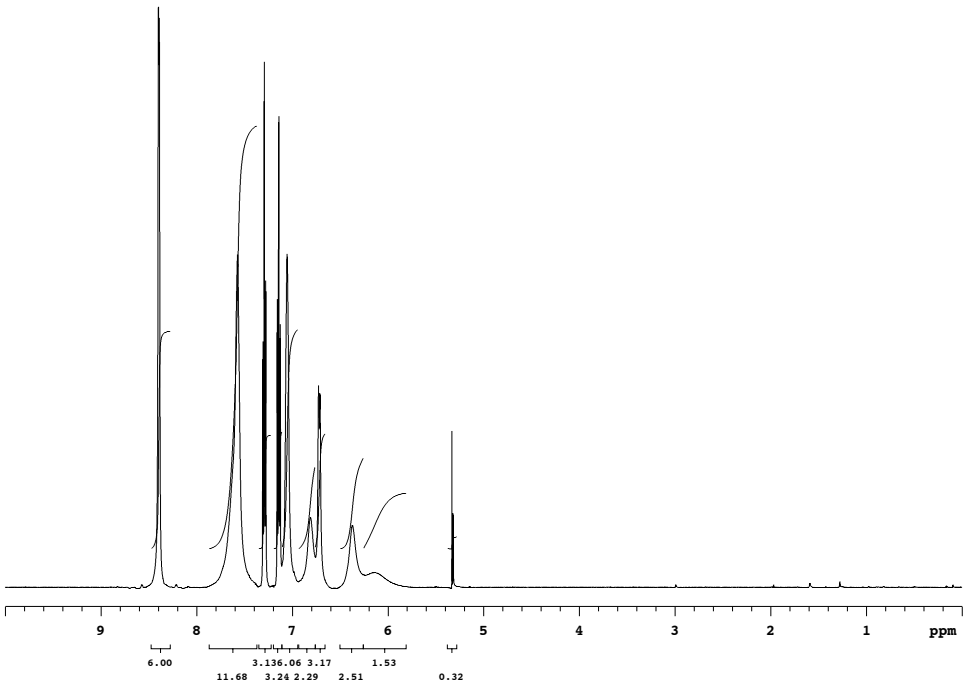

Figure B.1 ^{1}H NMR spectrum of **H_3L** in CD_2Cl_2 at 25 °C.

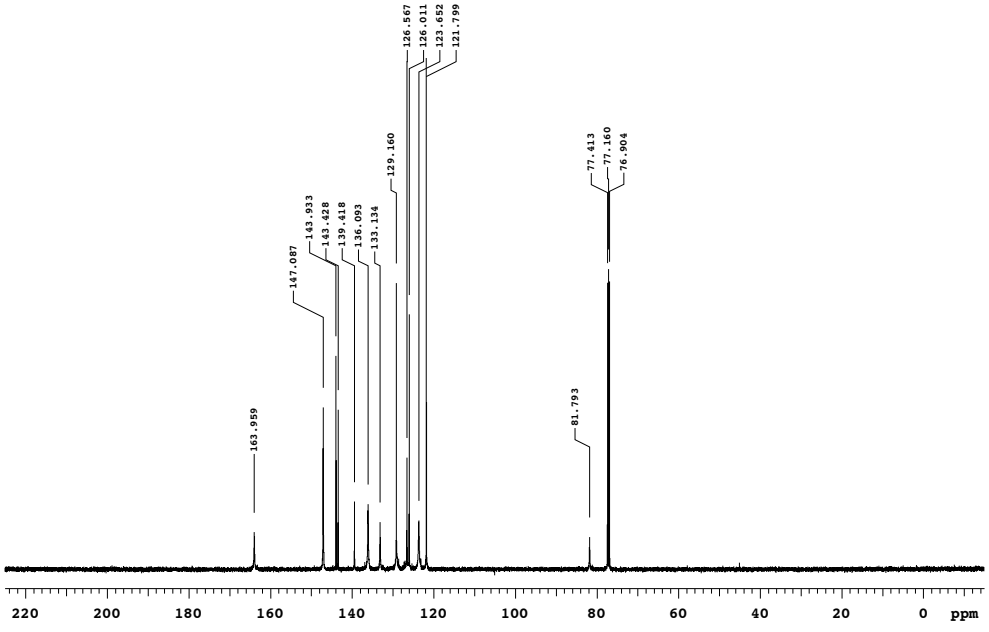

Figure B.2 ^{13}C NMR spectrum of **H_3L** in $CDCl_3$ at 25 °C.

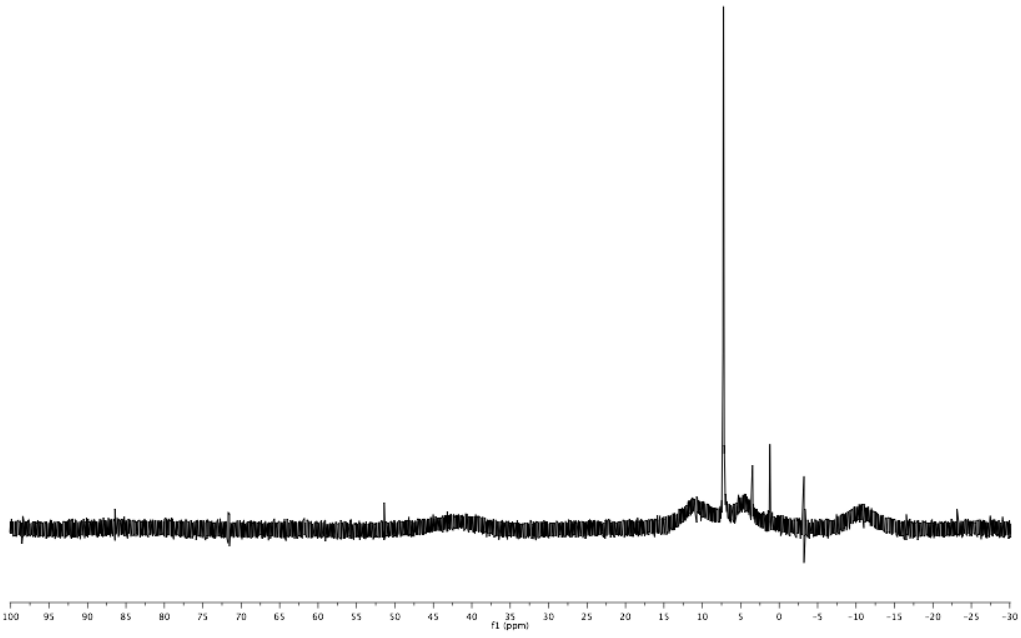

Figure B.3 ^{1}H NMR spectrum of $LMn_3(OAc)_3$ in $CDCl_3$ at 25 °C.

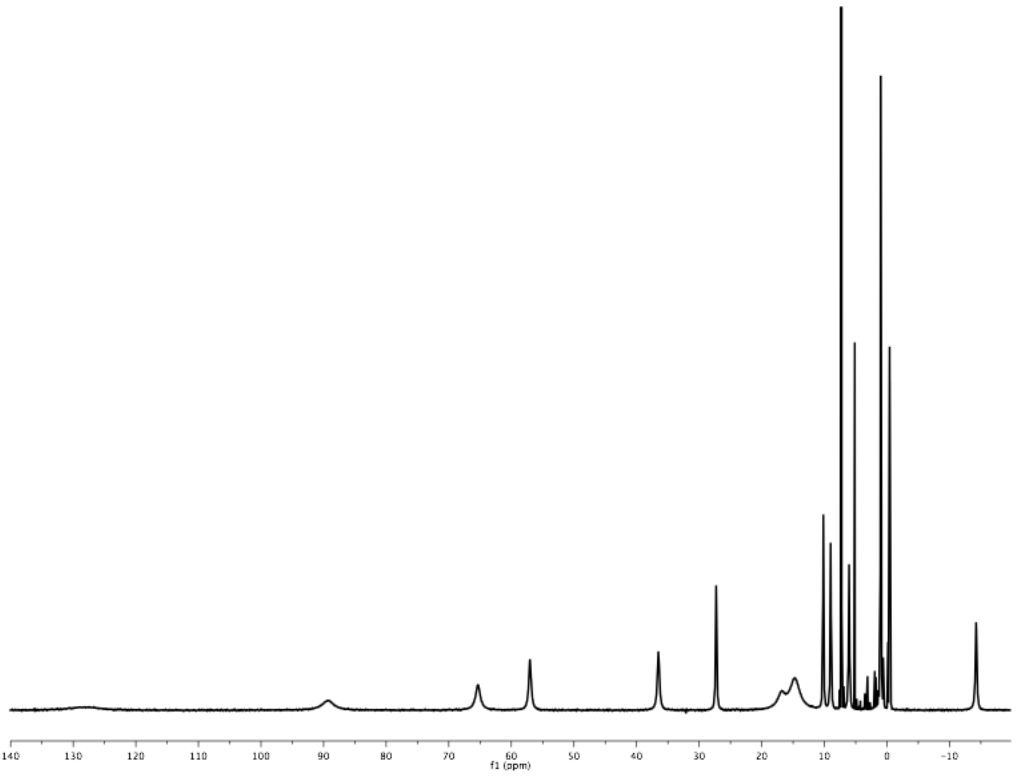

Figure B.4 ^{1}H NMR spectrum of $LCo_3(OAc)_3$ in $CDCl_3$ 25 °C.

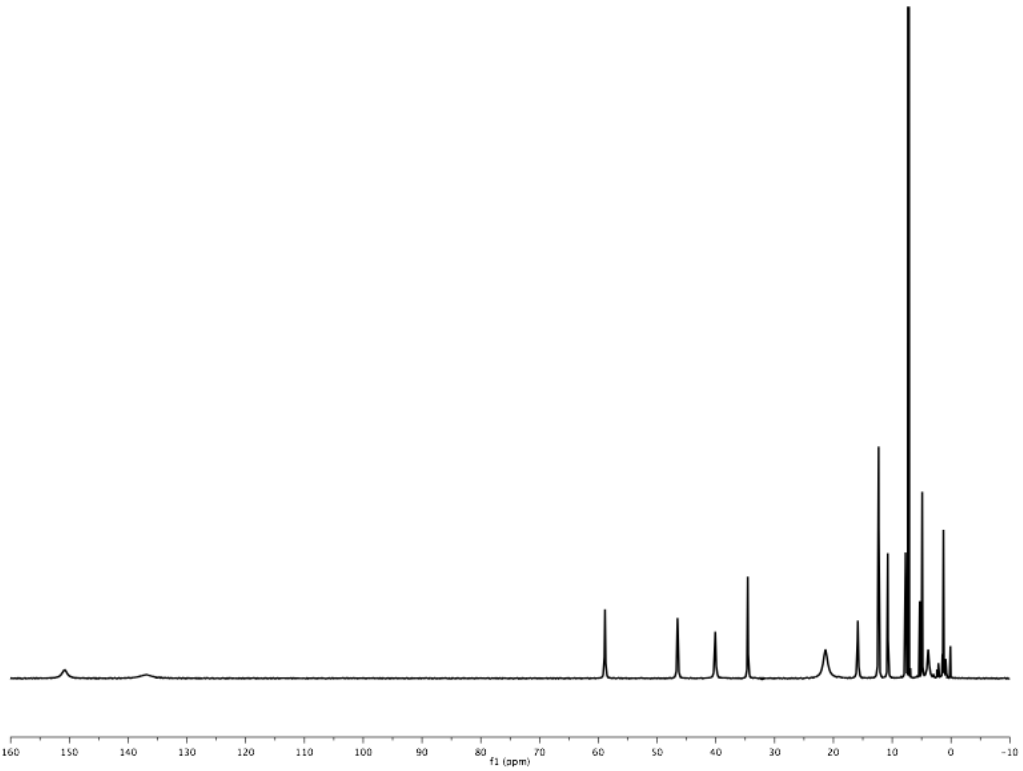

Figure B.5 ^{1}H NMR spectrum of $LNi_3(OAc)_3$ in $CDCl_3$ at 25 °C.

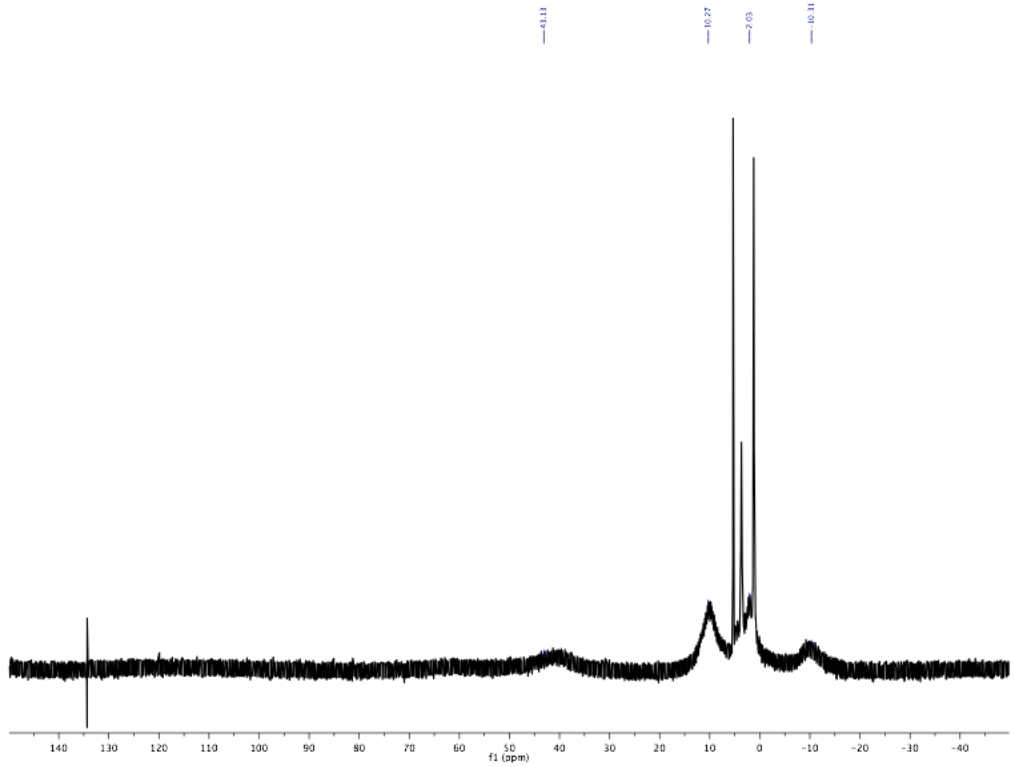

Figure B.6 ^{1}H NMR spectrum of $LMn_3(O_2CPh)_3$ in $CDCl_3$ at 25 °C.

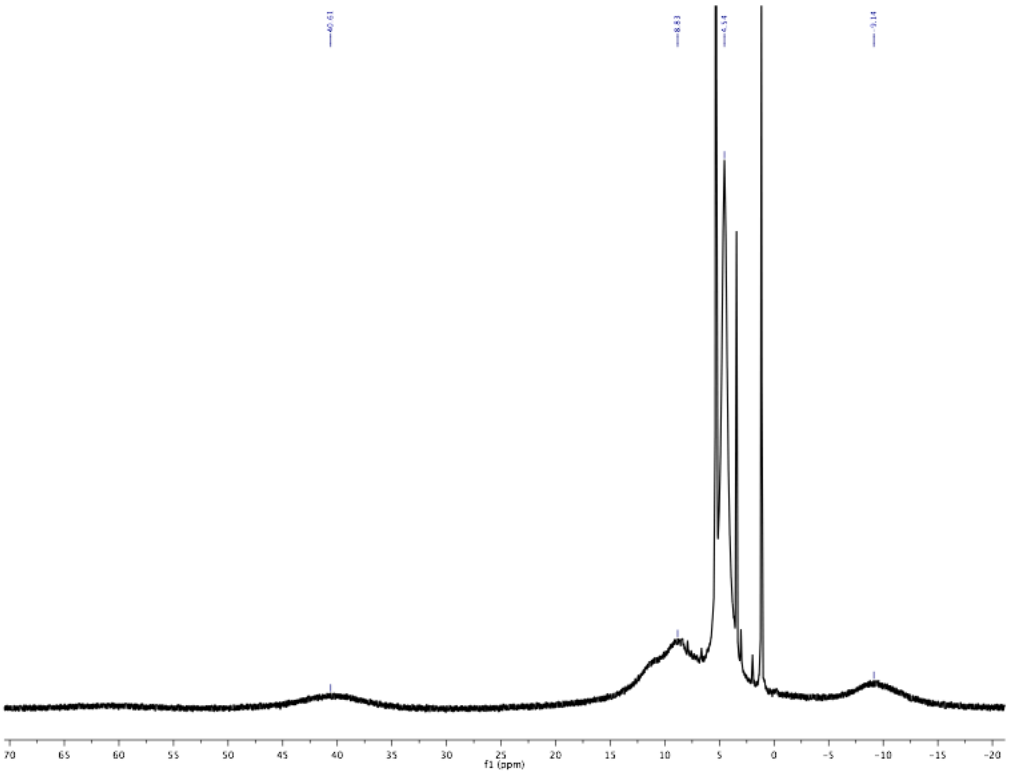

Figure B.7 ^{1}H NMR spectrum of LMn_3(*p*-dimethylaminobenzoate)$_3$ in CD_2Cl_2 at 25 °C.

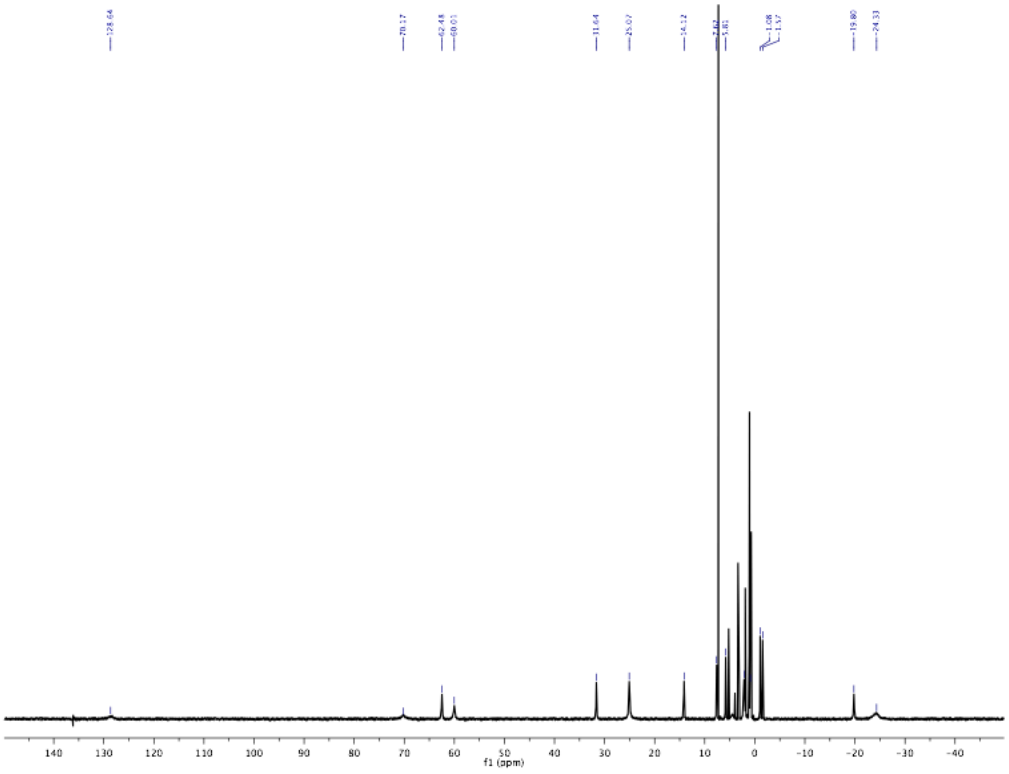

Figure B.8 ^{1}H NMR spectrum of $LCo_3(O_2CPh)_3$ in $CDCl_3$ at 25 °C

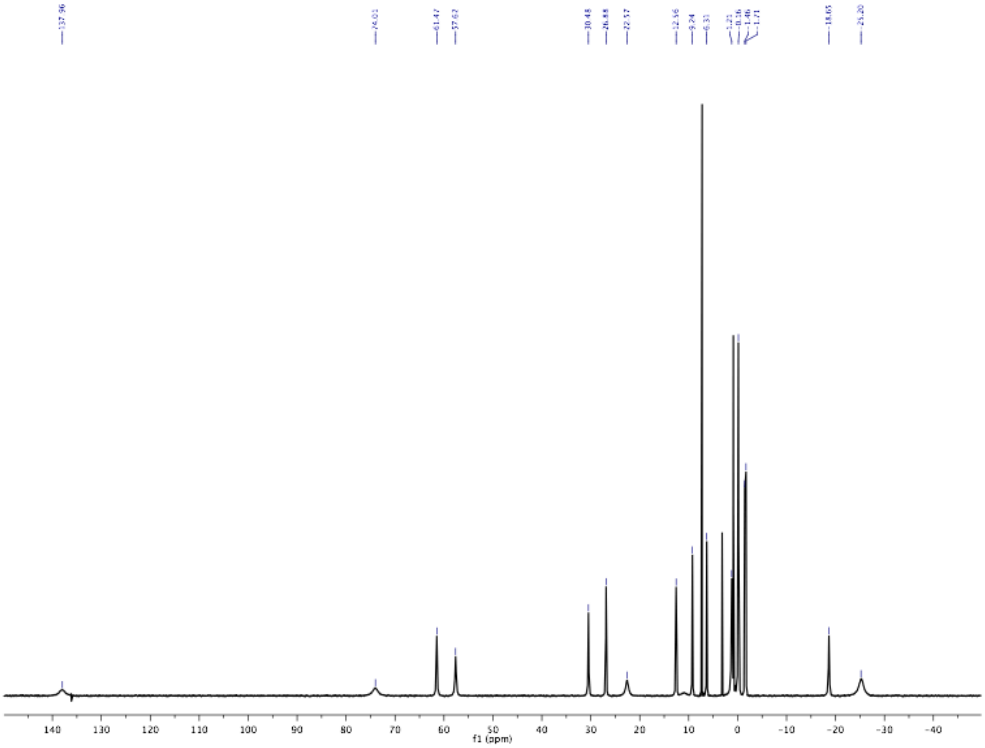

Figure B.9 ^{1}H NMR spectrum of LCo_3(*p*-toluate)$_3$ in $CDCl_3$ at 25 ºC.

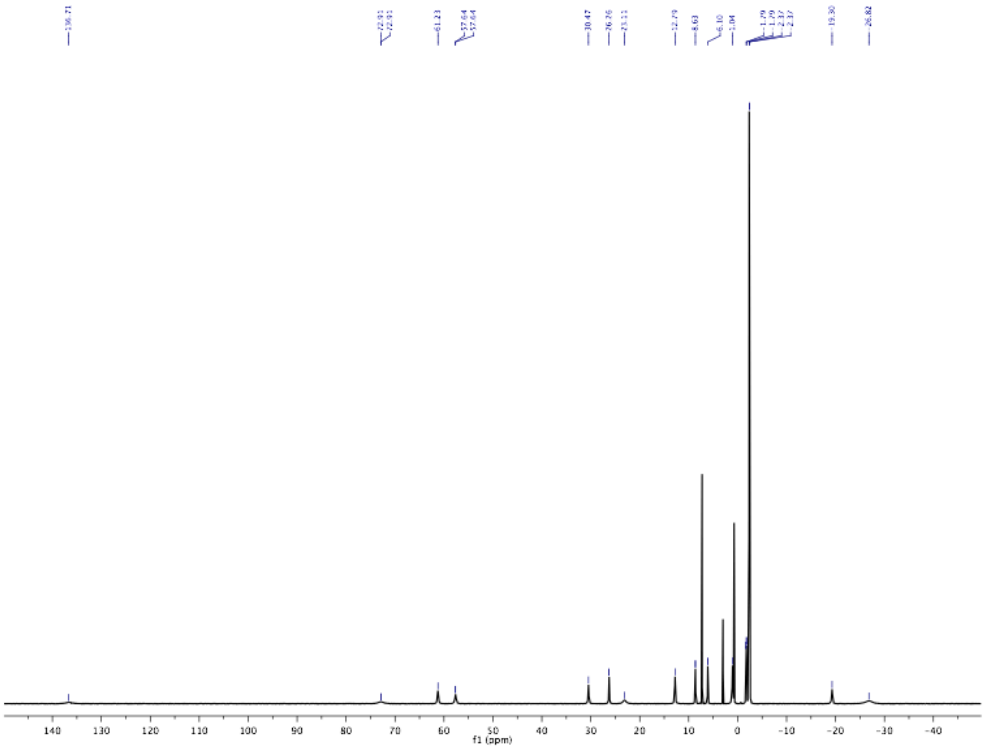

Figure B.10 ^{1}H NMR spectrum of LCo_3(*p*-^{t}butylbenzoate)$_3$ in $CDCl_3$ at 25 ºC.

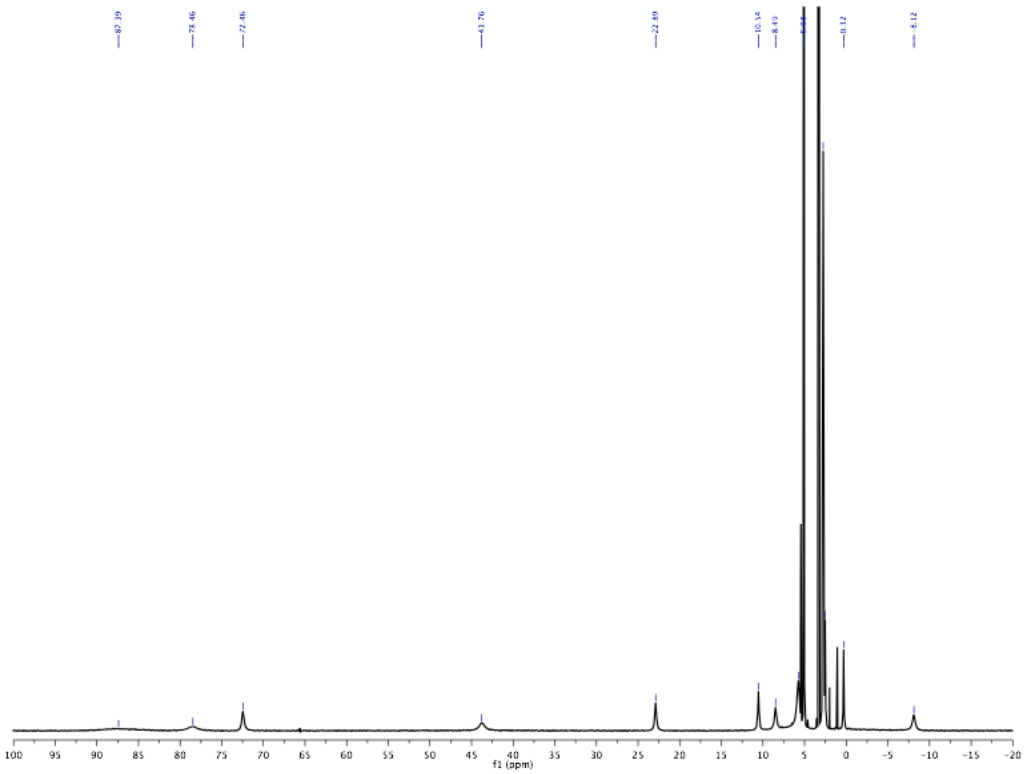

Figure B.11 ^{1}H NMR spectrum of LCo_3(*p*-dimethylaminobenzoate)$_3$ in CD_3OD at 25 ºC.

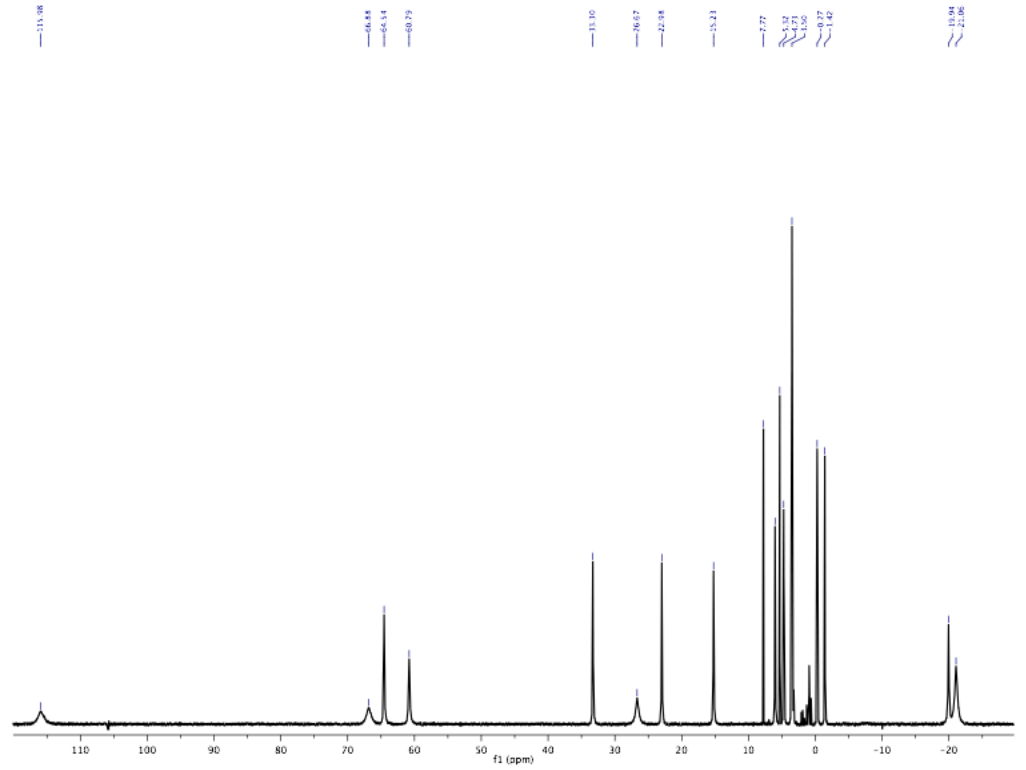

Figure B.12 ^{1}H NMR spectrum of LCo_3(*p*-trifluoromethylbenzoate)$_3$ in CD_2Cl_2 at 25 ºC.

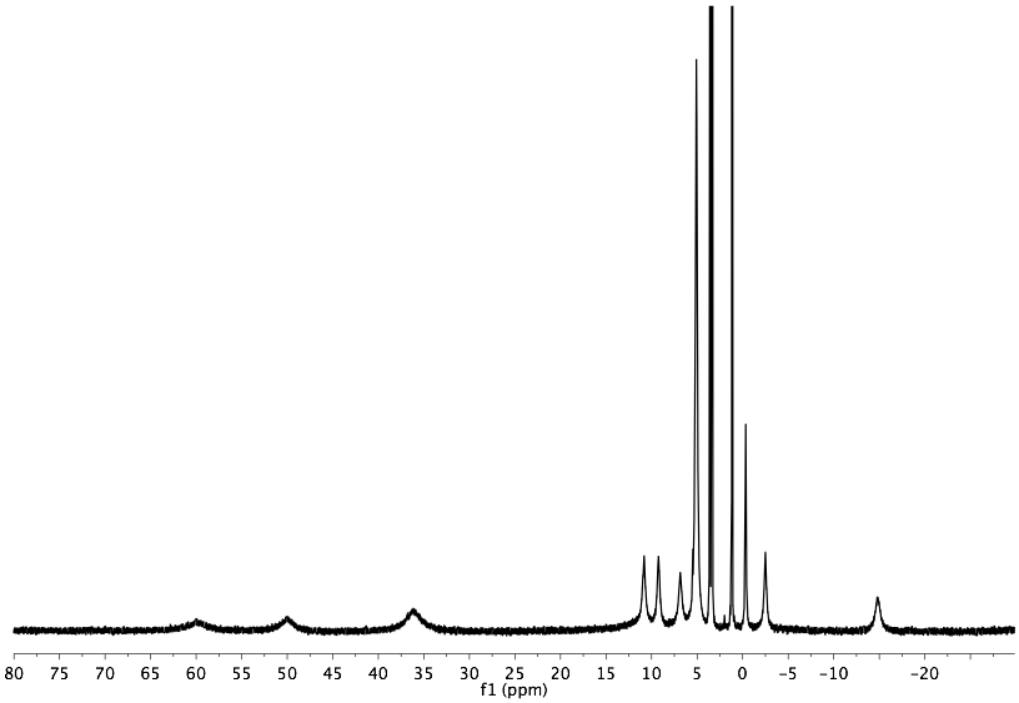

Figure B.13 ^{1}H NMR spectrum of $[LCo_3(EtOH)(NO_3)_2](NO_3)$ in CD_3OD at 25 °C.

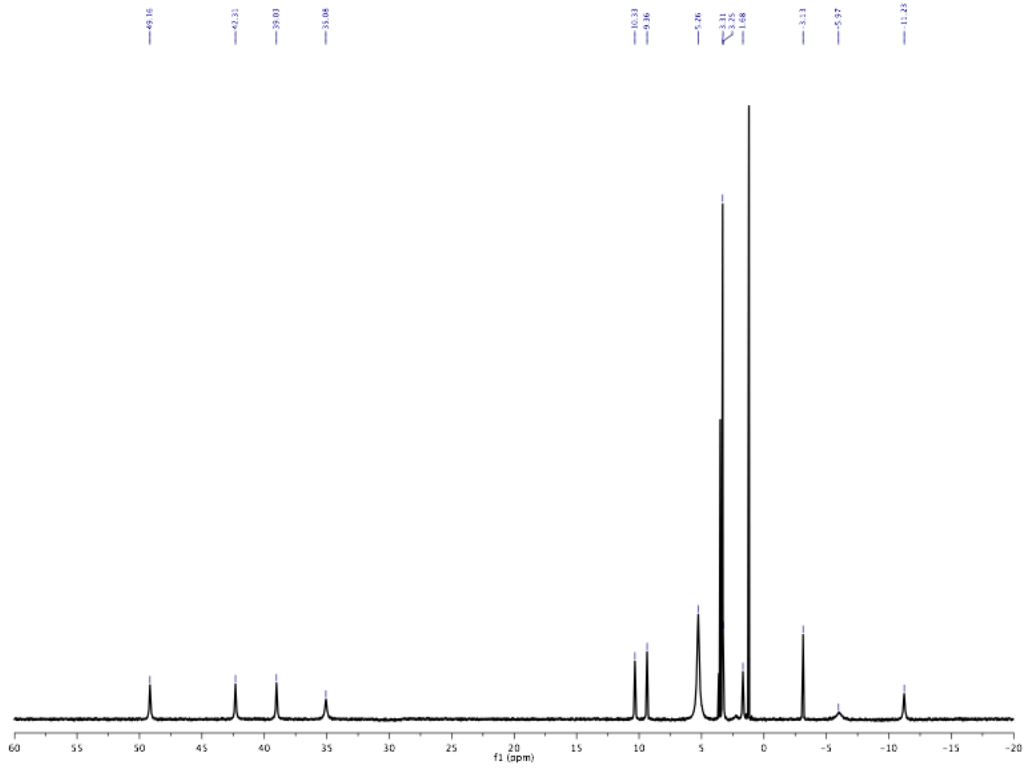

Figure B.14 ^{1}H NMR spectrum of $[LCo_3(EtOH)_3(OH)](BF_4)_2$ in in CD_3OD at 25 °C.

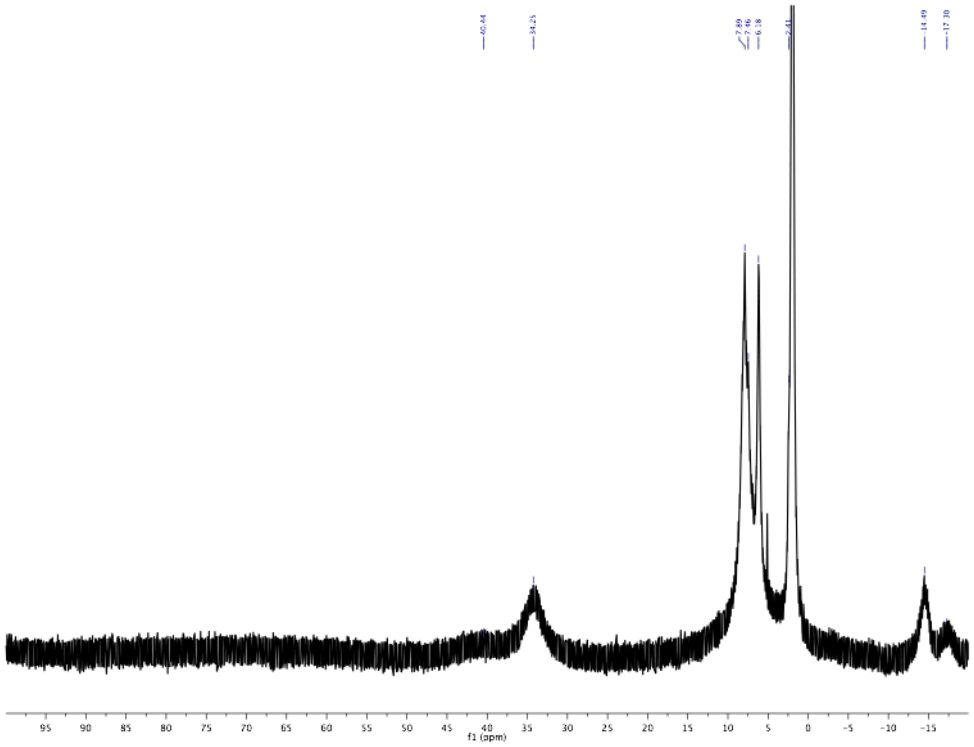

Figure B.15 ^{1}H NMR spectrum of $[LMn_3O(CH_3CN)_3]^{n+}(ClO_4)_n$ in CD_2Cl_2 at 25 ºC.

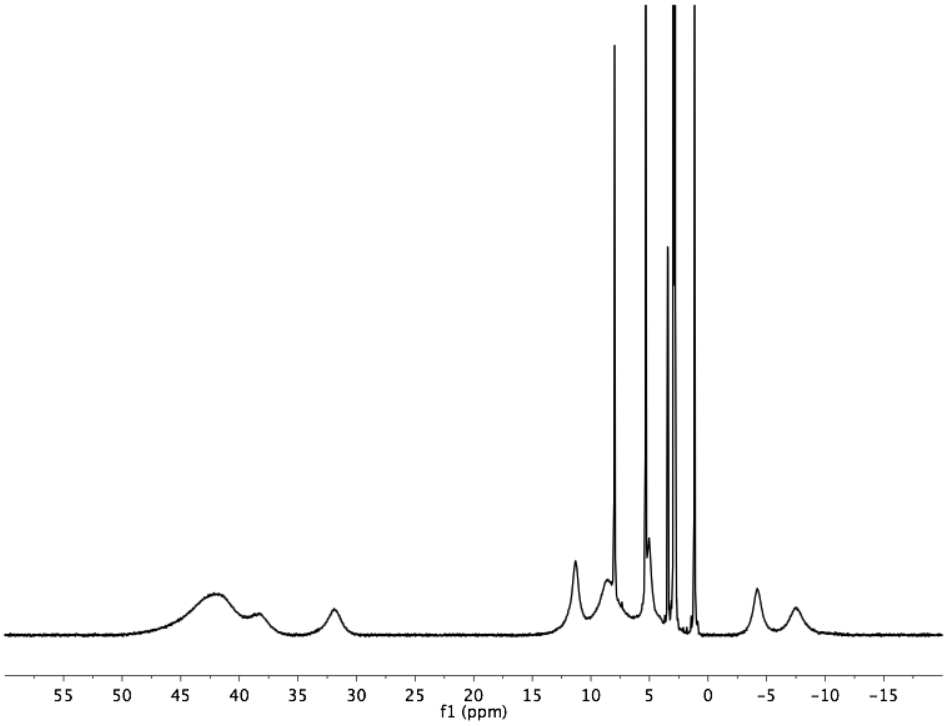

Figure B.16 ^{1}H NMR spectrum of **2** in CD_2Cl_2 at 25 ºC.

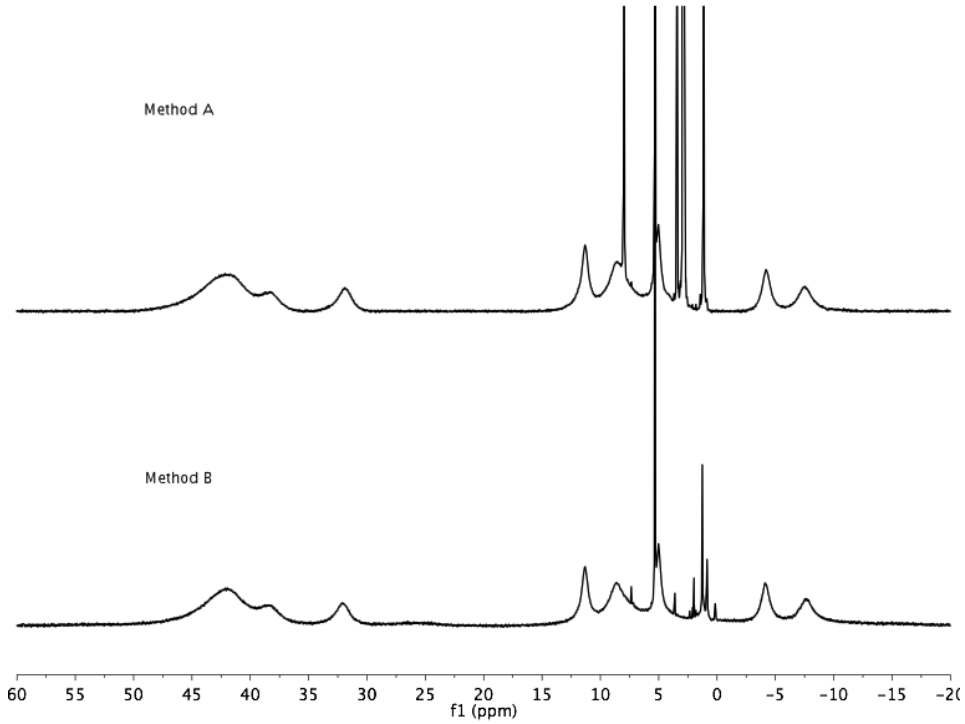

Figure B.17 ^{1}H NMR spectrum of **2** from Methods A and B in CD_2Cl_2 at 25 ºC.

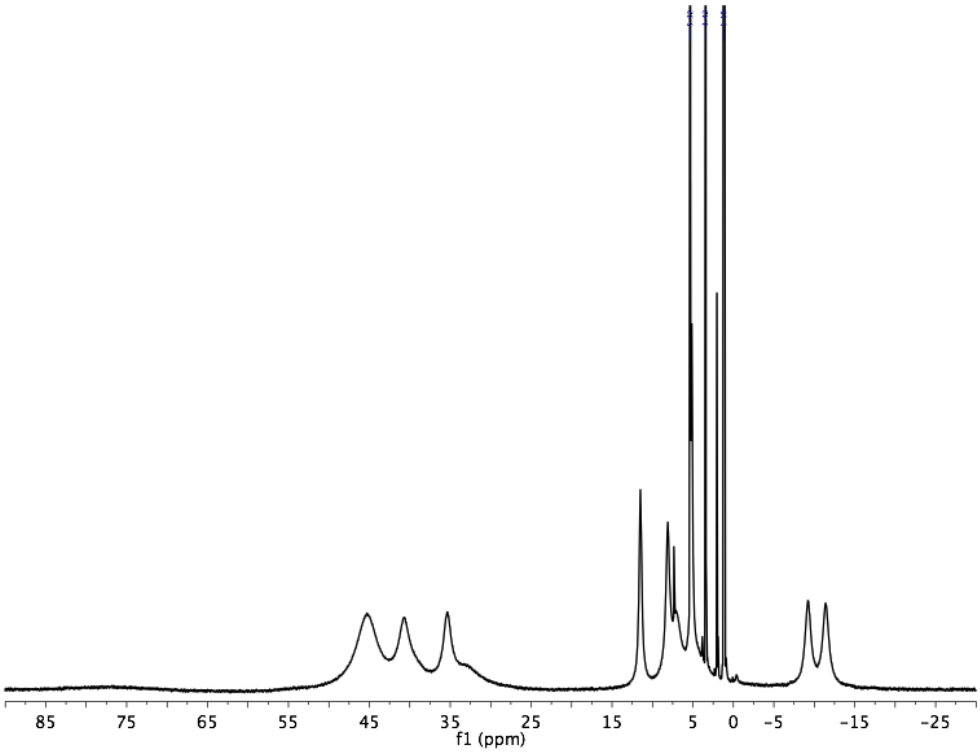

Figure B.18 ^{1}H NMR spectrum of **3** in CD_2Cl_2 at 25 ºC.

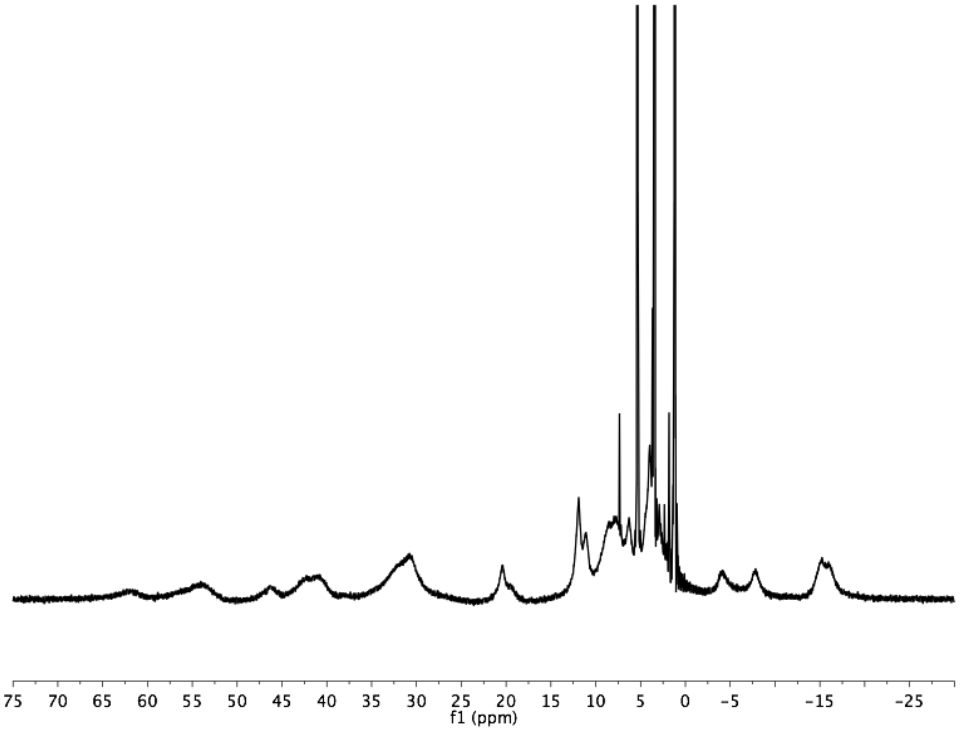

Figure B.19 ^{1}H NMR spectrum of **4** in CD_2Cl_2 at 25 ºC.

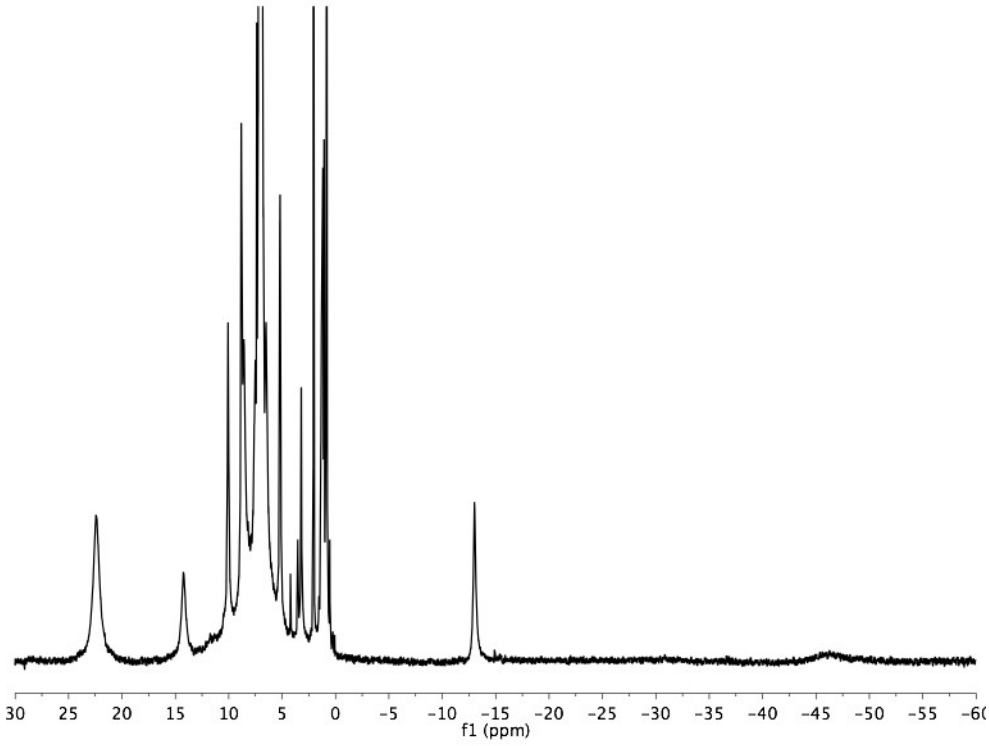

Figure B.20 ^{1}H NMR spectrum of **5** in C_6D_6 at 25 ºC.

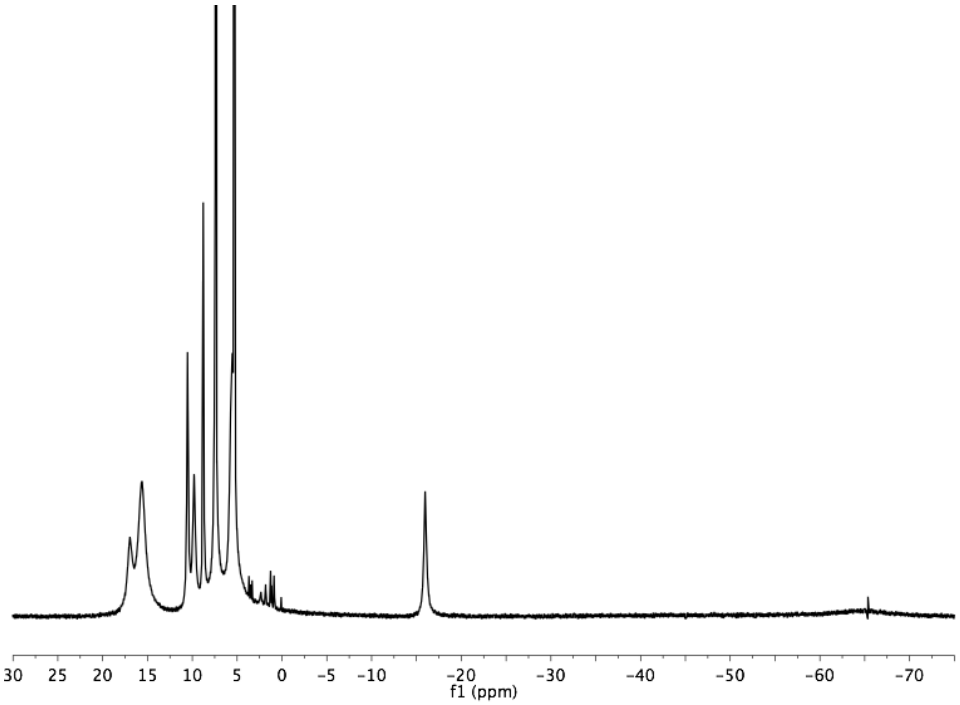

Figure 21 ^{1}H NMR spectrum of **6** in CD_2Cl_2 at 25 ºC.

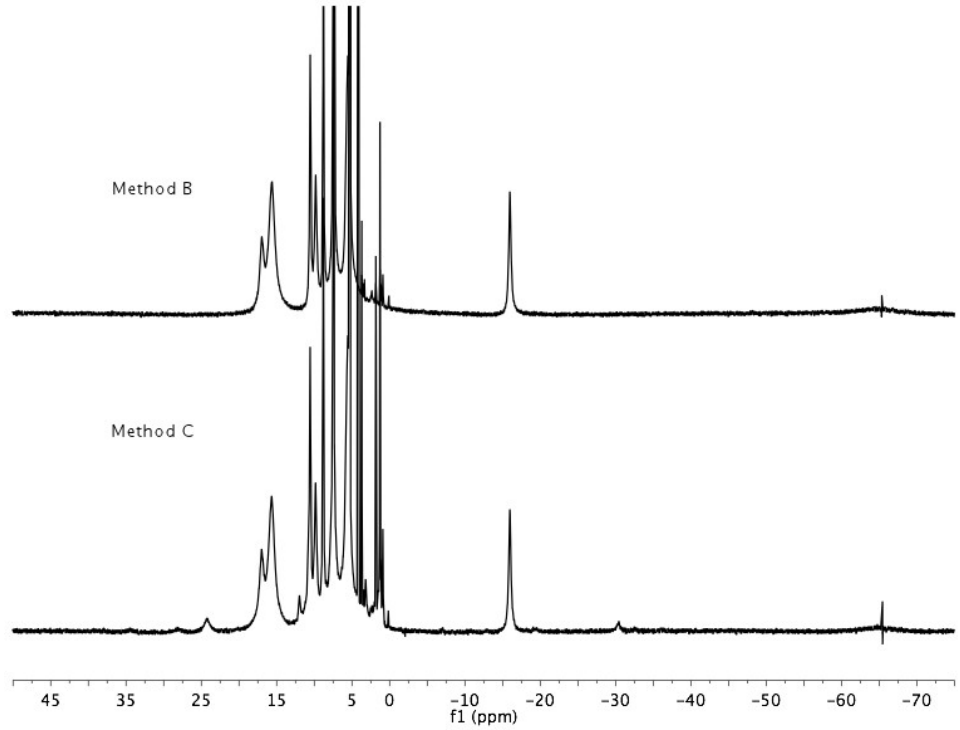

Figure B.22 ^{1}H NMR spectrum of **6** synthesized from Methods B and C in CD_2Cl_2 at 25 ºC.

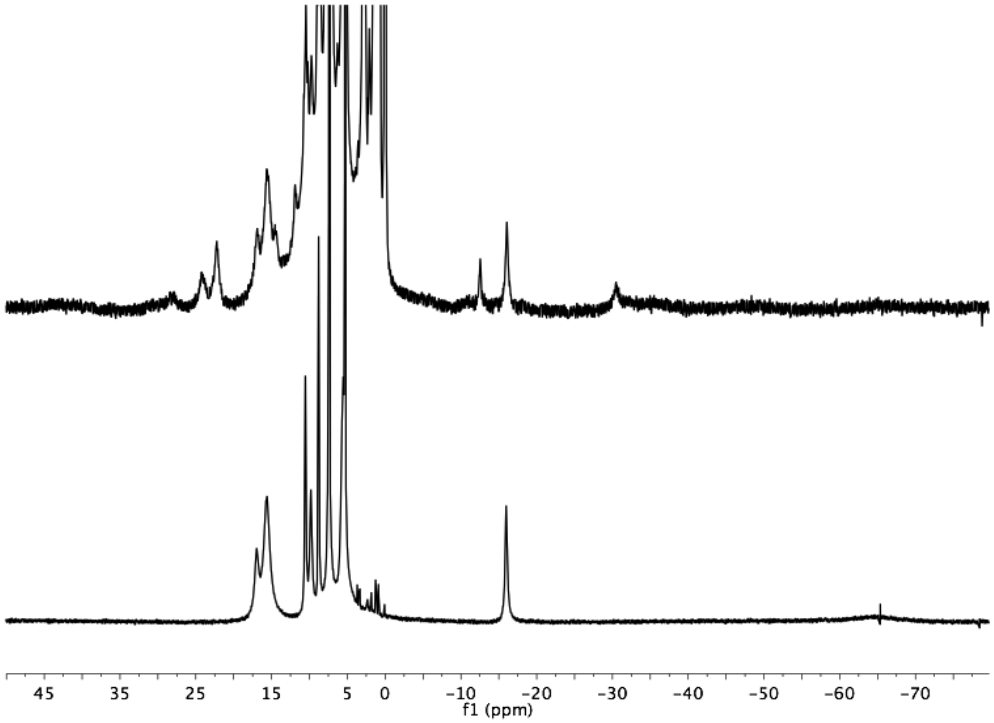

Figure B.23 ^{1}H NMR spectra of **6** both purified (bottom) and synthesized from **4** and O_2 (Method D; top) in CD_2Cl_2 at 25 °C.

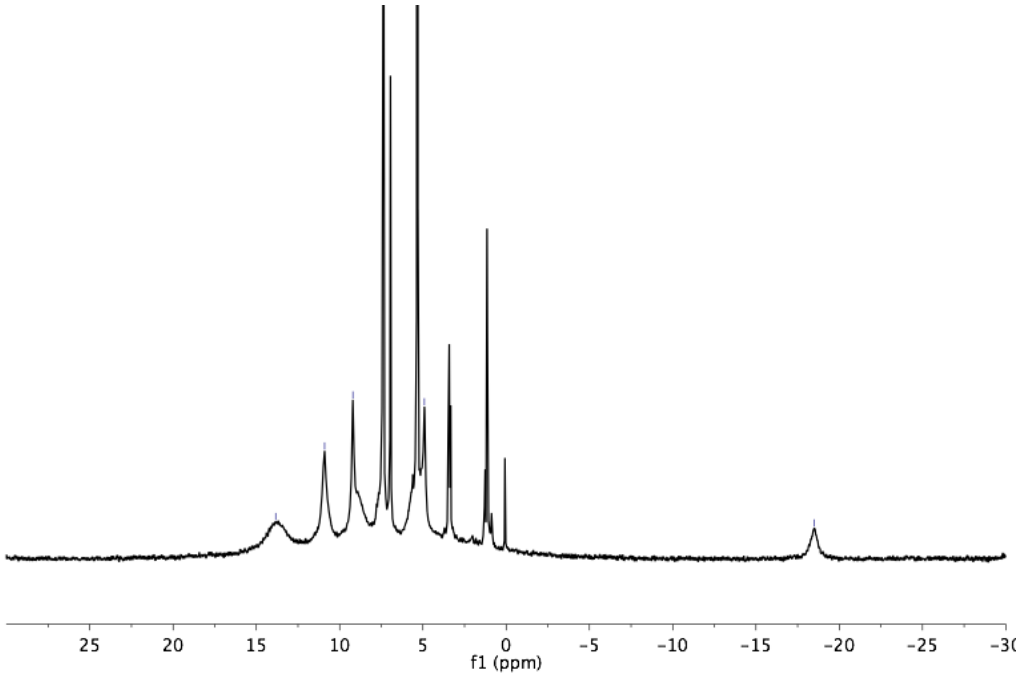

Figure B.24 ^{1}H NMR of $[LMn^{III}Mn^{IV}{}_3O_4(OAc)_3]SbCl_6$ (**6**$^{+}$) in CD_2Cl_2 at 25 °C.

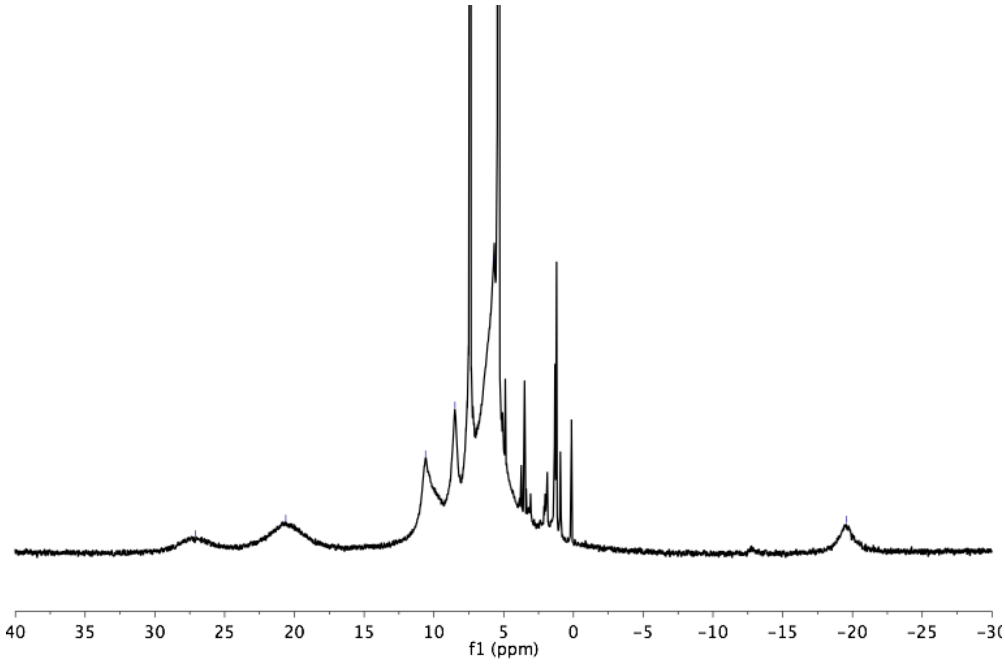

Figure B.25 ^{1}H NMR of [LMn$^{III}_{3}$Mn^{IV}O$_4$(OAc)$_3$]CoCp$_2$ (**6**$^{-}$) in CD_2Cl_2 at 25 °C.

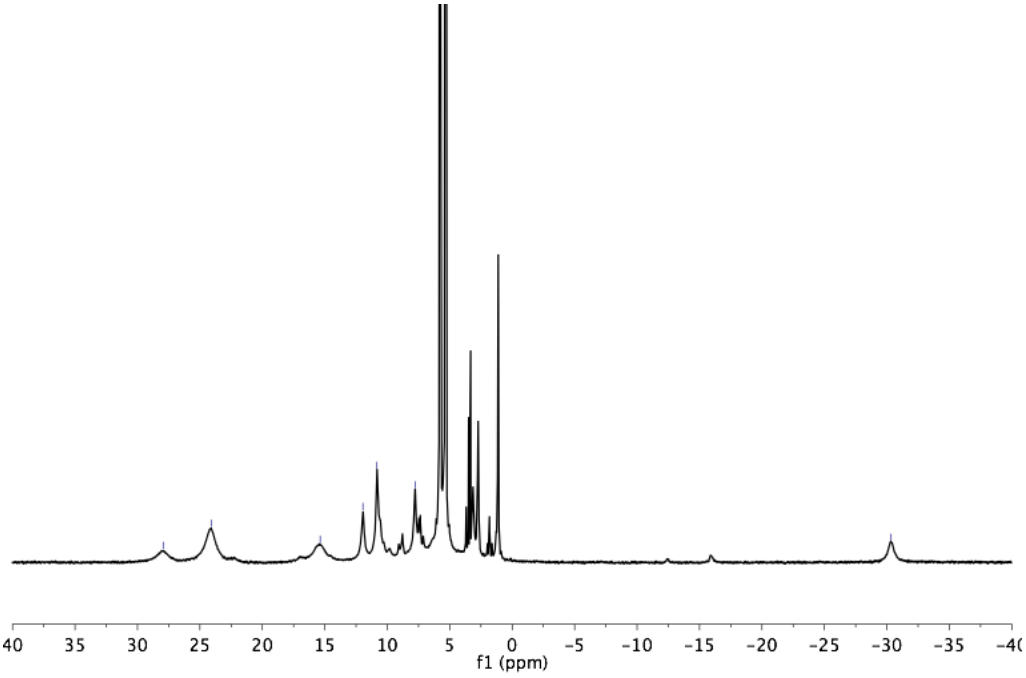

Figure B.26 ^{1}H NMR of [LMn$^{III}_{3}$Mn^{IV}O$_4$(OAc)$_3$]H (**6H**) in CD_2Cl_2 at 25 °C.

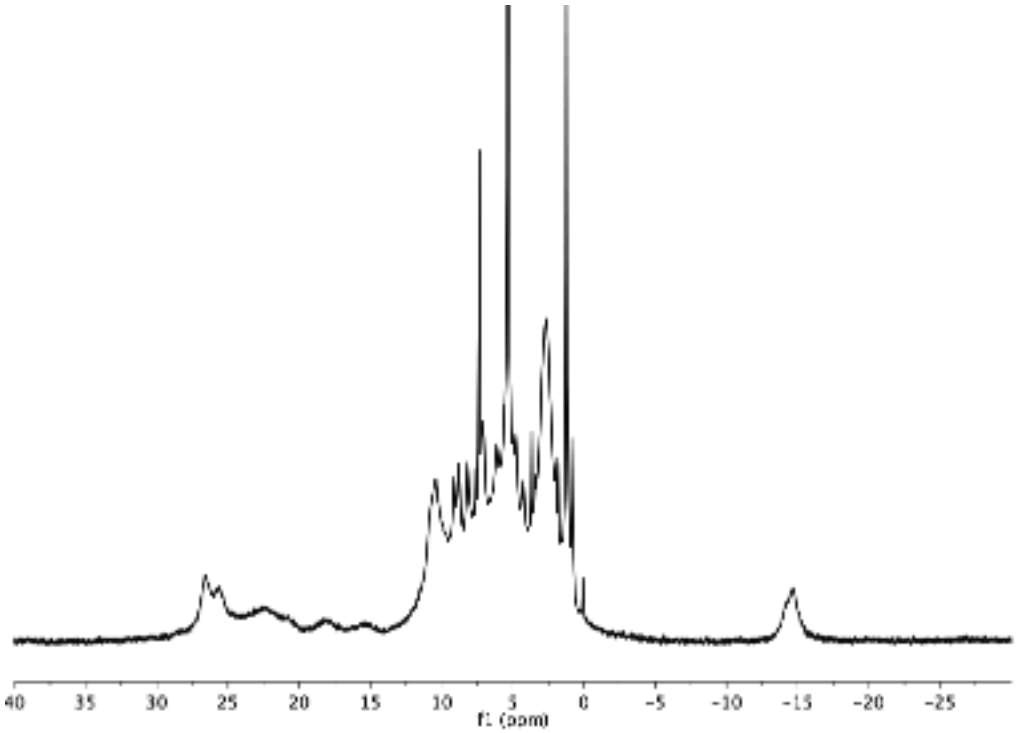

Figure B.27 ^{1}H NMR spectra of **7** in CD_2Cl_2 at 25 °C.

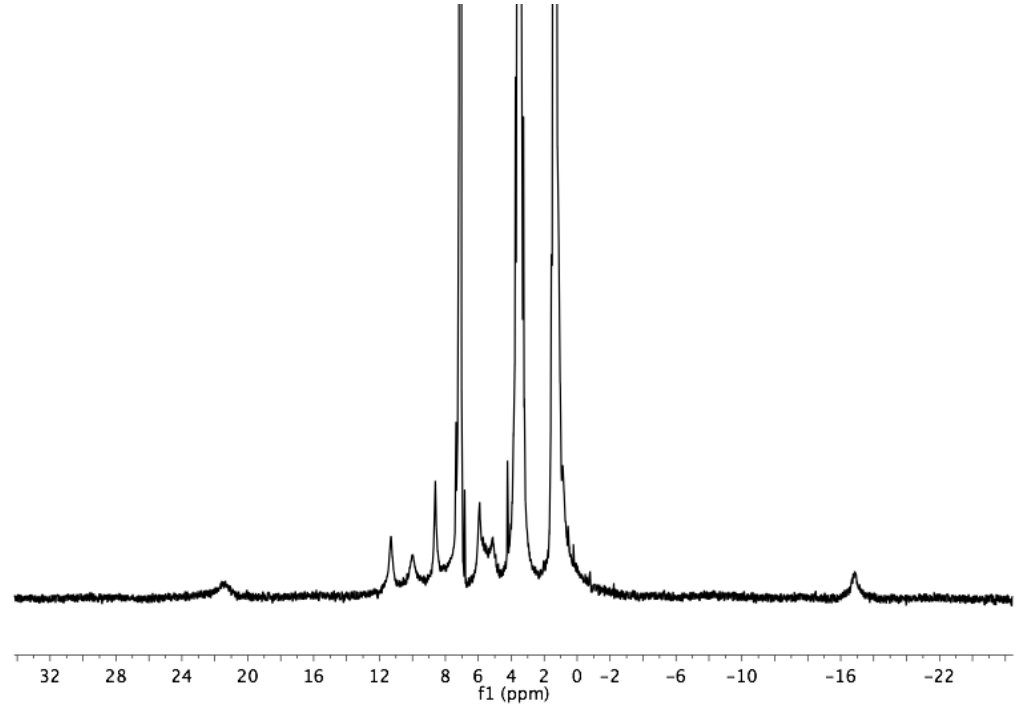

Figure B.28 ^{1}H NMR of **8** in C_6D_6 with a drop of THF for solubility at 25 °C.

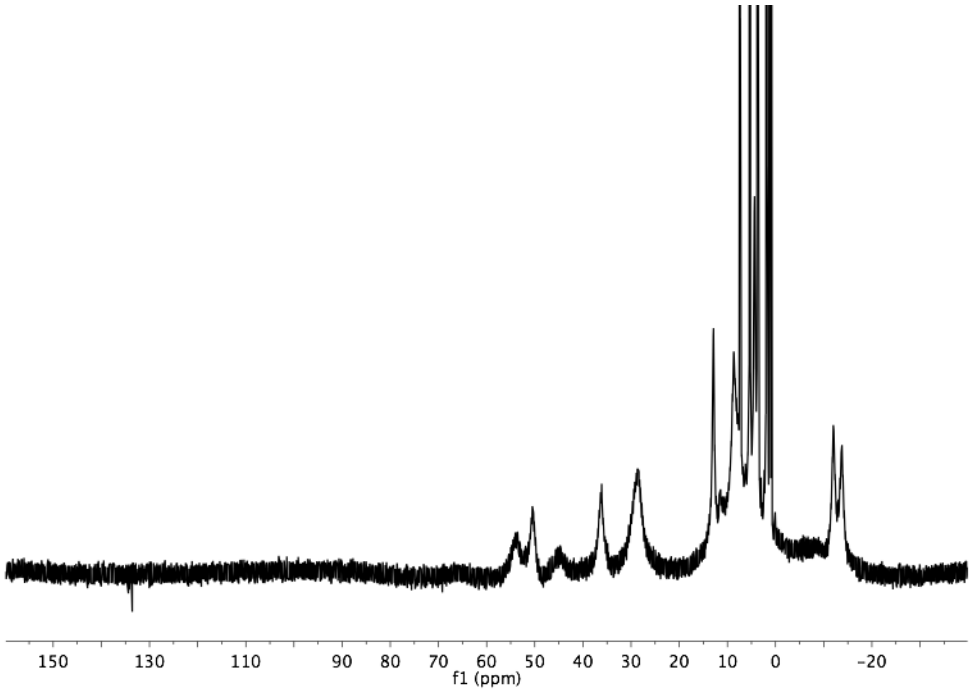

Figure B.29 ^{1}H NMR of **9** in CD_2Cl_2 at 25 ºC.

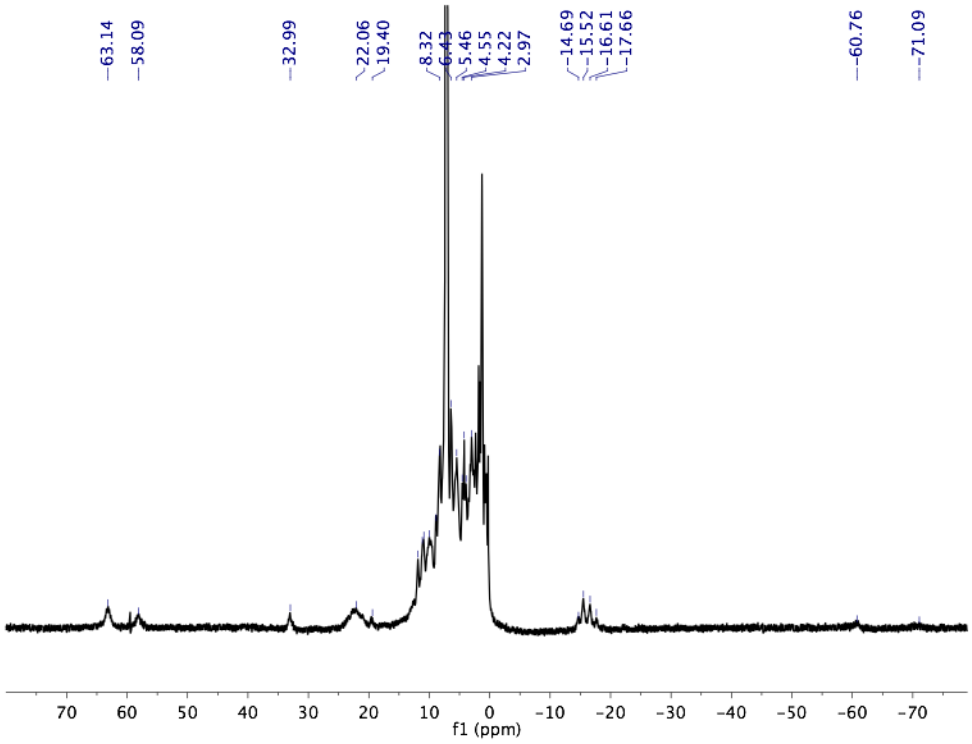

Figure B.30 ^{1}H NMR of $LMn^{IV}_3CaO_4(OAc)(PRABOH)$ (**11**) in C_6D_6 at 25 ºC.

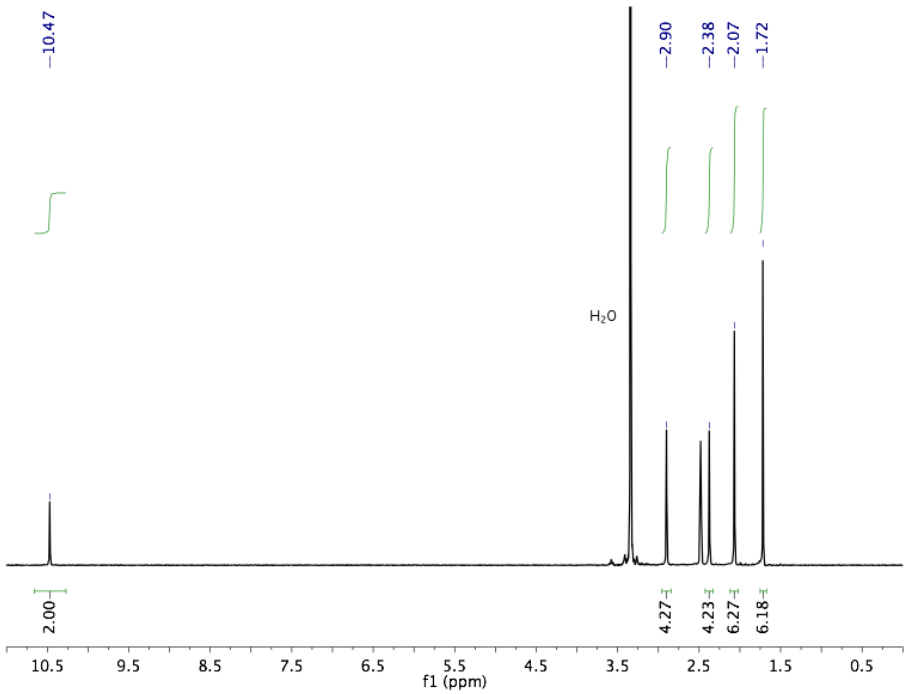

Figure B.31 ^{1}H NMR of **HON_4OH** in d_6-DMSO at 25 °C.

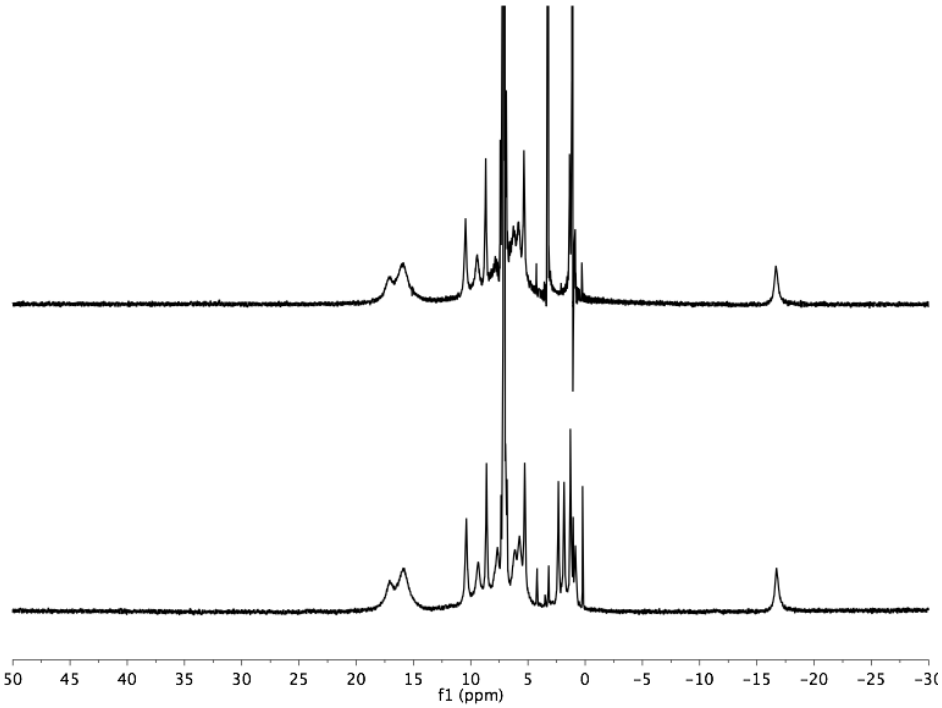

Figure B.32 ^{1}H NMR of **6** as synthesized by Method B (top), or from **8** and $Mn(OTf)_2$ (bottom). Both are in C_6D_6 at 25 °C.

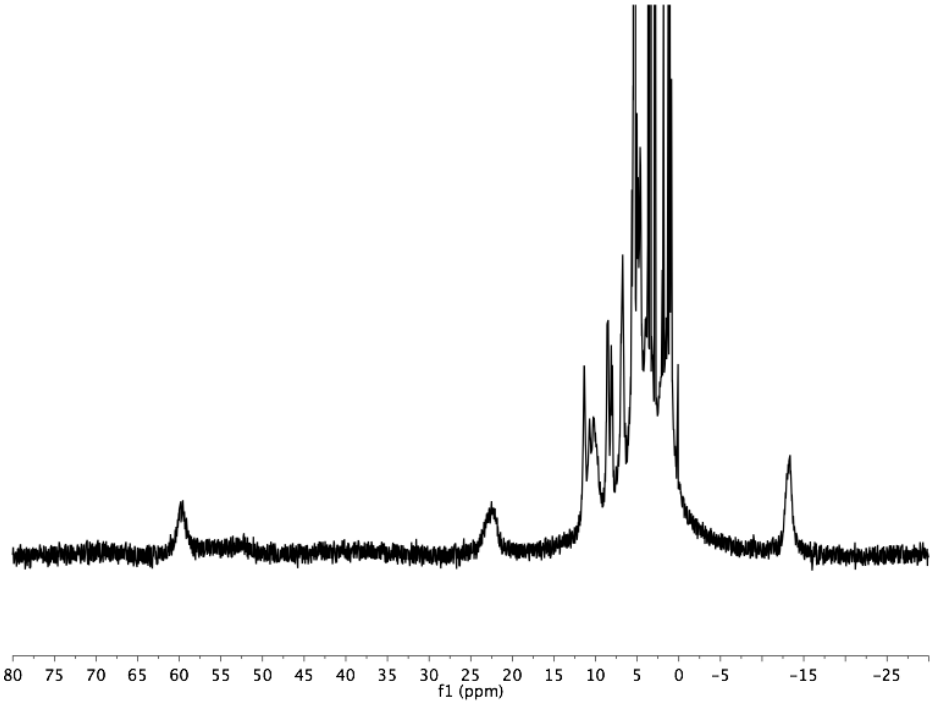

Figure B.33 ^{1}H NMR of $LMn^{IV}_{3}CaO_4(ON_4O)(OAc)$ (**14**) in CD_2Cl_2 at 25 °C.

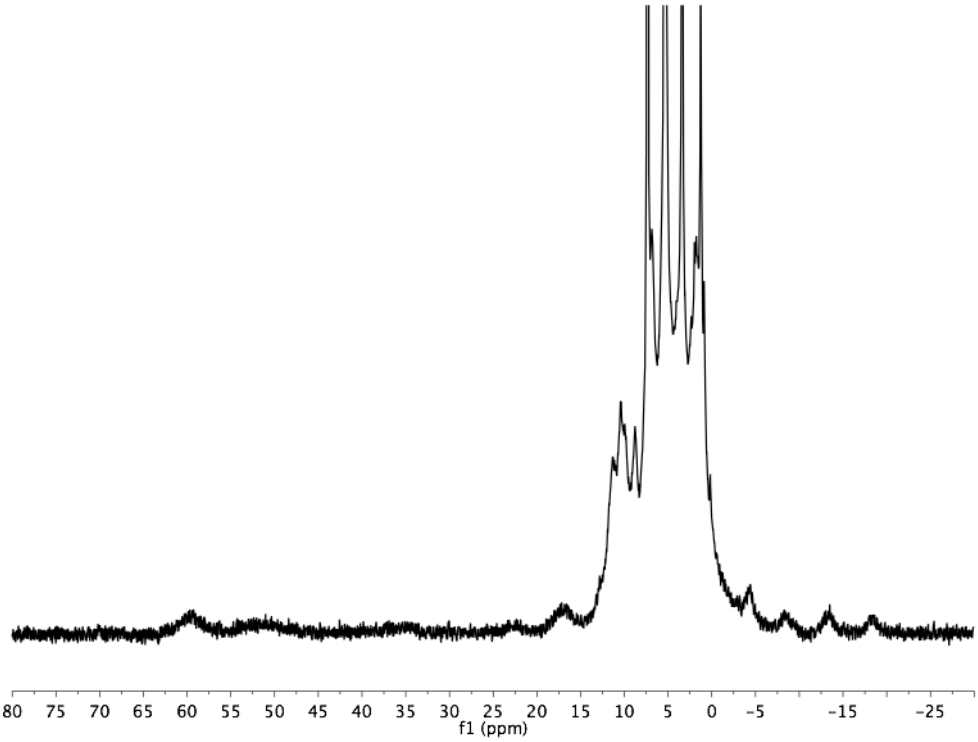

Figure B.34 ^{1}H NMR of **15** in CD_2Cl_2 at 25 °C.

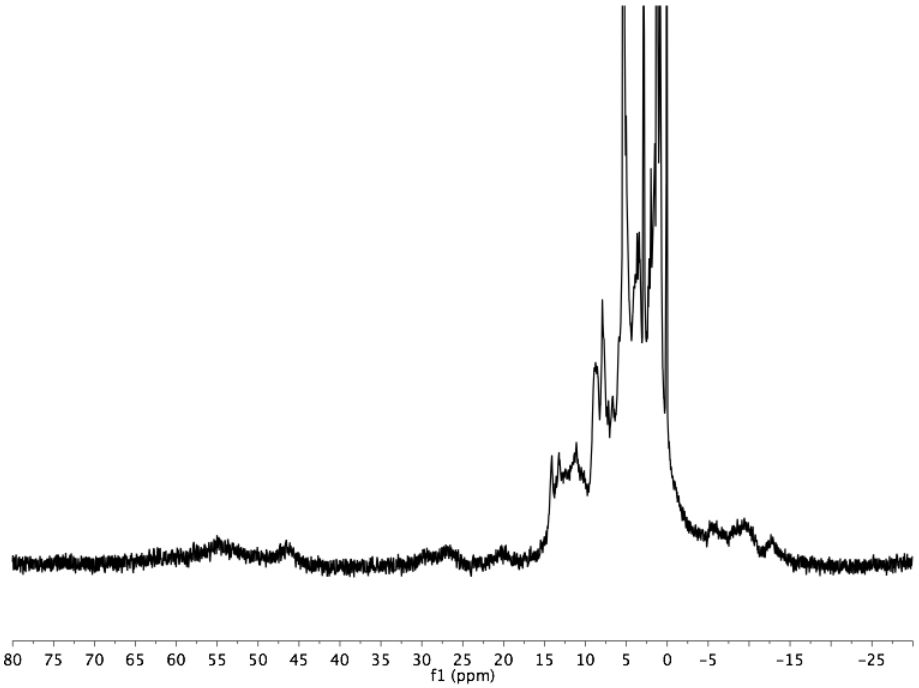

Figure B.35 ^{1}H NMR of **16** in CD_2Cl_2 at 25 ºC.

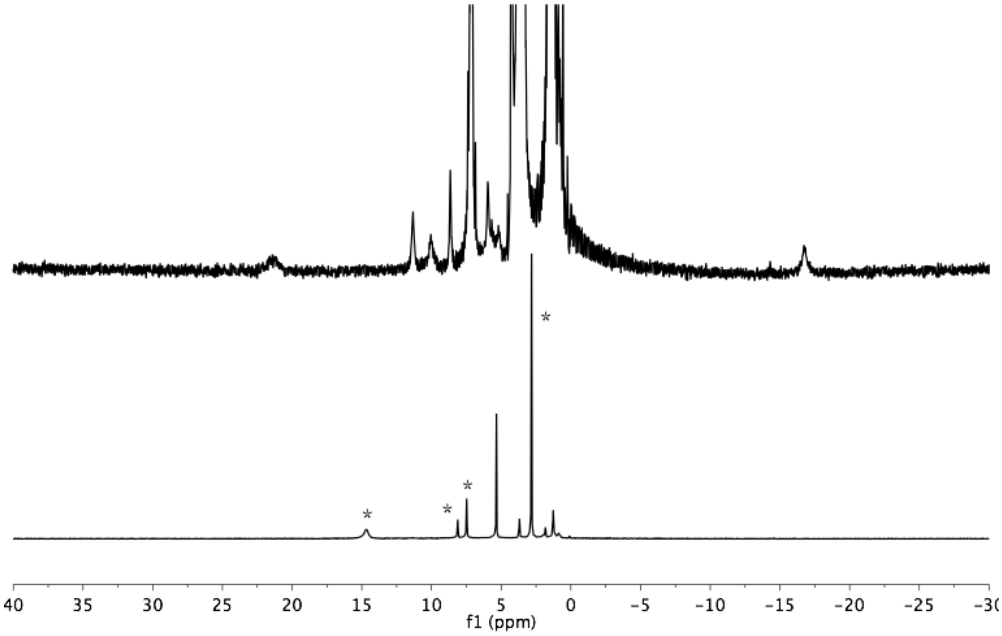

Figure B.36 ^{1}H NMR of the CH_2Cl_2 fraction (bottom, with peaks of LutHOTf starred, CD_2Cl_2 at 25 ºC) and benzene fraction (top, C_6D_6 w/ drop of THF, 25 ºC) of the non-reaction of **8** and LutHOTf. The paramagnetic peaks of the top spectrum match those of pure **8** (Figure B.28.)

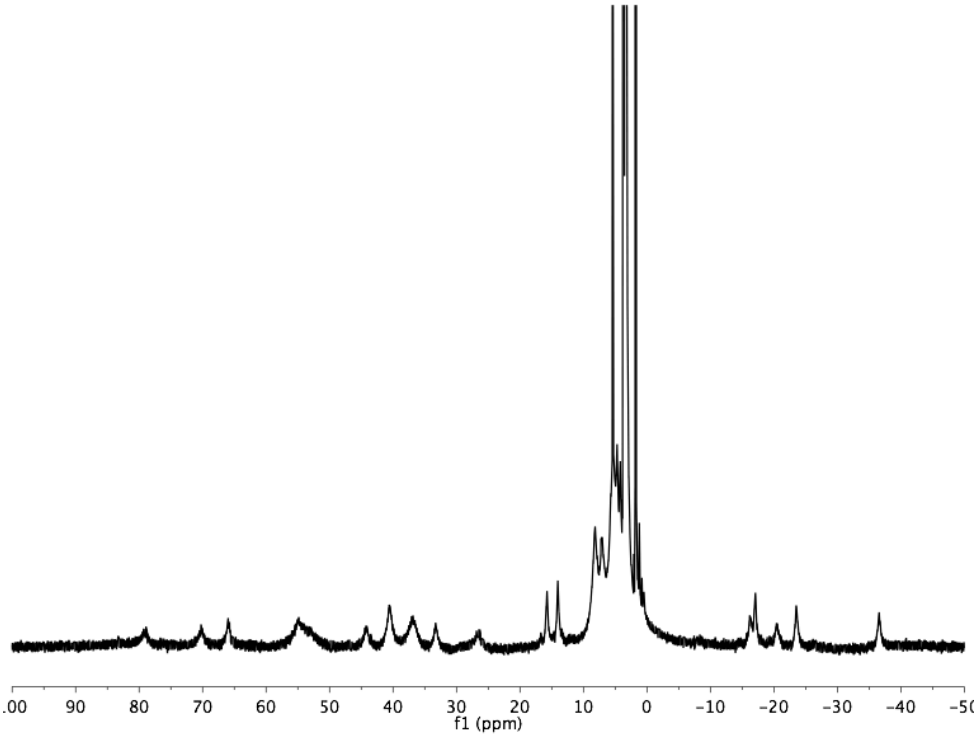

Figure B.37 ^{1}H NMR of $[LMn^{II}_{2}Mn^{III}_{2}O(OAc)_{2}(OMe)(OTf)]OTf$ in CD_3OD at 25 ºC.

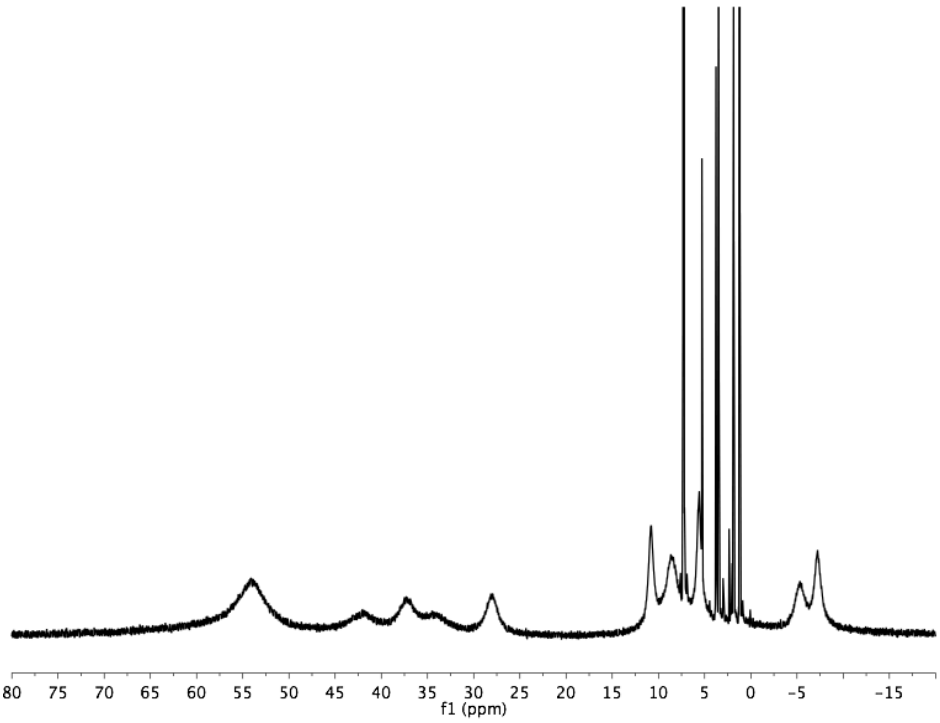

Figure B.38 ^{1}H NMR of $[LMn^{II}_{3}Mn^{III}O_{1}(OAc)_{3}]_{2}\bullet 2OTf^{-}$ in $CDCl_3$ at 25 ºC.

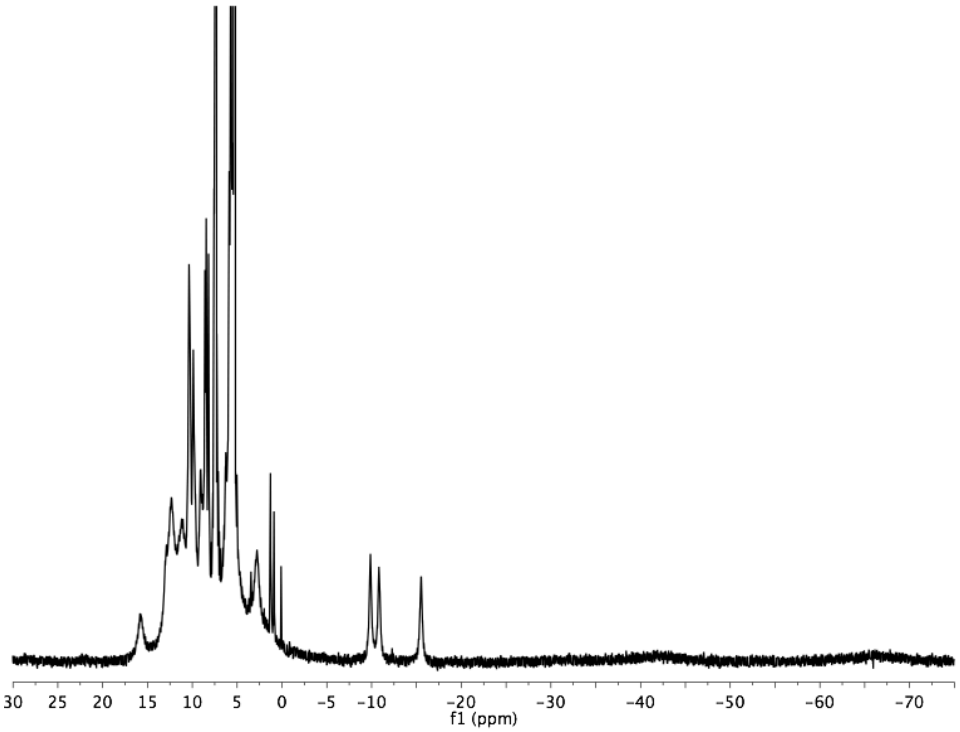

Figure B.39 ^{1}H NMR of $LMn^{III}_{2}Mn^{IV}_{2}O_{4}(OAc)_{2}(OTf)$ in $CD_{2}Cl_{2}$.

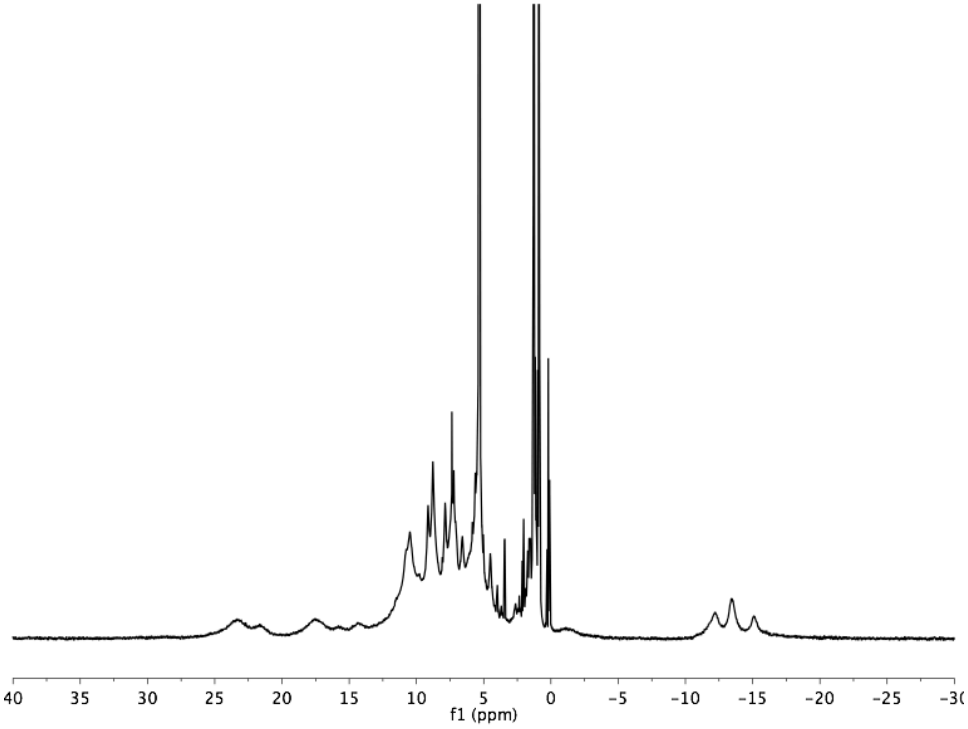

Figure B.40 ^{1}H NMR of $[LMn^{III}_{2}Mn^{IV}_{2}O_{4}(OAc)_{2}(pyr)_{2}][OTf]$ in $CD_{2}Cl_{2}$.

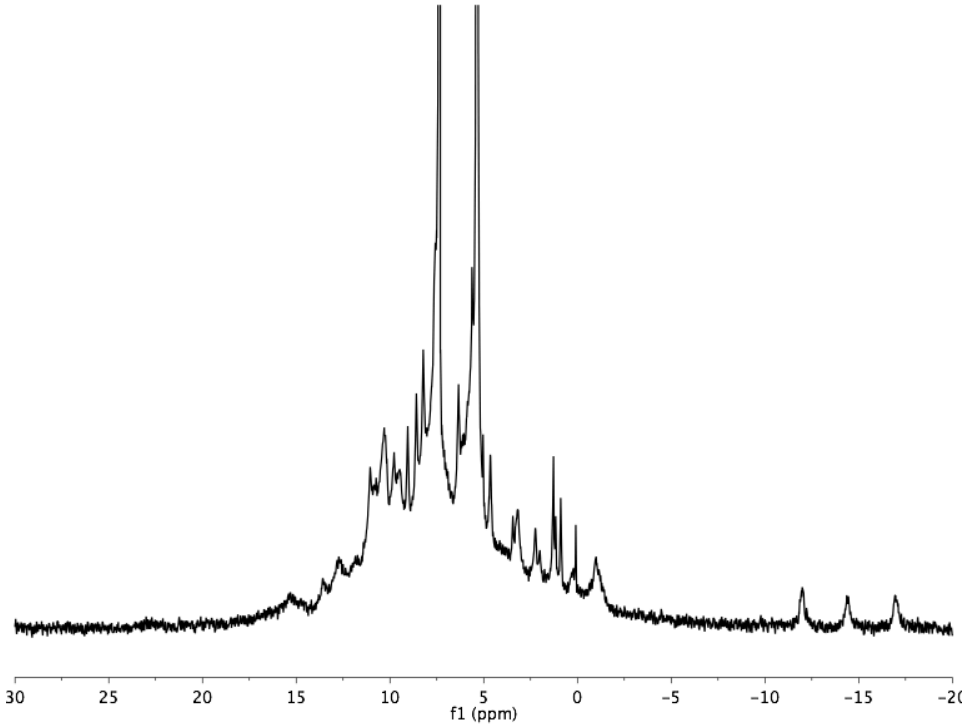

Figure B.41 ^{1}H NMR of $LMn_4O_4(OAc)(OTf)_2$ in CD_2Cl_2.

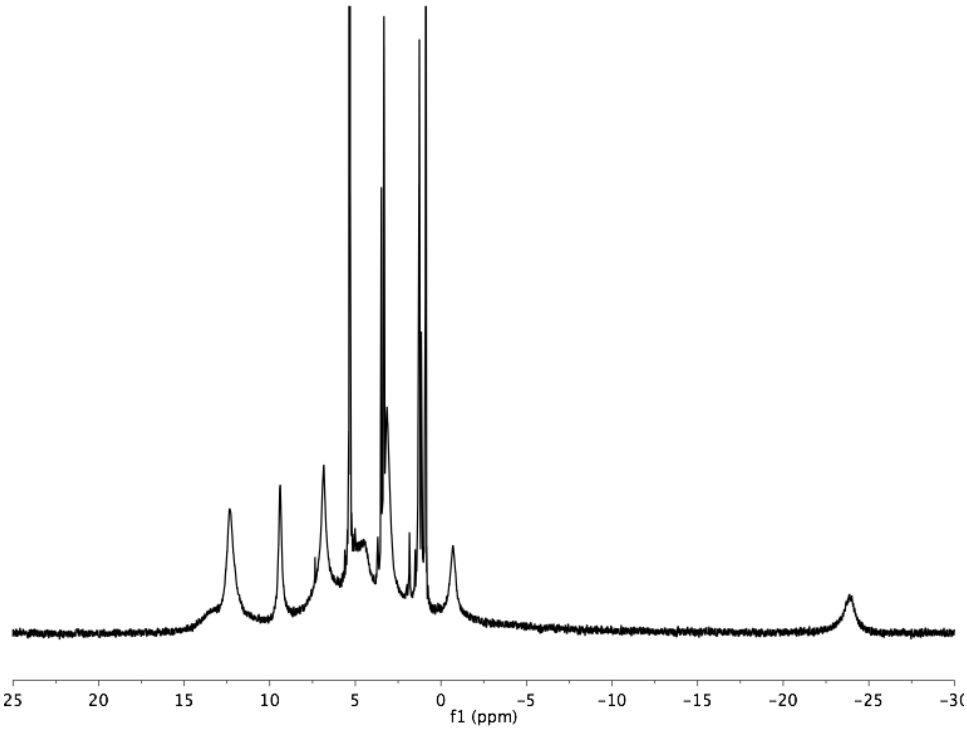

Figure B.42 ^{1}H NMR spectrum of **$LMn^{IV}_3ScO_4(cymCOO)_3(OTf)$** in CD_2Cl_2 at 25 °C.